

**Linear Acoustic Waves Induced in a Cylindrical Solid Target
by Particle Beam in $e^- - e^+$ Colliders**

A dissertation presented

by

Olufemi Segun Adeyemi

to

The Department of Physics

in partial fulfillment of the requirements

for the degree of

Doctor of Philosophy

in the subject of

Theoretical Physics

Universität Hamburg

Hamburg, Germany

March 2015

Committee for Dissertation: Dr. Klaus Flöttmann
Prof. Dr. Gudrid Moortgat-Pick

Committee for Disputation: Prof. Dr. Martin Eckstein
Prof. Dr. Gudrid Moortgat-Pick

Disputation Date: 20.05.2015

Chairman of the Board of Examiners: Prof. Dr. Ludwig Mathey

Chairman of the Doctoral Committee: Prof. Dr. Jan Louis

Head of Physics Department: Prof. Dr. Heinrich Graener

**Lineare akustische Wellen erzeugt durch Teilchenstrahlen in
einem zylindrischen Festkörpertarget eines $e^+ - e^-$ Colliders**

Dissertation

zur Erlangung des Doktorgrades
des Department Physik
der Universität Hamburg

vorgelegt von

OLUFEMI SEGUN ADEYEMI

aus Geburtsort

Lagos, Nigeria

Hamburg

2015

Gutachter/in der Dissertation:	Dr. Klaus Flöttmann Prof. Dr. Gudrid Moortgat-Pick
Gutachter/in der Disputation:	Prof. Dr. Martin Eckstein Prof. Dr. Gudrid Moortgat-Pick
Datum der Disputation:	20.05.2015
Vorsitzender des Prüfungsausschusses:	Prof. Dr. Ludwig Mathey
Vorsitzender des Promotionsausschusses:	Prof. Dr. Jan Louis
Dekan des Fachbereichs Physik:	Prof. Dr. Heinrich Graener

Abstract

A future high energy lepton collider will demand high luminosities to achieve its physics goals. For the electron-positron linear collider, the generation of the desired amount of positrons is a non-trivial problem: the positron production target has to survive huge amounts of energy deposited by the bombardment of intense beams of electrons or photons. This causes a rapid increase of the temperature in the target within a very short time period. The resulting deformation due to the induced pressure waves can substantially shorten the operating life-span of the target material. In this work, we study linear effects of induced stress in a solid target through pressure acoustic waves using continuum mechanics. We derived analytical solutions for different cases and imposed different boundary conditions. The application of the model to the SLC positron target gave us the results which are in agreement with the existing literature. In a similar manner, we investigated the effect of single and multiple photon bunches on the conversion target for ILC.

Zusammenfassung

Künftige Hochenergie-Lepton-Collider benötigen sehr hohe Luminositäten, um die physikalischen Zielstellungen zu erreichen. Die Erzeugung der erforderlichen Anzahl von Positronen für lineare Elektron-Positron Collider ist allerdings schwierig: das Positron-Produktionstarget muss erhebliche Belastungen aushalten, da beim Beschuss des Targets mit Elektronen oder Photonen in sehr kurzer Zeit ein enormer Temperaturanstieg erfolgt. Dies erzeugt Druckänderungen und Stresswellen, die die Lebensdauer des Targetmaterials erheblich verkürzen können. In dieser Arbeit wird die Wirkung des Stresses in Festkörpertargets mit Hilfe linearer akustischer Druckwellen aus der Kontinuumsmechanik untersucht. Es werden analytische Lösungen für verschiedene Belastungsfälle bei unterschiedlichen Randbedingungen abgeleitet. Bei Anwendung des Modells auf das SLC Positronentarget wurden die aus der Literatur bekannten Resultate reproduziert. In analoger Weise wurden die Auswirkungen eines einzelnen Photon-Bunches sowie von mehreren Photon-Bunchen auf das Konversionstarget für den ILC untersucht.

Contents

Title Page	i
Abstract	v
Zusammenfassung	vi
Table of Contents	vii
Acknowledgments	xi
Dedication	xii
1 Introduction	3
1.1 Background	4
1.1.1 Generating Positrons: Pair Production	4
1.1.2 Acoustic Generation by Particle Beams in Solid Target Material	6
1.2 Research Problem, Objective and Delimitation	7
1.2.1 Research Problem	7
1.2.2 Research Objective	8
1.2.3 Delimitation of Study	8
1.3 Contribution of this Work	9
1.4 Structure of the Thesis	9
2 The Model	11
2.1 Equation of Conservation of Mass	13
2.2 Equation of Motion (EOM): Cauchy's First and Second Law of Motion	15
2.3 Mie-Grüneisen Equation of State (EOS)	18
2.4 (LAW) Linear Acoustic Waves: Small Amplitude Oscillation	22
3 LAW in a Thin Rod	27
3.1 Dirichlet Problem	30
3.1.1 Energy Density Profile: Rectangular (Uniform) Distribution	31
3.1.2 Energy Density Profile: Triangular (Linear) Distribution	36
3.1.3 Energy Density Profile: Gaussian (Normal) Distribution	41
3.2 Neumann Problem	43
3.2.1 Energy Density Profile: Rectangular (Uniform) Distribution	44
3.2.2 Energy Density Profile: Triangular (Linear) Distribution	45
3.2.3 Energy Density Profile: Gaussian (Normal) Distribution	50

4	LAW in a Cylindrical Disc	55
4.1	Dirichlet Problem	57
4.1.1	Energy Density Profile: Rectangular (Uniform) Distribution	58
4.1.2	Energy Density Profile: Triangular (Linear) Distribution	61
4.2	Neumann Problem	64
4.2.1	Energy Density Profile: Rectangular (Uniform) Distribution	65
4.2.2	Energy Density Profile: Triangular (Linear) Distribution	68
5	Multiple Bunches Effect on LAW	70
5.1	Multi-Bunch Effect on Thin Rods	72
5.1.1	Dirichlet Boundary	72
5.1.2	Neumann Boundary	76
5.2	Multi-Bunch Effect on Cylindrical Disc	79
5.2.1	Dirichlet Boundary	80
5.2.2	Neumann Boundary	82
6	SLC and ILC - Overview and Application	85
6.1	SLAC Linear Collider	86
6.1.1	Overview of Typical Operation	87
6.1.2	Positron Source Production for SLC	89
	SLC Target for Positron Production	90
6.1.3	Stress Analysis in SLC Target	91
	Energy Deposition	91
	Using LAW to Simulate Stress in SLC Target	93
6.2	International Linear Collider	100
6.2.1	Overview of Typical Operation	101
6.2.2	Positron Source Production for ILC	103
	ILC Target for Positron Production	105
6.2.3	Stress Analysis in ILC Target	107
	Results of Thin Rod Approximation of ILC Target Material with Dirichlet BC	108
	Result of Disc Approximation of ILC Target Material	109
7	Conclusion	114
	Bibliography	117
A	Results of LAW in a Thin Rod	120
A.1	Dirichlet BC with Uniform Energy Distribution	121
A.1.1	P (Pa) versus z (m) for different t (s)	121
A.1.2	u (m) versus z (m) for different t (s)	122
A.1.3	P (Pa) versus t (s) for different z (m)	123
A.1.4	u (m) versus t (s) for different z (m)	124
A.2	Dirichlet BC with Linear Energy Distribution	125
A.2.1	P (Pa) versus z (m) for different t (s)	125

A.2.2	u (m) versus z (m) for different t (s)	126
A.2.3	P (Pa) versus t (s) for different z (m)	127
A.2.4	u (m) versus t (s) for different z (m)	128
A.3	Dirichlet BC with Normal Energy Distribution	129
A.3.1	P (Pa) versus z (m) for different t (s)	129
A.3.2	u (m) versus z (m) for different t (s)	130
A.3.3	P (Pa) versus t (s) for different z (m)	131
A.3.4	u (m) versus t (s) for different z (m)	132
A.4	Neumann BC with Linear Energy Distribution	133
A.4.1	P (Pa) versus z (m) for different t (s)	133
A.4.2	u (m) versus z (m) for different t (s)	134
A.4.3	P (Pa) versus t (s) for different z (m)	135
A.4.4	u (m) versus t (s) for different z (m)	136
A.5	Neumann BC with Normal Energy Distribution	137
A.5.1	P (Pa) versus z (m) for different t (s)	137
A.5.2	u (m) versus z (m) for different t (s)	138
A.5.3	P (Pa) versus t (s) for different z (m)	139
A.5.4	u (m) versus t (s) for different z (m)	140
B	Results of LAW in a Disc	141
B.1	Dirichlet BC with Uniform Energy Distribution	142
B.1.1	P (Pa) versus r (m) for different t (s)	142
B.1.2	u (m) versus r (m) for different t (s)	143
B.1.3	P (Pa) versus t (s) for different r (m)	144
B.1.4	u (m) versus t (s) for different r (m)	145
B.2	Dirichlet BC with Linear Energy Distribution	146
B.2.1	P (Pa) versus r (m) for different t (s)	146
B.2.2	u (m) versus r (m) for different t (s)	147
B.2.3	P (Pa) versus t (s) for different r (m)	148
B.2.4	u (m) versus t (s) for different r (m)	149
B.3	Neumann BC with Uniform Energy Distribution	150
B.3.1	P (Pa) versus r (m) for different t (s)	150
B.3.2	u (m) versus r (m) for different t (s)	151
B.3.3	P (Pa) versus t (s) for different r (m)	152
B.3.4	u (m) versus t (s) for different r (m)	153
B.4	Neumann BC with Linear Energy Distribution	154
B.4.1	P (Pa) versus r (m) for different t (s)	154
B.4.2	u (m) versus r (m) for different t (s)	155
B.4.3	P (Pa) versus t (s) for different r (m)	156
B.4.4	u (m) versus t (s) for different r (m)	157
C	Simulation Results for SLC Target	158
C.1	Thin Rod Approximation	159
C.1.1	Dirichlet BC with Normal Energy Distribution: P (Pa) versus t (s) for different z (m)	159

C.2	Disc Approximation	160
C.2.1	Dirichlet BC with Linear Energy Distribution: P (Pa) versus t (s) for different r (m)	160
C.2.2	Neumann BC with Linear Energy Distribution: Pressure (Pa) versus time (s) for different r (m)	161
D	Simulation Results for ILC Target	162
D.1	Thin Rod Approximation	163
D.1.1	Dirichlet BC with Normal Energy Distribution: P (Pa) versus t (s) for different z (m)	163
D.2	Disc Approximation	164
D.2.1	Dirichlet BC with Linear Energy Distribution: Pressure (Pa) versus time (s) for different r (m)	164
D.2.2	Neumann BC with Linear Energy Distribution: Pressure (Pa) versus time (s) for different r (m)	165

Acknowledgments

A journey of a thousand miles must come to an end somehow. And this happy ending of the chapter of my life was made possible because of the guidance, support and kindness of my supervisor, Prof. Dr. Gudrid Moortgat-Pick. I am forever grateful.

In my language there is a saying that “it takes two pair of eyes to bring a child into the world, but it takes the whole village to raise the child”. Beside my supervisor, I would like to express my appreciation to my host institutes, Deutsches Elektronen-Synchrotron and II. Institute for Theoretical Physics, Universität Hamburg, for being a community that encourages development of one’s research skills; also my special thanks to the whole FLC group members for their support, especially during my defence.

I would like to specially thank Dr. Klaus Flöttmann and Prof. Dr. Martin Eckstein for being part of my thesis committee and for their insightful comments and questions. Also my sincere thanks go to Prof. Dr. Ludwig Mathey for overseeing the disputation procedure and all who took time to attend.

I am indebted to Dr. Anthony Hartin, Dr. Ioannis Kourakis, Dr. Alexander Mikhailichenko, Dr. Andriy Ushakov and Dr. Sabine Riemann for their constructive criticism, recommendations, suggestions and words of encouragement during the period of my study.

Outside the “physics world”, I have the privilege of being among unique set of people that make me feel always at home and supported me in every way they could. Among these unique people is my very close friend, Richard S. Gray. His unquantifiable and relentless assistance have made this thesis more readable. I must also thank Mirjam and Tapiwa Samkange for always being there for me. Richard and Tapiwa, thank you for helping me to proofread the text.

My profound gratitude to my parents for supporting my dreams and for always being there to make the “load” lighter. I would also like to thank my brothers for their support and encouragement.

Last but not least, this work would be almost impossible without the financial support of the German Federal Ministry of Education and Research Project R & D Accelerator (“Spin Optimisation”, contract no. 05H12GU7).

*Dedicated to my grandparents,
my parents (Esther and Omotayo)
& my brothers (Adedeji, Olugbenga and Damilola).*

Nomenclature

Symbol	Units	Description
z	m	Longitudinal Coordinate
r	m	Radial Coordinate
ϕ	—	Angular Coordinate
L	m	Length of the Cylindrical Rod
R	m	Radius of the Cylindrical Rod
P	Pa	Pressure
σ	Pa	Stress Tensor
T	Pa	Deviatoric Stress Tensor
ρ	kg/m ³	Mass Density
ρ_0	kg/m ³	Mass Density at Initial State
V	m ³	Volume
V_0	m ³	Volume at Initial State
\mathbf{u}	m	Displacement
\mathbf{v}	m/s	Velocity
\mathbf{F}	N	Force
\mathbf{f}	N/m ³	Force per unit Volume
\mathbf{p}	kgm/s	Momentum
Q	J	Deposited Energy
Q_0	J	Deposited Energy at Initial State
q	J/kg	Deposited Energy per mass
σ_z	m	Standard Deviation of the Gaussian Energy Density Distribution in z-direction

B	m	Mean of the Gaussian Energy Density Distribution in z-direction
r_0	m	Spot size in r-direction
c_s	m/s	Speed of sound
m	kg	Mass
t	s	Time
T_b	s	Bunch Spacing
Γ	—	Grüneisen Coefficient
e^-	—	Electron
e^+	—	Positron
\mathbb{Z}	—	Integers
I	—	Imaginary Number
Erf	—	Error function
J_n	—	Bessel function of order n
\mathbf{H}_n	—	Struve function of order n
RHS	—	Right Hand Side
LHS	—	Left Hand Side

Chapter 1

Introduction

Hadron colliders (like the LHC) have served in many cases as energy frontier machines. As we have learned from past experience, we know that building a new $e^- - e^+$ machine is necessary to complement the physics potential of pp colliders. The discovery of a 125 GeV Higgs boson at the LHC, generates more intriguing questions than it answers [6]. Since the LHC collides protons whose components are quarks and gluons, their collisions produce strongly involved signatures with a large background noise. On the other hand, an $e^+ - e^-$ collider machine like the ILC, will collide electrons and positrons, that are elementary particles with no internal substructure. Also, the ILC measurement will not rely on theoretical assumptions since there is a well-defined initial state. Contrary to the LHC, most events that will be analysed in the ILC detector do not require a trigger. Hence, clean and fully reconstructable events are expected. Physics at the ILC will pave the way to investigate the internal consistency of any new theory with precise measurement.

Although the advantages of building a new $e^- - e^+$ machine are well established, there are still some hurdles to overcome. In building any high energy particle accelerator, it is necessary to critically analyse the materials that will be in direct or indirect contact with the particle beam. Most often, solid materials are used for this purpose. An important example where a solid material will take direct hits from an energetic particle beam is the process of creating the antiparticles¹ in accelerator machines, which is the area of interest of this thesis. Because of this direct interaction of solid material with energetic particles, it is necessary to study whether the foreseen solid material is able to withstand the “work

¹Gas and liquid targets are also used for the production of antiparticles in some accelerators [24, 31].

load”. This is necessary to understand the long-term survival of the solid target material.

Our main quest in this thesis is to answer such questions and to find an analytical approach to describe the reaction of the material thermoelastic behaviour. Before we embark on our main quest, first let us review how the anti-particles (positrons in our case) are produced in an accelerator followed by a brief summary of acoustic waves generation in solids.

1.1 Background

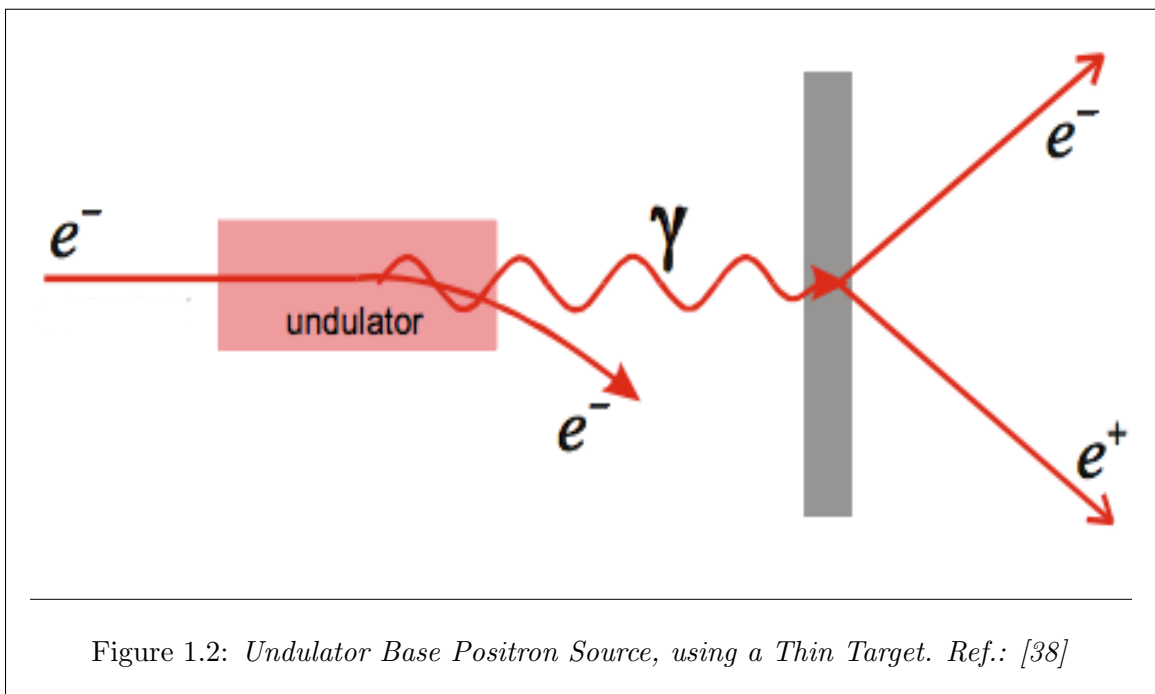
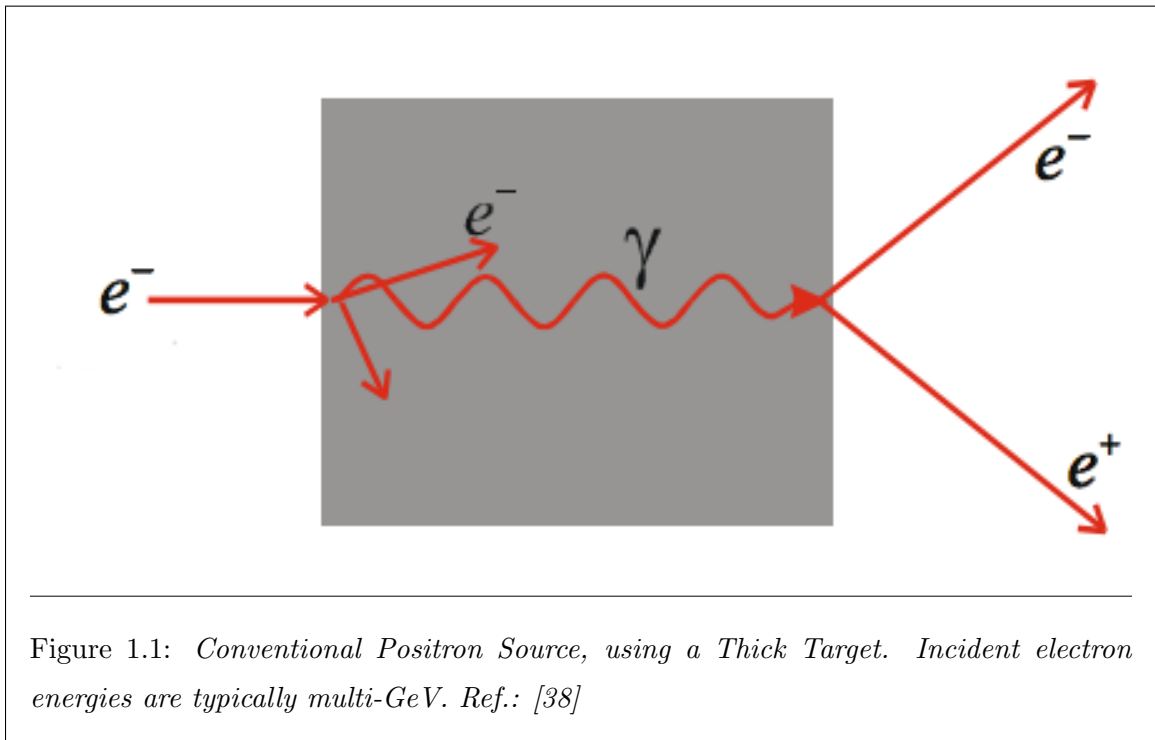
1.1.1 Generating Positrons: Pair Production

In principle, positrons may be created via β -decay or pair production [13, 40]. The most common method employed in high energy accelerators to produce positrons is via the pair-production method [13]. The pair-production is produced by a photon - nucleus interaction in which an $e^- - e^+$ pair is created [38], and the photon must have high enough energy to initiate this interaction. There are various techniques of creating the required photons for the pair production. We will focus on two of these techniques:

1. *Photon generation by bremsstrahlung*: this is commonly initiated by impinging high energy electrons onto high Z material. An electromagnetic cascade shower is triggered and photons are generated via radiation by bremsstrahlung. Within the same high Z material, the photons generated interact with the nucleus of the atoms toward the rear side of the high Z material (see Figure 1.1).

To get at least one positron for one electron hitting the target, the e^- beam is required to have multi-GeV energy and the high Z material must be thick enough to accommodate the shower [13, 38]. This scheme for positron production is called “conventional source”.

2. *Photon generation by undulator*: by passing high energy electrons through an undulator (which is basically a strong magnetic field that is alternating along the travel path of the electron), the electron undergoes oscillations and emits photons. These photons are then impinged on a thin target (see Figure 1.2) to create the needed $e^- - e^+$ pairs [13, 20, 38]. This technique is called the undulator based source.



Depending on the objectives, there are advantages of choosing one technique over the other. Irrespective of which one of the techniques is chosen, one fact is common to both schemes, namely that energy will be deposited on the target material by the incident beam.

This deposited energy causes the lattice of the material to oscillate and in turn induces stress in the material. Therefore, there are criteria to be considered when choosing the incident beam parameters and the design of the target material because there is a stress limit that a material can withstand. The shape and the characteristic of the stress induced are directly related to the deposited energy. So it is necessary to determine the profile of the energy deposition. Typically the distribution of the energy deposition is computed by using Monte-Carlo methods [22] and there are special codes (like FLUKA, EGS etc.) designed to carry out this kind of computation.

1.1.2 Acoustic Generation by Particle Beams in Solid Target Material

It is a known fact that the thermoelastic mechanism is predominant in generating acoustic waves in the case of either electron or photon beam traversing through a solid target [22]. Much work has been done to describe the propagation of elastic waves in solids, work that can be dated as far back as two centuries ago. Extensive studies have been carried out in order to fully understand the behaviour of solid materials under such induced stress.

Stress is the internal force per unit area of the material of a body reacting against an applied load [42]. Stress in a solid can be described using the Cauchy stress tensor; the detailed explanations will be provided in Chapter 2.

The typical approach is well laid out in most continuum mechanics textbooks and literature. To provide a brief background on this, we summarise the common approach (by using the work done in Ref.: [7]). Linear elastic wave equation in solids is derived by combining:

- linearised equation of motion,
- kinematic relations between strain and displacement, and finally
- Hooke's law.

Bargmann in 1973 solved the 1-D case (thin rod to be specific) of the stress waves equation by using the Laplace transform and the information from the incident particle beam

is described by using temperature distribution [7]. Sievers in 1974 also solved the same 1-D case of the stress waves equation for a thin rod by using Fourier-Bessel Series; again the information from the incident beam is described by using temperature distribution [30]. He also went a step further by solving the systems of equation for a disc and a cylindrical solid target. Since the stress state of the material must be described by a tensor, it is very complicated to solve it directly in a system that involves more than one dimension (1-D). The usually employed method was first to solve the equation for the displacement and second to transfer the displacement into stress by using the kinematic relationship and Hooke's law [30].

Worth noting is the implication of using the temperature distribution. This adds another level to the task at hand: transforming the deposited energy distribution into the temperature distribution, which is however relatively trivial in most cases.

The general case of an ideal elastic wave equation is often very complex to solve, and it might require that the equation is reduced by imposing some criteria or conditions like symmetry conditions. We are going to take a slightly different approach. Granted, this approach was initially thought to be hydrodynamical [31, 37] and it was applied to a liquid target or a solid material target that behaves in a fluid-like manner under energetic incident beam. Worth mentioning are some numerical simulations that were done by Ref.: [24] using the equation derived from the approach with a commercial code called FlexPDE. In reality, this methodology is more of a continuum mechanics approach. We are able to apply this approach successfully to solid materials even when the material behaviour under the influence of the incident beam can not yet be classified as fluid-like. Other major contributions of this thesis can be seen below. Furthermore, details of the approach is provided in Chapter 2.

1.2 Research Problem, Objective and Delimitation

1.2.1 Research Problem

As acknowledged earlier, much research work has been done in the field of stress analysis due to a vast application in various fields. Analytical results that can be dated to a century ago are just some of the evidence. With the invention of computers in the last century, numerical analysis software like ANSYS, COMSOL, Elmer etc., have become

a tool that is easy to use for computation and simulation, in order to solve the complex problems in this field.

However a careful consideration is required when using such a tool in order to get an accurate result, because all the numerical analysis solutions are just an approximation, which are prone to many errors. Ref.: [17] lists some common source of errors (like: mesh, mesh size, order, point constraint singularity, etc.) in the finite element analysis, and the result in Ref.: [19] shows some of these shortcomings as well.

1.2.2 Research Objective

In order to be able to justify any computation done on any numerical analysis software packages, we deemed it necessary to compare results obtained in an analytical form (at a very rough estimate if necessary) to the complex numerical solution obtained from the numerical analysis software. Therefore the objective of this study is to present an analytical solution, that can be easily used to calculate the stress induced in solid target. The study will therefore serve as a litmus test for the simulation software used in stress analysis for conversion target in linear collider machines. We considered a simplified version of the problem by studying cylindrical solid targets in an approximation, that is, disc and thin rod.

1.2.3 Delimitation of Study

This work was done under the following assumptions:

1. The study was restricted to an undamped system.
2. Rotational and axial symmetry was imposed on the model because the geometry of most solid targets in a linear collider is cylindrical.
3. Instantaneous energy deposition was assumed since the incident beam needs only a very short time to traverse the material, time that is very small compared to material response time. Obviously, the analytical result can not be used to describe the behaviour of the material during the time when the incident beam traverses the solid target.
4. The study is confined to the case where linear elastic property of the solid material is valid.

Other delimitation imposed will be stated where necessary.

1.3 Contribution of this Work

As stated earlier, the aim of this thesis is to provide an analytical solution: a solution that can be referenced to when solving a complex problem involving linear acoustic waves in solid targets due to incident particles (to be specific, electrons and photons). We can summarise our contribution as follows:

- we derived an analytical solution for a single bunch including different energy deposition profiles.
- we formulated a general expression for the effect of multiple bunches of particle beams hitting the target on the evolution of stress waves by considering two boundary conditions, namely Neumann and Dirichlet boundary conditions.
- we applied the model to the target of the Stanford Linear Collider (SLC), to serve as a test case for checking the model with an existing result. We further applied our findings to the conversion target of the International Linear Collider (ILC).

1.4 Structure of the Thesis

This thesis consists of seven chapters and each chapter is introduced by a content overview (in a written or pictorial form) of the chapter². Below is the brief roadmap of the thesis:

- Chapter 1 presents an introduction and mission statement of the thesis. It also contains background materials, which briefly review previous related literature.
- Chapter 2 provides necessary background knowledge needed to develop the model. In the end, this model (which is an equation to describe the propagation of linear acoustic waves in perfectly elastic solids) was formulated as a consequence of the continuity equation, the equation of motion and Mie-Grüneisen equation of state, by giving special consideration to small perturbations near equilibrium.

²In this chapter, (that is, Chapter 1) and Chapter 7, no content overview is provided

- In Chapter 3 and Chapter 4 analytical solutions for the linear acoustic waves equation in solids are derived. We considered the thin rod and the disc approximation of the solid target with two different boundary conditions and different profiles of deposited energy density.
- Chapter 5 extends the analytical solution in Chapter 3 and 4 to include the effect of multiple bunches.
- Chapter 6 focuses on the principal applications of the analytical solutions to the target of the past linear collider (SLC) and the future generations of linear collider (ILC).
- Chapter 7 concludes the whole thesis with a brief summary of the results, their applicability and suggestion for further studies.

Chapter 2

The Model

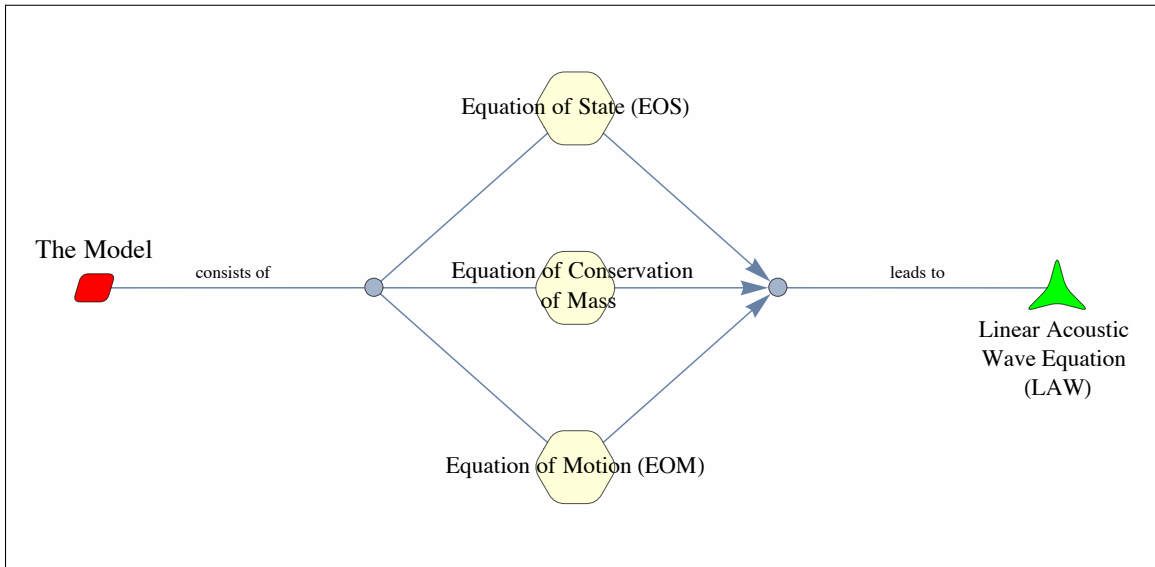


Figure 2.1: *Schematic representation of content overview for this chapter.*

In this chapter, we look at formulating a mathematical model to describe the behaviour of solid material under external load (caused by being struck by relativistic particles) within a linear regime. The linear regime “state” implies that any deformation produced by the external loading does not exceed a certain limit. However, this deformation disappears when the external load is removed and the solid material returns to its initial form. In the case of conversion target in linear accelerator machines, this external load is the deposited energy by the incident beam and our goal is to derive the linear acoustic wave equation caused by this incident beam in a solid conversion target.

To put things in a clear perspective, we itemise the necessary assumptions under which the model is valid [35, 42]:

1. the solid material under consideration is perfectly elastic, that is, it returns to its original form after the removal of stress or pressure;
2. for simplicity we assume that, the solid material is isotropic, meaning, the material properties are the same in all directions;
3. the material is homogeneous and continuously distributed over its volume so that the smallest element cut from the body possesses the same physical properties;
4. a linear regime is investigated by considering small deformation or perturbation in the system, so that any oscillation caused must be near equilibrium;
5. axial symmetry will be imposed since we are interested in a cylindrical solid target;
6. and lastly, no damping is considered.

In reality, no solid material completely satisfies the above assumptions [23, 35]. Experience has shown that microscopic structure of solid material like steel consists of crystals of various kinds and orientation. Hence, at the microscopic level, the material is far from being homogeneous [35]. Interestingly enough, experimental results reveal that, the assumption of homogeneity and isotropy in steel is valid with great accuracy. As put in Ref.: [35], the explanation for this “characteristic is that the crystals are very small; usually there are millions of them in one cubic inch of steel. While the elastic properties of a single crystal may be very different in different directions, the crystals are ordinarily distributed at random and elastic properties of a large piece of metal represent averages of properties of the crystals. As long as the geometrical dimensions defining the form of a body are very

large in comparison with the dimension of a single crystal, the assumption of homogeneity can be used with great accuracy, and if the crystals are orientated randomly the material can be treated as isotropic”.

Since it is obvious that we are not going to consider the behaviour of the solid material being struck by an energetic particle beam at the atomic scale, we will look at the dynamic behaviour of solid material using continuum mechanics. The state of any continuum can be described in terms of its velocity (\mathbf{v}) and density (ρ) and stress ($\boldsymbol{\sigma}$)¹ as a function of position (\mathbf{x}) and time (t). The relationship between these variables can be obtained from the conservation laws. Therefore, it is necessary to look into all the components used in setting up the model:

- equation of conservation of mass (or continuity equation)
- equation of motion
- equation of state.

2.1 Equation of Conservation of Mass

The premise of a continuum concept is that density (ρ), displacement (\mathbf{u}), velocity (\mathbf{v}) and other quantities are continuous differentiable functions in space (\mathbf{x}) and time (t). The total mass of a system is, however, an exception to this assumption.

Let us consider a solid material having a volume V . Let \mathbf{X} be an interior point of the body located in the small element of volume ΔV whose mass is Δm as indicated in Figure 2.2. We define the average density of this volume element by the ratio

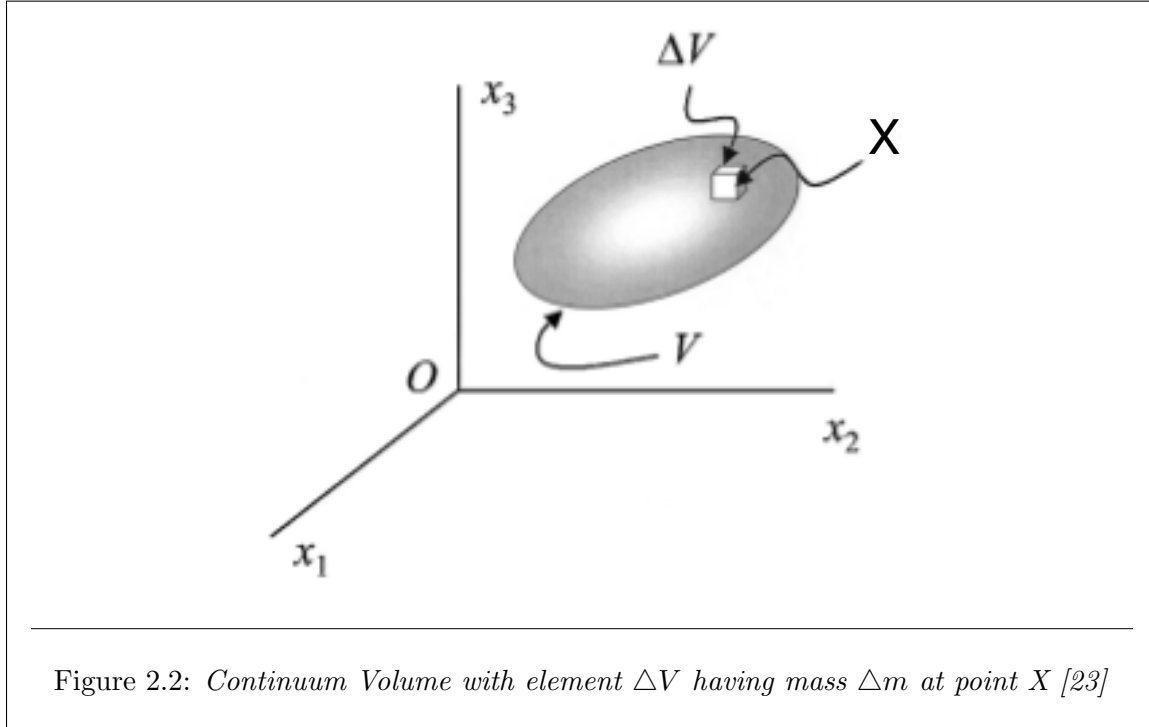
$$\rho_{ave} = \frac{\Delta m}{\Delta V} \quad (2.1)$$

and the density $\rho(\mathbf{X}, t)$ at point \mathbf{X} by the limit of this ratio as the volume shrinks,

$$\rho(\mathbf{X}, t) = \lim_{\Delta V \rightarrow 0} \frac{\Delta m}{\Delta V} = \frac{dm}{dV}. \quad (2.2)$$

Of course, the density is, in general, a scalar function of position and time (i.e. $\rho(\mathbf{x}, t)$) and thus may vary from point to point [23]. The unit ΔV is allowed to decrease to a minimum value. However, there is a limit to how small it becomes, because if it is too small, ρ would

¹or pressure as the case maybe in some scenarios



depend on the atomic structure of the material and in that case continuum mechanics can not be used for the description of the system.

The exception of mass compared to other quantities in a continuum material (as stated in the beginning of this section) is basically due to the conservation law that mass must obey. The mass of a given closed system (or subsystem as the case may be sometimes) must remain constant, hence:

$$\frac{Dm}{Dt} = 0 \quad (2.3)$$

where

$$\frac{D}{Dt} = \frac{\partial}{\partial t} + \mathbf{v} \cdot \nabla \quad (2.4)$$

is called the material derivative which describes the time rate of the change of a physical quantity. Applying Eqn. 2.4 to Eqn. 2.3 and using the vector identity with the incompressibility condition of the material property, that is ($\nabla \cdot \mathbf{v} = 0$), we can re-write Eqn. 2.3 as:

$$\frac{\partial}{\partial t} m + \nabla \cdot (m\mathbf{v}) = 0. \quad (2.5)$$

From Eqn. 2.2, we can get the expression for the total mass (m) of the volume (V) to be:

$$m = \int_V \rho(\mathbf{x}, t) dV \quad (2.6)$$

by substituting Eqn. 2.6 into Eqn. 2.5, we arrive at:

$$\int_V \left\{ \frac{\partial \rho(\mathbf{x}, t)}{\partial t} + \nabla \cdot (\rho(\mathbf{x}, t)\mathbf{v}) \right\} dV = 0. \quad (2.7)$$

Eqn 2.7 is valid for any arbitrary volume, therefore we have:

$$\frac{\partial \rho}{\partial t} + \nabla \cdot (\rho\mathbf{v}) = 0. \quad (2.8)$$

Eqn 2.8 is the differential form of the conservation of mass (also called continuity equation) and it can be expressed in cylindrical coordinate as follow:

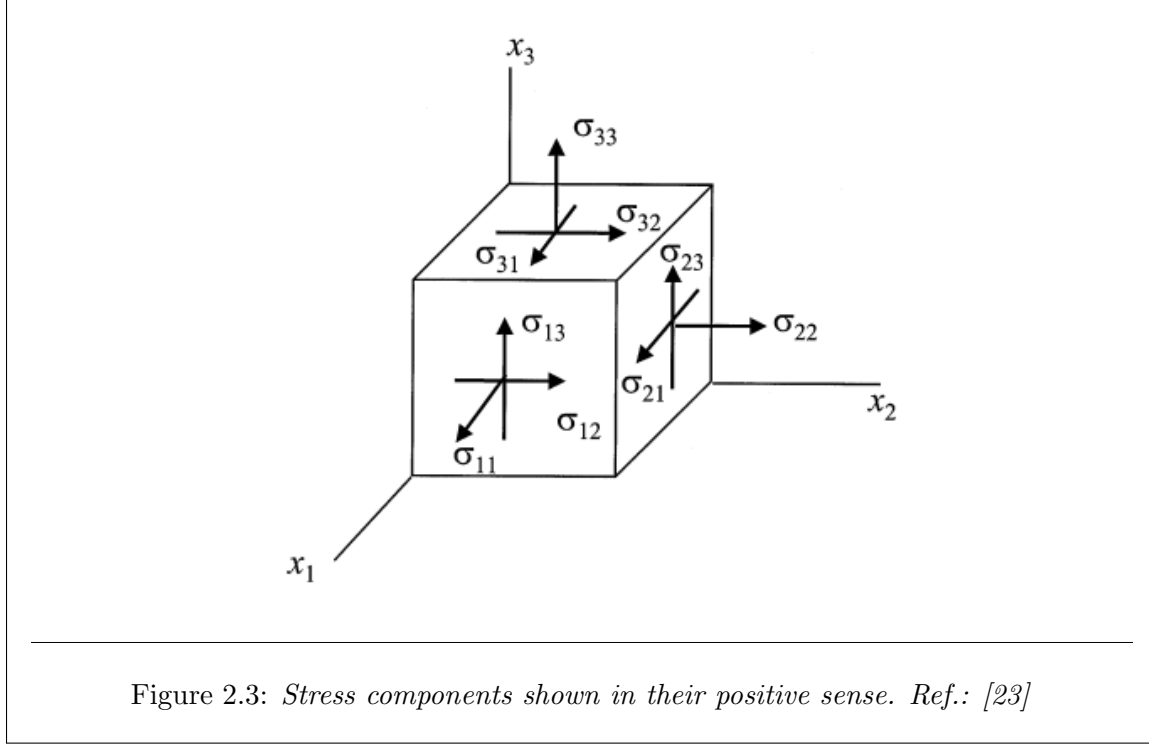
$$\frac{\partial \rho}{\partial t} + v_r \frac{\partial \rho}{\partial r} + \frac{v_\phi}{r} \frac{\partial \rho}{\partial \phi} + v_z \frac{\partial \rho}{\partial z} = 0. \quad (2.9)$$

Applying the axially symmetry condition to Eqn. 2.9, it is reduced to:

$$\frac{\partial \rho}{\partial t} + v_r \frac{\partial \rho}{\partial r} + v_z \frac{\partial \rho}{\partial z} = 0. \quad (2.10)$$

2.2 Equation of Motion (EOM): Cauchy's First and Second Law of Motion

To be able to derive the EOM and later simplify it, we need to first introduce stress. By definition, “stress is the internal force per unit area of the material of a body reacting against an applied load” [42]. In general (that is, without reference to any coordinate system), the stress tensor is a second order tensor with 9 components (σ_{ij}) that completely describes the state of stress at a point inside a continuum medium (see Figure 2.3 and Eqn. 2.11). If we consider an elemental cube as shown in Figure 2.3, each face of the cube is subjected to a stress that can be resolved into two components namely: normal and shear components. The normal components of the stress are the ones acting perpendicularly to the surface of the material (these are σ_{ij} , when $i = j$). The shear components (which are σ_{ij} , when $i \neq j$) act parallel or along the surface [42].



$$\boldsymbol{\sigma} \equiv \sigma_{ij} = \begin{pmatrix} \sigma_{11} & \sigma_{12} & \sigma_{13} \\ \sigma_{21} & \sigma_{22} & \sigma_{23} \\ \sigma_{31} & \sigma_{32} & \sigma_{33} \end{pmatrix} \quad (2.11)$$

The principle of conservation of angular momentum at equilibrium (Cauchy's second law of motion) requires that the summation of moments with respect to an arbitrary point is zero, which leads to the conclusion that the stress tensor is symmetrical, that is, $\sigma_{ij} = \sigma_{ji}$. Thus it can be described with 6 independent stress components instead of nine components. The Voigt notation is used to take the advantage of the stress tensor symmetry:

$$\boldsymbol{\sigma} = [\sigma_1 \quad \sigma_2 \quad \sigma_3 \quad \sigma_4 \quad \sigma_5 \quad \sigma_6]^T \equiv [\sigma_{11} \quad \sigma_{22} \quad \sigma_{33} \quad \sigma_{23} \quad \sigma_{31} \quad \sigma_{12}]^T. \quad (2.12)$$

The fact is that the stress tensor can also be expressed as sum of hydrostatic and deviatoric stress tensors:

$$\boldsymbol{\sigma} = -P\mathbb{I} + \mathbb{T} \quad (2.13)$$

where \mathbb{I} is the 3×3 identity matrix, \mathbb{T} is the deviatoric stress tensor (which holds information

about the shear stress) and P is the mean stress or simply pressure, which is basically:

$$P = \frac{1}{3} \text{Trace}(\boldsymbol{\sigma}) = \frac{1}{3} \sum_{k=1}^3 \sigma_{kk}. \quad (2.14)$$

The general equation of motion for any continuum medium, derived by Cauchy (also called Cauchy's first law of motion) is given by Ref. [2]:

$$\rho \frac{D\mathbf{v}}{Dt} = \nabla \cdot \boldsymbol{\sigma} + \mathbf{f}_b, \quad (2.15)$$

where \mathbf{f}_b is the body force (per unit volume) acting on the system and $\boldsymbol{\sigma}$ is the stress tensor. There are various ways of deriving Eqn. 2.15, one of the easiest way is by using Newton's second law of motion

$$\frac{D\mathbf{p}}{Dt} = \mathbf{F} \quad (2.16)$$

where $\mathbf{p} = m\mathbf{v}$ is the momentum and \mathbf{F} is the total force acting on the system and we define the total force per unit volume, \mathbf{f} to be $\frac{\mathbf{F}}{V}$.

This total force can be divided into two, namely: body force and surface force. The surface force per unit volume can be define as $\nabla \cdot \boldsymbol{\sigma}$. By using Eqn. 2.4 and imposing mass conservation law in Eqn. 2.8 on Eqn. 2.16, we arrive at

$$\rho \left[\frac{\partial \mathbf{v}}{\partial t} + (\mathbf{v} \cdot \nabla) \mathbf{v} \right] = \nabla \cdot \boldsymbol{\sigma} + \mathbf{f}_b \quad (2.17)$$

which is the same as Eqn. 2.15. In the absent of body force (\mathbf{f}_b), Eq. 2.17 becomes:

$$\rho \left[\frac{\partial \mathbf{v}}{\partial t} + (\mathbf{v} \cdot \nabla) \mathbf{v} \right] = \nabla \cdot \boldsymbol{\sigma}. \quad (2.18)$$

The geometry of the solid target that we are interested in is cylindrical, therefore we operate in a cylindrical coordinate system. Hence Eqn. 2.18 can be express as follow:

$$\begin{aligned} r : \rho \left(\frac{\partial u_r}{\partial t} + u_r \frac{\partial u_r}{\partial r} + \frac{u_\phi}{r} \frac{\partial u_r}{\partial \phi} + u_z \frac{\partial u_r}{\partial z} - \frac{u_\phi^2}{r} \right) &= \frac{\partial \sigma_{rr}}{\partial r} + \frac{1}{r} \frac{\partial \sigma_{\phi r}}{\partial \phi} + \frac{\partial \sigma_{zr}}{\partial z} + \frac{1}{r} (\sigma_{rr} - \sigma_{\phi\phi}) \\ \phi : \rho \left(\frac{\partial u_\phi}{\partial t} + u_r \frac{\partial u_\phi}{\partial r} + \frac{u_\phi}{r} \frac{\partial u_\phi}{\partial \phi} + u_z \frac{\partial u_\phi}{\partial z} + \frac{u_r u_\phi}{r} \right) &= \frac{1}{r} \left\{ \frac{\partial \sigma_{\phi\phi}}{\partial \phi} + \frac{1}{r} \frac{\partial (r^2 \sigma_{r\phi})}{\partial r} \right\} + \frac{\partial \sigma_{z\phi}}{\partial z} \\ z : \rho \left(\frac{\partial u_z}{\partial t} + u_r \frac{\partial u_z}{\partial r} + \frac{u_\phi}{r} \frac{\partial u_z}{\partial \phi} + u_z \frac{\partial u_z}{\partial z} \right) &= \frac{\partial \sigma_{zz}}{\partial z} + \frac{1}{r} \left\{ \frac{\partial \sigma_{\phi z}}{\partial \phi} + \frac{\partial (r \sigma_{rz})}{\partial r} \right\} \end{aligned} \quad (2.19)$$

Eqn. 2.12 is obviously reflected in the equation of motion in cylindrical coordinates expressed in Eqn. 2.19. Also worth noting at this point is the fact that we will only consider

cases where shear stress does not appear in a solid cylindrical target ² [35, 41], and we also impose that $\sigma_{rr} = \sigma_{\phi\phi}$, Eqn. 2.19 is now reduced to:

$$\begin{aligned} r : \rho \left(\frac{\partial u_r}{\partial t} + u_r \frac{\partial u_r}{\partial r} + \frac{u_\phi}{r} \frac{\partial u_r}{\partial \phi} + u_z \frac{\partial u_r}{\partial z} - \frac{u_\phi^2}{r} \right) &= \frac{\partial \sigma_{rr}}{\partial r} \\ z : \rho \left(\frac{\partial u_z}{\partial t} + u_r \frac{\partial u_z}{\partial r} + \frac{u_\phi}{r} \frac{\partial u_z}{\partial \phi} + u_z \frac{\partial u_z}{\partial z} \right) &= \frac{\partial \sigma_{zz}}{\partial z} \end{aligned} \quad (2.20)$$

Using Eqn. 2.13, the divergence of the stress tensor can be expressed as follows:

$$\nabla \cdot \boldsymbol{\sigma} = -\nabla P + \nabla \cdot \mathbb{T} \quad (2.21)$$

we can set the deviatoric stress tensor to zero (i.e., $\nabla \cdot \mathbb{T} = 0$). As stated earlier, when a cylindrical rod is considered or a body is subjected to an isotropic compression (or expansion) change, there is no shear stress. Finally (by factoring axial symmetry of the cylindrical material), we can write equation of motion for a cylindrical solid target in cylindrical coordinates as³

$$\begin{aligned} r : \rho \left(\frac{\partial u_r}{\partial t} + u_r \frac{\partial u_r}{\partial r} + \frac{u_\phi}{r} \frac{\partial u_r}{\partial \phi} + u_z \frac{\partial u_r}{\partial z} - \frac{u_\phi^2}{r} \right) &= -\frac{\partial P}{\partial r} \\ z : \rho \left(\frac{\partial u_z}{\partial t} + u_r \frac{\partial u_z}{\partial r} + \frac{u_\phi}{r} \frac{\partial u_z}{\partial \phi} + u_z \frac{\partial u_z}{\partial z} \right) &= -\frac{\partial P}{\partial z}. \end{aligned} \quad (2.22)$$

2.3 Mie-Grüneisen Equation of State (EOS)

Our main goal here is to derive the equation of state (EOS)⁴ for solid materials. Considering this, we will focus on the case where the atoms undergo small vibrations about their equilibrium positions. This vibration is caused mainly by energetic particle beam(s) striking the solid material. In the early twentieth century, Grüneisen derived a “beautiful” EOS by extending the solid EOS developed by Mie. He included lattice vibrations of solids even at low temperatures [16]. This was achieved by using the Debye model of solids, which is based on a continuous medium and an extension of the single frequency assumption in

²Since we investigated only 1-D cases.

³Henceforth, we are going to be using the word pressure and stress interchangeably.

⁴Most material covered here is based on Chapter 10 of Ref.: [16]

Einstein's model of solids with a spectrum of frequencies⁵. First, let us define what the equation of state is, after that we will show how to derive the Mie-Grüneisen equation of state.

For a given system at thermodynamic equilibrium, the equation of state describes the fundamental relationship between thermodynamic variables [16]. The number and form of such equations depend on the particular system being considered. In our case, a solid material undergoes thermal excitation, and one can write the energy (Q) and pressure (P) as superposition of contributing terms, in the following form:

$$\begin{aligned} Q &= Q_c + Q_{Ta} + Q_{Te} \\ P &= P_c + P_{Ta} + P_{Te} \end{aligned} \quad (2.23)$$

where Q_c and P_c are the energy and pressure at zero temperature ($T = 0$ K) called cold terms, Q_{Ta} and P_{Ta} are the contributions of the atom vibrations (about their mean position) while Q_{Te} and P_{Te} are the electron thermal contributions. We will neglect the thermal electron terms for the reasons stated in the introduction part of this chapter. The assumption of homogeneity and isotropy is valid with great accuracy and we do not need to go down to the microscopic level of the solid [35]. Hence we are left with the atom vibration term, so Eqn. 2.23 becomes:

$$\begin{aligned} Q &= Q_c + Q_{Ta} \\ P &= P_c + P_{Ta}. \end{aligned} \quad (2.24)$$

Using thermodynamic principles and choosing the suitable independent variable(s), it is possible to derive the EOS of a system [11]. If we know the partition function of a system, we can exhaust all that is thermodynamically relevant about that system. Therefore, to derive a valid equation of state for any system, a good place to start is to find the partition function of that system.

Let us assume a solid of N atoms to be described by a system of harmonic oscillators with $3N$ independent modes of vibrations. The vibrations are quantised so that the energy of the j mode of vibration is given by

$$Q_j = \left(n_j + \frac{1}{2}\right)h\nu_j \quad j = 1, 2, \dots, 3N \quad (2.25)$$

⁵See page 157 of Ref. [16] for more details on the Debye model.

where h is the Planck's constant, n_j is an integer (basically, number of phonons) and ν is the frequency of the j mode. The total energy (Q) of the solid can be expressed as the energy at the zero temperature (that is, the potential energy) Q_0 with the sum of energies in all modes of the vibration, so

$$Q_i \equiv Q_{n_1 n_2 \dots n_{3N}} = \sum_{j=1}^{3N} \left(n_j + \frac{1}{2} \right) h\nu_j + Q_0 \quad (2.26)$$

which is the same as:

$$Q_i = \sum_{j=1}^{3N} n_j h\nu_j + Q_c \quad (2.27)$$

where

$$Q_c = \frac{1}{2} \sum_{j=1}^{3N} h\nu_j + Q_0. \quad (2.28)$$

This is based on the assumption that Q_c , Γ_j (for $j = 1, \dots, 3N$)⁶ and $Q_{n_1 n_2 \dots n_{3N}}$ may be a function of the volume V but not temperature T . The partition function Z of the oscillator system with the energy expressed in Eqn. 2.28, is

$$Z = \sum_i \exp(-\beta Q_i) = \sum_{n_1=0}^{\infty} \dots \sum_{n_{3N}=0}^{\infty} \exp \left(- \sum_{j=1}^{3N} \beta n_j h\nu_j - \beta Q_c \right) \quad (2.29)$$

where $\beta = \frac{1}{kT}$ and k is the Boltzmann constant. The exponential sum in the above equation can be re-expressed as a product of terms

$$Z = \exp(-\beta Q_c) \sum_{n_1=0}^{3N} \exp(-\beta n_1 h\nu_1) \sum_{n_2=0}^{3N} \exp(-\beta n_2 h\nu_2) \dots \sum_{n_{3N}=0}^{3N} \exp(-\beta n_{3N} h\nu_{3N}). \quad (2.30)$$

Since each of the sum on the RHS of Eqn. 2.30 is a geometric series, we can write it as

$$\sum_{n_j=0}^{3N} \exp(-\beta n_j h\nu_j) = \frac{1}{1 - \exp(-\beta h\nu_j)} - \sum_{n_j=3N+1}^{\infty} \exp(-\beta n_j h\nu_j). \quad (2.31)$$

Taking note that the series will converge (since $\beta h\nu_j > 0 \quad \forall j$) and N is very large, which implies that we can neglect the second term of Eqn. 2.31. Therefore, the partition function Z of the oscillator system can now be written as:

⁶ Γ is the Grüneisen coefficient and it will be defined in later part of this section

$$Z = \exp(-\beta Q_c) \prod_{j=1}^{3N} [1 - \exp(\beta h\nu_j)]^{-1}. \quad (2.32)$$

Now we know the partition function of solids. Using our knowledge of the partition function, we determine the Helmholtz free energy⁷ F (in quasi-harmonic approximation) to be

$$F = -\frac{1}{\beta} \ln Z = Q_c + \beta^{-1} \sum_{j=1}^{3N} \ln[1 - \exp(-\beta h\nu_j)] \quad (2.33)$$

The average energy Q of the solid and its pressure P are obtained using appropriate thermodynamics relations

$$Q = F - T \left(\frac{\partial F}{\partial T} \right)_V = Q_c + \sum_{j=1}^{3N} \frac{h\nu_j}{\exp(\beta h\nu_j) - 1} \quad (2.34)$$

and

$$P = - \left(\frac{\partial F}{\partial V} \right)_T = - \frac{\partial Q_c}{\partial V} + \frac{1}{V} \sum_{j=1}^{3N} \Gamma_j \frac{h\nu_j}{\exp(\beta h\nu_j) - 1} \quad (2.35)$$

where Γ_j is defined by

$$\Gamma_j = - \frac{V}{\nu_j} \left(\frac{\partial \nu_j}{\partial V} \right)_T = - \left(\frac{\partial \ln \nu_j}{\partial \ln V} \right)_T. \quad (2.36)$$

Comparing Eqn. 2.24 with both Eqn. 2.34 and Eqn. 2.35, the first and second terms (in both Eqn. 2.34 and Eqn. 2.35) describe the cold and thermal terms respectively. Based on Eqn. 2.36, Γ_j can never vanish. This is a differentiating factor between thermal term and the cold term in Eqn. 2.35. The given fact that $\Gamma_j \neq 0$, implies that the vibrational frequency depends on volume. Dependence of vibrational frequency on volume can be explained by the fact that when a solid material is compressed, it becomes harder, thus its restoring force increases, leading to an increase in the vibrational frequencies with decreasing volume. Hence, Γ_j will always be positive.

For an isotropic and homogenous system, $\Gamma_j = \Gamma$ where $j = 1, 2, \dots, 3N$. Re-expressing Eqn. 2.35:

$$P = P_c + \frac{\Gamma Q_{Ta}}{V} \quad (2.37)$$

⁷ F is define as $F = Q - TS$: where T is the temperature and S is the final entropy

To determine what Γ is, we use the thermodynamics identity:

$$\left(\frac{\partial V}{\partial P}\right)_T \left(\frac{\partial T}{\partial V}\right)_P \left(\frac{\partial P}{\partial T}\right)_V = -1 \quad (2.38)$$

taking the derivative of Eqn. 2.37 with respect to T at constant V , gives:

$$\left(\frac{\partial P}{\partial T}\right)_V = \frac{\Gamma}{V} c_V \quad (2.39)$$

where c_v is the specific heat capacity at constant volume. The linear expansion coefficient α at constant pressure is

$$\alpha = \frac{1}{3V} \left(\frac{\partial V}{\partial T}\right)_P \quad (2.40)$$

and the definition of the isothermal compressibility κ ,

$$\kappa = -\frac{1}{V} \left(\frac{\partial V}{\partial P}\right)_T \quad (2.41)$$

inserting Eqn. 2.39 - 2.41 into Eqn. 2.38, one gets

$$\Gamma = \frac{3\alpha V}{\kappa c_v}. \quad (2.42)$$

The term Γ is called Grüneisen coefficient or constant which agrees very well with the experimental results. In a nutshell, taking into account only the thermal excitation effect, the EOS is

$$P = \frac{\Gamma}{V} Q. \quad (2.43)$$

This can also be expressed in the form:

$$P = \rho \Gamma q \quad (2.44)$$

where $q(\mathbf{x}, t)$ is the energy per unit mass.

2.4 (LAW) Linear Acoustic Waves: Small Amplitude Oscillation

With all the aforementioned assumptions, we have all the necessary “ingredients” we need to be able to formulate a mathematical description of a cylindrical solid material undergoing small vibrations or oscillations due to thermal excitations. In summary, here are the equations:

1. Continuity Equation:

$$\frac{\partial \rho}{\partial t} + \nabla \cdot (\rho \mathbf{v}) = 0, \quad (2.45)$$

2. Equation of Motion:

$$\rho \left[\frac{\partial \mathbf{v}}{\partial t} + (\mathbf{v} \cdot \nabla) \mathbf{v} \right] = -\nabla P, \quad (2.46)$$

3. Equation of State:

$$P = \rho \Gamma q, \quad (2.47)$$

4. lastly, the distribution of deposited energy density in space (\mathbf{x}) and time (t):

$$q = q(\mathbf{x}, t), \quad (2.48)$$

where:

ρ = density,

Γ = Grüneisen coefficient,

\mathbf{v} = velocity,

P = pressure,

$q \equiv \frac{Q}{m}$ = energy (Q) per unit mass (m),

t = time,

\mathbf{x} = spatial description in cylindrical coordinate, in this case (r, z).

We have four variables in the four equations above, hence we have a closed system. In order to investigate linear mode behaviour (that is, linear acoustic waves) in our system, we perturbed Eqns. 2.45 - 2.47 near equilibrium by linearisation. Perturbation near equilibrium implies that we linearised Eqns. 2.45 - 2.47 by putting $\rho = \rho_0 + \epsilon^1 \rho_1$, $\mathbf{v} = \mathbf{v}_0 + \epsilon^1 \mathbf{v}_1$, $q = q_0 + \epsilon^1 q_1$ and $P = P_0 + \epsilon^1 P_1$, therefore we get

$$\frac{\partial \rho_0}{\partial t} + \nabla \cdot (\rho_0 \mathbf{v}_0) + \epsilon^1 \frac{\partial \rho_1}{\partial t} + \epsilon^1 \nabla \cdot (\rho_0 \mathbf{v}_1) + \epsilon^1 \nabla \cdot (\rho_1 \mathbf{v}_0) + \epsilon^2 \nabla \cdot (\rho_1 \mathbf{v}_1) = 0 \quad (2.49)$$

$$\begin{aligned} & \rho_0 \frac{\partial \mathbf{v}_0}{\partial t} + \rho_0 \mathbf{v}_0 \cdot \nabla \mathbf{v}_0 + \epsilon^1 \rho_0 \frac{\partial \mathbf{v}_1}{\partial t} + \epsilon^1 \rho_1 \frac{\partial \mathbf{v}_0}{\partial t} + \epsilon^1 \rho_0 \mathbf{v}_0 \cdot \nabla \mathbf{v}_1 + \epsilon^1 \rho_0 \mathbf{v}_1 \cdot \nabla \mathbf{v}_0 + \\ & + \epsilon^1 \rho_1 \mathbf{v}_0 \cdot \nabla \mathbf{v}_0 + \epsilon^2 \rho_1 \frac{\partial \mathbf{v}_1}{\partial t} + \epsilon^2 \rho_0 \mathbf{v}_1 \cdot \nabla \mathbf{v}_1 + \epsilon^2 \rho_1 \mathbf{v}_0 \cdot \nabla \mathbf{v}_1 + \epsilon^2 \rho_1 \mathbf{v}_1 \cdot \nabla \mathbf{v}_0 + \\ & + \epsilon^3 \rho_1 \mathbf{v}_1 \cdot \nabla \mathbf{v}_1 = -\nabla P_0 - \epsilon^1 \nabla P_1 \end{aligned} \quad (2.50)$$

$$P + \epsilon^1 P_1 = \Gamma \rho_0 q_0 + \epsilon^1 \Gamma \rho_0 q_1 + \epsilon^1 \Gamma \rho_1 q_0 + \epsilon^2 \Gamma \rho_1 q_1 \quad (2.51)$$

This mean for physical variable or quantity X : X_0 is the equilibrium value or quantity and X_1 is the perturbed value or quantity, where $\epsilon \ll 1$: is a small real parameter.

At equilibrium, the system must satisfy these following conditions:

1. the solid target is at rest or immobile, so:

$$\mathbf{v}_0 = 0 \quad (2.52)$$

2. also, the solid target is uniform at equilibrium, meaning:

$$\nabla \rho_0 = 0 \quad (2.53)$$

although $\rho_0 \neq 0$;

3. all temporary derivatives of equilibrium quantities (or values) will be zero, since they are constant, this implies that:

$$\frac{\partial \rho_0}{\partial t} = \frac{\partial P_0}{\partial t} = \frac{\partial q_0}{\partial t} = \frac{\partial \mathbf{v}_0}{\partial t} = 0. \quad (2.54)$$

After linearisation of the equations, we can simplify further by applying the equilibrium conditions (see Eqns. 2.52 - 2.54). To derive the linearised system, we isolate terms with ϵ while terms containing higher orders of ϵ are neglected within the linear analysis. Therefore, Eqns. 2.49 - 2.51 becomes:

$$\frac{\partial \rho_1}{\partial t} + \nabla \cdot (\rho_0 \mathbf{v}_1) = 0 \quad (2.55)$$

$$\rho_0 \frac{\partial \mathbf{v}_1}{\partial t} = -\nabla P_1 \quad (2.56)$$

$$P_1 = \Gamma \rho_0 q_1 + \Gamma \rho_1 q_0. \quad (2.57)$$

Taking temporal derivative of Eqn. 2.57 twice and applying equilibrium condition (i.e Eqn. 2.52 - 2.54), we get:

$$\frac{\partial^2 P}{\partial t^2} = \Gamma \rho_0 \frac{\partial^2 q_1}{\partial t^2} + \Gamma q_0 \frac{\partial^2 \rho_1}{\partial t^2}. \quad (2.58)$$

Taking a temporal derivative of Eqn. 2.55:

$$\frac{\partial^2 \rho_1}{\partial t^2} + \nabla \cdot \left(\rho_0 \frac{\partial \mathbf{v}_1}{\partial t} \right) = 0. \quad (2.59)$$

Taking a divergence of Eqn. 2.56:

$$\nabla \cdot \left(\rho_0 \frac{\partial \mathbf{v}_1}{\partial t} \right) = -\nabla^2 P \quad (2.60)$$

since, $\nabla \cdot \nabla P = \nabla^2 P$. Substitute Eqn. 2.59 into Eqn. 2.60, we have;

$$\frac{\partial^2 \rho_1}{\partial t^2} = \nabla^2 P. \quad (2.61)$$

Eqn. 2.58 can also be express as

$$\frac{\partial^2 \rho_1}{\partial t^2} = \frac{1}{q_0 \Gamma} \left[\frac{\partial^2 P_1}{\partial t^2} - \rho_0 \Gamma \frac{\partial^2 q_1}{\partial t^2} \right]. \quad (2.62)$$

Inserting Eqn. 2.61 into Eqn. 2.62, dropping all the subscript and re-arranging, we obtain:

$$\frac{\partial^2 P}{\partial t^2} - c_s^2 \nabla^2 P = \rho_0 \Gamma \frac{\partial^2 q}{\partial t^2} \quad (2.63)$$

where $c_s \equiv \sqrt{q_0 \Gamma}$.

By substituting $q = \frac{Q}{m}$, Eqn. 2.63 can also be expressed as follows:

$$\frac{\partial^2 P}{\partial t^2} - c_s^2 \nabla^2 P = \frac{\Gamma}{V_0} \frac{\partial^2 Q}{\partial t^2} \quad (2.64)$$

where $c_s \equiv \sqrt{\frac{\Gamma}{m} Q_0}$ and V_0 is the equilibrium volume.

Eqn. 2.63 (or Eqn. 2.64) is the linear acoustic waves equation in a cylindrical solid target. In the next few chapters, we will attempt to solve this equation using different boundary conditions and energy distributions.

Chapter 3

LAW in a Thin Rod

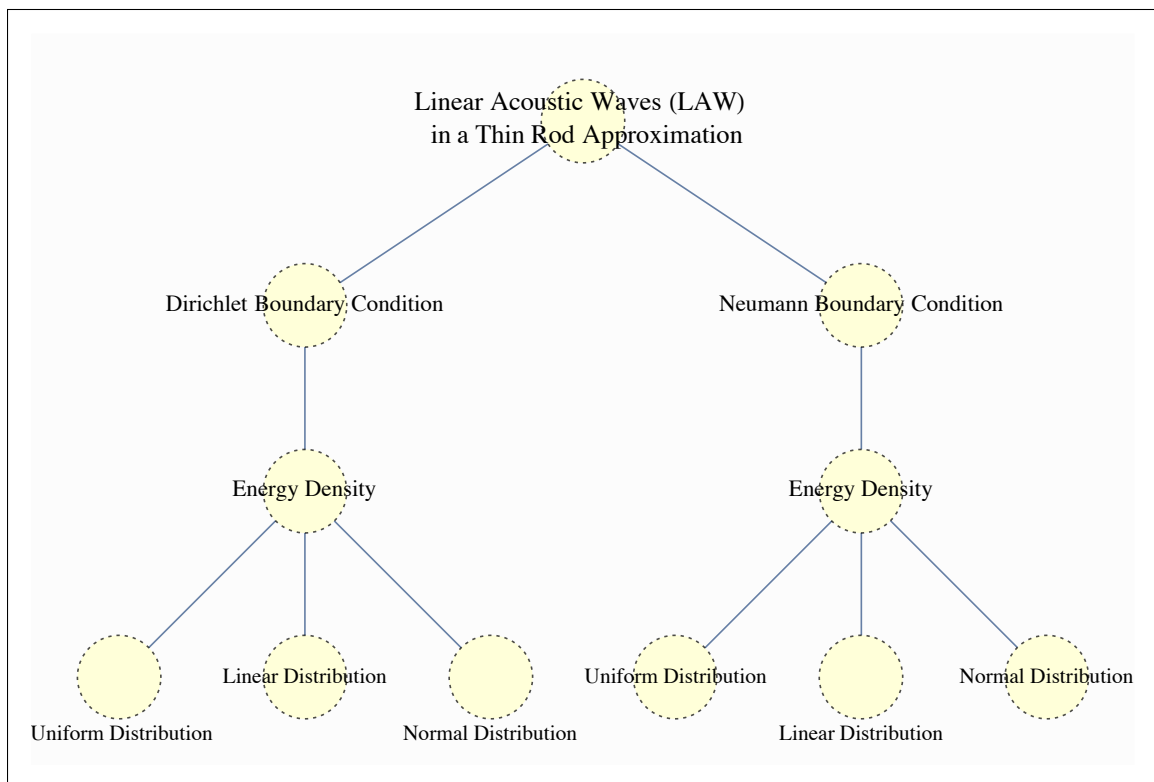


Figure 3.1: *Schematic representation of content overview for this chapter.*

The overview of this chapter is well laid out in Figure 3.1. The linear second order non-homogeneous partial differential equation (PDE) developed in the last chapter (see Eqn. 2.64) will be solved analytically here for a thin rod. The thin rod implies: $\nabla_r^2 P \approx 0$ or $\nabla_r^2 P \ll \nabla_z^2 P$ and reduces Eqn. 2.64 to

$$\frac{\partial^2 P}{\partial t^2} - c_s^2 \frac{\partial^2 P}{\partial z^2} = \frac{\Gamma}{V_0} \frac{\partial^2 Q}{\partial t^2}. \quad (3.1)$$

To obtain an analytical solution to PDE in Eqn. 3.1, we must first specify some conditions to complete the PDE problem setup. The required number of conditions is determined by the highest order derivative in each independent variable. Since Eqn. 3.1 is a second-order equation in t and z , hence it requires two conditions each in t and z . The two conditions in t are called the initial conditions and the other two in z are termed the boundary conditions.

For our system, we will assume instantaneous energy deposition. The justification of this assumption is based on the fact that the material will not respond at the relativistic time scale of the particle beam, this is due to the inertia of the material. In other words, the mass inertia of the solid material prevents it from an immediate response during the absorption of the energetic particle beam within a short period of time (say, in range of picoseconds to microseconds¹). Therefore, we can define the energy deposition as follow

$$Q(\mathbf{x}, t) = \delta(t)Q(\mathbf{x}), \quad (3.2)$$

where $Q(\mathbf{x})$ is the energy distribution² in space \mathbf{x} and $\delta(t)$ is the Dirac delta function which represents the instantaneousness of the energy deposition in time domain t and it is defined as

¹Basically the traverse time depends on the bunch length of the beam.

²We will study different distributions in later part of this chapter

$$\delta(t) = \begin{cases} 1 & \text{when } t = 0 \\ 0 & \text{when } t > 0 \end{cases}. \quad (3.3)$$

Interestingly, by using Eqn. 3.2 and Eqn. 3.3 we can reduce the non-homogeneous PDE in Eqn. 3.1 to homogeneous PDE:

$$\frac{\partial^2 P}{\partial t^2} - c_s^2 \frac{\partial^2 P}{\partial z^2} = 0 \quad \text{for } t > 0. \quad (3.4)$$

Since our investigation is to look into the aftermath of the bombardment of the rod by a relativistic particle beam, this leads to the following initial conditions, which are expressed as follows:

$$P(\mathbf{x}, t = 0) = \frac{\Gamma}{V_0} Q(\mathbf{x}) \quad (3.5)$$

and the time derivative of P at $t = 0$ is

$$\left. \frac{\partial P}{\partial t} \right|_{t=0} = 0. \quad (3.6)$$

To have a complete problem setup and to solve the PDE, boundary conditions (BCs) have to be included. The commonly encountered BCs can be classified into three namely: Dirichlet, Neumann and Robin BCs. With respect to our area of interest and solving the PDE analytically, we explore two extreme cases in terms of the BCs that we imposed on our system. These two extreme cases are the Dirichlet and Neumann BC: they depict “the best” and “worst” case scenario respectively (see Section 3.1 and 3.2 for their respective explanations).

Once the solution for the PDE in terms of $P(z, t)$ is found, we can derive a solution for the other parameters. For example, using the linearised equation of motion (see Eqn.

2.56) in chapter 2, we can determine the displacement (u) to be

$$u(z, t) = -\frac{1}{\rho_0} \iint_t \frac{\partial}{\partial z} P(z, t) dt^2. \quad (3.7)$$

There will be two integral constants as result of the double integral and these can be worked out by using the initial conditions

$$u(z, 0) = 0 = \left. \frac{\partial u}{\partial t} \right|_{t=0} \quad (3.8)$$

We will make reference to these two equations in all the different cases we are going to treat.

For each BC that we are going to look at, we will study different distributions (namely: uniform, linear and Gaussian³) of deposited energy density in the target.

Table 3.1: *Typical Case Analysis: Copper Target Material Parameters*

Parameters	Symbol	Unit	Value
Length	L	m	0.12
Standard deviation	σ_z	m	0.037
Mean	B	m	0.12
Speed of sound	c_s	m/s	3570

3.1 Dirichlet Problem

Dirichlet boundary conditions specify the value of the function on the surface [39]. In our case, this function is the pressure, $P(z, t)$. In this thesis, this is the so-called “best case scenario” because by imposing $P = 0$ on both sides of the rod, the thin rod material is allowed to move freely at both ends. This means that the displacement at both ends of the thin rod is free. It also implies that the boundary energy flow is kept at zero.

³The σ_z and B in Table 3.1 represents the typical standard deviation and mean value (respectively) in a Gaussian distribution.

This problem setup can be summarised as follows:

<p>Partial Differential Equation:</p> $\frac{\partial^2 P}{\partial t^2} - c_s^2 \frac{\partial^2 P}{\partial z^2} = 0$ <p>Initial condition:</p> $P(z, 0) = \frac{\Gamma}{V_0} Q(z) \quad \text{and}$ $\left. \frac{\partial P}{\partial t} \right _{t=0} = 0$ <p>Boundary condition:</p> $P(0, t) = 0 = P(L, t)$	(3.9)
--	-------

A solution to the above problem setup is given as [26]:

$$P(z, t) = \frac{2}{L} \sum_{n=1}^{\infty} \cos\left(\frac{\pi n}{L} c_s t\right) \sin\left(\frac{\pi n}{L} z\right) \int_0^L P(z, 0) \sin\left(\frac{\pi n}{L} z\right) dz. \quad (3.10)$$

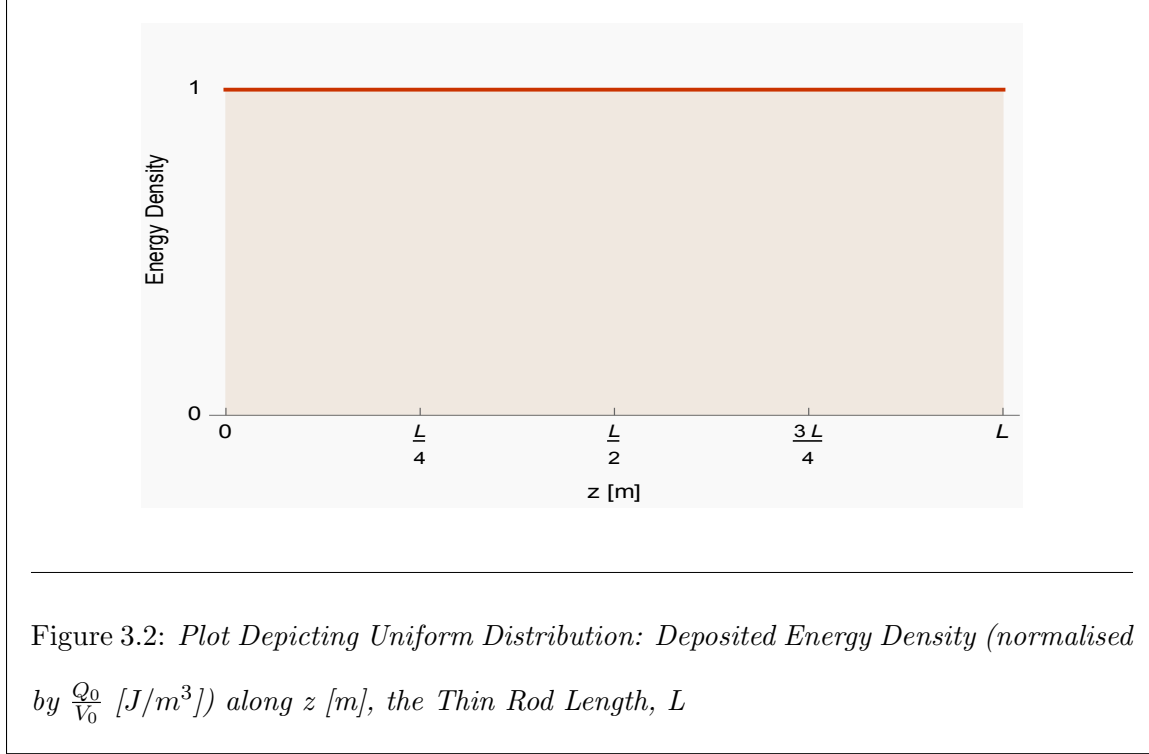
Substituting the initial condition of Eqn. 3.9, leads to:

$$P(z, t) = \frac{2\Gamma}{LV_0} \sum_{n=1}^{\infty} \cos\left(\frac{\pi n}{L} c_s t\right) \sin\left(\frac{\pi n}{L} z\right) \int_0^L Q(z) \sin\left(\frac{\pi n}{L} z\right) dz. \quad (3.11)$$

The expression above, Eqn. 3.11 indicates that the dynamic behaviour strongly depends on the distribution of energy deposited on the target material. So we are going to consider various energy distributions to see how these distributions affect the dynamic behaviour of the target materials.

3.1.1 Energy Density Profile: Rectangular (Uniform) Distribution

Solving the integral of the Eqn. 3.11 will give us a clear picture of the dynamic behaviour of the acoustic wave in the material. Hence, it is convenient to start from a very



easy case.

Let us assume that the energy density ($\frac{Q_0}{V_0}$) deposited on a material by the particle beam is uniformly distributed (see Figure 3.2). We can define the energy absorbed by the target as

$$Q(z) = Q_0 \quad (3.12)$$

and insert Eqn. 3.12 into 3.11:

$$P(z, t) = \frac{2\Gamma Q_0}{V_0 L} \sum_{n=1}^{\infty} \cos\left(\frac{\pi n}{L} c_s t\right) \sin\left(\frac{\pi n}{L} z\right) \int_0^L \sin\left(\frac{\pi n}{L} z\right) dz. \quad (3.13)$$

Evaluating the integral part of Eqn. 3.13, the problem is simplified to

$$P(z, t) = \frac{2\Gamma Q_0}{V_0 \pi} \sum_{n=1}^{\infty} \frac{1}{n} (1 - \cos(n\pi)) \cos\left(\frac{\pi n}{L} c_s t\right) \sin\left(\frac{\pi n}{L} z\right) \quad (3.14)$$

where⁴

$$1 - \cos(n\pi) = \begin{cases} 0 & \text{when } n \in \mathbb{Z}_{\text{even}}^+ \\ 2 & \text{when } n \in \mathbb{Z}_{\text{odd}}^+ \end{cases}. \quad (3.15)$$

We retain only $n \in \mathbb{Z}_{\text{odd}}^+$ by replacing n with $2n + 1$, this leads to:

$$P(z, t) = \frac{4\Gamma Q_0}{V_0\pi} \sum_{n=0}^{\infty} \frac{1}{(2n+1)} \cos\left(\frac{\pi(2n+1)}{L}c_s t\right) \sin\left(\frac{\pi(2n+1)}{L}z\right). \quad (3.16)$$

Eqn. 3.16 is the complete solution of the PDE of linear pressure acoustic waves caused by the deposition of uniformly distributed energy in a thin rod. Knowing the explicit expression for P opens the door to determine the effect of the thermoelastic waves on the other target material parameters of interest.

Thus, with the expression above (Eqn. 3.16), we can also determine the displacement evolution by using Eqn. 3.7. First, we take the gradient of Eqn. 3.16, which is given by

$$\nabla_z P(z, t) = \frac{4\Gamma Q_0}{V_0 L \pi} \sum_{n=0}^{\infty} \cos\left(\frac{\pi(2n+1)}{L}c_s t\right) \cos\left(\frac{\pi(2n+1)}{L}z\right). \quad (3.17)$$

Substituting Eqn. 3.17 into the Eqn. 3.7, we get

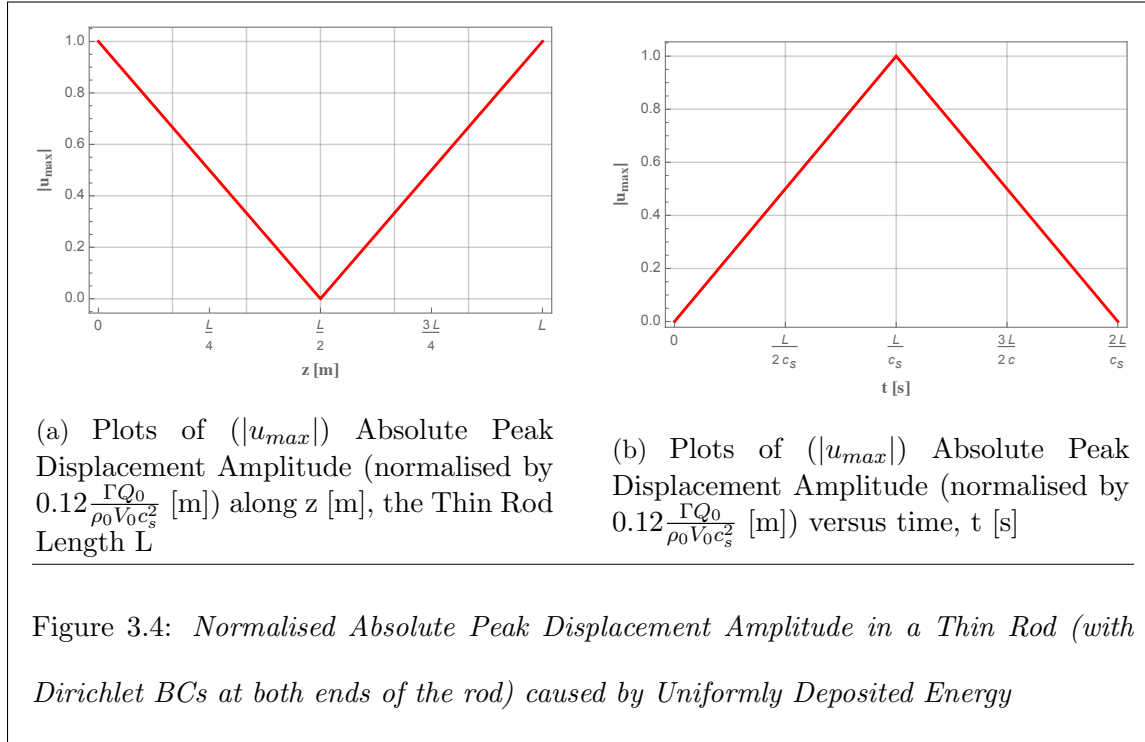
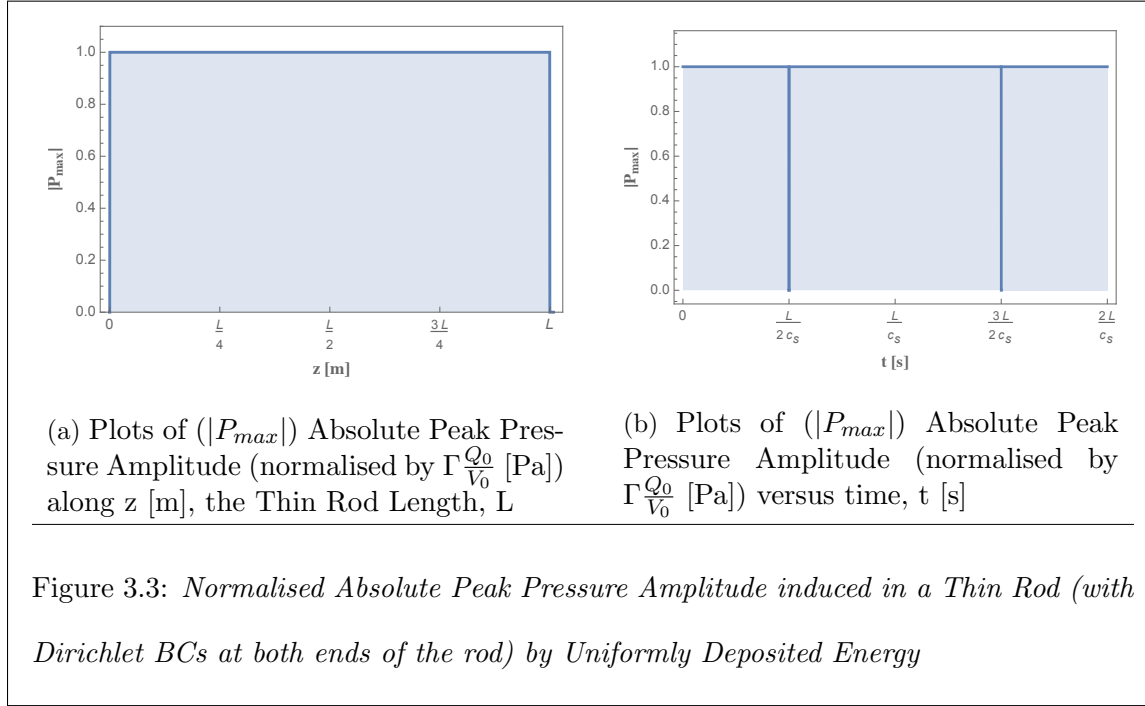
$$u(z, t) = -\frac{4\Gamma Q_0}{\rho_0 V_0 L \pi} \sum_{n=0}^{\infty} \cos\left(\frac{\pi(2n+1)}{L}z\right) \iint_t \cos\left(\frac{\pi(2n+1)}{L}c_s t\right) dt^2. \quad (3.18)$$

Solving the double integral and applying the initial conditions in Eqn. 3.8, we derived the expression for the displacement:

$$u(z, t) = \frac{4\Gamma Q_0 L}{\rho_0 V_0 c_s^2 \pi^2} \sum_{n=0}^{\infty} \frac{1}{(2n+1)^2} \left\{ \cos\left(\frac{\pi(2n+1)}{L}c_s t\right) - 1 \right\} \cos\left(\frac{\pi(2n+1)}{L}z\right) \quad (3.19)$$

Quantitative analysis of Eqn. 3.16 and 3.19 (for pressure and displacement respectively) using parameters listed in Table 3.1, reveal some interesting results (see section A.1 in Appendix A for the plots):

⁴ \mathbb{Z} : Integers



1. Due to the uniformity of the energy deposition in the thin rod target, the waves start developing at both ends of the thin rod and move towards each other simultaneously. These two waves, moving towards each other at the same speed, superpose and cause a total destructive interference at time $t = \frac{mL}{2c_s}$ ($m \in \mathbb{Z}_{odd}^+$), irrespective of z . This explains why at those times, P is zero (see Fig. 3.3b and Section A.1 in Appendix A). In summary, information in Fig. 3.3b can be expressed as follow

$$|P_{max}| = \begin{cases} 0 & \text{when } t = \frac{mL}{2c_s} \text{ and } m \in \mathbb{Z}_{odd}^+ \\ 1 & \text{otherwise} \end{cases}.$$

2. The movement of the two waves moving towards each other also manifest in the distribution of the displacement of the thin rod. When the total destructive interference occur (that is, at $t = \frac{mL}{2c_s}$ where $m \in \mathbb{Z}_{odd}^+$), the magnitude of the peak displacement at these times is always half of the highest absolute peak value of the displacement achievable by the system, that is

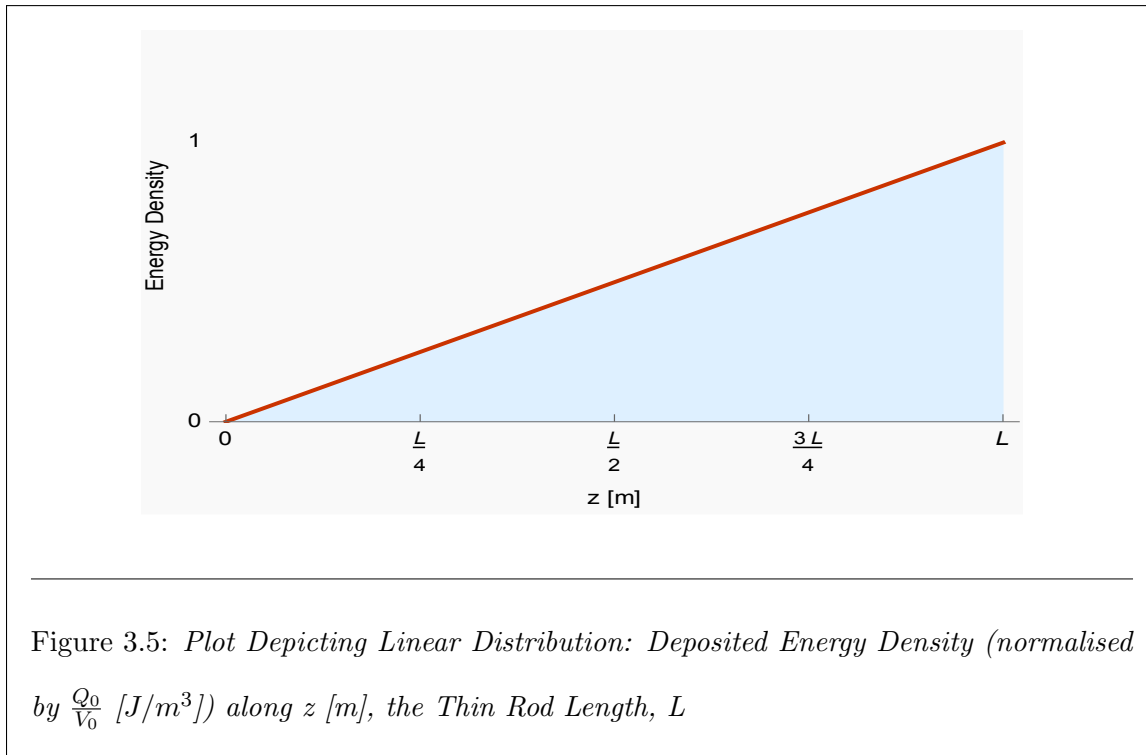
$$|u_{max}| = \frac{1}{2} \quad \text{when} \quad t = \frac{mL}{2c_s}$$

This is evident in Fig. 3.4b. This also makes the first and the other half part of the thin rod to expand in opposite direction (see Sub-section A.1.4 in the Appendix A, particularly the plot when t is $\frac{L}{2c_s}$) and the centre ($\frac{L}{2}$) does not move.

3. Also due to the uniform energy distribution, the absolute peak value the negative displacement is always equal to the absolute peak value the positive displacement at all times (see Sub-section A.1.4 in the Appendix A).
4. At the middle of the thin rod (that is, $\frac{L}{2} = 0.06$ m), there is no displacement ($u(\frac{L}{2}, t) = 0$) leading to peak stress (P) and strain ($\frac{\partial u}{\partial z}$) at all times with the exceptions at those times specified in the item no. 1 above (see Figure 3.4a).

5. As shown in Figures 3.3a and 3.3b, the absolute peak pressure amplitude, $|P_{max}|$ is always $\Gamma \frac{Q_0}{V_0}$ (irrespective of time and space except at those times stated in the item no. 1 above and at the boundaries (that is, at $z = 0$ and $z = L$)).
6. Also worth noting is the magnitude of the peak amplitude of the displacement $|u_{max}|$, which is maximal at $z = 0$ and $z = L$ (see Figure 3.4a).

3.1.2 Energy Density Profile: Triangular (Linear) Distribution



Here we consider energy deposition in form of triangular distribution, that is, the energy is linearly distributed in the thin rod (see Figure 3.5), which we define as follows:

$$Q = Q_0 z. \quad (3.20)$$

Inserting Eqn. 3.20 in Eqn. 3.11, we arrive at the solution for P :

$$P(z, t) = \frac{2\Gamma Q_0}{\pi^2 V_0} \sum_{n=1}^{\infty} \frac{1}{n^2} \cos\left(\frac{\pi n}{L} c_s t\right) \sin\left(\frac{\pi n}{L} z\right) (\sin(\pi n) - \pi n \cos(\pi n)). \quad (3.21)$$

With

$$\sin(\pi n) = 0 \quad \forall n \in \mathbb{Z}$$

one finally derives

$$P(z, t) = -\frac{2\Gamma Q_0}{\pi V_0} \sum_{n=1}^{\infty} \frac{1}{n} \cos\left(\frac{\pi n}{L} c_s t\right) \sin\left(\frac{\pi n}{L} z\right) \cos(\pi n), \quad (3.22)$$

which is the expression for linear acoustic waves in terms of pressure for a Dirichlet boundary condition under the assumption of a linearly distributed energy deposition in a thin rod.

In order to determine the displacement u , we again take the gradient of P (in Eqn. 3.22)

$$\nabla_z P(z, t) = -\frac{2\Gamma Q_0}{V_0 L} \sum_{n=1}^{\infty} \cos\left(\frac{n\pi}{L} c_s t\right) \cos\left(\frac{n\pi}{L} z\right) \cos(n\pi) \quad (3.23)$$

and substitute it in Eqn. 3.7, which leads to:

$$u(z, t) = \frac{2\Gamma Q_0}{\rho_0 V_0 L} \sum_{n=1}^{\infty} \cos\left(\frac{n\pi}{L} z\right) \cos(n\pi) \iint_t \cos\left(\frac{n\pi}{L} c_s t\right) dt^2. \quad (3.24)$$

Finally, solving the double integral and applying the initial conditions in Eqn. 3.8, we determine the expression for u to be

$$u(z, t) = -\frac{2\Gamma Q_0 L}{\rho_0 V_0 c_s^2 \pi^2} \sum_{n=1}^{\infty} \frac{1}{n^2} \left\{ \cos\left(\frac{n\pi}{L} c_s t\right) - 1 \right\} \cos\left(\frac{n\pi}{L} z\right) \cos(n\pi). \quad (3.25)$$

Unlike the case of the uniform energy deposition, investigation of the evolution of the waves (in both space and time, see Section A.2 in Appendix A) in the case of triangular distribution of deposited energy in a thin rod shows that the waves start their movement from the rear exit of the target and travel to the front of the target. This analysis is based on Eqn. 3.22 and 3.25. We summarise the results as follows:

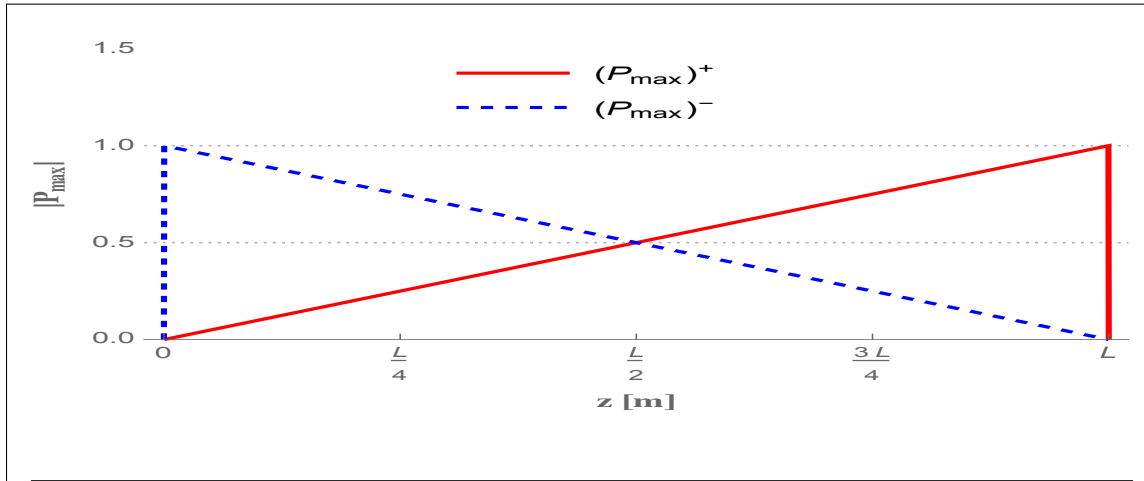


Figure 3.6: Peak Pressure Analysis For Linear Distribution of Deposited Energy in a Thin Rod with Dirichlet BCs: Plots of $(|P_{max}|)$ Absolute Peak Pressure Amplitude (normalised by $\Gamma \frac{Q_0}{V_0}$) along the Thin Rod Length, z (normalised by thin rod length, L). The $(P_{max})^+$ represents the Peak Amplitude of the Positive Pressure and the $(P_{max})^-$ represents the Peak Amplitude of the Negative Pressure.

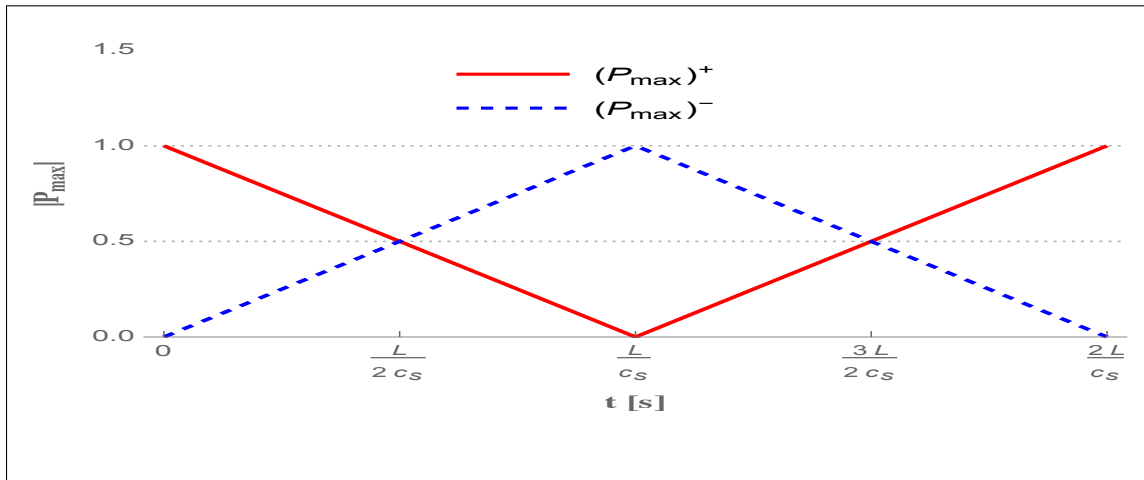


Figure 3.7: Peak Pressure Analysis For Linear Distribution of Deposited Energy in a Thin Rod with Dirichlet BCs: Plots of $(|P_{max}|)$ Absolute Peak Pressure Amplitude (normalised by $\Gamma \frac{Q_0}{V_0}$) versus time, t (normalised by $\frac{L}{c_s}$). The $(P_{max})^+$ represents the Peak Amplitude of the Positive Pressure and the $(P_{max})^-$ represents the Peak Amplitude of the Negative Pressure.

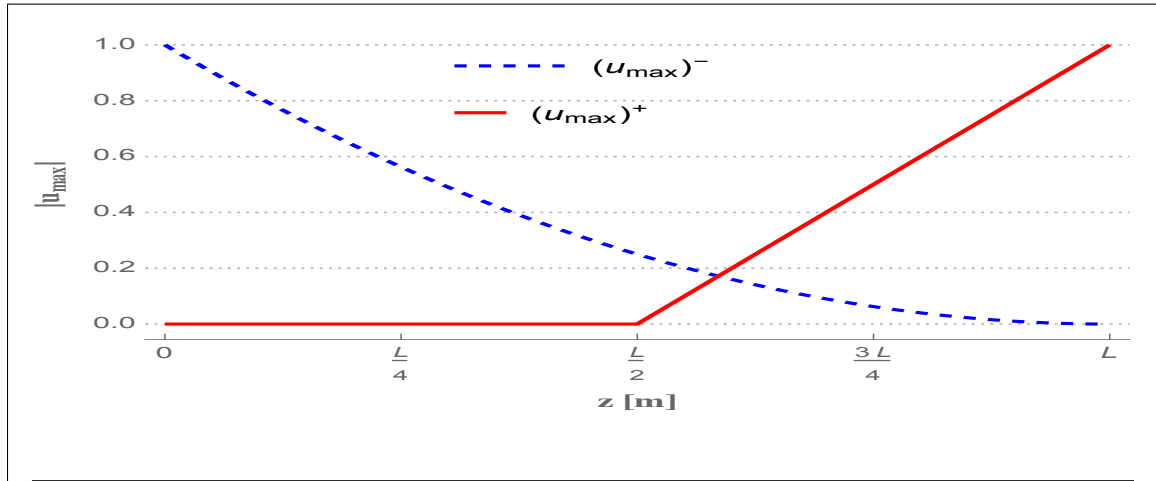


Figure 3.8: Peak Displacement Analysis For Linear Distribution of Deposited Energy in a Thin Rod with Dirichlet BCs: Plots of $(|u_{max}|)$ Absolute Peak Displacement Amplitude (normalised by $0.06 \frac{\Gamma Q_0}{\rho_0 V_0 c_s^2}$) along the Thin Rod Length, z [m]. The $(u_{max})^+$ represents the Peak Amplitude of the Positive Displacement and the $(u_{max})^-$ represents the Peak Amplitude of the Negative Displacement.

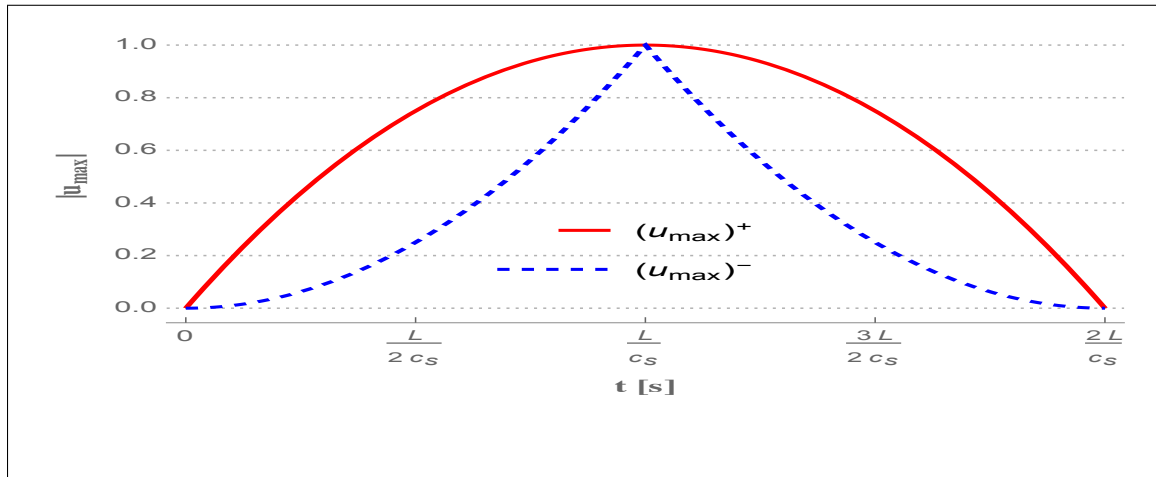


Figure 3.9: Peak Displacement Analysis For Linear Distribution of Deposited Energy in a Thin Rod with Dirichlet BCs: Plots of $(|u_{max}|)$ Absolute Peak Displacement Amplitude (normalised by $0.06 \frac{\Gamma Q_0}{\rho_0 V_0 c_s^2}$) versus time, t [s]. The $(u_{max})^+$ represents the Peak Amplitude of the Positive Displacement and the $(u_{max})^-$ represents the Peak Amplitude of the Negative Displacement.

1. Figures 3.6 and 3.7 indicate that the sum of the absolute peak amplitude pressure at any given time t and space z is equal to $\Gamma \frac{Q_0}{V_0}$ because

$$0 \leq \sum_{n=1}^{\infty} \frac{1}{n} \cos\left(\frac{\pi n}{L} c_s t\right) \sin\left(\frac{\pi n}{L} z\right) \cos(\pi n) \leq 1. \quad (3.26)$$

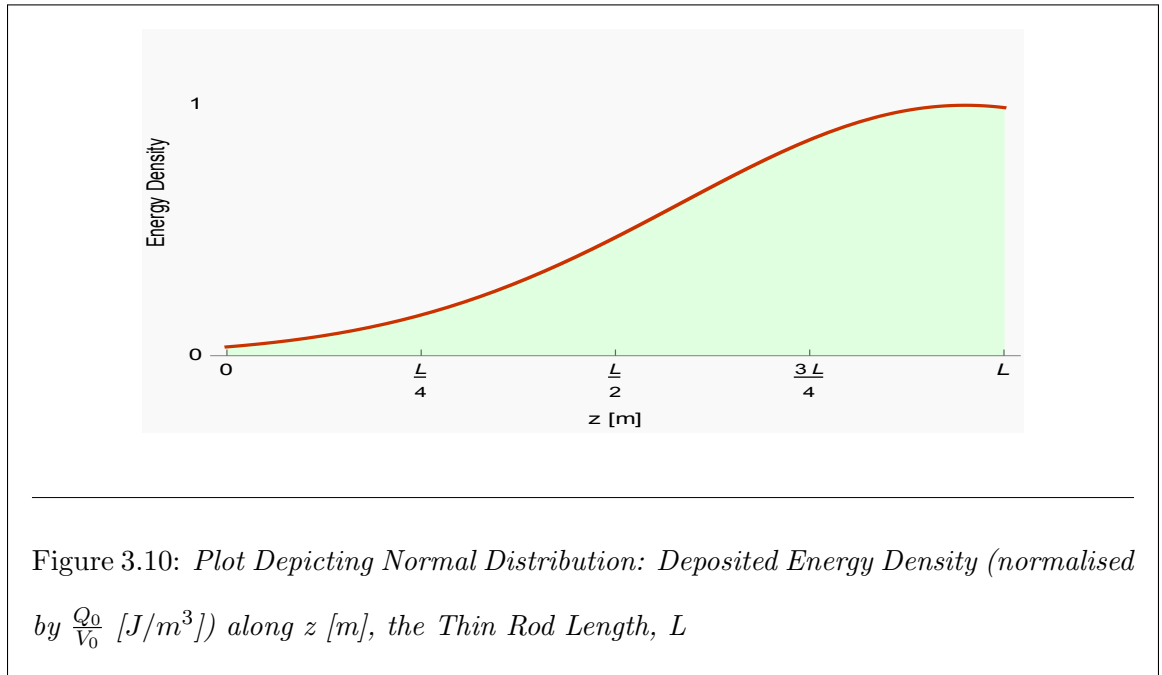
2. Figure 3.6 shows that, at the middle of the target ($\frac{L}{2}$), the absolute value of both the positive and negative peak amplitude of the pressure is $\frac{1}{2} \Gamma \frac{Q_0}{V_0}$. (See also Section A.2 in Appendix A.)
3. Also in Figure 3.7, at times $\frac{L}{2c_s}, \frac{3L}{2c_s}, \dots, \frac{mL}{2c_s}$ (where $m \in \mathbb{Z}_{odd}^+$), the absolute value of both the positive and negative peak amplitude of the pressure is $\frac{1}{2} \Gamma \frac{Q_0}{V_0}$.
4. As shown in Figure 3.8, between $z = 0$ and $\frac{L}{2}$, the positive peak amplitude of the displacement is zero and the negative peak amplitude of the displacement is zero at $z = L$.
5. The following is shown in Figure 3.9
- (a) at time $t = \frac{mL}{2c_s} \forall m \in \mathbb{Z}_{odd}^+$, the absolute value of the positive peak amplitude of the displacement (u_{max}^+) is approximately three times the absolute value of the negative peak amplitude of the displacement (u_{max}^-)
 - (b) at time $t = \frac{mL}{c_s}$ for $m \in \mathbb{Z}^+$, the absolute value of the positive peak amplitude of the displacement (u_{max}^+) is always equal to the absolute value of the negative peak amplitude of the displacement (u_{max}^-)
 - (c) at time $t = \frac{mL}{c_s}$ for $m \in \mathbb{Z}_{odd}^+$, the absolute value of the peak amplitude of the displacement $|u_{max}|$ is always equal to 1 for both (u_{max}^-) and (u_{max}^+)
 - (d) at time $t = \frac{mL}{c_s}$ for $m \in \mathbb{Z}_{even}^+$, the absolute value of the peak amplitude of the displacement $|u_{max}|$ is always equal to 0 for both (u_{max}^-) and (u_{max}^+)

3.1.3 Energy Density Profile: Gaussian (Normal) Distribution

We now address a more complicated mathematical description of the energy deposition. Let assume that the energy deposited in the thin rod is normally distributed, that is, Gaussian distribution (see Figure 3.10), and is defined in such a way as

$$Q(z) = Q_0 \exp(-A^2(z - B)^2) \quad (3.27)$$

where $A = \frac{1}{\sqrt{2}\sigma_z}$, σ_z is the standard deviation of the distribution and B is the mean.



To arrive at the following expression, we substitute the energy distribution definition in Eqn. 3.27 into Eqn. 3.11

$$P(z, t) = \frac{2\Gamma Q_0}{V_0 L} \sum_{n=1}^{\infty} \cos\left(\frac{\pi n}{L} c_s t\right) \sin\left(\frac{\pi n}{L} z\right) \int_0^L \exp(-A^2(z - B)^2) \sin\left(\frac{\pi n}{L} z\right) dz, \quad (3.28)$$

and solving the integral part of Eqn. 3.28 by using integration by parts method, we have

$$\int_0^L \exp(-A^2(z-B)^2) \sin\left(\frac{\pi n}{L}z\right) dz = \frac{\sqrt{\pi}}{4A} I \exp\left[-\frac{n\pi}{4A^2L^2}(4IA^2BL + n\pi)\right] \left(\text{Erf}\left[AB - \frac{In\pi}{2AL}\right] + \right. \\ \left. - \text{Erf}\left[A(B-L) - \frac{In\pi}{2AL}\right] - \exp\left(2IB\frac{n\pi}{L}\right) \times \right. \\ \left. \left\{ \text{Erf}\left[A(L-B) - \frac{In\pi}{2AL}\right] + \text{Erf}\left[AB + \frac{In\pi}{2AL}\right] \right\} \right). \quad (3.29)$$

$I^2 = -1$, where I is an imaginary number. Inserting the above solution for the integration into Eqn. 3.28 gives

$$P(z, t) = \frac{\Gamma Q_0 \sqrt{\pi}}{2LV_0 A} I \sum_{n=1}^{\infty} \cos\left(\frac{n\pi}{L}c_s t\right) \sin\left(\frac{n\pi}{L}z\right) \exp\left[-\frac{n\pi}{4A^2L^2}(4IA^2BL + n\pi)\right] \times \\ \left(\text{Erf}\left[AB - \frac{In\pi}{2AL}\right] - \text{Erf}\left[A(B-L) - \frac{In\pi}{2AL}\right] - \exp\left(2IB\frac{n\pi}{L}\right) \times \right. \\ \left. \left\{ \text{Erf}\left[A(L-B) - \frac{In\pi}{2AL}\right] + \text{Erf}\left[AB + \frac{In\pi}{2AL}\right] \right\} \right), \quad (3.30)$$

which is a complete expression for the linear acoustic wave in a thin rod (with Dirichlet boundary condition at both ends of the rod) caused by Gaussian distributed energy deposition.

We evaluate the gradient of P (by using Eqn. 3.30) to be

$$\nabla_z P(z, t) = \frac{\Gamma Q_0 \pi \sqrt{\pi}}{2AV_0 L} I \sum_{n=1}^{\infty} \cos\left(\frac{n\pi}{L}c_s t\right) \cos\left(\frac{n\pi}{L}z\right) \exp\left[-\frac{n\pi}{4A^2L^2}(4IA^2BL + n\pi)\right] \times \\ \left(\text{Erf}\left[AB - \frac{In\pi}{2AL}\right] - \text{Erf}\left[A(B-L) - \frac{In\pi}{2AL}\right] - \exp\left(2IB\frac{n\pi}{L}\right) \times \right. \\ \left. \left\{ \text{Erf}\left[A(L-B) - \frac{In\pi}{2AL}\right] + \text{Erf}\left[AB + \frac{In\pi}{2AL}\right] \right\} \right), \quad (3.31)$$

and inserting this expression above for the gradient of P (in Eqn. 3.31) into Eqn. 3.7, we

obtain the expression for displacement in this case to be

$$\begin{aligned}
u(z, t) = & -\frac{\Gamma Q_0 \pi \sqrt{\pi}}{2AV_0 L^2} I \sum_{n=1}^{\infty} n \cos\left(\frac{n\pi}{L} z\right) \exp\left[-\frac{n\pi}{4A^2 L^2} (4IA^2 BL + n\pi)\right] \left(\text{Erf}\left[AB - \frac{In\pi}{2AL}\right] + \right. \\
& - \text{Erf}\left[A(B-L) - \frac{In\pi}{2AL}\right] - \exp\left(2IB\frac{n\pi}{L}\right) \times \left\{ \text{Erf}\left[A(L-B) - \frac{In\pi}{2AL}\right] + \right. \\
& \left. \left. + \text{Erf}\left[AB + \frac{In\pi}{2AL}\right]\right\} \right) \iint_t \cos\left(\frac{n\pi}{L} c_s t\right) dt^2. \tag{3.32}
\end{aligned}$$

Clearly we need to solve for the double integral and applying the initial conditions in Eqn. 3.8 to get the complete expression for the displacement, which turns out to be

$$\begin{aligned}
u(z, t) = & \frac{\Gamma Q_0 \sqrt{\pi}}{2\pi \rho_0 AV_0 L^2 c_s^2} I \sum_{n=1}^{\infty} \frac{1}{n} \cos\left(\frac{n\pi}{L} z\right) \left\{ \cos\left(\frac{n\pi}{L} c_s t\right) - 1 \right\} \times \\
& \exp\left[-\frac{n\pi}{4A^2 L^2} (4IA^2 BL + n\pi)\right] \left(\text{Erf}\left[AB - \frac{In\pi}{2AL}\right] - \text{Erf}\left[A(B-L) - \frac{In\pi}{2AL}\right] + \right. \\
& \left. - \exp\left(2IB\frac{n\pi}{L}\right) \left\{ \text{Erf}\left[A(L-B) - \frac{In\pi}{2AL}\right] + \text{Erf}\left[AB + \frac{In\pi}{2AL}\right]\right\} \right). \tag{3.33}
\end{aligned}$$

Results of the analysis of Eqn. 3.30 and 3.33 (for pressure and displacement respectively) using parameters in Table 3.1 are in Section A.3 in the Appendix A. Comparing the results with the linear case reveal remarkable resemblance, hence we can confirm that the linear case is a suitable approximation to the Gaussian case. Thus the same physical interpretation in linear case can be applied here too.

3.2 Neumann Problem

Neumann boundary conditions specify the normal derivative of the function on a surface [39]. We exploit the worst case scenario by imposing $\nabla_z P = 0$ at both ends of the rod. This implies that the system is insulated. This means also that the boundary is not allowed to move.

This problem setup can be summarised as follows:

Partial Differential Equation:

$$\frac{\partial^2 P}{\partial t^2} - c_s^2 \frac{\partial^2 P}{\partial z^2} = 0.$$

Initial condition:

$$P(z, 0) = \frac{\Gamma}{V_0} Q(z) \quad \text{and} \quad \frac{\partial P}{\partial t} \Big|_{t=0} = 0. \quad (3.34)$$

Boundary conditions:

$$\frac{\partial P}{\partial z} \Big|_{z=0} = 0 = \frac{\partial P}{\partial z} \Big|_{z=L}.$$

A solution to the above problem setup is given as [26]:

$$P(z, t) = \frac{2}{L} \left[\frac{1}{2} \int_0^L P(z, 0) dz + \sum_{n=1}^{\infty} \cos(\lambda_n c_s t) \cos(\lambda_n z) \int_0^L P(z, 0) \cos(\lambda_n z) dz \right], \quad (3.35)$$

where $\lambda_n = \frac{n\pi}{L}$. Substituting for the expression for $P(z, 0)$ specified in Eqn. 3.34 into Eqn. 3.35, we have:

$$P(z, t) = \frac{2\Gamma}{LV_0} \left[\frac{1}{2} \int_0^L Q(z) dz + \sum_{n=1}^{\infty} \cos(\lambda_n c_s t) \cos(\lambda_n z) \int_0^L Q(z) \cos(\lambda_n z) dz \right]. \quad (3.36)$$

As one might suspect, the complete solution depends on the spatial distribution of the energy deposited on the target, just as in case of the Dirichlet boundary problem. Our task now is to solve Eqn. 3.36 for different energy distributions analytically and numerically.

3.2.1 Energy Density Profile: Rectangular (Uniform) Distribution

The uniform energy deposition is defined as

$$Q(z) = Q_0. \quad (3.37)$$

Substituting Eqn. 3.37 into Eqn 3.36, gives:

$$P(z, t) = \frac{2\Gamma Q_0}{LV_0} \left[\frac{L}{2} + \sum_{n=1}^{\infty} \frac{1}{\lambda_n} \cos(\lambda_n c_s t) \cos(\lambda_n z) \sin(\lambda_n L) \right]. \quad (3.38)$$

Interestingly, the last term on the RHS of Eqn. 3.38 is zero, because $\sin(\lambda_n L) = \sin(n\pi) = 0$ (since, $\lambda_n = \frac{n\pi}{L}$) $\forall n \in \mathbb{Z}$. Therefore, Eqn. 3.38 can be reduced to

$$P(z, t) = \frac{\Gamma Q_0}{V_0}. \quad (3.39)$$

This result (in Eqn. 3.39) is rather remarkable but not unexpected. It implies that in an insulated system or a system with immovable boundaries, the pressure will remain constant throughout the material at all times.

Obviously,

$$\nabla_z P(z, t) = 0. \quad (3.40)$$

Therefore, we expect

$$u(z, t) = 0, \quad (3.41)$$

implying that no displacement occurred in the material.

3.2.2 Energy Density Profile: Triangular (Linear) Distribution

As we did in case of Dirichlet BC problem, we define the linear energy distribution in a thin rod as follows:

$$Q(z) = Q_0 z. \quad (3.42)$$

Substituting Eqn. 3.42 into Eqn. 3.36, gives

$$P(z, t) = \frac{2\Gamma Q_0}{L^2 V_0} \left[\frac{1}{2} \int_0^L z dz + \sum_{n=1}^{\infty} \cos(\lambda_n c_s t) \cos(\lambda_n z) \int_0^L z \cos(\lambda_n z) dz \right] \quad (3.43)$$

solving the integrals, we have:

$$P(z, t) = \frac{2\Gamma Q_0}{L^2 V_0} \left[\frac{L^2}{4} + \sum_{n=1}^{\infty} \frac{1}{\lambda_n^2} \{ \lambda_n L \sin(\lambda_n L) + \cos(\lambda_n L) - 1 \} \cos(\lambda_n c_s t) \right. \\ \left. \cos(\lambda_n z) \right]. \quad (3.44)$$

Putting $\lambda_n = \frac{n\pi}{L}$ into the above equation and since, $\sin(n\pi) = 0 \quad \forall n \in \mathbb{Z}$, we can reduce Eqn. 3.44 to:

$$P(z, t) = \frac{2\Gamma Q_0}{V_0} \left[\frac{1}{4} + \frac{1}{\pi^2} \sum_{n=1}^{\infty} \frac{1}{n^2} \cos\left(\frac{n\pi}{L} ct\right) \cos\left(\frac{n\pi}{L} z\right) \{ \cos(n\pi) - 1 \} \right] \quad (3.45)$$

because

$$\cos(n\pi) = \begin{cases} 1 & \text{when } n \in \mathbb{Z}_{\text{even}}^+ \\ -1 & \text{when } n \in \mathbb{Z}_{\text{odd}}^+ \end{cases}. \quad (3.46)$$

At every $n \in \mathbb{Z}_{\text{even}}^+$, the value of $(\cos(n\pi) - 1)$ will be zero, hence we can eliminate that by substituting $n = 2n + 1$, which leads to

$$P(z, t) = \frac{2\Gamma Q_0}{V_0} \left[\frac{1}{4} + \frac{1}{\pi^2} \sum_{n=0}^{\infty} \frac{1}{[2n+1]^2} \cos\left(\frac{[2n+1]\pi}{L} c_s t\right) \cos\left(\frac{[2n+1]\pi}{L} z\right) \right. \\ \left. \{ \cos([2n+1]\pi) - 1 \} \right]. \quad (3.47)$$

Interestingly, $\cos([2n+1]\pi) = -1 \quad \forall n \in \mathbb{Z}$, therefore we can simply express the pressure as

$$P(z, t) = \frac{4\Gamma Q_0}{V_0} \left[\frac{1}{8} - \frac{1}{\pi^2} \sum_{n=0}^{\infty} \frac{1}{[2n+1]^2} \cos\left(\frac{[2n+1]\pi}{L} c_s t\right) \cos\left(\frac{[2n+1]\pi}{L} z\right) \right]. \quad (3.48)$$

To see how the displacement evolves in this case, we determine

$$\nabla_z P(z, t) = -\frac{2\Gamma Q_0}{V_0 L^2 \pi^4} \sum_{n=1}^{\infty} n \cos\left(\frac{n\pi}{L} c_s t\right) \sin\left(\frac{n\pi}{L} z\right) [\cos(n\pi) - 1] \quad (3.49)$$

and substitute the above equation into Eqn. 3.7, which gives

$$u(z, t) = \frac{2\Gamma Q_0 \pi}{\rho_0 V_0 L^2 \pi^4} \sum_{n=1}^{\infty} \sin\left(\frac{n\pi}{L} z\right) \cos(n\pi) \iint_t \cos\left(\frac{n\pi}{L} c_s t\right) dt^2. \quad (3.50)$$

Solving the double integral and applying Eqn. 3.8 to determine the integration constants, the displacement in a thin rod, in which the energy deposited is linearly distributed and the boundaries are fixed (in terms of displacement), can be written as

$$u(z, t) = -\frac{2\Gamma Q_0 L}{\rho_0 V_0 c_s^2 \pi^3} \sum_{n=1}^{\infty} \frac{1}{n^3} \left\{ \cos\left(\frac{n\pi}{L} c_s t\right) - 1 \right\} \sin\left(\frac{n\pi}{L} z\right) [\cos(n\pi) - 1]. \quad (3.51)$$

We analyse Eqn. 3.48 and 3.51 numerically by using the parameter in Table 3.1. The result of the analysis is presented in the plots that can be found in Section A.4 of the Appendix A. By observing those plots, it is evident that the movement of the waves is similar to the case of uniform energy deposition with Dirichlet BC, in that the waves develop at both ends of the target at the same time. Also, these waves start moving toward each other from both ends. To have an in-depth understanding of this behaviour, we look into the peak amplitude of both the pressure and the displacement (see Figures 3.11, 3.12, 3.13 and 3.14). We summarise as below:

1. The value of the pressure waves is always positive: compressive waves
2. At any given time and space, the sum of the maximum and minimum peak pressure is always equal to $\frac{\Gamma Q_0}{V_0}$.
3. Due to the superposition of the waves, at times $\frac{L}{2c_s}, \frac{3L}{2c_s}, \frac{5L}{2c_s}, \dots, \frac{mL}{2c_s}$ (where $m \in \mathbb{Z}_{odd}^+$), there is a destructive interference occurring at those times. This is why

$$P_{max} = P_{min} = \frac{1}{2} \Gamma \frac{Q_0}{V_0} \quad (3.52)$$

and normalised displacement,

$$|u_{peak}| = \frac{1}{2}$$

(see Figures 3.11 and 3.13).

4. Also, Eqn. 3.52 holds at the middle of the target (that is, at $z = \frac{L}{2}$) and the displacement is highest at this point because the boundary is not allowed to move (see Figures 3.12 and 3.14).
5. Based on Figure 3.13 we further observed that at time $t = \frac{mL}{c_s}$ the following occurs

$$|u_{peak}| = \begin{cases} 1 & \text{when } m \in \mathbb{Z}_{odd}^+ \\ 0 & \text{when } m \in \mathbb{Z}_{even}^+ \end{cases} .$$

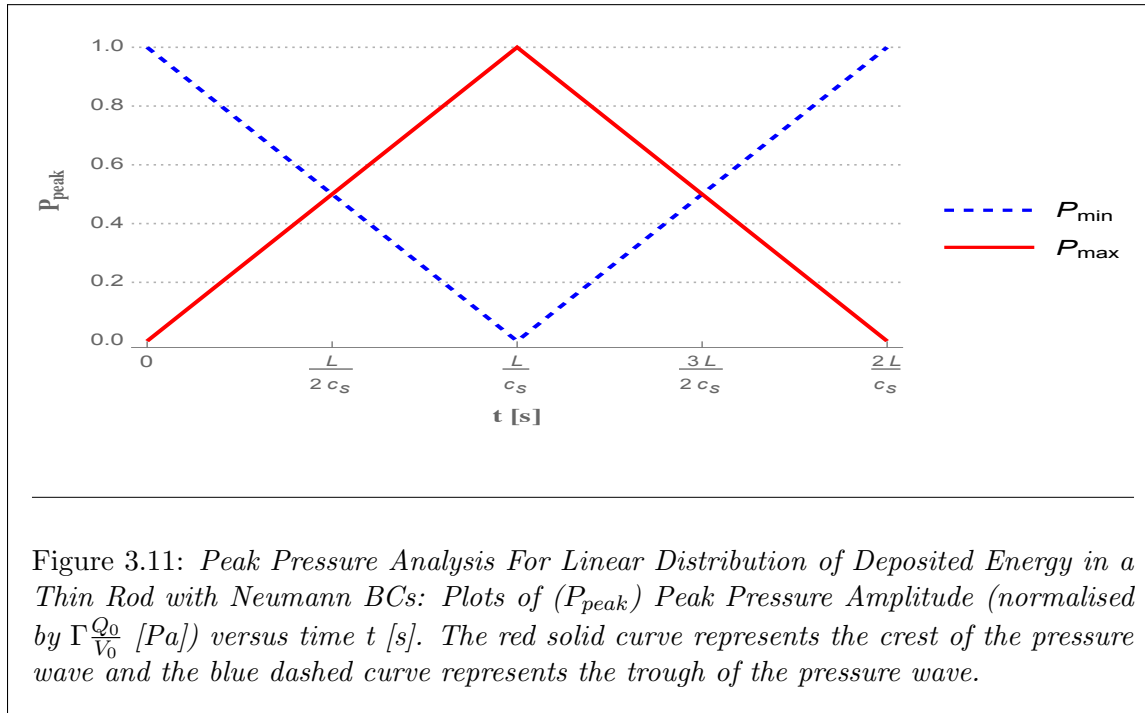


Figure 3.11: *Peak Pressure Analysis For Linear Distribution of Deposited Energy in a Thin Rod with Neumann BCs: Plots of (P_{peak}) Peak Pressure Amplitude (normalised by $\Gamma \frac{Q_0}{V_0}$ [Pa]) versus time t [s]. The red solid curve represents the crest of the pressure wave and the blue dashed curve represents the trough of the pressure wave.*

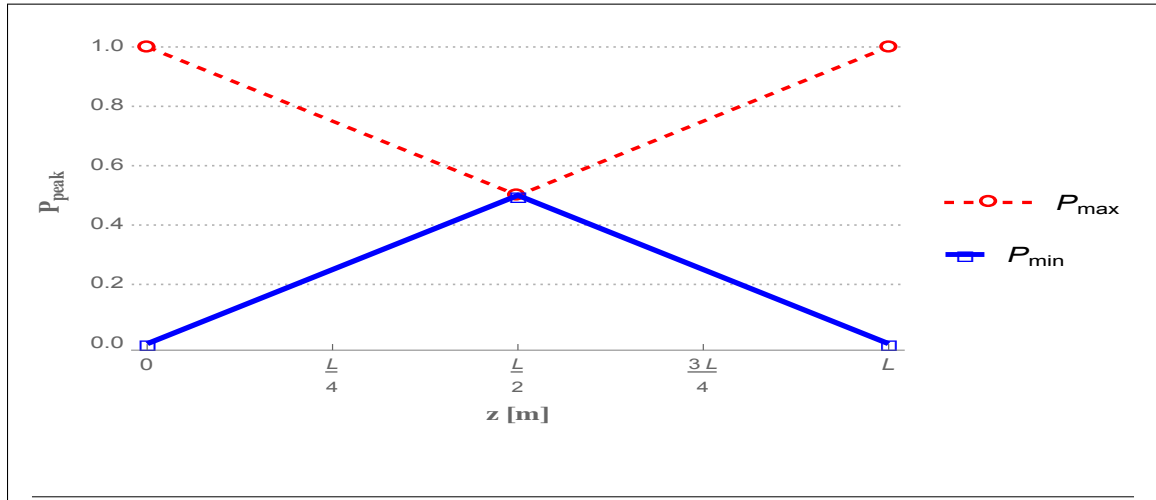


Figure 3.12: Peak Pressure Analysis For Linear Distribution of Deposited Energy in a Thin Rod with Neumann BCs: Plots of (P_{peak}) Peak Pressure Amplitude (normalised by $\Gamma \frac{Q_0}{V_0}$ [Pa]) along the Thin Rod Length, z [m]. The red dashed curve represents the crest of the pressure wave and the blue solid curve represents the trough of the pressure wave.

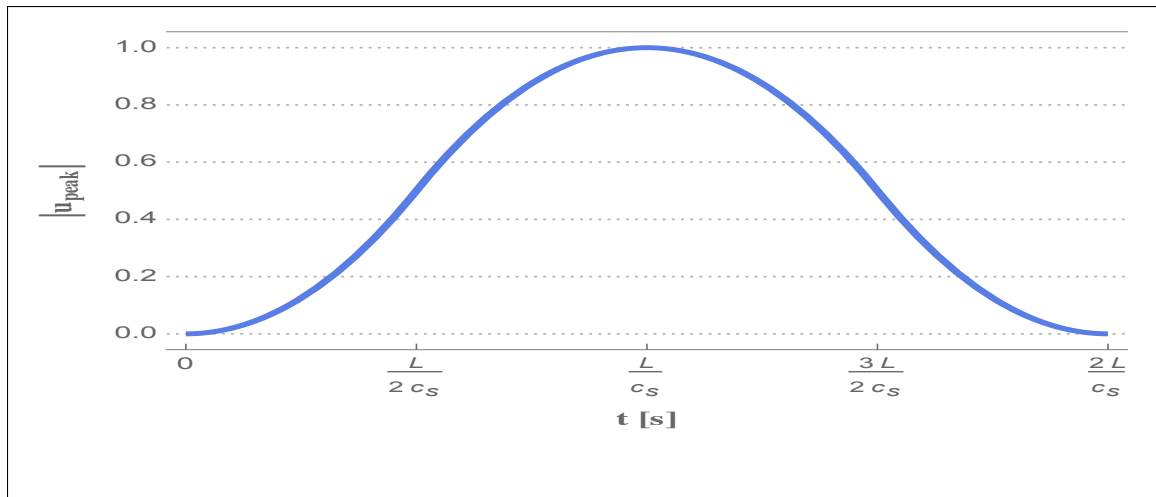
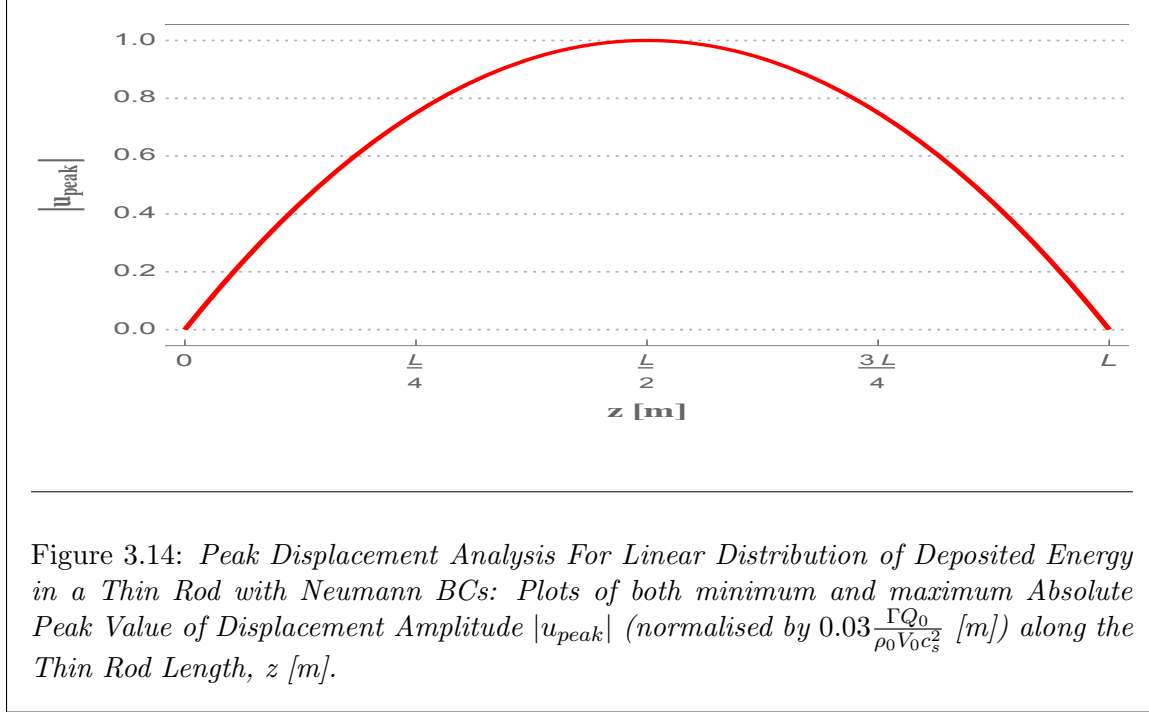


Figure 3.13: Peak Displacement Analysis For Linear Distribution of Deposited Energy in a Thin Rod with Neumann BCs: Plots of Absolute Peak Displacement Amplitude $|u_{peak}|$ (normalised by $0.03 \frac{\Gamma Q_0}{\rho_0 V_0 c_s^2}$ [m]) versus time t [s].



3.2.3 Energy Density Profile: Gaussian (Normal) Distribution

We use the same energy distribution definition in Eqn. 3.27, which is

$$Q(z) = Q_0 \exp(-A^2(z - B)^2), \quad (3.53)$$

where all the terms in Eqn. 3.53 still maintain their previous meaning here too. We start by substituting Eqn. 3.53 into the general solution (expressed in Eqn. 3.36), hence we can write P as

$$P(z, t) = \frac{2\Gamma Q_0}{LV_0} \left[\frac{1}{2} \int_0^L \exp(-A^2(z - B)^2) dz + \sum_{n=1}^{\infty} \cos(\lambda_n c_s t) \cos(\lambda_n z) \times \int_0^L \exp(-A^2(z - B)^2) \cos(\lambda_n z) dz \right]. \quad (3.54)$$

By solving those integrals in Eqn. 3.54, we can write the pressure acoustic waves in a thin rod with Neumann boundary conditions imposed on both ends of the target as

$$\begin{aligned}
P(z, t) = & \frac{\Gamma Q_0 \sqrt{\pi}}{2LV_0 A} \left[\text{Erf}(AB) - \text{Erf}(A[B - L]) + \sum_{n=1}^{\infty} \exp \left[-\frac{\lambda_n}{4} \left(4IB + \frac{\lambda_n}{A^2} \right) \right] \times \right. \\
& \times \cos(\lambda_n c_s t) \cos(\lambda_n z) \left(\text{Erf} \left[AB - \frac{I\lambda_n}{2A} \right] - \text{Erf} \left[A(B - L) - \frac{I\lambda_n}{2A} \right] + \right. \\
& \left. \left. + \exp(2IB\lambda_n) \left\{ \text{Erf} \left[A(L - B) - \frac{I\lambda_n}{2A} \right] + \text{Erf} \left[AB + \frac{I\lambda_n}{2A} \right] \right\} \right) \right]. \quad (3.55)
\end{aligned}$$

In this case, we are left with determining the displacement $u(z, t)$, which we did (as usual) by first evaluating gradient of P

$$\begin{aligned}
\nabla_z P(z, t) = & -\frac{\Gamma Q_0 \pi \sqrt{\pi}}{2AV_0 L^2} \sum_{n=1}^{\infty} n \cos \left(\frac{n\pi}{L} c_s t \right) \sin \left(\frac{n\pi}{L} z \right) \exp \left[-\frac{\lambda_n}{4} \left(4IB + \frac{\lambda_n}{A^2} \right) \right] \times \\
& \times \left(\text{Erf} \left[AB - \frac{I\lambda_n}{2A} \right] - \text{Erf} \left[A(B - L) - \frac{I\lambda_n}{2A} \right] + \exp(2IB\lambda_n) \times \right. \\
& \left. \times \left\{ \text{Erf} \left[A(L - B) - \frac{I\lambda_n}{2A} \right] + \text{Erf} \left[AB + \frac{I\lambda_n}{2A} \right] \right\} \right) \quad (3.56)
\end{aligned}$$

and then, we insert Eqn. 3.56 into Eqn. 3.7 to get

$$\begin{aligned}
u(z, t) = & \frac{\Gamma Q_0 \pi \sqrt{\pi}}{2\rho_0 AV_0 L^2} \sum_{n=1}^{\infty} n \sin \left(\frac{n\pi}{L} z \right) \exp \left[-\frac{\lambda_n}{4} \left(4IB + \frac{\lambda_n}{A^2} \right) \right] \left(\exp(2IB\lambda_n) \times \right. \\
& \times \left\{ \text{Erf} \left[A(L - B) - \frac{I\lambda_n}{2A} \right] + \text{Erf} \left[AB + \frac{I\lambda_n}{2A} \right] \right\} - \text{Erf} \left[A(B - L) - \frac{I\lambda_n}{2A} \right] + \\
& \left. + \text{Erf} \left[AB - \frac{I\lambda_n}{2A} \right] \right) \iint_t \cos \left(\frac{n\pi}{L} c_s t \right) dt^2. \quad (3.57)
\end{aligned}$$

We re-express the above (Eqn. 3.57) by solving for the double integrals and applying Eqn. 3.8, and thereby arrive at

$$\begin{aligned}
u(z, t) = & -\frac{\Gamma Q_0 \sqrt{\pi}}{2\pi\rho_0 AV_0 c_s^2} \sum_{n=1}^{\infty} \frac{1}{n} \sin \left(\frac{n\pi}{L} z \right) \left\{ \cos \left(\frac{n\pi}{L} c_s t \right) - 1 \right\} \exp \left[-\frac{\lambda_n}{4} \left(4IB + \frac{\lambda_n}{A^2} \right) \right] \times \\
& \times \left(\exp(2IB\lambda_n) \left\{ \text{Erf} \left[A(L - B) - \frac{I\lambda_n}{2A} \right] + \text{Erf} \left[AB + \frac{I\lambda_n}{2A} \right] \right\} + \right. \\
& \left. - \text{Erf} \left[A(B - L) - \frac{I\lambda_n}{2A} \right] + \text{Erf} \left[AB - \frac{I\lambda_n}{2A} \right] \right). \quad (3.58)
\end{aligned}$$

Interestingly, the behaviour here is quite similar to that of linear case, as matter of fact, is it an approximation of the linear case. By analysing Eqn. 3.55 and 3.58 (for pressure and displacement respectively) and using the parameters in Table 3.1, the results in Section A.5 of Appendix A were obtained. To grasp the full meaning of these results, we examine the dynamic behaviour in term of the peak amplitude, and the results are presented in Figures 3.15, 3.16, 3.17 and 3.18. We summarise as follows:

1. The value of the pressure waves is always positive: compressive waves.
2. Due to the superposition of the waves, at times $\frac{L}{2c_s}, \frac{3L}{2c_s}, \frac{5L}{2c_s}, \dots, \frac{mL}{2c_s}$ (where $m \in \mathbb{Z}_{odd}^+$), there is a destructive interference occurring at those times. This is why there is no displacement at those times and

$$P_{max} = P_{min} = \frac{1}{2}\Gamma \frac{Q_0}{V_0} \quad (3.59)$$

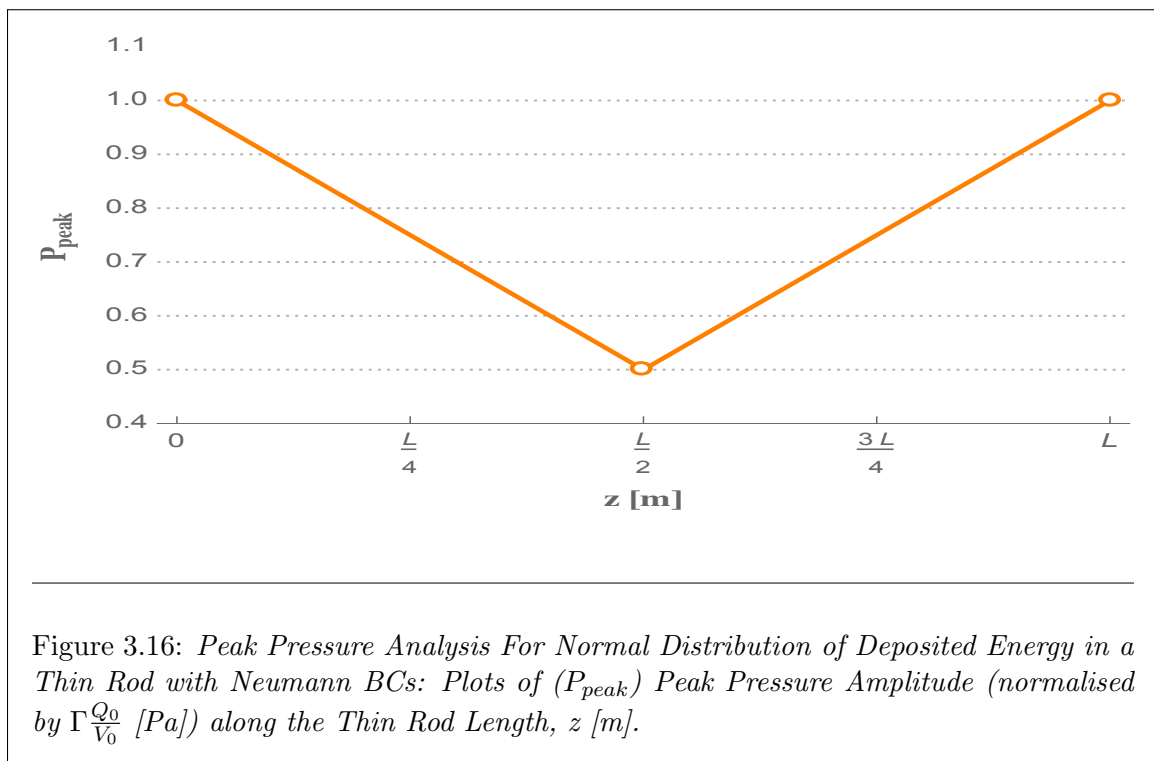
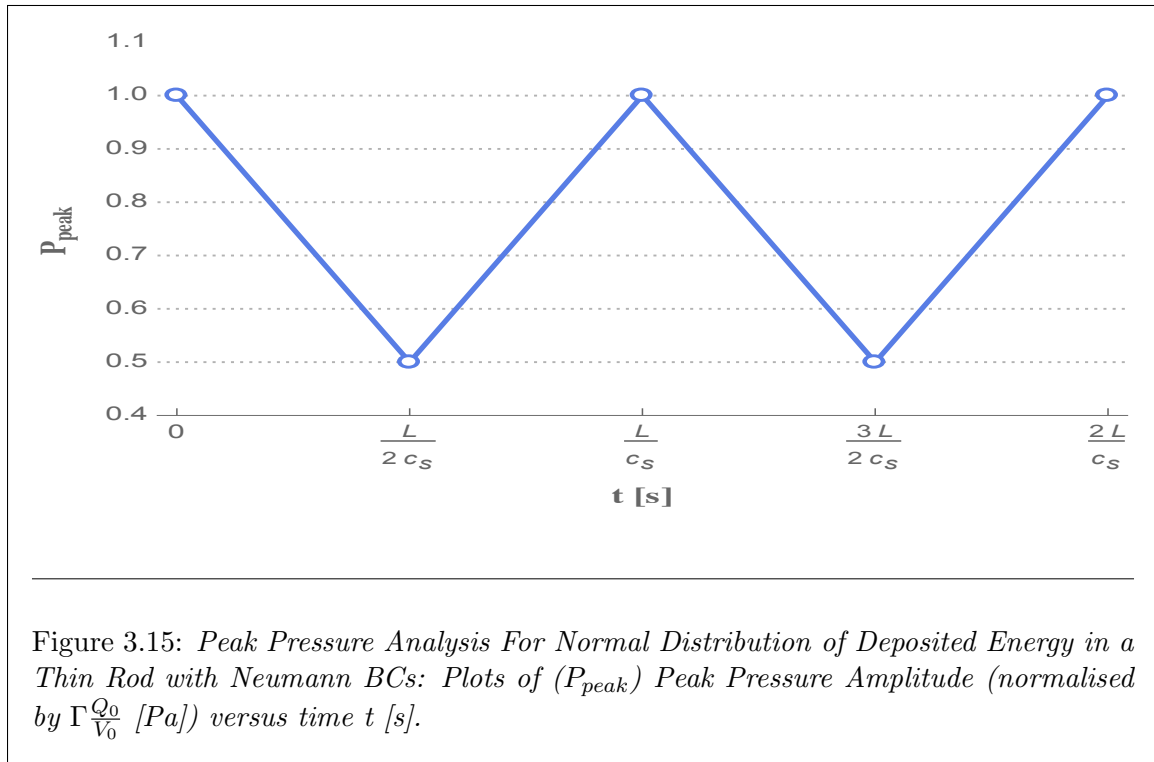
and normalised displacement,

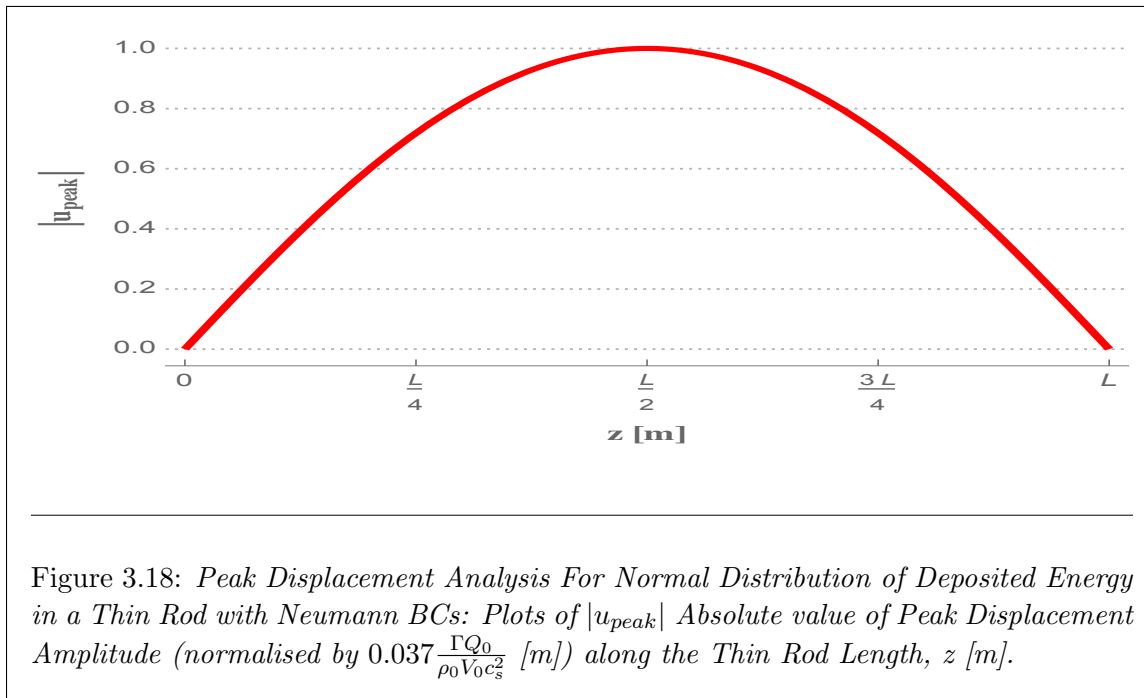
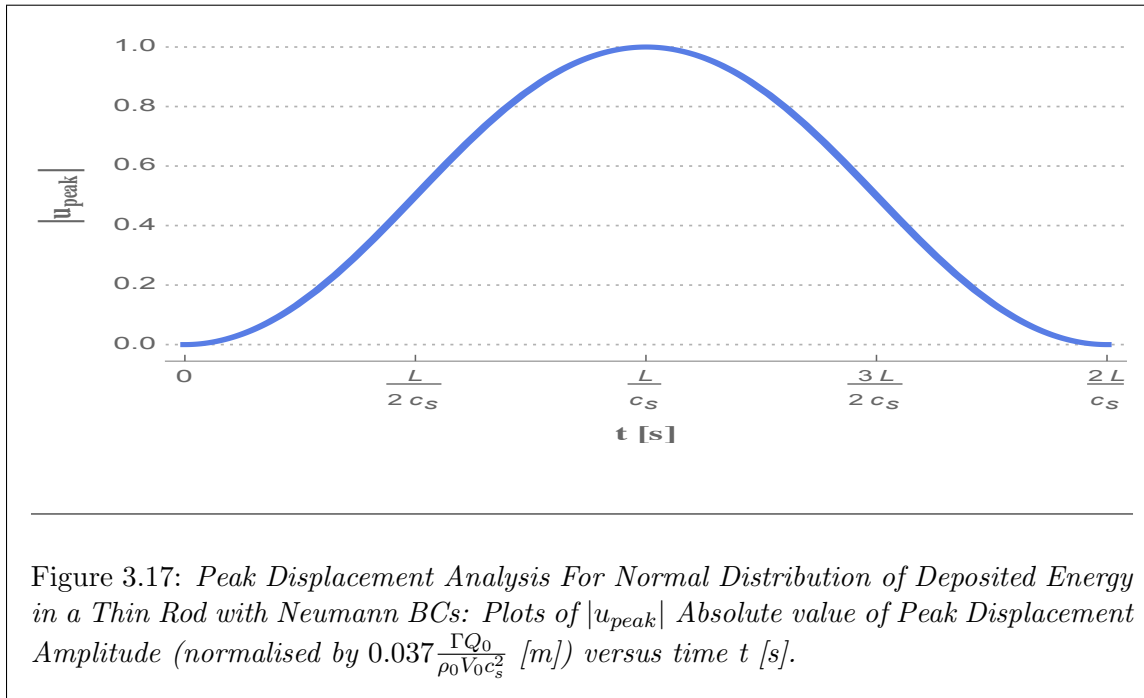
$$|u_{peak}| = \frac{1}{2}$$

(see Figures 3.15 and 3.17).

3. Eqn. 3.59 also holds at the middle of the target (that is, at $z = \frac{L}{2}$) and the displacement is highest at this point because the boundary is not allowed to move (see Figures 3.16 and 3.18).
4. Based on Figure 3.17 we further observed that at time $t = \frac{mL}{c_s}$ the following occurs

$$|u_{peak}| = \begin{cases} 1 & \text{when } m \in \mathbb{Z}_{odd}^+ \\ 0 & \text{when } m \in \mathbb{Z}_{even}^+ \end{cases} .$$





Chapter 4

LAW in a Cylindrical Disc

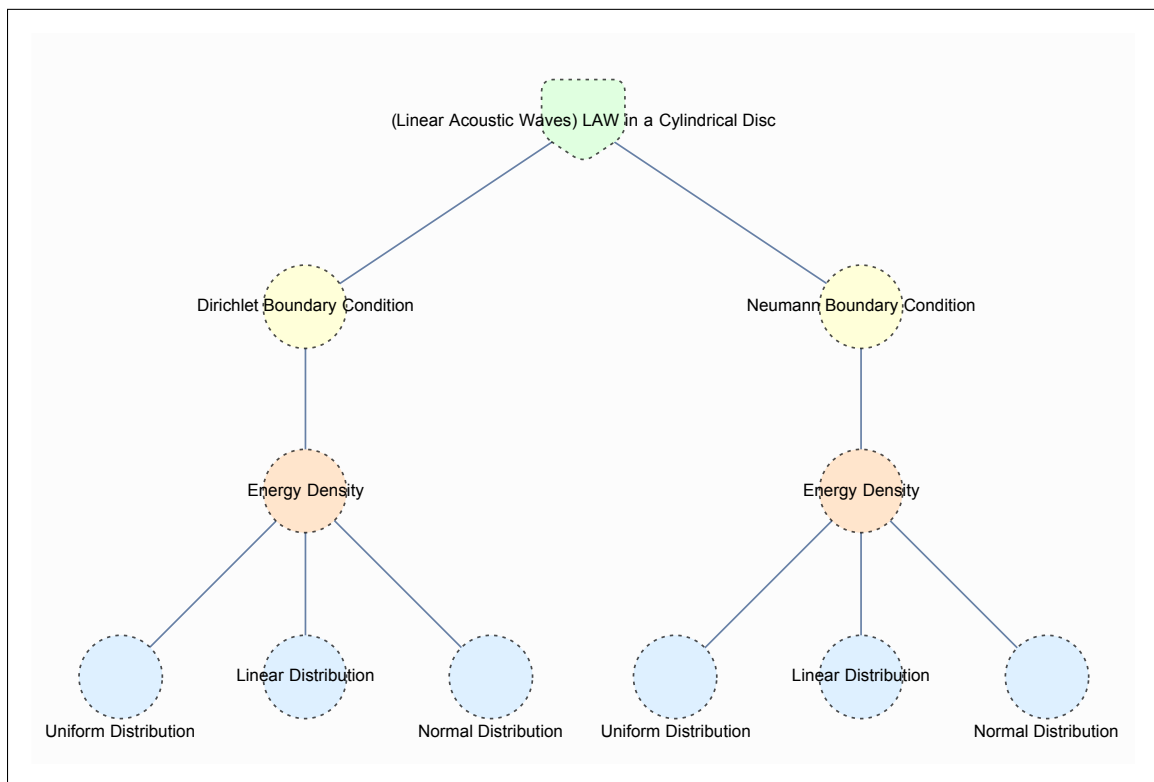


Figure 4.1: Schematic representation of content overview for this chapter.

In this chapter, we investigate linear acoustic waves using a disc approximation of the cylindrical solid target. This is a very good approximation in the case of a cylindrical target with a very tiny thickness (or when we assume that: $\frac{\partial^2 P}{\partial z^2} \approx 0 \parallel \frac{\partial^2 P}{\partial z^2} \ll \nabla_r^2 P$). We treat the energy deposition to be instantaneous as we did in Chapter 3. Thus, Eqn. 2.56 in Chapter 2 can be reduced to

$$\frac{\partial^2 P}{\partial t^2} - c_s^2 \left(\frac{\partial^2 P}{\partial r^2} + \frac{1}{r} \frac{\partial P}{\partial r} \right) = 0, \quad t > 0. \quad (4.1)$$

Solving Eqn. 4.1 requires initial conditions (ICs) and boundary conditions (BCs). In our case, we will study the Dirichlet and Neumann boundary condition.

In each case, we will consider two different radial energy density distributions, namely: rectangular distribution (also called uniform distribution) and triangular distribution. When P is known, we can easily evaluate for the displacement (\mathbf{u}) using

$$\mathbf{u}(r, t) = -\frac{1}{\rho_0} \iint_t \frac{\partial}{\partial r} P(r, t) dt^2 \quad (4.2)$$

with the initial conditions

$$\mathbf{u}(r, 0) = 0 = \left. \frac{\partial \mathbf{u}}{\partial t} \right|_{t=0} \quad (4.3)$$

to determine the values of the two integration constants that will appear as result of the double integral. For all cases that will be consider, we gave a quantitative analysis using the parameters in Table 4.1.

Table 4.1: Typical Case Analysis: Copper Target Material Parameters

Parameters	Symbol	Unit	Value
Radius	R	m	0.004
Spot size	r_0	m	0.001
Speed of sound	c_s	m/s	3570

4.1 Dirichlet Problem

Dirichlet boundary conditions specify the value of the function (in our case, this function is pressure, P at the circumference of the disc) on the surface [39]. This is our so-called “best case scenario”, in that at the boundary, energy is kept at zero degrees.

The problem setup can be summarised as follow:

Partial Differential Equation:

$$\frac{\partial^2 P}{\partial t^2} - c_s^2 \left(\frac{\partial^2 P}{\partial r^2} + \frac{1}{r} \frac{\partial P}{\partial r} \right) = 0.$$

Initial condition (IC):

$$\begin{aligned} P(r, 0) &= \frac{\Gamma}{V_0} Q(r) \quad \text{and} \\ \left. \frac{\partial P}{\partial t} \right|_{t=0} &= 0. \end{aligned} \tag{4.4}$$

Boundary condition (BC):

$$P(R, t) = 0.$$

The solution to the PDE above with the prescribed BC and IC can be presented in this form[26]:

$$P(r, t) = \frac{\partial}{\partial t} \int_0^R P(\xi, 0) G(r, \xi, t) d\xi \tag{4.5}$$

where Green’s function $G(r, \xi, t)$ is defined by the equation

$$G(r, \xi, t) = \frac{2\xi}{cR} \sum_{n=1}^{\infty} \frac{1}{\lambda_n J_1^2(\lambda_n)} J_0 \left(\lambda_n \frac{r}{R} \right) J_0 \left(\lambda_n \frac{\xi}{R} \right) \sin \left(\lambda_n \frac{c_s t}{R} \right). \tag{4.6}$$

The λ_n in Eqn. 4.6 are positive zeros of the Bessel function, $J_0(\lambda) = 0$. We can re-express Eqn.4.5 as

$$P(r, t) = \int_0^R P(\xi, 0) \frac{\partial}{\partial t} G(r, \xi, t) d\xi. \tag{4.7}$$

The time derivative of Green's function $G(r, \xi, t)$ (Eqn. 4.6) gives

$$\frac{\partial}{\partial t} G(r, \xi, t) = \frac{2\xi}{R^2} \sum_{n=1}^{\infty} \frac{1}{J_1^2(\lambda_n)} J_0\left(\lambda_n \frac{r}{R}\right) J_0\left(\lambda_n \frac{\xi}{R}\right) \cos\left(\lambda_n \frac{c_s t}{R}\right). \quad (4.8)$$

Thus, inserting Eqn. 4.8 and Eqn. 4.4 into Eqn. 4.7, the (pressure) equation for linear acoustic waves in a disc with Dirichlet BC is given as

$$P(r, t) = \frac{2\Gamma}{V_0 R^2} \sum_{n=1}^{\infty} \frac{1}{J_1^2(\lambda_n)} J_0\left(\lambda_n \frac{r}{R}\right) \cos\left(\lambda_n \frac{c_s t}{R}\right) \int_0^R \xi Q(\xi) J_0\left(\lambda_n \frac{\xi}{R}\right) d\xi. \quad (4.9)$$

Although Eqn. 4.9 is the solution for the pressure acoustic waves in a disc with Dirichlet BC, we can only have a complete description of the acoustic waves by defining how the deposited energy (by the particle beam) is distributed in the material. In the next two sub-sections, we looked at two different energy deposition distributions.

4.1.1 Energy Density Profile: Rectangular (Uniform) Distribution

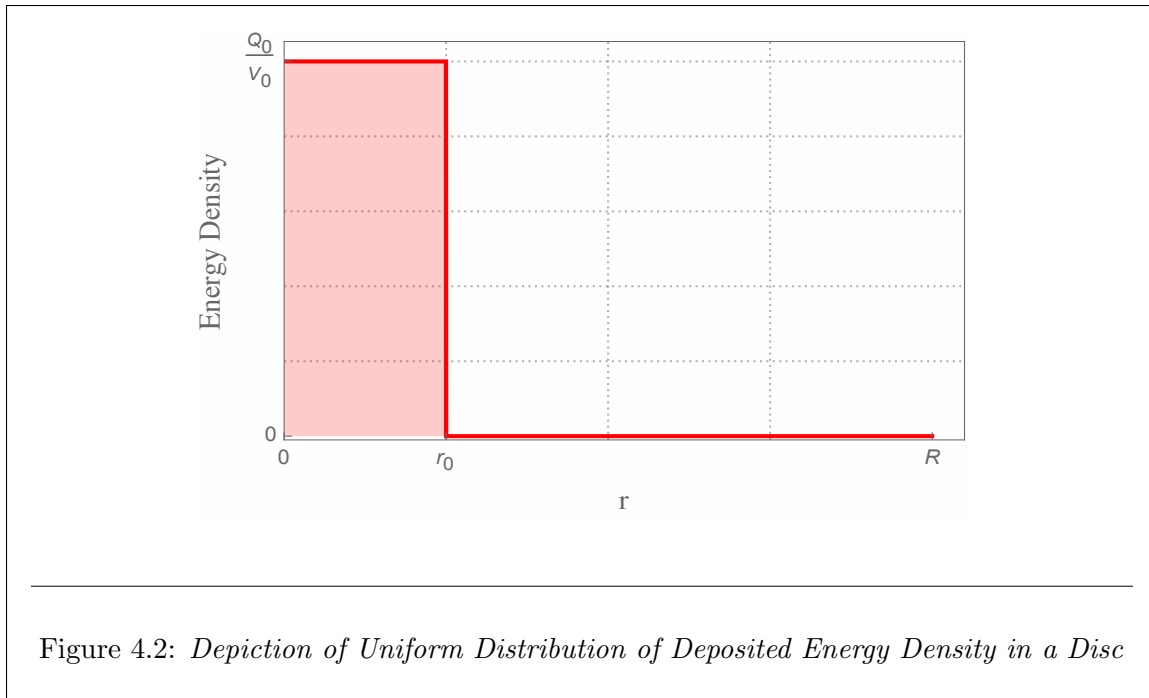


Figure 4.2: *Depiction of Uniform Distribution of Deposited Energy Density in a Disc*

Let us consider a case in which the deposited energy is constant within a localised region of the disc. For the sake of simplicity, we assume that this region is at the centre of the disc (see Figure 4.2). Hence, we can easily define the energy distribution as follows:

$$Q(r) = \begin{cases} Q_0 & \text{when } 0 < r \leq r_0 \\ 0 & \text{when } r > r_0 \end{cases}. \quad (4.10)$$

Using the definition for the energy distribution in Eqn. 4.10, we can write Eqn. 4.9 as

$$P(r, t) = \frac{2\Gamma}{V_0 R^2} \sum_{n=1}^{\infty} \frac{1}{J_1^2(\lambda_n)} J_0\left(\lambda_n \frac{r}{R}\right) \cos\left(\lambda_n \frac{c_s t}{R}\right) \left(\int_0^{r_0} \xi Q(\xi) J_0\left(\lambda_n \frac{\xi}{R}\right) d\xi + \int_{r_0}^R \xi Q(\xi) J_0\left(\lambda_n \frac{\xi}{R}\right) d\xi \right). \quad (4.11)$$

Obviously, the second term on the RHS of the Eqn. 4.11 is zero (see Figure 4.2). Therefore, we can reduce Eqn. 4.11 to

$$P(r, t) = \frac{2\Gamma Q_0}{V_0 R^2} \sum_{n=1}^{\infty} \frac{1}{J_1^2(\lambda_n)} J_0\left(\lambda_n \frac{r}{R}\right) \cos\left(\lambda_n \frac{c_s t}{R}\right) \int_0^{r_0} \xi J_0\left(\lambda_n \frac{\xi}{R}\right) d\xi. \quad (4.12)$$

And finally, by solving the integral in Eqn. 4.12, the solution to the pressure acoustic waves with Dirichlet BC and uniform energy deposition within a localised region can be expressed as

$$P(r, t) = \frac{2\Gamma Q_0 r_0}{V_0 R} \sum_{n=1}^{\infty} \frac{1}{\lambda_n J_1^2(\lambda_n)} J_0\left(\lambda_n \frac{r}{R}\right) \cos\left(\lambda_n \frac{c_s t}{R}\right) J_1\left(\lambda_n \frac{r_0}{R}\right). \quad (4.13)$$

By determining

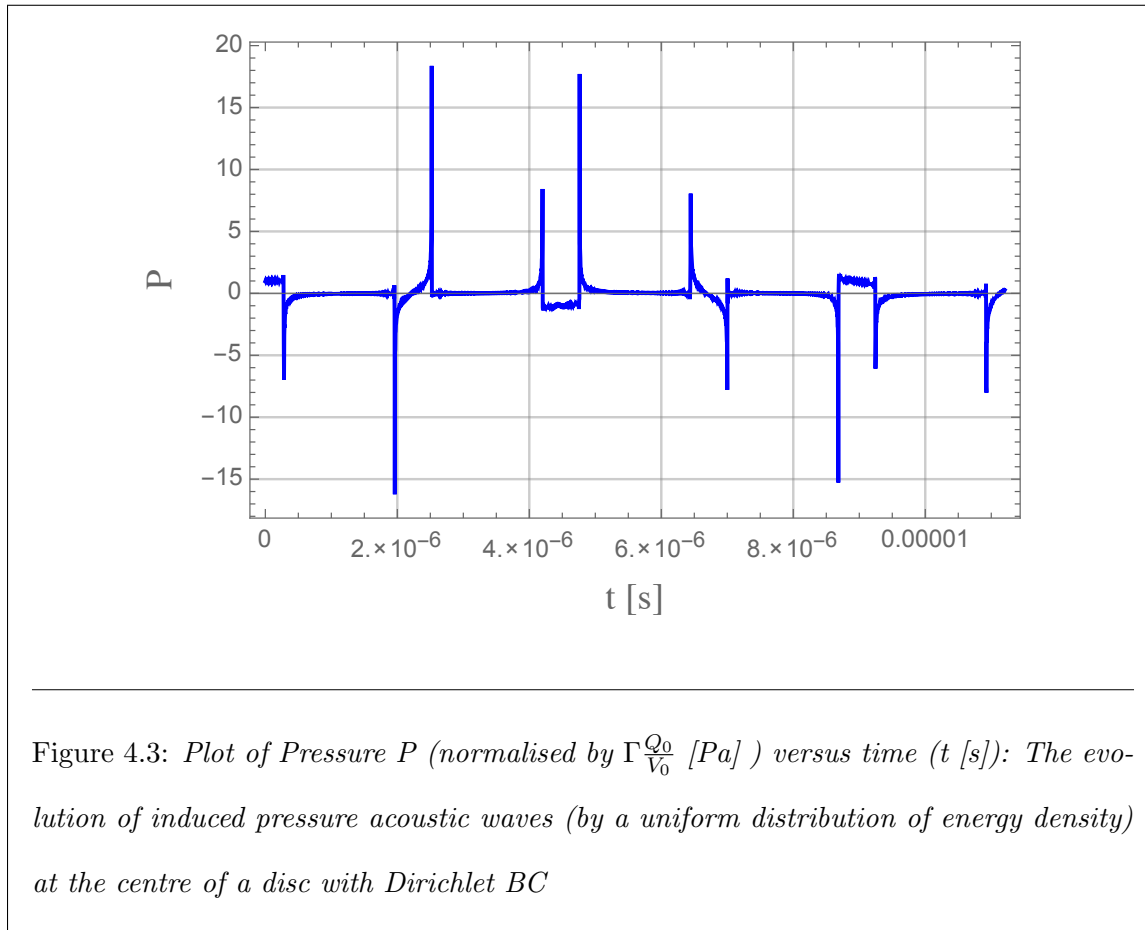
$$\nabla_r P(r, t) = -\frac{2\Gamma Q_0 r_0}{V_0 R^2} \sum_{n=1}^{\infty} \frac{1}{J_1^2(\lambda_n)} J_1\left(\lambda_n \frac{r}{R}\right) \cos\left(\lambda_n \frac{c_s t}{R}\right) J_1\left(\lambda_n \frac{r_0}{R}\right), \quad (4.14)$$

we evaluate the expression for displacement by using Eqns. 4.2 and 4.3 to be

$$u(r, t) = -\frac{2\Gamma Q_0 r_0}{V_0 \rho_0 c_s^2} \sum_{n=1}^{\infty} \frac{1}{\lambda_n^2 J_1^2(\lambda_n)} J_1\left(\lambda_n \frac{r}{R}\right) J_1\left(\lambda_n \frac{r_0}{R}\right) \left\{ \cos\left(\lambda_n \frac{c t}{R}\right) - 1 \right\}. \quad (4.15)$$

Using parameters in Table 4.1, plots based on numerical analysis of Eqn. 4.13 and 4.15 are presented in section B.1 of Appendix B. Worth noting is the behaviour of the waves

at the centre of the disc. At $r = 0$, there is no displacement, which we can easily verify by using Eqn. 4.15. Interestingly, the pressure acoustic waves behaviour (in Eqn. 4.13) for a uniform energy distribution (see the pictorial depiction of the distribution in Figure 4.2) at a localised region of the disc is not as trivial as one might expect. The plot of P at $r = 0$ over time, is presented in Figure 4.3.



Noticeable in Figure 4.3 are spikes which appear at very specific times. Analysis reveals that these spikes occur at these following times:

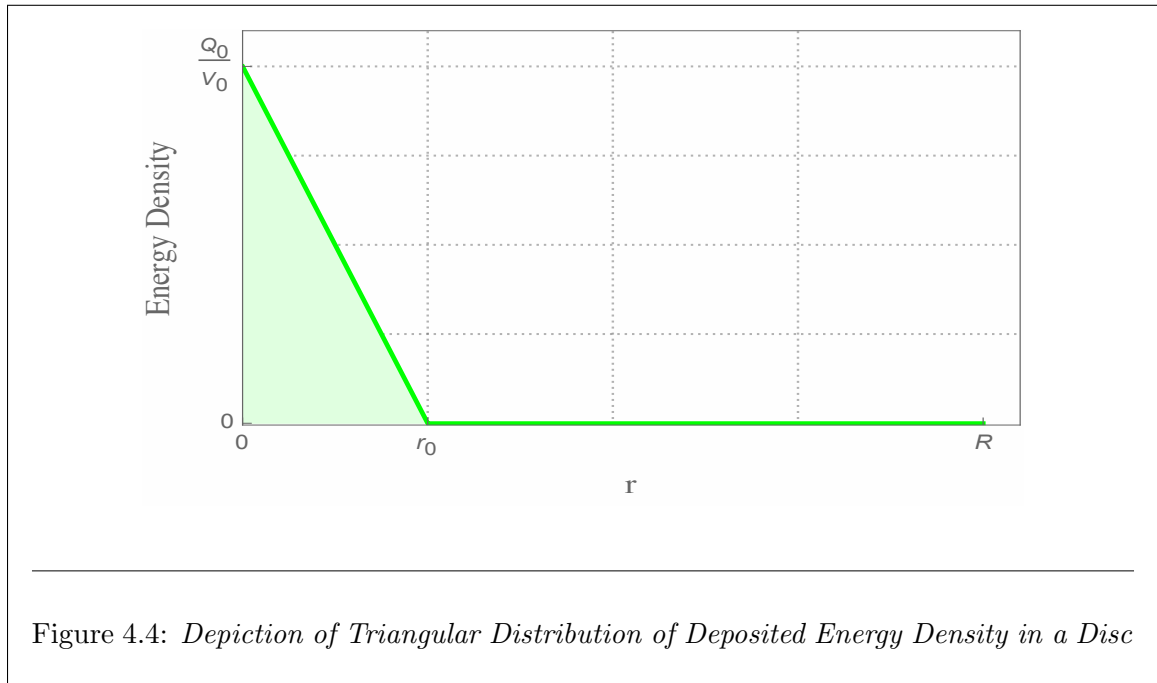
$$\frac{1}{4} \frac{R}{c_s}, \frac{7}{4} \frac{R}{c_s}, \frac{9}{4} \frac{R}{c_s}, \frac{15}{4} \frac{R}{c_s}, \frac{17}{4} \frac{R}{c_s}, \dots$$

These are the times when the wave passes through r_0 . The value of these spikes keep

increasing as one increases the value of n in the computation of Eqn. 4.13, and admittedly some increase faster than others. Basically, this implies that the solution is unstable at those times and this can be attributed to the step-like function used in describing the energy distribution.

4.1.2 Energy Density Profile: Triangular (Linear) Distribution

In this sub-section, we considered the energy distribution within a localised region of the disc is distributed in a linear manner as shown in Figure 4.4 and defined in Eqn. 4.16.



$$Q(r) = \begin{cases} Q_0 \left(1 - \frac{r}{r_0}\right) & : 0 < r \leq r_0 \\ 0 & : r > r_0 \end{cases} . \quad (4.16)$$

In order to investigate the effect of linearly deposited energy, we insert Eqn. 4.16 into Eqn. 4.9

$$P(r, t) = \frac{2\Gamma}{V_0 R^2} \sum_{n=1}^{\infty} \frac{1}{J_1^2(\lambda_n)} J_0\left(\lambda_n \frac{r}{R}\right) \cos\left(\lambda_n \frac{c_s t}{R}\right) \left(\int_0^{r_0} \xi Q(\xi) J_0\left(\lambda_n \frac{\xi}{R}\right) d\xi + \int_{r_0}^R \xi Q(\xi) J_0\left(\lambda_n \frac{\xi}{R}\right) d\xi \right). \quad (4.17)$$

Noticeably, the second term of the RHS of Eqn. 4.17 is zero, so we re-write it as

$$P(r, t) = \frac{2\Gamma Q_0}{V_0 R^2} \sum_{n=1}^{\infty} \frac{1}{J_1^2(\lambda_n)} J_0\left(\lambda_n \frac{r}{R}\right) \cos\left(\lambda_n \frac{c_s t}{R}\right) \int_0^{r_0} \xi \left(1 - \frac{\xi}{r_0}\right) J_0\left(\lambda_n \frac{\xi}{R}\right) d\xi. \quad (4.18)$$

By solving the integral part of Eqn. 4.18, the complete solution is formed, which is given by:

$$P(r, t) = \frac{\pi\Gamma Q_0}{V_0} \sum_{n=1}^{\infty} \frac{1}{\lambda_n J_1^2(\lambda_n)} J_0\left(\lambda_n \frac{r}{R}\right) \cos\left(\lambda_n \frac{c_s t}{R}\right) \left[J_1\left(\lambda_n \frac{r_0}{R}\right) \mathbf{H}_0\left(\lambda_n \frac{r_0}{R}\right) - J_0\left(\lambda_n \frac{r_0}{R}\right) \mathbf{H}_1\left(\lambda_n \frac{r_0}{R}\right) \right], \quad (4.19)$$

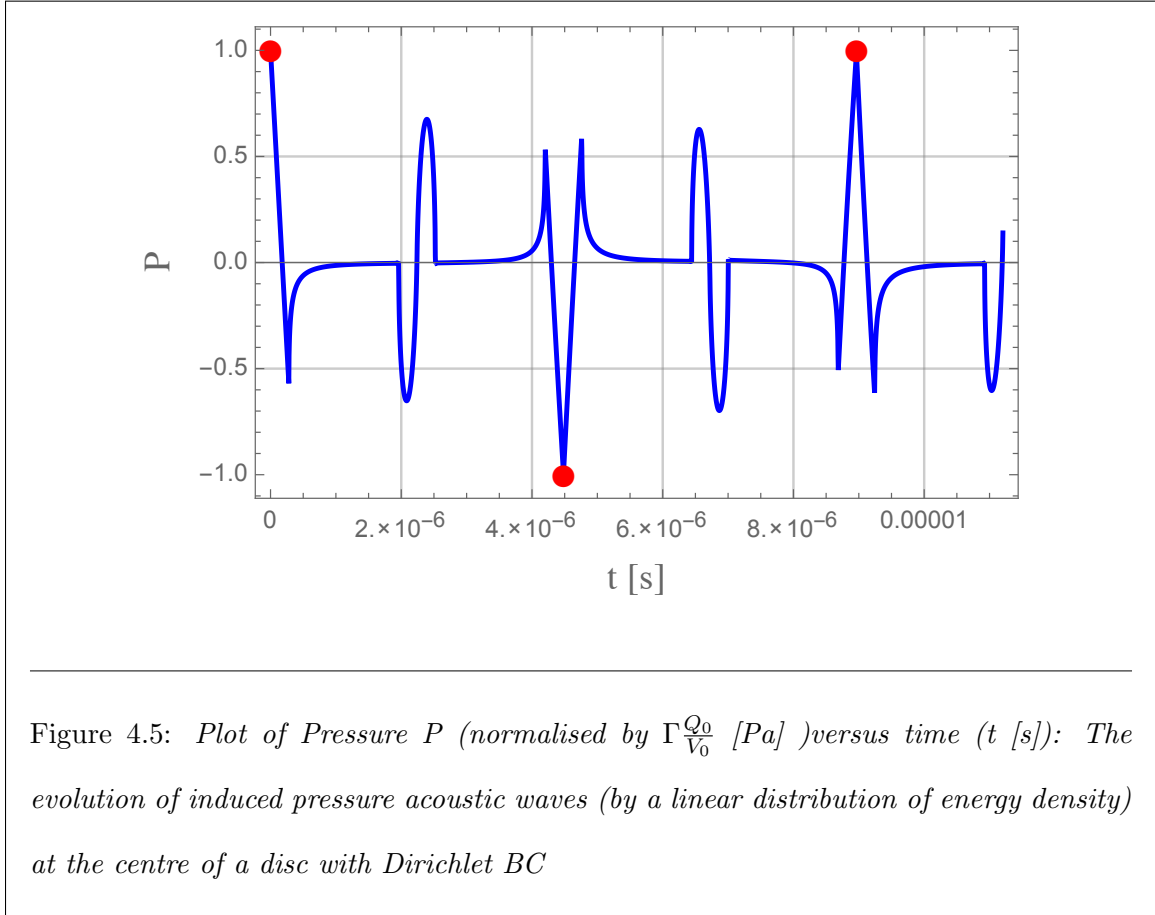
where $\mathbf{H}_n(z)$ denote the Struve function of order n .

We evaluate

$$\nabla_r P(r, t) = \frac{\pi\Gamma Q_0}{RV_0} \sum_{n=1}^{\infty} \frac{1}{\lambda_n J_1^2(\lambda_n)} J_1\left(\lambda_n \frac{r}{R}\right) \cos\left(\lambda_n \frac{c_s t}{R}\right) \left[J_1\left(\lambda_n \frac{r_0}{R}\right) \mathbf{H}_0\left(\lambda_n \frac{r_0}{R}\right) - J_0\left(\lambda_n \frac{r_0}{R}\right) \mathbf{H}_1\left(\lambda_n \frac{r_0}{R}\right) \right], \quad (4.20)$$

by using Eqn. 4.20, inserting it into Eqn. 4.2 and using Eqn. 4.3 to determine the necessary integration constants, the expression for linear acoustic waves in terms of displacement, which was derived to be

$$u(r, t) = -\frac{\pi\Gamma Q_0 R}{\rho_0 c_s^2 V_0} \sum_{n=1}^{\infty} \frac{1}{\lambda_n J_1^2(\lambda_n)} J_1\left(\lambda_n \frac{r}{R}\right) \left[J_1\left(\lambda_n \frac{r_0}{R}\right) \mathbf{H}_0\left(\lambda_n \frac{r_0}{R}\right) - J_0\left(\lambda_n \frac{r_0}{R}\right) \mathbf{H}_1\left(\lambda_n \frac{r_0}{R}\right) \right] \left\{ \cos\left(\lambda_n \frac{c_s t}{R}\right) - 1 \right\}. \quad (4.21)$$



The pressure acoustic waves are well behaved in the case of linear distribution. Details of numerical analysis results of Eqn. 4.19 and 4.21 are represented in section B.2 of Appendix B. As we did in the case of the uniform distribution, we will focus our attention on what happens at the centre of the disc. Figure 4.5 shows the time evolution of pressure waves at $r = 0$. Unlike the uniform distribution case, results here converge. The maximum peak value (which is $P_{max} = \Gamma \frac{Q_0}{V_0}$), indicated with the red “ball” in the Figure 4.5, always appears when

$$t = 4m \frac{R}{c_s}, \quad m \in \mathbb{Z}^+. \quad (4.22)$$

We can see why the maximum peak appears when it does, by analysing Eqn. 4.17

at $r = 0$. To do this analytically, we take the series expansion of λ_n to be

$$\lambda_n \approx \pi \left(n - \frac{1}{4} \right) \quad (4.23)$$

with approximation of λ_n , we can expressed the cosine in Eqn. 4.17 as

$$\cos \left(\lambda_n \frac{c_s}{R} t \right) \approx \cos \left(\pi \left(n - \frac{1}{4} \right) \frac{c_s}{R} t \right). \quad (4.24)$$

Substituting Eqn.4.22 into Eqn. 4.24

$$\cos \left(4m\pi \left(n - \frac{1}{4} \right) \right) = \begin{cases} 1 & : m \in \mathbb{Z}_{\text{even}}^+ \ \& \ \forall n \in \mathbb{Z} \\ -1 & : m \in \mathbb{Z}_{\text{odd}}^+ \ \& \ \forall n \in \mathbb{Z} \end{cases}. \quad (4.25)$$

Therefore, when $\cos \left(\lambda_n \frac{c_s}{R} t \right) \approx -1$, a negative maximum peak pressure will appear, while positive maximum peak pressure will appear when the value of the cosine is unity.

4.2 Neumann Problem

Neumann boundary conditions specify the normal derivative of the function on a surface [39]. In this thesis, this is the so-called “worst case scenario”. When $\frac{\partial P}{\partial r} = 0$ at the boundary, it can be easily be understood that at the circumference of the disc, no displacement is allowed. It can also imply that the system is insulated.

The problem setup can be summarised as follows:

<p>Partial Differential Equation:</p> $\frac{\partial^2 P}{\partial t^2} - c_s^2 \left(\frac{\partial^2 P}{\partial r^2} + \frac{1}{r} \frac{\partial P}{\partial r} \right) = 0.$ <p>Initial condition:</p> $P(r, 0) = \frac{\Gamma}{V_0} Q(r) \quad \text{and} \quad \frac{\partial P}{\partial t} \Big _{t=0} = 0. \quad (4.26)$
--

Boundary condition:

$$\left. \frac{\partial P}{\partial r} \right|_{r=R} = 0.$$

The solution to the PDE above with the prescribed BC and IC can be presented in this form[26]:

$$P(r, t) = \frac{\partial}{\partial t} \int_0^R P(\xi, 0) G(r, \xi, t) d\xi \quad (4.27)$$

where Green's function $G(r, \xi, t)$ is defined by the formula

$$G(r, \xi, t) = \frac{2t\xi}{R^2} + \frac{2\xi}{cR} \sum_{n=1}^{\infty} \frac{1}{\lambda_n J_0^2(\lambda_n)} J_0\left(\lambda_n \frac{r}{R}\right) J_0\left(\lambda_n \frac{\xi}{R}\right) \sin\left(\lambda_n \frac{c_s t}{R}\right). \quad (4.28)$$

The λ_n in Eqn. 4.28 are positive zeros of Bessel function, $J_1(\lambda) = 0$. Substituting Eqn. 4.28 into 4.27

$$\begin{aligned} P(r, t) &= \frac{\partial}{\partial t} \int_0^R P(\xi, 0) \frac{2t\xi}{R^2} d\xi + \frac{\partial}{\partial t} \int_0^R P(\xi, 0) \frac{2\xi}{cR} \sum_{n=1}^{\infty} \frac{1}{\lambda_n J_0^2(\lambda_n)} J_0\left(\lambda_n \frac{r}{R}\right) \times \\ &\quad \times J_0\left(\lambda_n \frac{\xi}{R}\right) \sin\left(\lambda_n \frac{c_s t}{R}\right) d\xi \\ &= \frac{2\Gamma}{V_0 R^2} \left[\int_0^R \xi Q(\xi) d\xi + \sum_{n=1}^{\infty} \frac{1}{J_0^2(\lambda_n)} J_0\left(\lambda_n \frac{r}{R}\right) \cos\left(\lambda_n \frac{c_s t}{R}\right) \times \right. \\ &\quad \left. \times \int_0^R \xi Q(\xi) J_0\left(\lambda_n \frac{\xi}{R}\right) d\xi \right]. \end{aligned} \quad (4.29)$$

4.2.1 Energy Density Profile: Rectangular (Uniform) Distribution

As we did in the Dirichlet problem, the uniform energy is described as

$$Q(r) = \begin{cases} Q_0 & \text{when } 0 < r \leq r_0 \\ 0 & \text{when } r > r_0 \end{cases}. \quad (4.30)$$

Thus, we can separate the integrals in Eqn. 4.29 into two, like this

$$P(r, t) = \frac{2\Gamma}{V_0 R^2} \left[\left(\int_0^{r_0} Q(\xi) \xi d\xi + \int_{r_0}^R Q(\xi) \xi d\xi \right) + \sum_{n=1}^{\infty} \frac{1}{J_0^2(\lambda_n)} J_0 \left(\lambda_n \frac{r}{R} \right) \cos \left(\lambda_n \frac{c_s t}{R} \right) \times \right. \\ \left. \times \left(\int_0^{r_0} \xi Q(\xi) J_0 \left(\lambda_n \frac{\xi}{R} \right) d\xi + \int_{r_0}^R \xi Q(\xi) J_0 \left(\lambda_n \frac{\xi}{R} \right) d\xi \right) \right]. \quad (4.31)$$

Inserting the definition of the distribution (Eqn. 4.30) into Eqn. 4.31 and knowing that the integration of any function with a product of the energy distribution from r_0 to R is zero, we obtain

$$P(r, t) = \frac{2\Gamma Q_0}{V_0 R^2} \left[\int_0^{r_0} \xi d\xi + \sum_{n=1}^{\infty} \frac{1}{J_0^2(\lambda_n)} J_0 \left(\lambda_n \frac{r}{R} \right) \cos \left(\lambda_n \frac{c_s t}{R} \right) \times \right. \\ \left. \times \int_0^{r_0} \xi J_0 \left(\lambda_n \frac{\xi}{R} \right) d\xi \right]. \quad (4.32)$$

Solving the integrals leads to

$$P(r, t) = \frac{2\Gamma Q_0 r_0}{V_0 R^2} \left[\frac{r_0}{2} + R \sum_{n=1}^{\infty} \frac{1}{\lambda_n J_0^2(\lambda_n)} J_0 \left(\lambda_n \frac{r}{R} \right) \cos \left(\lambda_n \frac{c_s t}{R} \right) J_1 \left(\lambda_n \frac{r_0}{R} \right) \right], \quad (4.33)$$

which is the expression for pressure acoustic waves in a disc with Neumann BC and a uniform energy distribution as define in Eqn. 4.30.

Taking it a step further, we evaluate

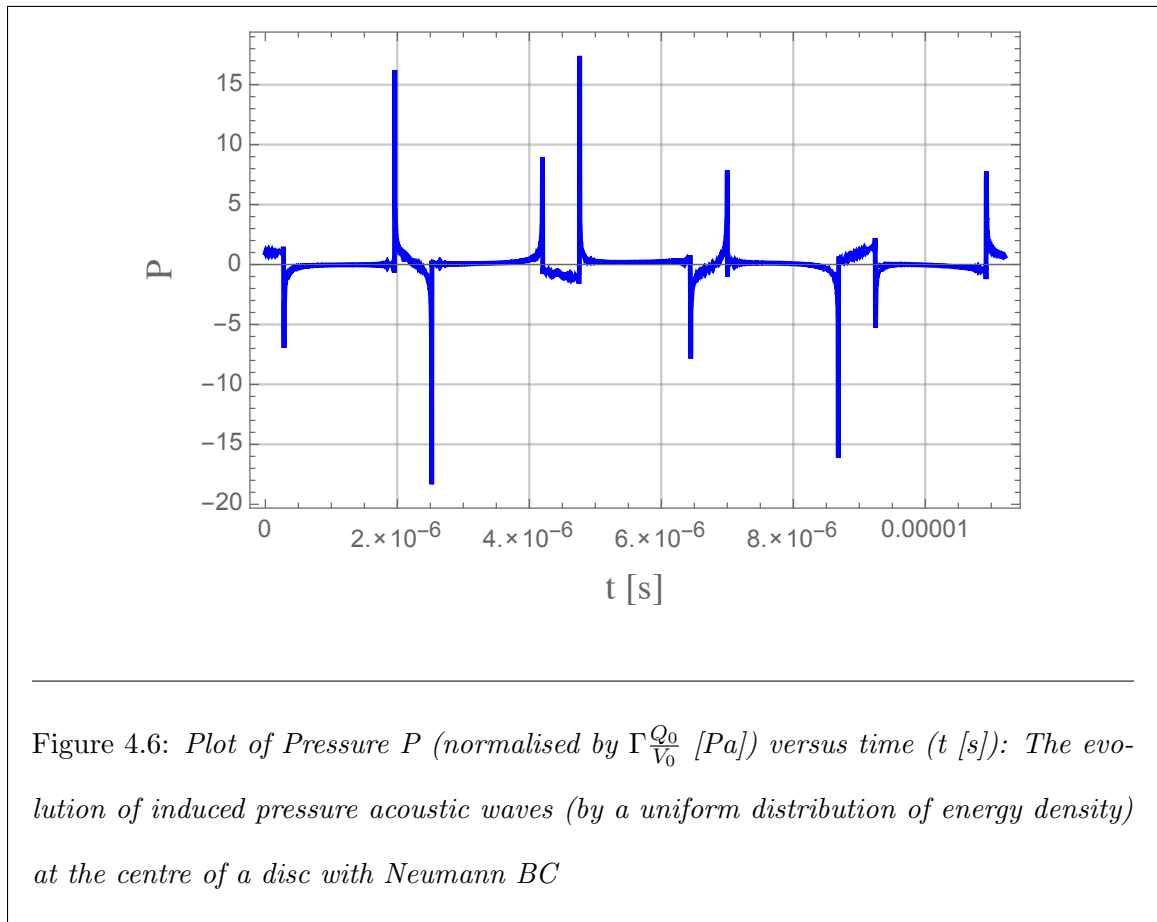
$$\frac{\partial P}{\partial r} = -\frac{2\Gamma Q_0 r_0}{V_0 R^2} \sum_{n=1}^{\infty} \frac{1}{J_0^2(\lambda_n)} J_1 \left(\lambda_n \frac{r}{R} \right) \cos \left(\lambda_n \frac{c_s t}{R} \right) J_1 \left(\lambda_n \frac{r_0}{R} \right) \quad (4.34)$$

and using Eqn. 4.2 with Eqn. 4.3, we derive the expression for displacement to be

$$u(r, t) = -\frac{2\Gamma Q_0 r_0}{\rho_0 V_0 c_s^2} \sum_{n=1}^{\infty} \frac{1}{\lambda_n^2 J_0^2(\lambda_n)} J_1 \left(\lambda_n \frac{r}{R} \right) \left\{ \cos \left(\lambda_n \frac{c_s t}{R} \right) - 1 \right\} J_1 \left(\lambda_n \frac{r_0}{R} \right). \quad (4.35)$$

With the parameters in Table 4.1, plots based on numerical analysis of Eqn. 4.33 and 4.35 are presented in section B.3 of Appendix B. Of interest is the behaviour at the centre of the disc. Figure 4.6 shows the dynamic evolution of the pressure acoustic wave induced by the localised uniformly deposited energy at the centre of the disc. We observed and obtained the same result in Ref. [30].

Another remarkable observation is the similarity between Figure 4.6 and Figure 4.3 (which is for the Dirichlet BC). This similarity extends to when the spikes appear. Also the solutions for both cases appear to be unstable and this instability can be attributed to the description of the energy deposition. The similarity ends when the boundary condition is in play. Since a Neumann BC will cause a free end reflection, the sign of the spikes is reversed when compared to the Dirichlet BC.



4.2.2 Energy Density Profile: Triangular (Linear) Distribution

We use the same definition used in Eqn. 4.16, which is

$$Q(r) = \begin{cases} Q_0 \left(1 - \frac{r}{r_0}\right) & \text{when } 0 < r \leq r_0 \\ 0 & \text{when } r > r_0 \end{cases}. \quad (4.36)$$

From Eqn. 4.29, we can separate the integral into two parts. Inserting the definition of the distribution (Eqn. 4.36) into Eqn. 4.29 we get

$$\begin{aligned} P(r, t) &= \frac{2\Gamma}{V_0 R^2} \left[\left(\int_0^{r_0} Q(\xi) \xi d\xi + \int_{r_0}^R Q(\xi) \xi d\xi \right) + \sum_{n=1}^{\infty} \frac{1}{J_0^2(\lambda_n)} J_0 \left(\lambda_n \frac{r}{R} \right) \times \right. \\ &\quad \left. \times \cos \left(\lambda_n \frac{c_s t}{R} \right) \left(\int_0^{r_0} \xi Q(\xi) J_0 \left(\lambda_n \frac{\xi}{R} \right) d\xi + \int_{r_0}^R \xi Q(\xi) J_0 \left(\lambda_n \frac{\xi}{R} \right) d\xi \right) \right] \\ &= \frac{2\Gamma Q_0}{V_0 R^2} \left[\int_0^{r_0} \xi \left(1 - \frac{r}{\sigma_r}\right) d\xi + \sum_{n=1}^{\infty} \frac{1}{J_0^2(\lambda_n)} J_0 \left(\lambda_n \frac{r}{R} \right) \cos \left(\lambda_n \frac{c_s t}{R} \right) \times \right. \\ &\quad \left. \times \int_0^{r_0} \xi \left(1 - \frac{r}{\sigma_r}\right) J_0 \left(\lambda_n \frac{\xi}{R} \right) d\xi \right]. \quad (4.37) \end{aligned}$$

By solving the integrals, we determine the solution to be

$$\begin{aligned} P(r, t) &= \frac{2\Gamma Q_0}{V_0 R^2} \left[\frac{r_0^2}{6} + \frac{\pi R^2}{2} \sum_{n=1}^{\infty} \frac{1}{\lambda_n^2 J_0^2(\lambda_n)} J_0 \left(\lambda_n \frac{r}{R} \right) \cos \left(\lambda_n \frac{c_s t}{R} \right) \left\{ J_1 \left(\lambda_n \frac{r_0}{R} \right) \mathbf{H}_0 \left(\lambda_n \frac{r_0}{R} \right) - \right. \right. \\ &\quad \left. \left. + J_0 \left(\lambda_n \frac{r_0}{R} \right) \mathbf{H}_1 \left(\lambda_n \frac{r_0}{R} \right) \right\} \right]. \quad (4.38) \end{aligned}$$

To figure out the expression for the displacement using Eqn. 4.2, we calculate

$$\begin{aligned} \frac{\partial P}{\partial r} &= -\frac{\Gamma Q_0 \pi}{V_0 R} \sum_{n=1}^{\infty} \frac{1}{\lambda_n J_0^2(\lambda_n)} J_1 \left(\lambda_n \frac{r}{R} \right) \cos \left(\lambda_n \frac{c_s t}{R} \right) \left\{ J_1 \left(\lambda_n \frac{r_0}{R} \right) \mathbf{H}_0 \left(\lambda_n \frac{r_0}{R} \right) - \right. \\ &\quad \left. + J_0 \left(\lambda_n \frac{r_0}{R} \right) \mathbf{H}_1 \left(\lambda_n \frac{r_0}{R} \right) \right\} \quad (4.39) \end{aligned}$$

and substitute Eqn. 4.39 into 4.2 in conjunction with Eqn. 4.3 to get

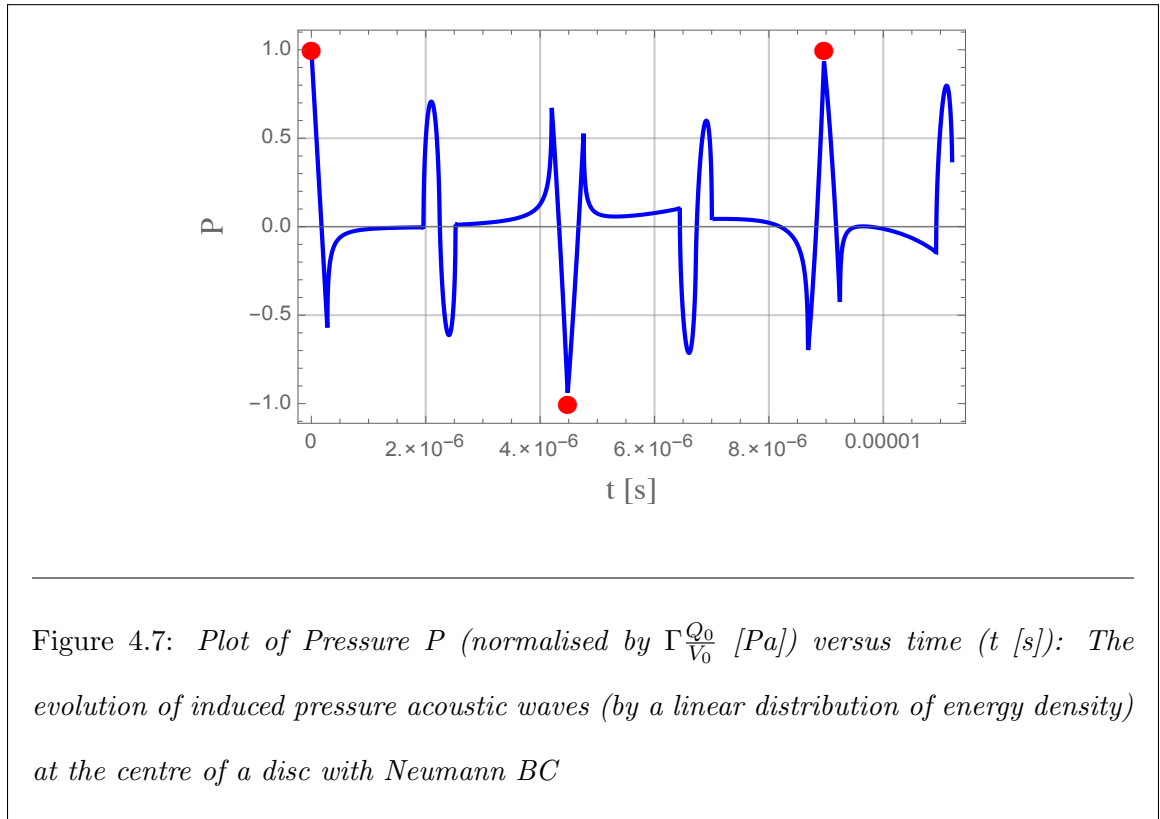
$$\begin{aligned} u(r, t) &= -\frac{\Gamma Q_0 \pi R}{V_0 \rho_0 c_s^2} \sum_{n=1}^{\infty} \frac{1}{\lambda_n^3 J_0^2(\lambda_n)} J_1 \left(\lambda_n \frac{r}{R} \right) \left[J_1 \left(\lambda_n \frac{r_0}{R} \right) \mathbf{H}_0 \left(\lambda_n \frac{r_0}{R} \right) - \right. \\ &\quad \left. + J_0 \left(\lambda_n \frac{r_0}{R} \right) \mathbf{H}_1 \left(\lambda_n \frac{r_0}{R} \right) \right] \left\{ \cos \left(\lambda_n \frac{c_s t}{R} \right) - 1 \right\}. \quad (4.40) \end{aligned}$$

The pressure acoustic waves are well behaved in the case of linear distribution. Numerical analysis of Eqn. 4.38 and 4.40 were performed. The results obtained in the form of plots are represented in section B.4 of Appendix B.

In Figure 4.7 shows the time evolution of pressure waves at $r = 0$. The maximum peak value (which is $P_{max} = \Gamma \frac{Q_0}{V_0}$) indicated with red “ball” appears when

$$t = 4m \frac{R}{c_s}, \quad m \in \mathbb{Z}^+, \quad (4.41)$$

just as it is in the case of the Dirichlet BC. Between the red “balls” in Figure 4.7 for the Neumann BC and Figure 4.5 for the Dirichlet BC, one can easily notice the boundary role, since the sign of reflected wave from the boundary determines the sign of the wave amplitude.



Chapter 5

Multiple Bunches Effect on LAW

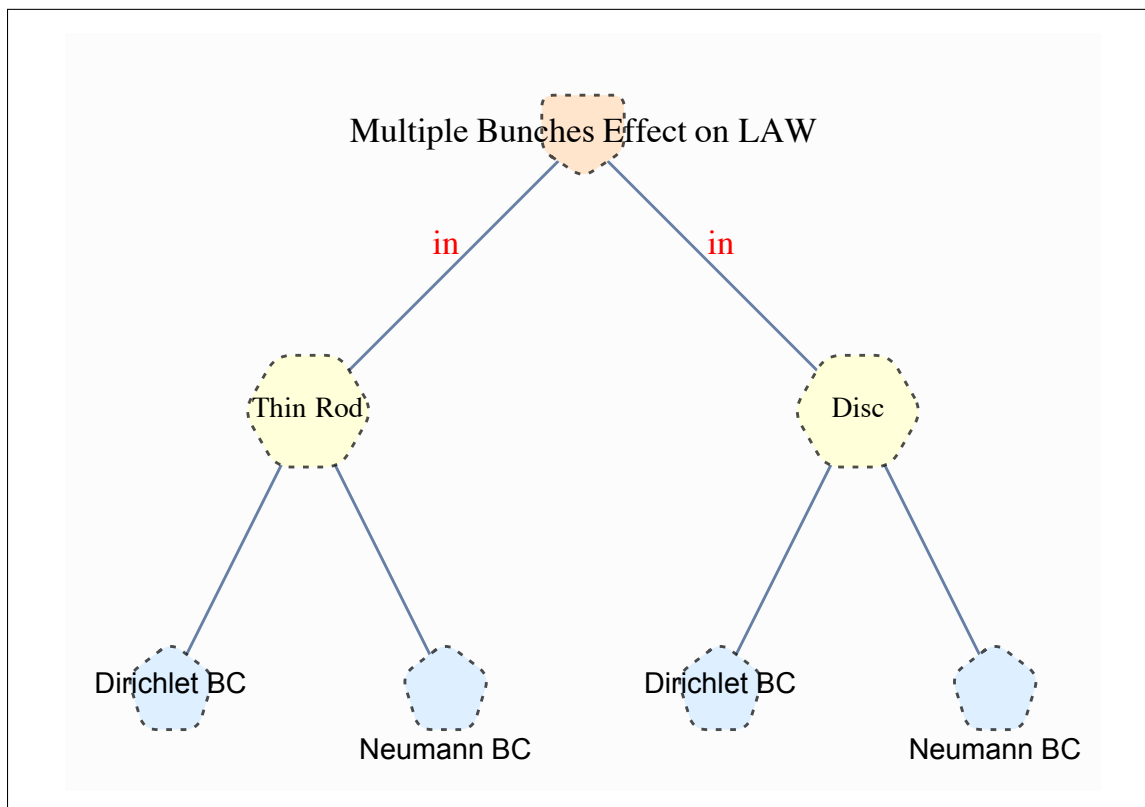


Figure 5.1: Schematic representation of content overview for this chapter

In an accelerator machine, a number of particles are squeezed and grouped together to form a bunch. These bunches are equally spaced, packed and accelerated together in a pulse train and the pulse trains are equally spaced as well. For example, at the ILC, the distance between two consecutive trains is 0.2 s (since the pulse repetition rate is 5 Hz), and a train contains 1312 bunches with 300 ns separating one bunch¹ from the next [36]. In this chapter, our aim is to look at linear acoustic waves evolution and cumulative effect as a result of multiple bunches hitting the same spot on the solid target material.

In general, linear waves are the result of a set of linear equations. Thus, all tools for the analysis of linear systems are available for use. Since our aim is to investigate effects of multiple bunches on the solid target, it is prudent to apply superposition principle. We will consider the multiple bunch effect in both thin rod and disc approximation of the cylindrical solid target under Dirichlet and Neumann boundary conditions (see Figure 5.1 schematic overview of the chapter). Although, in a real cylindrical solid material, the coupled effect between the z and r will play a prominent role on how the linear acoustic waves superimpose. Therefore, this coupled effect will contribute to the dissipation of the energy which will reduce the acoustic wave in the longitudinal direction [21]. Since we are mainly investigating 1D cases, this “coupled-effect” is not considered and without taking it into account this implies that we have investigated the worst case possible. It is also worth noting that throughout this chapter, we assume that:

- there is no damping;
- each bunch is identical and the energy deposited by each bunch is instantaneous;
- lastly, the bunches are equally spaced (let T_b represent the bunch spacing)

¹There are 2×10^{10} electrons per bunch in the electron beam source

5.1 Multi-Bunch Effect on Thin Rods

In Chapter 3, we investigated two different boundary conditions on solid target using the thin rod approximation, and the analytical results presented there were mainly for stress waves induced by a single bunch. Now, we are going to investigate the multiple bunches effect for the two different boundary conditions namely, the Dirichlet and the Neumann boundary conditions. In the subsequence of two sub-sections, we considered both boundary conditions and derived an expression (for each case) of the pressure acoustic waves for m -th number of bunches, which are equally spaced and pass through a thin solid target material.

5.1.1 Dirichlet Boundary

From Eqn. 3.10, we knew that for an instantaneously deposited energy by a single bunch, we can express the pressure acoustic waves as

$$P(z, t) = \frac{2}{L} \sum_{n=1}^{\infty} \cos(\lambda_n c_s t) \sin(\lambda_n z) \int_0^L P(z, 0) \sin(\lambda_n z) dz, \quad (5.1)$$

where $P(z, 0)$ is the initial condition with respect to the bunch in consideration.

So, we start off by considering the first bunch. Using Eqn. 5.1, the pressure acoustic wave for the first bunch ($P_1(z, t)$) can be expressed as

$$P_1(z, t) = \frac{2}{L} \sum_{n=1}^{\infty} \cos(\lambda_n c_s t) \sin(\lambda_n z) \int_0^L P_1(z, 0) \sin(\lambda_n z) dz. \quad (5.2)$$

For clarity purpose, as stated in the assumption above, the bunches are identical, this implies that the *initial* stress induced by any single bunch $P(z, 0)$ (which is caused by the instantaneous energy deposited), will be the same. Therefore, for the first bunch, which is our starting point, our initial condition in terms of pressure $P_1(z, 0)$ for the first bunch can be expressed as

$$P_1(z, 0) \equiv P(z, 0) \quad (5.3)$$

because no stress is in the material before the first bunch pass through the target. Hence, the pressure acoustic waves induced by the first bunch can be written as

$$P_1(z, t) = \frac{2}{L} \sum_{n=1}^{\infty} \cos(\lambda_n c_s t) \sin(\lambda_n z) \int_0^L P(z, 0) \sin(\lambda_n z) dz. \quad (5.4)$$

We can describe the effect of the second bunch on the system by using Eqn. 5.1:

$$P_2(z, t) = \frac{2}{L} \sum_{n=1}^{\infty} \cos(\lambda_n c_s t) \sin(\lambda_n z) \int_0^L P_2(z, 0) \sin(\lambda_n z) dz. \quad (5.5)$$

Since the solid target is already stressed by the first bunch, the initial condition $P_2(z, 0)$ can not be just the second bunch instantaneous stress $P(z, 0)$ alone. Hence, we need to take into the account the stress state of the system $P_1(z, T_b)$ just before the second bunch arrives. Thus, the initial condition $P_2(z, 0)$ for the second bunch will be

$$P_2(z, 0) = P(z, 0) + P_1(z, T_b). \quad (5.6)$$

where T_b is the time interval between the bunches. Inserting Eqn. 5.6 into 5.5, gives

$$\begin{aligned} P_2(z, t) = & \frac{2}{L} \sum_{n=1}^{\infty} \cos(\lambda_n c_s t) \sin(\lambda_n z) \int_0^L P(z, 0) \sin(\lambda_n z) dz + \\ & + \frac{2}{L} \sum_{n=1}^{\infty} \cos(\lambda_n c_s t) \sin(\lambda_n z) \int_0^L P_1(z, T_b) \sin(\lambda_n z) dz \end{aligned} \quad (5.7)$$

To define $P_1(z, T_b)$, we use Eqn. 5.4. So

$$P_1(z, T_b) = \frac{2}{L} \sum_{m=1}^{\infty} \cos(\lambda_m c_s T_b) \sin(\lambda_m z) \int_0^L P(z, 0) \sin(\lambda_m z) dz \quad (5.8)$$

and we substitute Eqn. 5.8 into 5.7, leading to

$$\begin{aligned} P_2(z, t) = & \frac{2}{L} \sum_{n=1}^{\infty} \cos(\lambda_n c_s t) \sin(\lambda_n z) \int_0^L P(z, 0) \sin(\lambda_n z) dz + \frac{2}{L} \sum_{n=1}^{\infty} \cos(\lambda_n c_s t) \sin(\lambda_n z) \times \\ & \times \frac{2}{L} \sum_{m=1}^{\infty} \cos(\lambda_m c_s T_b) \left\{ \int_0^L P(z, 0) \sin(\lambda_m z) dz \right\} \int_0^L \sin(\lambda_m z) \sin(\lambda_n z) dz. \end{aligned} \quad (5.9)$$

Considering that

$$\int_0^L \sin(\lambda_m z) \sin(\lambda_n z) dz = \begin{cases} \frac{L}{2} & : n = m \\ 0 & : n \neq m \end{cases}, \quad (5.10)$$

Eqn. 5.9 can be reduce to

$$P_2(z, t) = \frac{2}{L} \sum_{n=1}^{\infty} \cos(\lambda_n c_s t) \sin(\lambda_n z) \int_0^L P(z, 0) \sin(\lambda_n z) dz + \frac{2}{L} \sum_{n=1}^{\infty} \cos(\lambda_n c_s t) \sin(\lambda_n z) \times \\ \times \cos(\lambda_n c_s T_b) \int_0^L P(z, 0) \sin(\lambda_n z) dz. \quad (5.11)$$

By factoring out the common factor, we can simply express the pressure acoustic wave due to the second bunch as

$$P_2(z, t) = \frac{2}{L} \sum_{n=1}^{\infty} \sin(\lambda_n z) \cos(\lambda_n c_s t) \{1 + \cos(\lambda_n c_s T_b)\} \int_0^L P(z, 0) \sin(\lambda_n z) dz. \quad (5.12)$$

Please note that the time $t = 0$ here (that is, the starting point for the second bunch) is equivalent to time $t = T_b$ in the first bunch. When considering multiple bunches with this methodology, the first bunch expression for the pressure acoustic waves (in this case Eqn. 5.12) becomes insufficient to describe any event that happens at time $t > T_b$.

Next is the third bunch, which passes through the target after another time T_b . Using the same equation we used in the last two bunches, that is Eqn. 5.1, we can write the expression for third bunch as

$$P_3(z, t) = \frac{2}{L} \sum_{n=1}^{\infty} \cos(\lambda_n c_s t) \sin(\lambda_n z) \int_0^L P_3(z, 0) \sin(\lambda_n z) dz. \quad (5.13)$$

Obviously, the initial condition $P_3(z, 0)$ can be defined as

$$P_3(z, 0) = P(z, 0) + P_2(z, T_b). \quad (5.14)$$

Inserting the definition of $P_3(z, 0)$ into Eqn. 5.13

$$P_3(z, t) = \frac{2}{L} \sum_{n=1}^{\infty} \cos(\lambda_n c_s t) \sin(\lambda_n z) \int_0^L P(z, 0) \sin(\lambda_n z) dz + \\ + \frac{2}{L} \sum_{n=1}^{\infty} \cos(\lambda_n c_s t) \sin(\lambda_n z) \int_0^L P_2(z, T_b) \sin(\lambda_n z) dz. \quad (5.15)$$

Using Eqn. 5.12, $P_2(z, T_b)$ is found to be

$$P_2(z, T_b) = \frac{2}{L} \sum_{m=1}^{\infty} \cos(\lambda_m c_s T_b) \{1 + \cos(\lambda_m c_s T_b)\} \sin(\lambda_m z) \int_0^L P(z, 0) \sin(\lambda_m z) dz. \quad (5.16)$$

Substituting Eqn. 5.12 into 5.15, $P_3(z, t)$ becomes

$$\begin{aligned} P_3(z, t) &= \frac{2}{L} \sum_{n=1}^{\infty} \cos(\lambda_n c_s t) \sin(\lambda_n z) \int_0^L P(z, 0) \sin(\lambda_n z) dz + \frac{2}{L} \sum_{n=1}^{\infty} \cos(\lambda_n c_s t) \sin(\lambda_n z) \times \\ &\quad \times \frac{2}{L} \sum_{m=1}^{\infty} \cos(\lambda_m c_s T_b) \{1 + \cos(\lambda_m c_s T_b)\} \left\{ \int_0^L P(z, 0) \sin(\lambda_m z) dz \right\} \times \\ &\quad \times \int_0^L \sin(\lambda_m z) \sin(\lambda_n z) dz \end{aligned} \quad (5.17)$$

and is further reduced to

$$\begin{aligned} P_3(z, t) &= \frac{2}{L} \sum_{n=1}^{\infty} \sin(\lambda_n z) \cos(\lambda_n c_s t) [1 + \cos(\lambda_n c_s T_b) + \cos^2(\lambda_n c_s T_b)] \times \\ &\quad \times \int_0^L P(z, 0) \sin(\lambda_n z) dz. \end{aligned} \quad (5.18)$$

Also worth pointing out is that the time $t = 0$ at the third bunch is equivalent to $t = T_b$ at the second bunch and $t = 2T_b$ at the first bunch. Interestingly enough, looking through Eqn. 5.4, 5.12 and 5.18 for the first, second and third bunch respectively, a specific pattern emerges. Thus, we can now generalise as follows: for the m -th bunch, the pressure acoustic waves can be described as

$$P_m(z, t) = \frac{2}{L} \sum_{n=1}^{\infty} \sin(\lambda_n z) \cos(\lambda_n c_s t) \left\{ \sum_{i=1}^m \cos^{i-1}(\lambda_n c_s T_b) \right\} \int_0^L P(z, 0) \sin(\lambda_n z) dz. \quad (5.19)$$

Generalising, the starting time will be shifted by $(m - 1)T_b$ for any bunch m (and where $m > 1$). This means that for a second bunch, the zeroth time is T_b relative to the first bunch and for the third bunch, the zeroth time is $2T_b$ relative to first bunch and T_b relative to the the second bunch.

5.1.2 Neumann Boundary

In Section 3.2 of Chapter 3, we derived an equation to describe pressure acoustic waves in a thin rod with Neumann boundary condition to be

$$P(z, t) = \frac{1}{L} \int_0^L P(z, 0) dz + \frac{2}{L} \sum_{n=1}^{\infty} \cos(\lambda_n z) \cos(\lambda_n c_s t) \int_0^L P(z, 0) \cos(\lambda_n z) dz, \quad (5.20)$$

The pressure acoustic waves as a result of the first bunch that impinge on the target can be expressed as

$$P_1(z, t) = \frac{1}{L} \int_0^L P_1(z, 0) dz + \frac{2}{L} \sum_{n=1}^{\infty} \cos(\lambda_n z) \cos(\lambda_n c_s t) \int_0^L P_1(z, 0) \cos(\lambda_n z) dz, \quad (5.21)$$

where the initial condition is $P_1(z, 0) = P(z, 0)$, since there is no stress in the system before.

Therefore, $P_1(z, t)$ can be written as

$$P_1(z, t) = \frac{1}{L} \int_0^L P(z, 0) dz + \frac{2}{L} \sum_{n=1}^{\infty} \cos(\lambda_n z) \cos(\lambda_n c_s t) \int_0^L P(z, 0) \cos(\lambda_n z) dz. \quad (5.22)$$

The aftermath effect of the second bunch in terms of pressure can be rendered as

$$P_2(z, t) = \frac{1}{L} \int_0^L P_2(z, 0) dz + \frac{2}{L} \sum_{n=1}^{\infty} \cos(\lambda_n z) \cos(\lambda_n c_s t) \int_0^L P_2(z, 0) \cos(\lambda_n z) dz. \quad (5.23)$$

Considering the wake of the first bunch at time T_b and adding it to the second bunch instantaneous pressure induced leads to the following initial condition:

$$P_2(z, 0) = P(z, 0) + P_1(z, T_b). \quad (5.24)$$

Substituting Eqn. 5.24 into 5.23, we have

$$\begin{aligned} P_2(z, t) = & \frac{1}{L} \int_0^L P(z, 0) dz + \frac{2}{L} \sum_{n=1}^{\infty} \cos(\lambda_n z) \cos(\lambda_n c_s t) \int_0^L P(z, 0) \cos(\lambda_n z) dz + \\ & + \frac{1}{L} \int_0^L P_1(z, T_b) dz + \frac{2}{L} \sum_{n=1}^{\infty} \cos(\lambda_n z) \cos(\lambda_n c_s t) \int_0^L P_1(z, T_b) \times \\ & \times \cos(\lambda_n z) dz. \end{aligned} \quad (5.25)$$

We know the first and second term of Eqn. 5.25 above. In order to work on the third and the last term, we use Eqn. 5.22 and define

$$P_1(z, T_b) = \frac{1}{L} \int_0^L P(z, 0) dz + \frac{2}{L} \sum_{n=1}^{\infty} \cos(\lambda_n z) \cos(\lambda_n c_s T_b) \int_0^L P(z, 0) \cos(\lambda_n z) dz. \quad (5.26)$$

Hence, we substitute $P_1(z, T_b)$ (in Eqn. 5.26) into the third term in Eqn. 5.25, this gives

$$\begin{aligned} \frac{1}{L} \int_0^L P_1(z, T_b) dz &= \frac{1}{L} \int_0^L \left\{ \frac{1}{L} \int_0^L P(z, 0) dz + \frac{2}{L} \sum_{n=1}^{\infty} \cos(\lambda_n z) \cos(\lambda_n c_s T_b) \times \right. \\ &\quad \left. \times \int_0^L P(z, 0) \cos(\lambda_n z) dz \right\} dz. \end{aligned} \quad (5.27)$$

Simplifying and solving the necessary integrals, leads to

$$\begin{aligned} \frac{1}{L} \int_0^L P_1(z, T_b) dz &= \frac{1}{L} \int_0^L P(z, 0) dz + \frac{2}{L} \sum_{n=1}^{\infty} \cos(\lambda_n c_s T_b) \frac{\sin(n\pi)}{n\pi} \times \\ &\quad \int_0^L P(z, 0) \cos(\lambda_n z) dz \end{aligned} \quad (5.28)$$

since

$$\sin(n\pi) = 0 \quad \forall n \in \mathbb{Z}^+.$$

Thus, the second term of Eqn. 5.28 vanishes, leading to

$$\frac{1}{L} \int_0^L P_1(z, T_b) dz = \frac{1}{L} \int_0^L P(z, 0) dz. \quad (5.29)$$

For the fourth term in Eqn. 5.25, we substitute for $P_1(z, T_b)$ using definition in Eqn. 5.26. Solving all the necessary integrals, and using the orthogonality property

$$\int_0^L \cos(\lambda_m z) \cos(\lambda_n z) dz = \begin{cases} \frac{L}{2} & : n = m \\ 0 & : n \neq m \end{cases}, \quad (5.30)$$

we reduce the fourth term in Eqn. 5.25 to

$$\begin{aligned} \frac{2}{L} \sum_{n=1}^{\infty} \cos(\lambda_n z) \cos(\lambda_n c_s t) \int_0^L P_1(z, T_b) \cos(\lambda_n z) dz \\ = \frac{2}{L} \sum_{n=1}^{\infty} \cos(\lambda_n z) \cos(\lambda_n c_s t) \cos(\lambda_n c_s T_b) \int_0^L P(z, 0) \cos(\lambda_n z) dz. \end{aligned} \quad (5.31)$$

We substitute for the third and fourth terms in Eqn. 5.6 by using Eqn. 5.29 and 5.31 respectively. Finally the second bunch effect can be given as

$$P_2(z, t) = \frac{2}{L} \int_0^L P(z, 0) dz + \frac{2}{L} \sum_{n=1}^{\infty} \cos(\lambda_n z) \cos(\lambda_n c_s t) \{1 + \cos(\lambda_n c_s T_b)\} \times \\ \times \int_0^L P(z, 0) \cos(\lambda_n z) dz \quad (5.32)$$

Following the same procedure above for the third bunch, we have

$$P_3(z, t) = \frac{1}{L} \int_0^L P_3(z, 0) dz + \frac{2}{L} \sum_{n=1}^{\infty} \cos(\lambda_n z) \cos(\lambda_n c_s t) \int_0^L P_3(z, 0) \cos(\lambda_n z) dz. \quad (5.33)$$

The initial condition $P_3(z, 0)$, can be expressed as

$$P_3(z, 0) = P(z, 0) + P_2(z, T_b). \quad (5.34)$$

Inserting Eqn. 5.34 into 5.33, we get

$$P_3(z, t) = \frac{1}{L} \int_0^L P(z, 0) dz + \frac{2}{L} \sum_{n=1}^{\infty} \cos(\lambda_n z) \cos(\lambda_n c_s t) \int_0^L P(z, 0) \cos(\lambda_n z) dz + \\ + \frac{1}{L} \int_0^L P_2(z, T_b) dz + \frac{2}{L} \sum_{n=1}^{\infty} \cos(\lambda_n z) \cos(\lambda_n c_s t) \times \\ \times \int_0^L P_2(z, T_b) \cos(\lambda_n z) dz. \quad (5.35)$$

Using Eqn. 5.32, we define $P_2(z, T_b)$ to be

$$P_2(z, T_b) = \frac{2}{L} \int_0^L P(z, 0) dz + \frac{2}{L} \sum_{n=1}^{\infty} \cos(\lambda_n z) \cos(\lambda_n c_s T_b) \{1 + \cos(\lambda_n c_s T_b)\} \times \\ \times \int_0^L P(z, 0) \cos(\lambda_n z) dz. \quad (5.36)$$

The third term of Eqn. 5.35 can be simplified by substituting for $P_2(z, T_b)$ (by using the definition in Eqn. 5.36) and solving the integral. Thus we have

$$\frac{1}{L} \int_0^L P_2(z, T_b) dz = \frac{2}{L} \int_0^L P(z, 0) dz. \quad (5.37)$$

Simplifying the fourth term of Eqn 5.35 as we did the third term, we arrive at

$$\begin{aligned} \frac{2}{L} \sum_{n=1}^{\infty} \cos(\lambda_n z) \cos(\lambda_n c_s t) \int_0^L P_2(z, T_b) \cos(\lambda_n z) dz &= \frac{2}{L} \sum_{n=1}^{\infty} \cos(\lambda_n z) \cos(\lambda_n c_s t) \cos(\lambda_n c_s T_b) \times \\ &\times \{1 + \cos(\lambda_n c_s T_b)\} \int_0^L P(z, 0) \cos(\lambda_n z) dz. \end{aligned} \quad (5.38)$$

Substituting Eqn. 5.37 and Eqn. 5.38 into the third and fourth terms of Eqn. 5.35 respectively, will lead to

$$\begin{aligned} P_3(z, t) &= \frac{3}{L} \int_0^L P(z, 0) dz + \frac{2}{L} \sum_{n=1}^{\infty} \cos(\lambda_n c_s t) \{1 + \cos(\lambda_n c_s T_b) + \cos^2(\lambda_n c_s T_b)\} \times \\ &\times \cos(\lambda_n z) \int_0^L P(z, 0) \cos(\lambda_n z) dz \end{aligned} \quad (5.39)$$

Looking at Eqn. 5.22, 5.32 and 5.39 for the case of first, second and third bunch respectively, we again see a specific pattern. As a result, we can now generalise as follows: for m -th bunch, the pressure acoustic waves can be expressed as

$$\begin{aligned} P_m(z, t) &= \frac{m}{L} \int_0^L P(z, 0) dz + \frac{2}{L} \sum_{n=1}^{\infty} \cos(\lambda_n z) \cos(\lambda_n c_s t) \left\{ \sum_{i=1}^m \cos^{i-1}(\lambda_n c_s T_b) \right\} \times \\ &\times \int_0^L P(z, 0) \cos(\lambda_n z) dz. \end{aligned} \quad (5.40)$$

5.2 Multi-Bunch Effect on Cylindrical Disc

In Chapter 4, we investigated two different boundary conditions on solid targets using disc approximation. In this section, we derive expressions for the multiple bunch effect for two different boundary conditions namely: Dirichlet and Neumann boundary conditions. These derived expressions can be applied to any deposited energy distribution profile.

5.2.1 Dirichlet Boundary

In Section 4.1, we derived the linear acoustic waves for a disc with Dirichlet BC to be

$$P(r, t) = \frac{2}{R^2} \sum_{n=1}^{\infty} \frac{1}{J_1^2(\lambda_n)} J_0\left(\lambda_n \frac{r}{R}\right) \cos\left(\lambda_n \frac{c_s t}{R}\right) \int_0^R \xi P(\xi, 0) J_0\left(\lambda_n \frac{\xi}{R}\right) d\xi. \quad (5.41)$$

For the first bunch,

$$P_1(r, t) = \frac{2}{R^2} \sum_{n=1}^{\infty} \frac{1}{J_1^2(\lambda_n)} J_0\left(\lambda_n \frac{r}{R}\right) \cos\left(\lambda_n \frac{c_s t}{R}\right) \int_0^R \xi P_1(\xi, 0) J_0\left(\lambda_n \frac{\xi}{R}\right) d\xi. \quad (5.42)$$

The initial condition for the first bunch is

$$P_1(\xi, 0) = P(\xi, 0), \quad (5.43)$$

so we can re-write Eqn. 5.42 as follows:

$$P_1(r, t) = \frac{2}{R^2} \sum_{n=1}^{\infty} \frac{1}{J_1^2(\lambda_n)} J_0\left(\lambda_n \frac{r}{R}\right) \cos\left(\lambda_n \frac{c_s t}{R}\right) \int_0^R \xi P(\xi, 0) J_0\left(\lambda_n \frac{\xi}{R}\right) d\xi. \quad (5.44)$$

The disc behaviour in terms of the pressure acoustic waves can be described as

$$P_2(r, t) = \frac{2}{R^2} \sum_{n=1}^{\infty} \frac{1}{J_1^2(\lambda_n)} J_0\left(\lambda_n \frac{r}{R}\right) \cos\left(\lambda_n \frac{c_s t}{R}\right) \int_0^R \xi P_2(\xi, 0) J_0\left(\lambda_n \frac{\xi}{R}\right) d\xi \quad (5.45)$$

where the initial condition $P_2(r, 0)$ is the contribution of the bunch itself with the wake effect of the previous bunch, hence we have

$$P_2(r, 0) = P(r, 0) + P_1(r, T_b). \quad (5.46)$$

Substituting for $P_2(r, 0)$ into Eqn. 5.45 using 5.46 leads us to

$$\begin{aligned} P_2(r, t) = & \frac{2}{R^2} \sum_{n=1}^{\infty} \frac{1}{J_1^2(\lambda_n)} J_0\left(\lambda_n \frac{r}{R}\right) \cos\left(\lambda_n \frac{c_s t}{R}\right) \int_0^R \xi P(\xi, 0) J_0\left(\lambda_n \frac{\xi}{R}\right) d\xi + \\ & + \frac{2}{R^2} \sum_{n=1}^{\infty} \frac{1}{J_1^2(\lambda_n)} J_0\left(\lambda_n \frac{r}{R}\right) \cos\left(\lambda_n \frac{c_s t}{R}\right) \int_0^R \xi P_1(\xi, T_b) J_0\left(\lambda_n \frac{\xi}{R}\right) d\xi. \end{aligned} \quad (5.47)$$

Using Eqn. 5.44, we define $P_1(r, T_b)$ as

$$P_1(r, T_b) = \frac{2}{R^2} \sum_{m=1}^{\infty} \frac{1}{J_1^2(\lambda_m)} J_0\left(\lambda_m \frac{r}{R}\right) \cos\left(\lambda_m \frac{c_s T_b}{R}\right) \int_0^R \xi P(\xi, 0) J_0\left(\lambda_m \frac{\xi}{R}\right) d\xi. \quad (5.48)$$

Inserting Eqn. 5.48 into 5.47 leads to

$$\begin{aligned} P_2(r, t) &= \frac{2}{R^2} \sum_{n=1}^{\infty} \frac{1}{J_1^2(\lambda_n)} J_0\left(\lambda_n \frac{r}{R}\right) \cos\left(\lambda_n \frac{c_s t}{R}\right) \int_0^R \xi P(\xi, 0) J_0\left(\lambda_n \frac{\xi}{R}\right) d\xi + \\ &+ \frac{2}{R^2} \sum_{n=1}^{\infty} \frac{1}{J_1^2(\lambda_n)} J_0\left(\lambda_n \frac{r}{R}\right) \cos\left(\lambda_n \frac{c_s t}{R}\right) \frac{2}{R^2} \sum_{m=1}^{\infty} \frac{1}{J_1^2(\lambda_m)} \cos\left(\lambda_m \frac{c_s T_b}{R}\right) \times \\ &\times \int_0^R \xi P(\xi, 0) J_0\left(\lambda_m \frac{\xi}{R}\right) d\xi \left\{ \int_0^R \xi J_0\left(\lambda_m \frac{r}{R}\right) J_0\left(\lambda_n \frac{\xi}{R}\right) d\xi \right\}. \quad (5.49) \end{aligned}$$

Simplifying things further, we solve the integral in the curly bracket, by using the orthogonality property, which is

$$\int_0^R \xi J_0\left(\lambda_m \frac{\xi}{R}\right) J_0\left(\lambda_n \frac{\xi}{R}\right) d\xi = \begin{cases} \frac{R^2}{2} J_1^2(\lambda_n) & : \lambda_n = \lambda_m \\ 0 & : \lambda_n \neq \lambda_m \text{ \& } J_0(\lambda_n) = J_0(\lambda_m) \end{cases} \quad (5.50)$$

Thus, Eqn. 5.49 becomes

$$\begin{aligned} P_2(r, t) &= \frac{2}{R^2} \sum_{n=1}^{\infty} \frac{1}{J_1^2(\lambda_n)} J_0\left(\lambda_n \frac{r}{R}\right) \cos\left(\lambda_n \frac{c_s t}{R}\right) \int_0^R \xi P(\xi, 0) J_0\left(\lambda_n \frac{\xi}{R}\right) d\xi + \frac{2}{R^2} \sum_{n=1}^{\infty} \frac{1}{J_1^2(\lambda_n)} \times \\ &\times J_0\left(\lambda_n \frac{r}{R}\right) \cos\left(\lambda_n \frac{c_s t}{R}\right) \cos\left(\lambda_n \frac{c_s T_b}{R}\right) \int_0^R \xi P(\xi, 0) J_0\left(\lambda_n \frac{\xi}{R}\right) d\xi. \quad (5.51) \end{aligned}$$

Factoring out necessary terms, we further reduce Eqn. 5.51 to

$$\begin{aligned} P_2(r, t) &= \frac{2}{R^2} \sum_{n=1}^{\infty} \frac{1}{J_1^2(\lambda_n)} J_0\left(\lambda_n \frac{r}{R}\right) \cos\left(\lambda_n \frac{c_s t}{R}\right) \left\{ 1 + \cos\left(\lambda_n \frac{c_s T_b}{R}\right) \right\} \times \\ &\times \int_0^R \xi P(\xi, 0) J_0\left(\lambda_n \frac{\xi}{R}\right) d\xi. \quad (5.52) \end{aligned}$$

From Eqn. 5.44 and 5.52, we can deduce that the pattern in thin rod approximation is been followed here, hence, we can generalise. For m -th bunch, the pressure acoustic

waves can be expressed as

$$P_m(r, t) = \frac{2}{R^2} \sum_{n=1}^{\infty} \frac{1}{J_1^2(\lambda_n)} J_0\left(\lambda_n \frac{r}{R}\right) \cos\left(\lambda_n \frac{c_s t}{R}\right) \left\{ \sum_{i=1}^m \cos^{i-1}(\lambda_n c_s T_b) \right\} \times \int_0^R \xi P(\xi, 0) J_0\left(\lambda_n \frac{\xi}{R}\right) d\xi. \quad (5.53)$$

5.2.2 Neumann Boundary

In the case of the Neumann boundary condition for a disc, the solution of linear waves in terms of pressure was derived analytically in Section 4.2 (on page 64) as

$$P(r, t) = \frac{2}{R^2} \left[\sum_{n=1}^{\infty} \frac{J_0\left(\lambda_n \frac{r}{R}\right)}{J_0^2(\lambda_n)} \cos\left(\lambda_n \frac{c_s t}{R}\right) \int_0^R \xi P(\xi, 0) J_0\left(\lambda_n \frac{\xi}{R}\right) d\xi + \int_0^R \xi P(\xi, 0) d\xi \right]. \quad (5.54)$$

Using Eqn. 5.54 above, the effect of the first bunch can be expressed as

$$P_1(r, t) = \frac{2}{R^2} \left[\sum_{n=1}^{\infty} \frac{J_0\left(\lambda_n \frac{r}{R}\right)}{J_0^2(\lambda_n)} \cos\left(\lambda_n \frac{c_s t}{R}\right) \int_0^R \xi P_1(\xi, 0) J_0\left(\lambda_n \frac{\xi}{R}\right) d\xi + \int_0^R \xi P_1(\xi, 0) d\xi \right] \quad (5.55)$$

where initial condition $P_1(r, 0) = P(r, 0)$, so

$$P_1(r, t) = \frac{2}{R^2} \left[\sum_{n=1}^{\infty} \frac{J_0\left(\lambda_n \frac{r}{R}\right)}{J_0^2(\lambda_n)} \cos\left(\lambda_n \frac{c_s t}{R}\right) \int_0^R \xi P(\xi, 0) J_0\left(\lambda_n \frac{\xi}{R}\right) d\xi + \int_0^R \xi P(\xi, 0) d\xi \right]. \quad (5.56)$$

For the next bunch, that is, the second bunch, the pressure acoustic waves can be expressed as follows using Eqn. 5.54:

$$P_2(r, t) = \frac{2}{R^2} \left[\sum_{n=1}^{\infty} \frac{J_0\left(\lambda_n \frac{r}{R}\right)}{J_0^2(\lambda_n)} \cos\left(\lambda_n \frac{c_s t}{R}\right) \int_0^R \xi P_2(\xi, 0) J_0\left(\lambda_n \frac{\xi}{R}\right) d\xi + \int_0^R \xi P_2(\xi, 0) d\xi \right] \quad (5.57)$$

with the initial condition

$$P_2(r, 0) = P(r, 0) + P_1(r, T_b). \quad (5.58)$$

We insert Eqn. 5.58 into 5.57:

$$\begin{aligned} P_2(r, t) = & \frac{2}{R^2} \left[\sum_{n=1}^{\infty} \frac{J_0\left(\lambda_n \frac{r}{R}\right)}{J_0^2(\lambda_n)} \cos\left(\lambda_n \frac{c_s t}{R}\right) \int_0^R \xi P(\xi, 0) J_0\left(\lambda_n \frac{\xi}{R}\right) d\xi + \right. \\ & + \sum_{n=1}^{\infty} \frac{J_0\left(\lambda_n \frac{r}{R}\right)}{J_0^2(\lambda_n)} \cos\left(\lambda_n \frac{c_s t}{R}\right) \int_0^R \xi P_1(\xi, T_b) J_0\left(\lambda_n \frac{\xi}{R}\right) d\xi + \\ & \left. + \int_0^R \xi P(\xi, 0) d\xi + \int_0^R \xi P_1(\xi, T_b) d\xi \right]. \quad (5.59) \end{aligned}$$

Defining $P_1(r, T_b)$ by using Eqn. 5.56:

$$\begin{aligned} P_1(r, T_b) = & \frac{2}{R^2} \left[\sum_{m=1}^{\infty} \frac{J_0\left(\lambda_m \frac{r}{R}\right)}{J_0^2(\lambda_m)} \cos\left(\lambda_m \frac{c_s T_b}{R}\right) \int_0^R \xi P(\xi, 0) J_0\left(\lambda_m \frac{\xi}{R}\right) d\xi + \right. \\ & \left. + \int_0^R \xi P(\xi, 0) d\xi \right] \quad (5.60) \end{aligned}$$

and exploiting the orthogonality property²

$$\int_0^R \xi J_0\left(\lambda_m \frac{\xi}{R}\right) J_0\left(\lambda_n \frac{\xi}{R}\right) d\xi = \begin{cases} \frac{R^2}{2} J_0^2(\lambda_n) & : \lambda_n = \lambda_m \\ 0 & : \lambda_n \neq \lambda_m \text{ \& } J_1(\lambda_n) = J_1(\lambda_m) \end{cases} \quad (5.61)$$

Substituting Eqn. 5.60 and using Eqn. 5.61, we can reduce Eqn. 5.59 to

$$\begin{aligned} P_2(r, t) = & \frac{2}{R^2} \left[\sum_{n=1}^{\infty} \frac{J_0\left(\lambda_n \frac{r}{R}\right)}{J_0^2(\lambda_n)} \cos\left(\lambda_n \frac{c_s t}{R}\right) \{1 + \cos(\lambda_n c_s T_b)\} \int_0^R \xi P(\xi, 0) J_0\left(\lambda_n \frac{\xi}{R}\right) d\xi + \right. \\ & \left. + 2 \int_0^R \xi P(\xi, 0) d\xi \right]. \quad (5.62) \end{aligned}$$

From Eqn. 5.55 and 5.62, we can deduce that the pattern in the thin rod approximation has been followed here, hence, we can generalise. For the m -th bunch, the pressure

²The λ_m and λ_n in this sub-section is different from the ones in the previous sub-section. Please see Sections 4.1 and 4.2 in Chapter 4 for their definitions

acoustic waves can be expressed as

$$P_m(r, t) = \frac{2}{R^2} \left[\sum_{n=1}^{\infty} \frac{J_0\left(\lambda_n \frac{r}{R}\right)}{J_0^2(\lambda_n)} \cos\left(\lambda_n \frac{c_s t}{R}\right) \left\{ \sum_{i=1}^m \cos^{i-1}(\lambda_n c_s T_b) \right\} \int_0^R \xi P(\xi, 0) J_0\left(\lambda_n \frac{\xi}{R}\right) d\xi + m \int_0^R \xi P(\xi, 0) d\xi \right]. \quad (5.63)$$

Remarks

An interesting characteristic is observed when one looks at all the analytical solutions derived for both the thin rod and disc approximations of the cylindrical target under both the Dirichlet and Neumann BCs. Common to them all, that is, Eqns. 5.19, 5.40, 5.53 and 5.63 is:

$$\sum_{i=1}^m \cos^{i-1}(\lambda_n c_s T_b). \quad (5.64)$$

Eqn. 5.64 differentiates the analytical solutions here from that of the single bunch obtained in Chapters 3 and 4. Basically, if Eqn. 5.64 equals 1, we have the solution for the single bunch effect. Remarkably, since the value of a cosine ranges from -1 to +1, one can deduce that it is probable to make Eqn. 5.64 equal zero, meaning that the superposition of the waves can be made to be a total destructive interference. Hence, it will be a great advantage if

$$0 \leq \left| \sum_{i=1}^m \cos^{i-1}(\lambda_n c_s T_b) \right| \leq 1. \quad (5.65)$$

The implication is that, by choosing the right parameters, it is theoretically possible to construct a system of multiple bunches of particle beams in such a way that the induced stress on the target material being hit will not pile up or superimpose additively.

Chapter 6

SLC and ILC - Overview and Application

Overview

In this chapter we look at

- a general operational overview of SLC and ILC machines.
- positron production on each machine described with emphasis on the target.
- a test case, in which we applied the model in this study to the SLC target and confirm the existing result.
- the application of the analytical solutions derived in this thesis to the ILC target.

6.1 SLAC Linear Collider

SLAC Linear Collider (SLC) is a linear collider just as the name implies and it was designed to collide bunches of electrons (e^-) and positrons (e^+) head-on at a single interaction point (IP) with centre of mass energies of over $90 \text{ GeV}/c^2$ [29]. SLC is the first and still the only linear collider built up to date [32]. The construction of SLC began in 1983 and was completed in 1987 [32]. The aim of the SLC project was to use the machine to help better understand the physics world through experiments performed. Also it was to pioneer a new accelerator technology that can be used for synchrotron radiation sources, free electron lasers, high brightness beam sources, etc. Another important aim of the SLC project was to help in reducing the cost of future ($e^- - e^+$ collider) machines [29, 33].

SLC runs can be divided into two eras in terms of the detector used and also in terms of the electron source. SLC first physics run used a Mark II detector (between 1989 and 1990) and an unpolarised electron source [25].

After the Mark II detector era, a new state of the art detector called SLAC Large Detector (SLD) was installed during 1991 [25] and in 1992 the electron source was replaced by a polarised electron source. Some major upgrading was done to increase the luminosity of the beam and some other components were added for diagnosis and measurement purposes (See Ref. [25] for details on Polarisation at SLC).

Description of the typical operation cycle of these two eras of SLC stated above can be merged into one (see Figure 6.1 for the SLC schematic layout). Before describing a typical cycle of SLC, here are the main components of the machine [33]:

- LINAC (Linear Accelerator)
- Transport System from the end of the LINAC to a small aperture magnet arc
- Final focus: a special focusing system near the IP (Interaction Point)

- Positron production target
- Transport system from the positron target at the two-thirds point of the LINAC back to the injection end of the LINAC
- A new high peak current electron gun
- Two small storage rings to reduced emittance of e^+ and e^- beams by radiation damping
- Pulse compressors to reduce the length of the bunches in the storage ring before injection into the LINAC
- And other necessary instrumentation and control system for both the LINAC and collider system.

6.1.1 Overview of Typical Operation

A cycle begins with two bunches of electrons and one positron bunch, these bunches are accelerated to 1.2 GeV at the end of 100 m section of LINAC. Right after this LINAC, the bunches are injected by pulsed magnets into their respective damping rings. The emittance of each bunches (that is, e^+ and e^-) are reduced by radiation damping in their respective damping rings for duration of 1/120 s. After 1/120 s, the e^+ bunch is extracted from the ring, passes through a pulse compressor which reduces the bunch length from cm to mm range (which is the requirement for the main LINAC) and is injected into the LINAC. The two e^- bunches and the e^+ bunch were kicked from their respective damping rings by the first pulsed magnet and later pass through the second pulse compressor, which inject them into the LINAC with the required bunch length. The e^+ bunch leads, followed by the two e^- bunches. There is a distance of 15 m between the bunches in the LINAC [33].

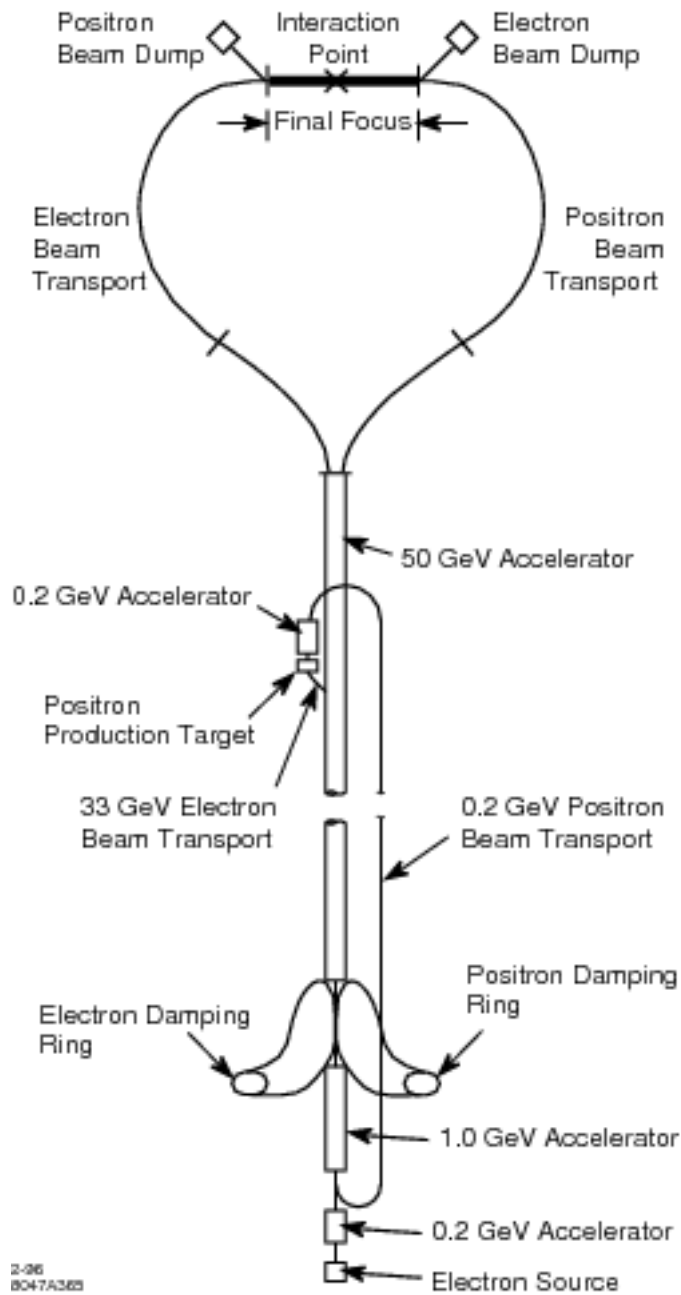


Figure 6.1: Schematic of SLC. Ref.: [33]

The three (two e^- and one e^+) bunches are accelerated down the LINAC. At two-thirds of the LINAC (at this point, the bunches have been accelerated from 1.2 GeV to 33 GeV) the trailing electron bunch is extracted from the LINAC with a pulsed magnet and is directed onto a positron production target. The e^+ bunch and the leading e^- bunch continue to the end of the LINAC, where they reach an energy of about 50 GeV [33].

At the end of the LINAC, e^- and e^+ bunches are separated by a DC magnet, pass through a transport system which matches the focusing of the LINAC to that of the main collider arc, and then begin to travel around the arc in opposite directions. In the collider arc, there is a small aperture magnet with very strong alternating gradient focusing to hold down emittance growth of the bunches in the collider arcs. After emerging from the collider arcs, the bunches pass through an achromatic matching and focusing section which focuses the beams to a very small size at the interaction point [33].

It is worth mentioning that the electrons are produced from a special gun. During the SLC first era, an unpolarised electron gun [29, 33] was used, and later, a polarised gun was installed [25]. For the SLC positron production process, please see the sub-section below.

6.1.2 Positron Source Production for SLC

SLC requires a positron production system that will produce as many positrons as there are electrons in an accelerator. SLC positrons are produced through a conversion target (see chapter 1 for details of positron production in general). The conversion target is bombarded by incident electron beams, initiating an electromagnetic cascade shower of positrons, electrons and photons. This requirement implies that one incident electron must produce at least one positron. This is why a high energetic beam is needed and a good positrons collection system [14, 15] is required.

Here are the essential components in the SLC positron source [15]:

- beam transport to bring 33 GeV electrons to a target room
- conversion target
- pulsed magnet to produce a 5 T solenoid field near the target
- DC solenoid magnet of 0.5 T to provide extended focusing while the positrons are being accelerated in 0.2 GeV accelerating structure
- high gradient accelerator
- 200 MeV beam transport line that brings positrons 2 km to the far end of the LINAC for acceleration and subsequent damping in the damping ring

The positron production process “starts” when the 33 GeV trailing electron bunch (recall that three bunches are accelerated at a time in the main LINAC, a positron bunch and two electron bunches) is extracted at the two-thirds point of the LINAC. This “scavenger” electron bunch will pass through an extraction transport line and be made to strike a tungsten alloy target. A portion of the produced positron spectrum is carefully focused by a pulsed solenoid (called flux concentrator) placed just downstream of the target. The positrons are accelerated and bunched by a 1.4 m “capture” accelerator with a gradient of 40 MeV/m. The energy of positron bunch is raised to 210 MeV in the “booster region”, enters the return line and then transported back to the injector LINAC 2 km upstream [29]. The positron bunch has to make a 180° bend downstream and upstream [33].

SLC Target for Positron Production

The hardest part of any anti-particle source production is the conversion target development. The SLC positron production target is no exception. The target was designed

in order to withstand the huge energy deposited by the intense high power electron beam [29] (see Tabel 6.1). Figure 6.2 below shows the geometry of the target. The SLC target material is a disc of 2.5 inches (0.0634 m) in diameter and 0.81 inches (0.0205 m) in thickness (equivalent of 6 radiation length). Tungsten alloy (made-up of 75% of Tungsten and 25% of Rhenium) was selected for the target material due to its high melting point, very high strength, and reasonable ductility and thermal conductivity [33]. The target was slowly rotated (or trolled) in such a way that each impinging electron beam pulse struck a different part of the target during operation [34].

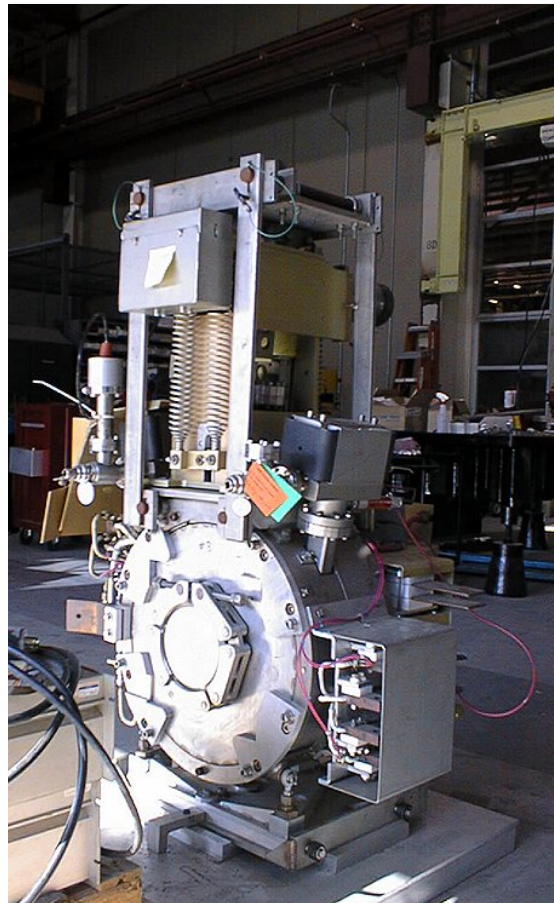
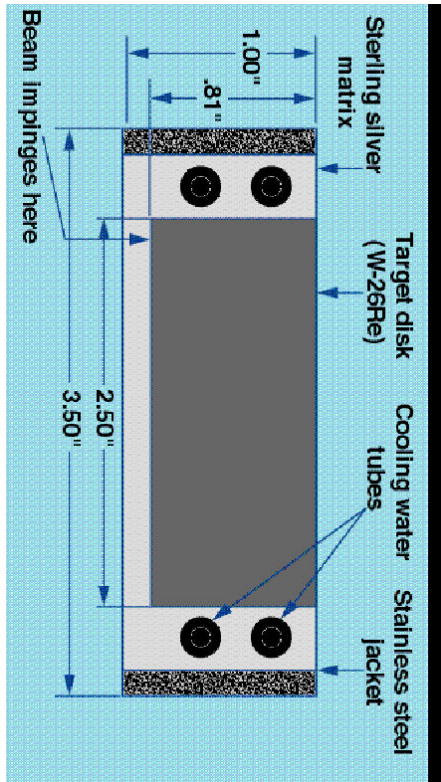
The target gave many years of reliable service [10] before it was decommissioned in 1998 because of a failure [13]. The failure developed as a small leakage in the target vacuum [10]. Close inspection of the target revealed not only the leakage but also showed a considerable damage on the beam exit side of the target (see Figure 6.3) [34].

6.1.3 Stress Analysis in SLC Target

The target gave 6 years of operation; its failure was a surprise because the simulation result during the conceptual design of the SLC was interpreted to indicate that the target “will probably last indefinitely” for 0.8 mm incident beam spot-size [33]. Many analyses have been carried out to determine the cause of this failure, like in Ref.: [10, 13]. We applied the model in this thesis to study if we could reach the same conclusion as in Ref.: [10] (see the stress analysis below).

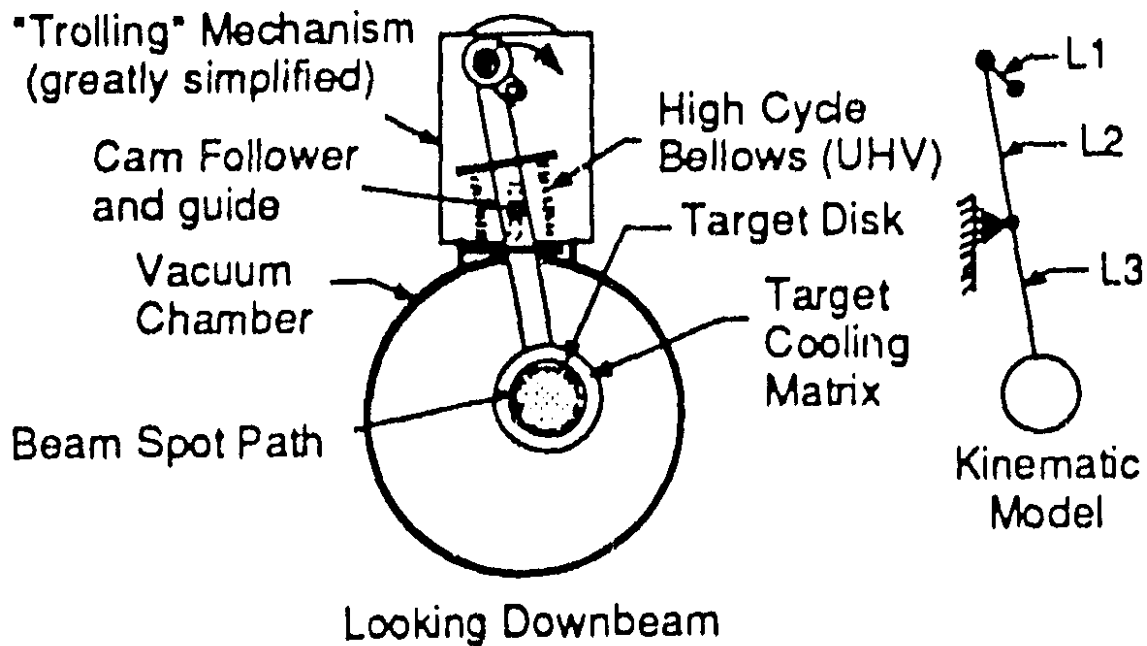
Energy Deposition

Stress analysis of this nature requires that we know precisely the distribution of energy density deposition in the material. Relativistic incident beams impinge on the target containing 4×10^{10} electrons per bunch at 33 GeV. This beam deposits its energy within



(a) SLC Target Disc Cross Section. Ref.: [34]

(b) SLC Target Housing. Ref.: [27]



(c) SLC Target Housing Schematic. Ref.: [28]

Figure 6.2: SLC Target Housing



Figure 6.3: *Rear view of SLC Decommission Target. Ref.: [18]*

a matter of picoseconds [29]. It is worth noting that, to avoid the target being destroyed by a single pulse, the incoming beam diameter has to be enlarged by a factor of two by using a scattering foil, placed a meter in front of the target [29]. This “electron beam of 4.0×10^{10} electrons/bunch at 33 GeV impinging on the target deposits 5 kW of power into the target at a frequency of 120 Hz” [34]. The beam has a Gaussian radial distribution with a spot size of 0.8 mm [34]. FLUKA or SLAC EGS codes can be used and have been used to determine the energy deposition profile in the target (see Ref. [34]), but here we are going to use a very simple analytical profile to simulate the energy profile.

Using LAW to Simulate Stress in SLC Target

The justification for using an instantaneous energy deposition can be reiterated here, since the electron bunch deposits its energy within a matter of picoseconds and the

material during this time scale would not react to this deposition because of its inertia. Also worth mentioning is the rotation of the target, the frequency at which the electron pulses strike the target and the cooling system. This ensures that two pulses will not hit the same point on the target consecutively and the target will have been cooled down to its nominal state before the next pulse hits the target again. Therefore, our calculation for induced stress in the SLC target will be confined to just a single strike by a single electron pulse.

Table 6.1: *SLC Target Material and Beam Parameters.*

Parameters	Symbol	Units	Value
Target Length	L	m	0.0205
Target Radius	R	m	0.0317
Standard deviation	σ_z	m	0.0062
mean	B	m	0.0205
beam spot size	σ	mm	0.8
Peak Energy Density Dep.	$\frac{Q_0}{V_0}$	J/m ³	5.91×10^8 [34]
Grüneisen Coef.	Γ		2.095
Density	ρ	Kg/m ³	19700
Speed of sound	c_s	m/s	4671.982

Detailed analyses on how the linear acoustic waves dynamically evolve in both thin rod and disc approximations of the cylindrical solid target have been done in Chapter 3 and 4 respectively. To serve as a test case and a proof of principle, we will now apply our analytical solutions to the SLC target and compare the results with the existing simulation results. Since the beam spot size on the target is extremely small compared to the target radius (about 22 times smaller), the radial effect of the linear acoustic wave quickly dissipates and

can be overlooked but not for being insignificant in peak value. Thus, in reality, the BC of the thin rod approximation of the cylindrical target will be Dirichlet BC and as for the disc approximation, it is in between the Dirichlet and Neumann BC. Hence, we applied both the Dirichlet and Neumann BC to the disc approximation.

For a thin rod approximation with Dirichlet BC at both ends: we would use Gaussian distribution to describe the energy density profile along the thin rod [34]. The numerical result obtained using Eqn. 3.30 with the parameter in Table 6.1 can be seen in Figure 6.4. The plot shows the behaviour of the acoustic waves in the body at different time shots. At $t = 0$, the SLC target experiences a compressive wave (that is, positive pressure only), which can be attributed to the instantaneous energy deposition by the incident electron bunch. The peak amplitude appears toward the rear exit of the target. As the time goes on, the waves are reflected (and the role of the boundary conditions becomes visible) and negative pressure starts to appear (for example, at time $t = 0.25 \frac{L}{c_s}$).

The amplitude of the negative pressure continues to grow as the positive pressure decreases. Since the boundary is fixed in terms of pressure ($P = 0$ at both ends), by the time (that is, when $t = \frac{L}{c_s}$) the wave has travelled from the rear exit of the target to the front, the complete inverted and reflected wave is seen (that is, negative pressure which implies tension) and the peak amplitude appears close to the front of the target.

For disc approximation: the behaviour of linear acoustic waves here is a bit different from the one in the thin rod approximation. One of the reasons was noted earlier which is the fact that the region at which the energy is deposited is very small compared to the whole disc, causing quick dissipation of the acoustic wave. This is evident, when one compares Figures 6.5, 6.6 and either Figure 6.7 or 6.8, which show rapid decrease in the peak amplitude of the pressure acoustic wave. Another reason is that at the centre of the disc (that is, at $r = 0$), there is no displacement, which in turn implies that the pressure

at the centre changes freely. This attribute at the centre of the disc is imposed by default, irrespective of the boundary condition imposed at $r = R$. For simplicity, in our analytical result, we described the energy density profile in the disc using the linear distribution and applying the parameter in Table 6.1 to Eqns. 4.19 and 4.40 for both the Dirichlet and Neumann boundary conditions respectively. Figure 6.5 shows a small region at which the stress is induced as a result of the instantaneous energy deposition (this applies to both boundary conditions).

Figures 6.7 and 6.8 are plots (for Dirichlet and Neumann respectively) showing what happens in the disc just after the instantaneous deposition. The remarkable similarity between Figures 6.7 and 6.8 can be attributed to the fact that the role of boundary condition is not observable at $t = \frac{R}{c_s}$. The reflected wave will be inverted for the Dirichlet BC (Figure 6.7) but not for the Neumann BC (Figure 6.8). This explains why all the curves in both plots, except the black dot-dashed curve (which is for $t = \frac{R}{c_s}$), are the same.

Summary of SLC Target Results

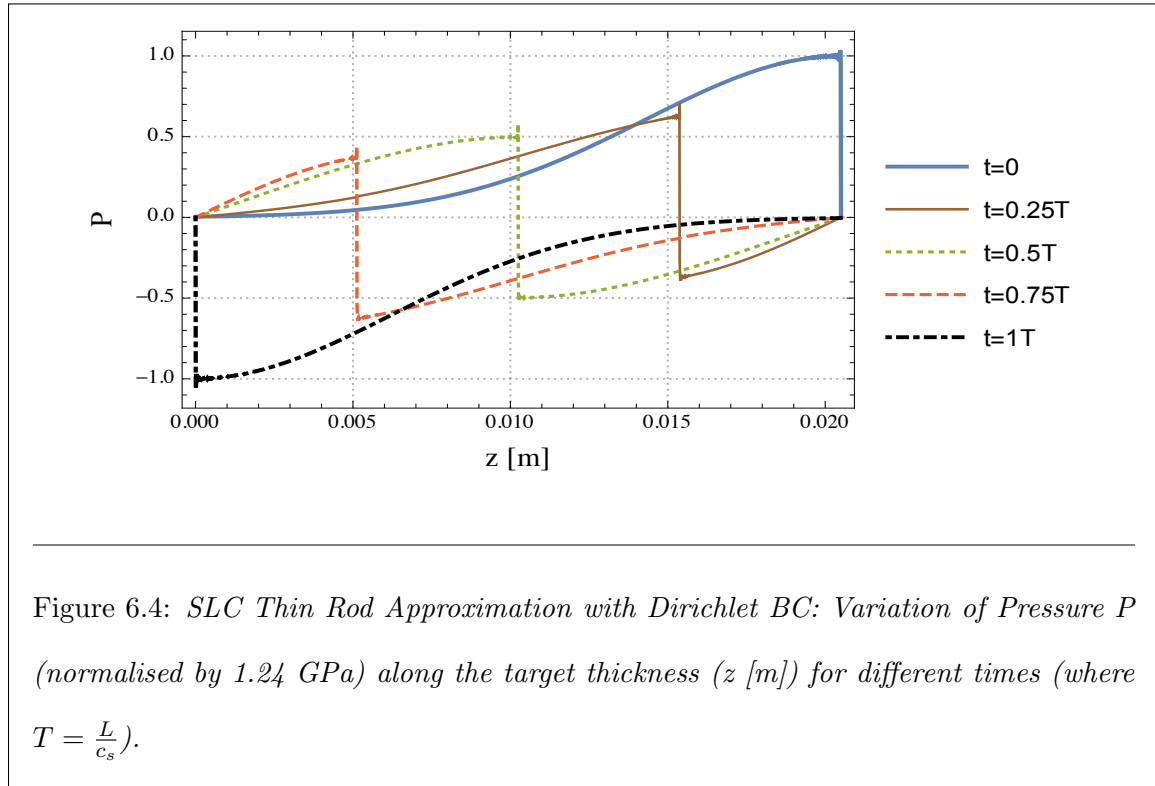
Based on our analysis above (see Appendix C for the time analysis plots), which is evident in Chapters 3 and 4, we know that the absolute peak pressure induced can be calculated by using

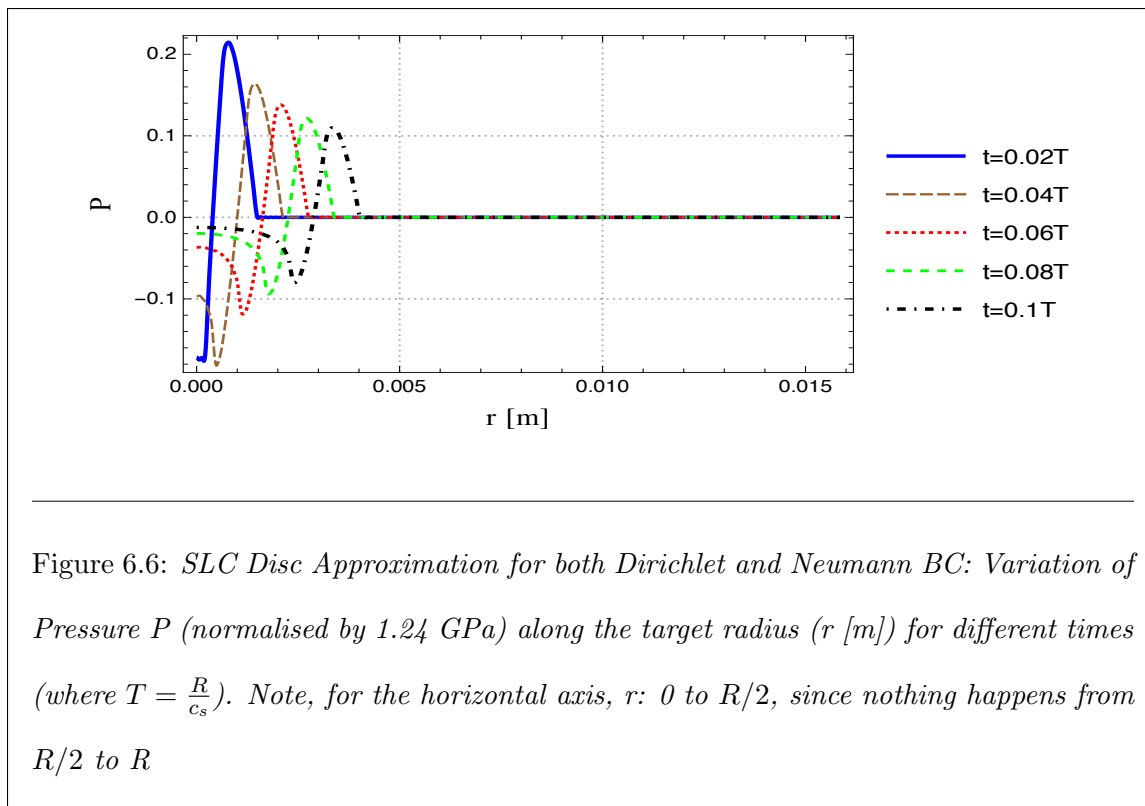
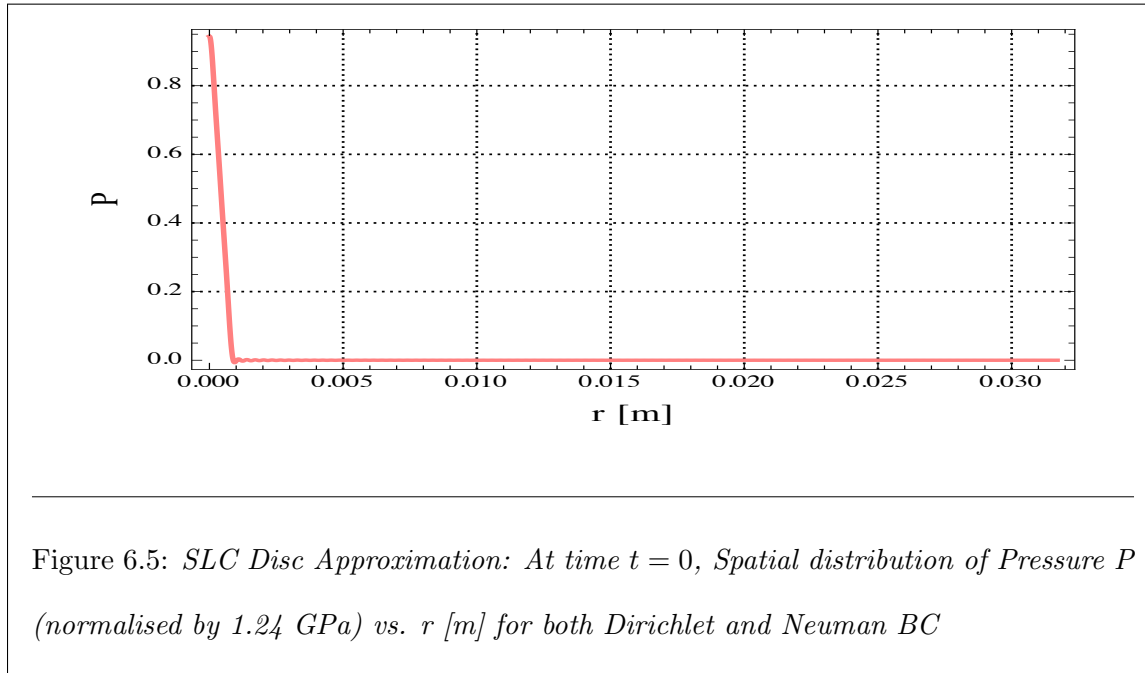
$$P_{peak} = \left| \Gamma \frac{Q_0}{V_0} \right|, \quad (6.1)$$

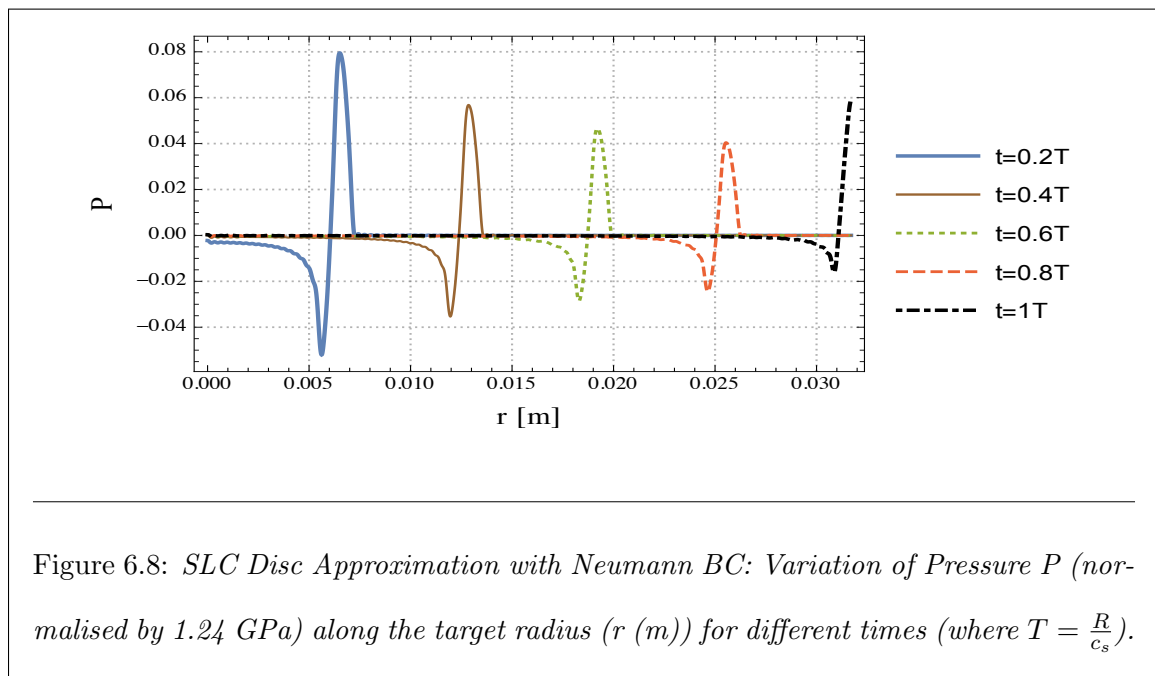
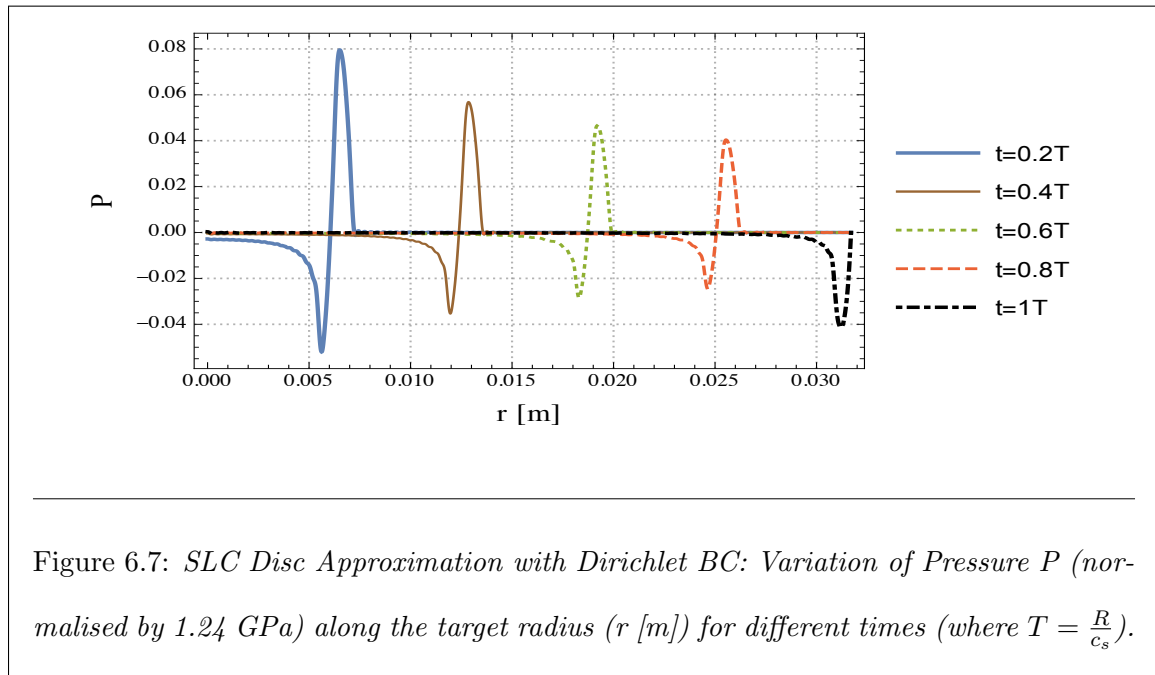
irrespective of the space and time. With the parameter in Table 6.1, we estimated the absolute peak pressure to be 1.24 GPa, which is the result obtained in Ref.: [28, 33].

As stated earlier, in reality there is a cooling system in the SLC target and the target is rotated, so that the same spot would not be struck twice in a row, thus reducing the impact of the induced stress. Also, the BC of the disc approximation of the SLC target

lies between the two boundary conditions, that is, Dirichlet and Neumann BC. Using this approximation we already know the two extreme possibilities.







6.2 International Linear Collider

The International Linear Collider (ILC) is another $e^- - e^+$ linear collider design that will probably be built in Japan in the near future. According to the executive summary of the technical design report of the ILC [8] by the Global Design Effort (GDE): “ILC is a 200 - 500 GeV (extendable to 1 TeV) centre-of-mass high luminosity linear electron-positron collider, based on 1.3 GHz superconducting radio-frequency (SCRF) accelerating technology.” The R&D design of ILC spans a period of 2 decades and involves worldwide collaboration.

There are good reasons to anticipate more new discoveries because of some open questions, like unification of all forces, supersymmetry, dark-matter, superstrings, etc. The ILC will be able to tell us, for example, if extra-dimensions exist, which might be invisible to LHC. Table 6.2 list some of the reactions that will be studied in various energy level at ILC and detailed information can be found in Ref.: [8].

Figure 6.10 shows the schematic view of the accelerator as a whole, indicating the major components, which are [8]

- polarised source for electrons and positrons;
- 5 GeV electron and positron damping rings (DR) hosted in a common tunnel;
- beam transport from the damping rings to the main LINACs, followed by a two-stage bunch-compressor system prior to injection into the main LINACs;
- two 11 km main LINACs;
- two beam delivery systems to the IP.

Table 6.2: Major physics cases for ILC. Ref:[8]

Energy	Reaction	Physics Goal
91 GeV	$e^+e^- \rightarrow Z$	ultra-precision electroweak
160 GeV	$e^+e^- \rightarrow WW$	ultra-precision W mass
250 GeV	$e^+e^- \rightarrow Zh$	precision Higgs couplings
350 - 400 GeV	$e^+e^- \rightarrow t\bar{t}$	top quark mass and couplings
	$e^+e^- \rightarrow WW$	precision W couplings
	$e^+e^- \rightarrow v\bar{v}h$	precision Higgs couplings
500 GeV	$e^+e^- \rightarrow f\bar{f}$	precision search for Z'
	$e^+e^- \rightarrow t\bar{t}h$	Higgs coupling to top
	$e^+e^- \rightarrow Zhh$	Higgs self-coupling
	$e^+e^- \rightarrow \tilde{\chi}\tilde{\chi}$	search for supersymmetry
	$e^+e^- \rightarrow AH, H^+H^-$	search for extended Higgs states
700 - 1000 GeV	$e^+e^- \rightarrow v\bar{v}hh$	Higgs self-coupling
	$e^+e^- \rightarrow v\bar{v}VV$	composite Higgs sector
	$e^+e^- \rightarrow v\bar{v}t\bar{t}$	composite Higgs and top
	$e^+e^- \rightarrow \tilde{t}\tilde{t}^*$	search for supersymmetry

6.2.1 Overview of Typical Operation

A typical operation cycle at the ILC starts from the electron source. The 90% polarised electron beams are produced using a photocathode DC gun, which is close to the SLC design. After production, the electrons are sent into a normal conducting structure in which the beams are bunched together and pre-accelerated to 76 MeV and to 5 GeV thereafter in a SCRF LINAC [3]. Next is the damping ring (DR), but before the electrons are transported into DR, they pass through “superconducting solenoids that rotate the spin vector into the vertical, and a separate superconducting RF structure is used for energy

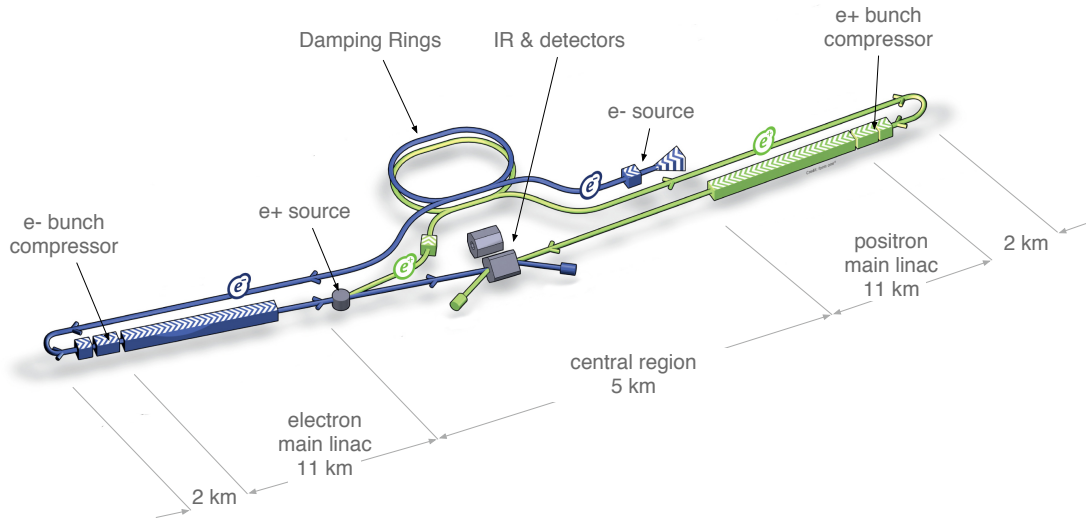


Figure 6.9: Schematic layout of ILC, indicating all the major components. Ref.: [8]

compression" [3].

The beam from the 5 GeV LINAC has a large emittance (both transversely and longitudinally). In order to achieve the high luminosity (as desired) at the interaction point, a low emittance beam is required. To reduce the large emittance beam from the 5 GeV SCRF LINAC, the beam will be injected into the damping ring of 3.2 km circumference. This beam will travel round the ring for about 20,000 times within a very short period of time (200 ms to be precise) [3, 12]. This process makes the beam emit synchrotron light, hence the radiation damping results in reducing the emittance of the beam.

The extracted electron and positron bunches, although small, still need to be compressed before they are transported with great speed to the interaction point [3]. Immediately after extraction, the electron and positron bunches are transported in opposite directions and will travel some 15 km and later bend gently in an arc of magnets. The bunch length is compressed from 6 mm down to 0.3 mm through a two-stage bunch compressor in a 2 km LINAC section before the main LINAC. During the compression, the bunch is also

accelerated from 5 GeV to 15 GeV [12].

The next step is to accelerate both the electron and positron bunches from 15 GeV to 250 GeV (or even twice that). This is done in the main LINAC of 11 km operating at -271 °C and utilising approximately 8000¹ of 1.3 GHz SCRF cavities operating at an average gradient of 31.5 MV/m, with a pulse length of 1.6 ns [3, 12]. “Once accelerated through the main LINAC, the positrons are ready” to be transported to the interaction point. Before being transported to the IP, the electrons have to be used for positron production² [12]. It is worth mentioning that this electron pulse will collide with the positrons generated in the previous machine pulse [12].

The beams have to travel a distance of 2.2 km from the exit of the main LINAC to reach the IP. During the transportation the beam will pass through a series of specially designed and arranged magnets. These magnets provide the final focus for the beam down to a factor of about 300. Basically, these magnets are serving as focusing “lenses” in order to bring the beams into collision with a 14 mrad crossing angle at a single interaction point, which is occupied by two detectors in so-called “push-pull” configuration. Before collision, the beams are extremely small³ and a great amount of care is needed for their delivery [3, 9]. Hence, ultra-fast diagnostics and correction systems are used to analyse and correct any small EM field fluctuations and vibrations that could make the beam wobble.

6.2.2 Positron Source Production for ILC

The ILC makes use of the 250 GeV electron beam (on its way to the IP) to generate photons (via undulator) that will be used to produce the positrons. The major components

¹Total of 16000 cavities for both main LINACs

²Details of the process are explained in the next subsection below.

³For 250 GeV centre of mass energy: nominal horizontal and vertical beam size at the interaction point are 727 nm and 7.7 nm respectively [3].

of the positron production unit of ILC are (see figure 6.10 for the layout)

- Superconducting Helical Undulator;
- Photon Collimator;
- Conversion Target;
- Flux Concentrator;
- Capture RF;
- Two dumps (one for the electron beam and the other for the photon beam);
- Pre-accelerator;
- SCRF Booster;
- Spin rotation solenoid;
- Energy compressor

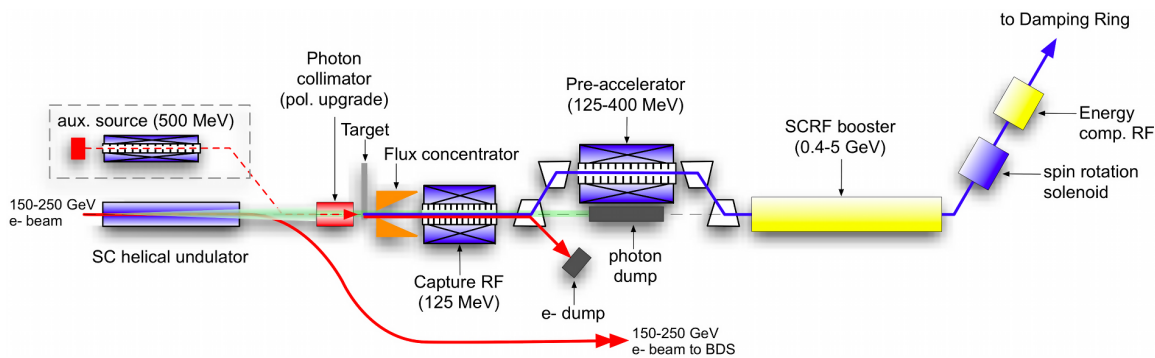


Figure 6.10: *Layout of the Positron Source, indicating all the major components. Ref.: [3]*

The 250 GeV electron beam will pass through a superconducting helical undulator. This SC helical undulator uses the polarised electron beam to generate a circularly polarised

photon beam with energy range of ~ 10 MeV up to ~ 30 MeV. The range of photon beam energy varies with respect to the drive electron beam energy. After the primary (250 GeV) electrons have been used to generate the photons, the former will be gently bent away from the generated photons and they will be “displaced horizontally by 1.5 m using a low emittance preserving chicane” [3]. The photon beam hit the Ti-Alloy target⁴ placed downstream. By hitting the target, the energetic photon produces positron electron pairs. The electrons produced and the photons that were not absorbed by the target will be discarded in their respective dumps.

The polarised positrons produced (baseline design provides 30% polarisation and with upgrade option of 60% by increasing the length of the undulator by a factor of two) are captured and accelerated to 5 GeV before they are injected into their damping ring.

ILC Target for Positron Production

⁵ The conversion target is a wheel of titanium alloy (Ti6Al4V) that rotates at 100 m/s at the rim. The photon beam (of ≈ 300 kW) from the undulator is incident on the rim of the spinning wheel. The diameter of the wheel is 1 m and the thickness is 0.4 radiation lengths (1.4 cm)[3, 4, 36].

Shown in Figure 6.11 is a picture of the conceptual target layout. For cooling, the wheel has a rotating water cooling system. The beam power is too high to allow a vacuum window downstream of the target. The target wheels sit in a vacuum enclosure at a very low pressure (10^{-8} Torr). This low pressure is needed for NC RF operation [3]. However the motor driving the wheel will be outside the vacuum [3]. This implies that a rotating vacuum seal is needed. This vacuum seal must be capable of operating at high velocity,

⁴See “ILC Target For Positron Production” for the operation description of the target.

⁵Everything here in this sub-sub-section is from Ref.: [3, 4]

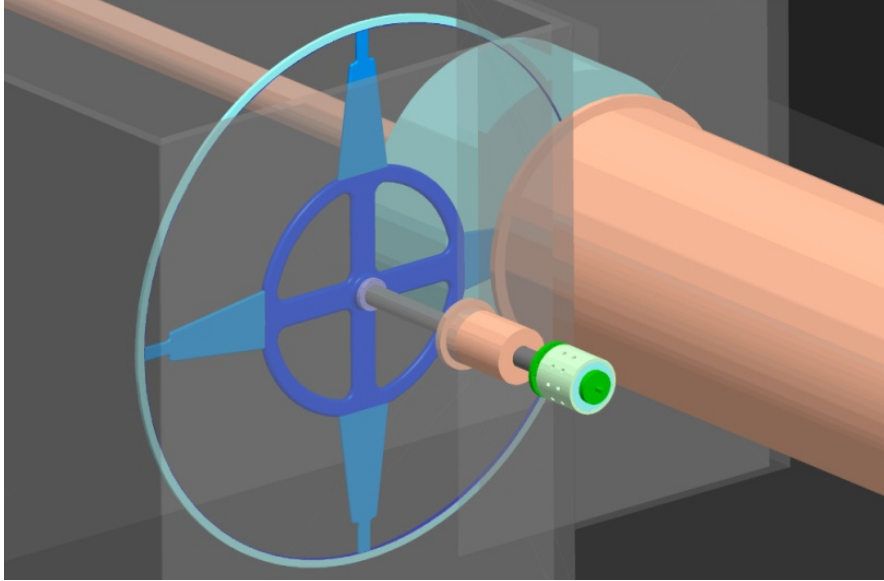


Figure 6.11: *Conceptual design of the target for positron production. Ref.: [3]*

near a magnet (called adiabatic matching device) and in a high radiation environment. All this has proved to be a very daunting task and various solutions have been proposed [3, 36]

Another unit mounted on the ILC target that is worth mentioning is the adiabatic matching device (AMD). The AMD has a very strong magnetic field and it is used to increase the positron-capture efficiency. This strong magnetic field combined with the fact that the target is being rotated causes the eddy-current effect which in turn causes the heating of the target. This effect has been studied and experiments have been performed. The conclusion is that the target and motor can be designed to tolerate the eddy-current heating.

“A series of sensors provides information on the target behaviour. An infrared camera tracks temperatures on the wheel, to allow for quick shutdown in case of a cooling failure. Flowmeters monitor cooling water flowing in and out of the wheel (to check for leaks), and thermocouples check ingoing and outgoing flow temperature. There is a torque sensor on the shaft, and vibration sensors on the wheel to monitor mechanical behaviour”

[3].

The target-wheel assembly is designed for an operational life of two years. If the target should fail during a run, there is a replacement that can be installed within a day by “using a vertically removable target remote-handling scheme” [3, 36].

6.2.3 Stress Analysis in ILC Target

Based on past experience, concerns were raised with respect to possible material damage of the target as a consequence of the intense pulses of gamma photons generated by the undulator. As stated in Chapter 1, our aim is to calculate the amount of stress induced on the target and to investigate the dynamic effect of the stress on the target, with special consideration on multi-bunches. To do our calculation, we used the parameters in Table 6.3 by considering the following:

1. Boundary condition: we investigated both the so-called best and the worst case scenarios, that is, Dirichlet and Neumann BC respectively.
2. Geometry: we considered the cylindrical solid target in an approximation: both as a thin rod and a disc.
3. Energy distribution: in r and z direction, we assumed the energy distribution density to be linear and Gaussian respectively.

For a single bunch, we can calculate the absolute peak pressure in the target (by using Eqn. 6.1 with the parameters in Table 6.3) to be approximately 2.2 MPa. Although the value of the peak pressure here is far less than the tensile strength of Ti6Al4V, we can not stop here because the bunch spacing T_b is less than the time taken for LAW to travel through the target material both radially and longitudinally, therefore special attention is given to the effect of the multiple bunches striking the same spot on the target. As we did

Table 6.3: *ILC Target Material and Beam Parameters*

Parameters	Symbol	Units	Value
Target Thickness	L	m	0.014
Target Radius	R	m	0.01
Standard deviation	σ_z	m	0.003
Mean of the Distribution	B	m	0.014
beam spot size	r_0	m	0.003
Bunch per Train	N_b		1312
bunch spacing	T_b	ns	300
Peak Energy Density Dep.	$\frac{Q_0}{V_0}$	J/m ³	1.8×10^6 [1]
Grüneisen Coef.	Γ		1.262
Density	ρ	Kg/m ³	4430
Speed of sound	c	m/s	5072.833
Wheel Rotation Speed	v	m/s	100
Ultimate Tensile Strength	UTS	MPa	950 [5]

in the case of the SLC target, we considered both the thin rod and disc approximations of the ILC target just as a purely academic exercise.

Results of Thin Rod Approximation of ILC Target Material with Dirichlet BC

We assumed $P = 0$ at both ends of the rod. Assuming a Gaussian energy density distribution, we applied Eqn. 5.19 in Chapter 5 and the numerical investigation revealed results presented in Figures 6.12 to 6.15. If we assume that 100 bunches⁶ struck the target at the same spot with time spacing (T_b) between the bunches, then we summarise the stages

⁶This assumption of 100 bunches hitting the same spot is a rough estimate based on the rotation speed of the wheel, the bunch spacing and the spot size ($\frac{r_0}{T_b v}$).

of induced pressure in the target as follows:

1. Figure 6.12 shows what is going on inside the target immediately after the energy of first bunch is deposited (Figure 6.12A) and the state of the target at time $T_b = 300$ ns after the bunch left the target (Figure 6.12B). Comparing the two plots reveals that the wave movement starts from the exit end of the target, making part of the compressive wave reflect back and become a tensile wave. At this time, the amplitude of the tensile wave induced is about 0.0463% of the ultimate tensile strength of the material, hence the target is still very safe in this region.
2. If the second bunch hits the target, Figure 6.13A gives the result of the immediately induced pressure (acoustic) wave and Figure 6.13B shows the target material state at time T_b after the second bunch left.
3. Figure 6.14 shows the aftermath of 10 bunches hitting the target and what happens at time T_b after the 10th bunch (Figure 6.14 A and B respectively)
4. For 100 bunches hitting the target at the same spot with time spacing (T_b), the peak pressure induced is approximately 22 MPa (Figure 6.15).

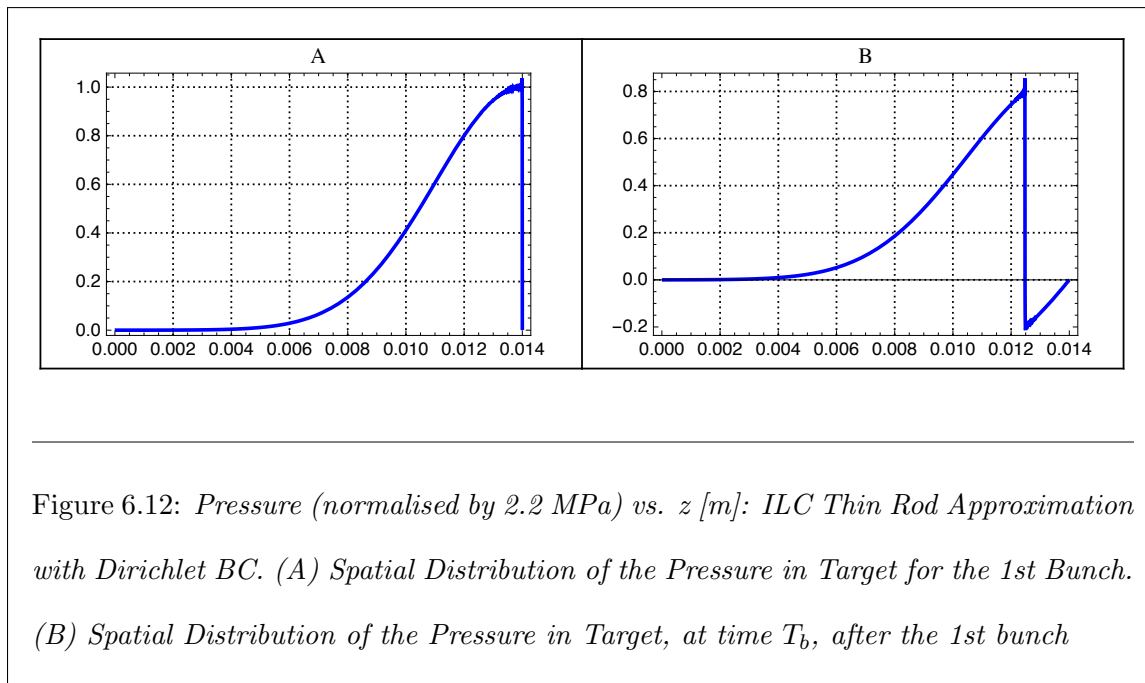
Result of Disc Approximation of ILC Target Material

We used Eqns. 5.53 and 5.63 in Chapter 5 for numerical analysis of Dirichlet and Neumann boundary conditions, respectively. For our investigation, we used linear energy density distribution in both BCs. Results obtained are presented in Figure 6.16 and 6.17. As one might have expected, the boundary effect starts playing a significant role after a large numbers of bunches had hit the target. For example, at the 100th bunch, the peak pressure induced in the case of Neumann BC is a factor of 1.5 higher than in the case of Dirichlet BC. The study shows that this factor difference continues to grow as the number

of bunches hitting the same spot on the target increases. Detailed plots of the evolution of the pressure acoustic wave in time after 100 bunches hit the same spot is given in Section D.2 of Appendix D.

Summary

Worth noting is the significant difference in terms of the peak pressure induced in both the thin rod and disc, even though the same peak energy density is imposed. The effect can be attributed to the fact that in the disc, the beam spot size is far less than the radius of the target, whereas, in the case of the thin rod, the energy density distribution is over the whole length of the target.



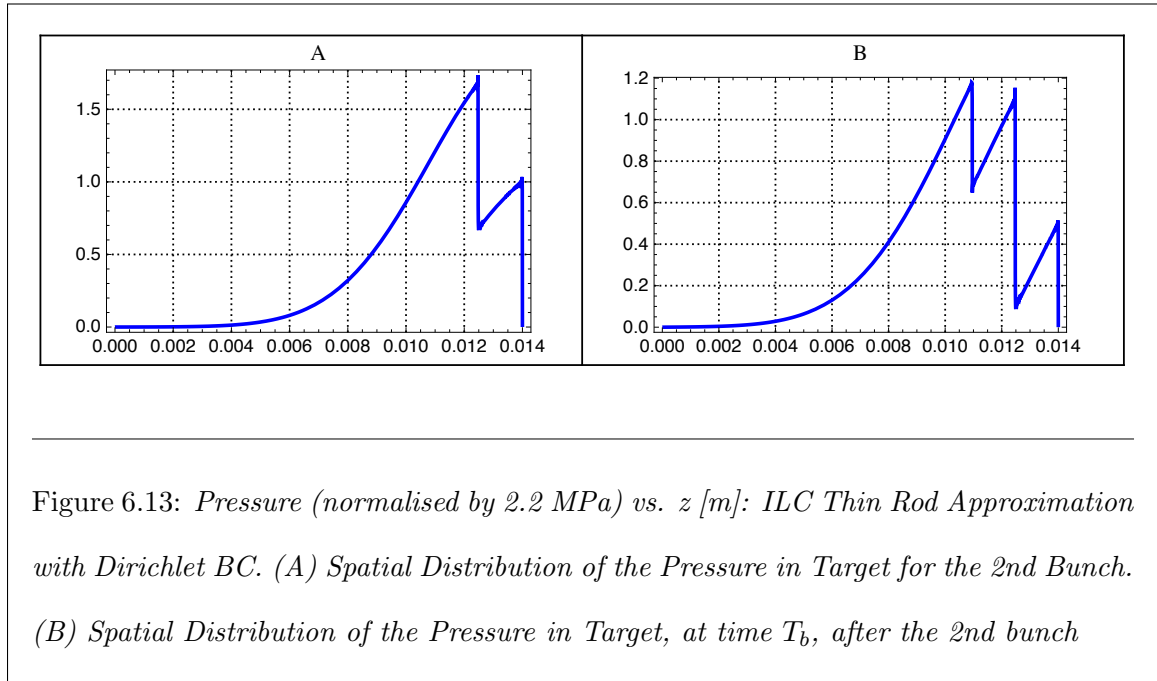


Figure 6.13: Pressure (normalised by 2.2 MPa) vs. z [m]: ILC Thin Rod Approximation with Dirichlet BC. (A) Spatial Distribution of the Pressure in Target for the 2nd Bunch. (B) Spatial Distribution of the Pressure in Target, at time T_b , after the 2nd bunch

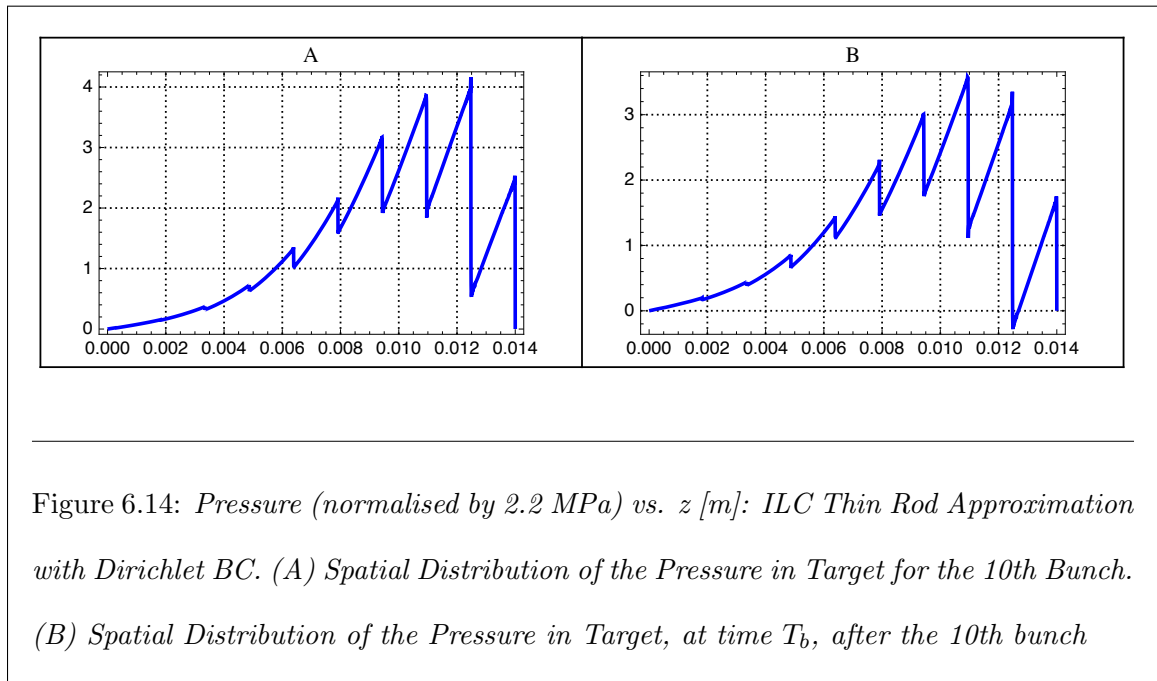


Figure 6.14: Pressure (normalised by 2.2 MPa) vs. z [m]: ILC Thin Rod Approximation with Dirichlet BC. (A) Spatial Distribution of the Pressure in Target for the 10th Bunch. (B) Spatial Distribution of the Pressure in Target, at time T_b , after the 10th bunch

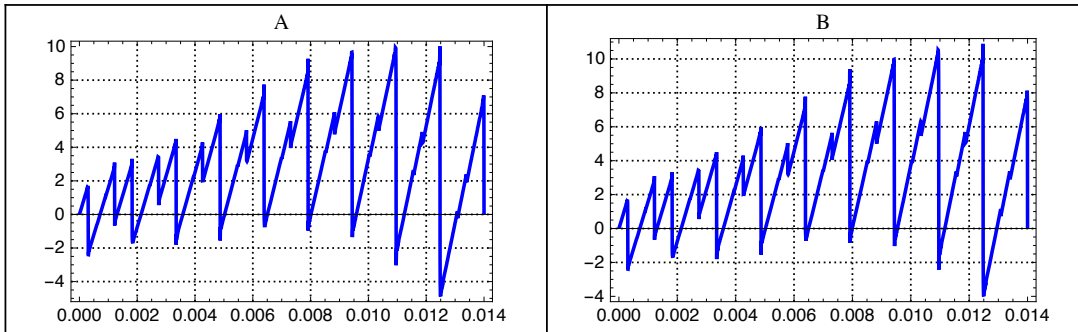


Figure 6.15: Pressure (normalised by 2.2 MPa) vs. z [m]: ILC Thin Rod Approximation with Dirichlet BC. (A) Spatial Distribution of the Pressure in Target after time T_b , that is, after 99th bunch and just before the 100th bunch. (B) Spatial Distribution of the Pressure in Target for the 100th Bunch.

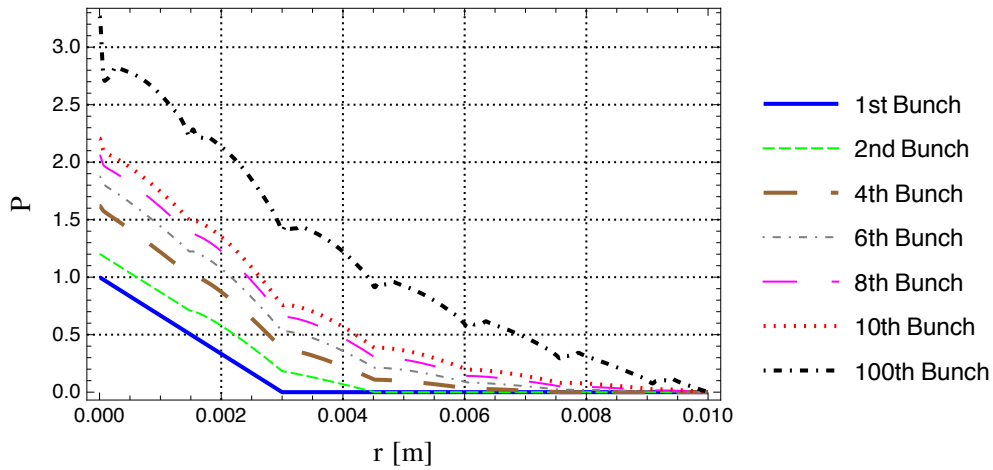
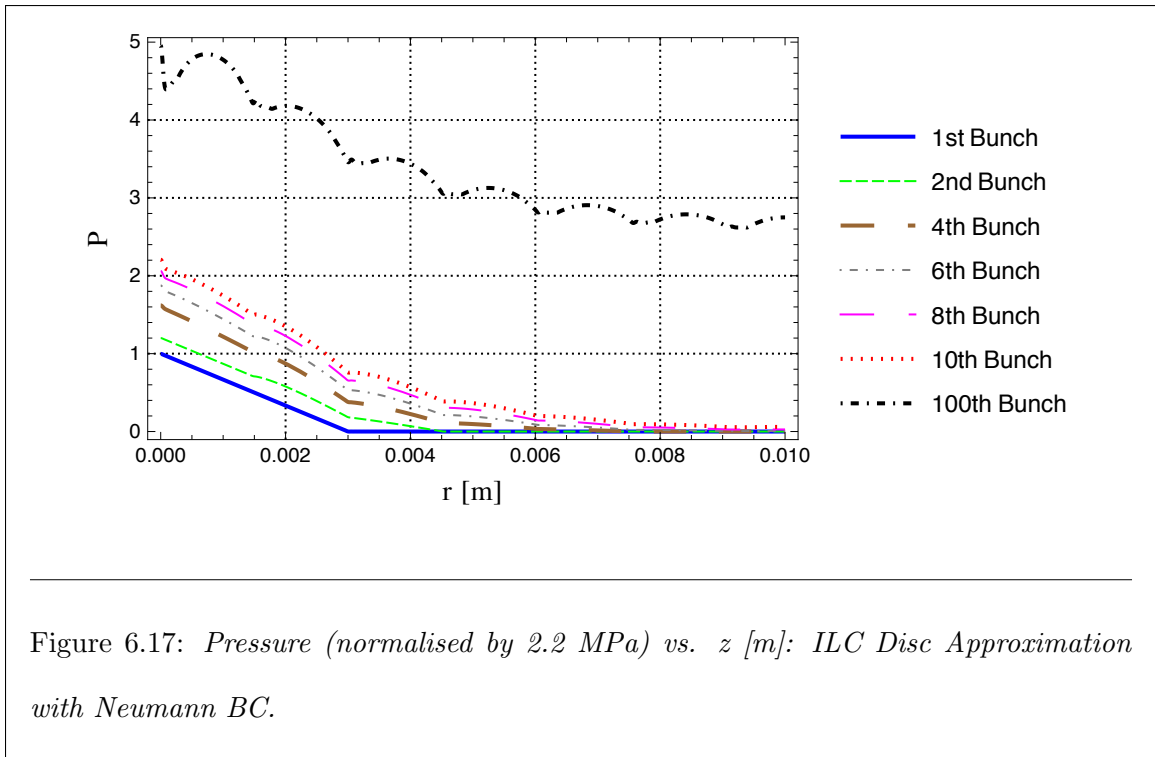


Figure 6.16: Pressure (normalised by 2.2 MPa) vs. z [m]: ILC Disc Approximation with Dirichlet BC.



Chapter 7

Conclusion

A formalism which expresses the dynamic behaviour of induced stress in solid target materials by the incident particle beam was derived and solved analytically for various appropriate cases. The analytical solutions (free of numerical errors) provide a good opportunity without huge simulation tools to calculate the peak stress value and to observe the evolution of the linear stress wave in a target material in a lepton collider. Calculating this value and observing the evolution of the stress waves is the first step in determining the lifetime of the solid target material. To summarise, in this thesis we have studied a single bunch effect in respect to

1. three different energy distributions (uniform, linear and normal)
2. two different approximations of cylindrical geometry (thin rod and disc)
3. two different boundary conditions (Dirichlet and Neumann BC)

and we have also derived analytical solutions (irrespective of the deposited energy density profile) to describe the effect of multiple bunches in two different approximations of cylindrical geometry and two boundary conditions.

As a test case, we applied the model to the target of the former SLC machine. The result obtained in this thesis (shown in Chapter 6) for the peak pressure (1.24 GPa) in the SLC target was in full agreement with the existing simulation results in Refs.: [28] and [33]. Even though we can not directly compare our result with Ref.: [34] because the result obtained there is based on von Mises stress (which is obtained from 3D numerical calculation) and ours is just the principal stress, we can still infer that they are in comparison since Ref.: [28] agrees with Ref.: [34].

Based on the results obtained from both analytical and numerical analyses, we came to the following conclusion for the International Linear Collider (ILC) positron conversion target:

1. Since the induced stress (≈ 2.2 MPa) by a single bunch is far less than the ultimate tensile strength (950 MPa) of the currently discussed Ti-Alloy target material, a single bunch of the photon beam coming from the undulator will not destroy the target.
2. For a worst case scenario, when no cooling and no damping is implemented, and 100 bunches of the photons hit the same spot on the target consecutively, the peak stress induced is about 70 MPa, which is still well below the ultimate tensile strength of the target material. This implies that 100 bunches of photon beam impinging on the Ti6Al4V target will not cause any immediate damage on the target.

On a general note, the results obtained from the analysis of both the thin rod and the disc approximation of a cylindrical solid target lead to the following inferences:

1. *The deposited energy density profile* of the incident particle beam determines how the compressive waves will look like at the initial state. It also determines how the wave evolves in time.

2. *A single bunch* of the incident particle beam will induce an absolute peak pressure of

$$|\Gamma \frac{Q_0}{V_0}|, \quad (7.1)$$

irrespective of the time, the geometry of the target and the boundary condition imposed.

3. *In the case of multiple bunches*, the boundary condition, the geometry and the bunch spacing play a big role on the amplitude of the induced peak pressure. This implies that careful considerations are required when determining the necessary parameters for the positron source unit of the collider machine. As a rule of thumb, one wants to keep the absolute value of

$$\sum_{i=1}^m \cos^{i-1}(\lambda_n c_s T_b) \quad (7.2)$$

between zero and unity.

So far, our solution is an approximation (albeit a good one) which is valid under certain conditions and regimes. In order to obtain an analytical solution which will completely describe how a cylindrical solid target behaves under the influence of impinging particles in reality, this project, like many others, would suggest areas that can be further explored by including the following in future models:

- the effect of damping which can not be neglected especially when considering multiple bunches of the particle beam. (One way to include the damping effect would be to describe the thermal diffusion mechanism.)
- the analytical solution of the linear acoustic wave should be described in terms of the full cylindrical geometry of the target.
- the BC description can be improved since in reality the BC behaviour is between Dirichlet and Neumann BC, hence the improved BC should be described using Robin BC.

Bibliography

- [1] A. Ushakov, A. Schälike and S. Riemann. Simulation of polarised positron sources for linear colliders. *Journal of Physics: Conference Series*, 298(012021):1–7, 2011.
- [2] D. J. Acheson. *Elementary Fluid Dynamics*. Oxford University Press, 1990.
- [3] C. Adolphsen et al., editors. *International Linear Collider Technical Design Report*, volume 3.2. ILC Global Design Effort and World Wide Study, 2013. Baseline Design.
- [4] C. Adolphsen et al., editors. *International Linear Collider Technical Design Report*, volume 3.1. ILC Global Design Effort and World Wide Study, 2013. Accelerator R&D.
- [5] ASM. Titanium Ti-6Al-4V (Grade 5), Annealed. <http://asm.matweb.com/search/SpecificMaterial.asp?bassnum=MTP641>.
- [6] H. Baer et al., editors. *International Linear Collider Technical Design Report*, volume 2. ILC Global Design Effort and World Wide Study, 2013. Physics.
- [7] H. Bargmann. Dynamic response of external target under thermal shock. Technical report, European Organisation for Nuclear Research, May 1973. CERN LAB II/BT/Int./73-3.
- [8] T. Behnke et al., editors. *International Linear Collider Technical Design Report*, volume 1. ILC Global Design Effort and World Wide Study, 2013. Executive Summary.
- [9] T. Behnke et al., editors. *International Linear Collider Technical Design Report*, volume 4. ILC Global Design Effort and World Wide Study, 2013. Detectors.
- [10] V. K. Bharadwaj et al. Analysis of beam-induced damage to the SLC positron production target. In *Proceedings of the 2001 Particle Accelerator Conference*. IEEE, 2001.
- [11] B. A. Bosley and J. H. Weiner. *Theory of Thermal Stresses*. Dover Publication, Inc., NY, 1997.
- [12] P. Burrows et al., editors. *International Linear Collider Technical Design Report*, volume 5. ILC Global Design Effort and World Wide Study, 2013. From Design to Reality.
- [13] J. E. Clendenin. High-yield positron systems for linear colliders. In *Proceedings of IEEE Particle Accelerator Conference*. IEEE Particle Accelerator Conference, March. 1989.

-
- [14] J. E. Clendenin et al. SLC positron source startup. In *Proceedings of the 1988 Linear Accelerator Conference*, 1988.
- [15] S. Ecklund. The Stanford Linear Collider positron source, October 1987. Invited talk presented at the Workshop on Intense Positron Beams, Idaho Falls.
- [16] S. Eliezer, A. Ghatak and H. Hora. *Fundamentals of Equations of State*. World Scientific Publishing Co. Pte. Ltd., 2002.
- [17] D. J. Grieve. Error arising in FEA. <http://www.tech.plym.ac.uk/sme/mech335/feaerrors.htm>.
- [18] J. Gronberg. *Positron Source Technology R&D*, November 2010. Talk at the ILC PAC meeting.
- [19] P. Jones and N. Kessissoglou. An evaluation of current commercial acoustic FEA software for modelling small complex muffler geometries: prediction vs experiment. In *Proceedings of ACOUSTICS*. Australian Acoustical Society, Nov. 2009. http://www.acoustics.asn.au/conference_proceedings/AAS2009/papers/p85.pdf.
- [20] K. Flöttmann. *Investigations Toward the Development of Polarised and Unpolarised High Intensity Positron Sources for Linear Colliders*. PhD thesis, Universität Hamburg, 1993.
- [21] K. Flöttmann. personal communication, March 2015.
- [22] A. I. Kalinichenko, V. T. Lazurik and I. I. Zalyubovsky. *Introduction to Radiation Acoustics*, volume 9 of *The Particle and Technology of Particle and Photon Beams*. Harwood Academic Publishers, 2001.
- [23] G.T. Mase and G. E. Mase. *Continuum Mechanics for Engineers*. CRC Press, 2nd edition, 1999.
- [24] A. Mikhailichenko. Positron source for ILC - a perspective. Technical report, LEPP, Ithaca, NY, April 2006. CBN06-1.
- [25] N. Phinney. SLAC linear collider. In *Proceedings of the 1992 Linear Accelerator Conference*, 1992.
- [26] A. D. Polyanin. *Handbook of Linear Partial Differential Equations for Engineers and Scientists*. CRC Press, 2002.
- [27] E. M. Reuter et al. Mechanical design and development of a high power target system for the SLC positron source. In *Proceedings of the 1991 IEEE Particle Accelerator Conference*, 1991.
- [28] E. M. Reuter and J. A. Hodgson. 3D numerical thermal analysis of the high power target for the SLC positron source. In *Proceedings of the 1991 Particle Accelerator Conference*, 1991.

- [29] J. T. Seeman. The Stanford Linear Collider, July 1991. SLAC - PUB - 5607.
- [30] P. Sievers. Elastic stress waves in matter due to rapid heating by an intense high-energy particle beam. Technical report, European Organisation For Nuclear Research, June 1974. CERN LAB II/BT/74-2.
- [31] G. I. Silvestrov and T. A. Vsevolozhskaya. Limitations of energy deposition in solid and liquid targets and jet liquid target description.
- [32] SLAC Linear Collider (SLC). <http://www-sldnt.slac.stanford.edu/alr/slc.htm>.
- [33] SLAC Linear Collider Conceptual Design Report, June 1980. SLAC - 229 UC - 34d.
- [34] W. Stein et al. Thermal shock structural analyses of a positron target. In *Proceedings of the IEEE Particle Accelerator Conference*. IEEE, 2001.
- [35] S. P. Timoshenko and J. N. Goodier. *Theory of Elasticity*. McGraw-Hill, 3rd edition edition, 1970.
- [36] N. Phinney, N. Toge and N. Walker, editors. *International Linear Collider Reference Design Report*, volume 3. ILC Global Design Effort and World Wide Study, August 2007.
- [37] T. A. Vsevolozhskaya. The linear approximation to the hydrodynamic consideration of target behaviour under high density beam exposure. Technical report, Institute of Nuclear Physics, Novosibirsk, USSR, May 1984. Preprint 84-88.
- [38] N. Walker. Introduction and Overview. http://www.desy.de/~njwalker/uspas/coursemat/notes/unit_1_notes.pdf, June 2003. USPAS Course Material (Presented at Santa Barbara).
- [39] E. W. Weisstein. Boundary Conditions. <http://mathworld.wolfram.com/BoundaryConditions.html>.
- [40] K. Wille. *The Physics of Particle Accelerators: An Introduction*. Oxford University Press, New York, 2000.
- [41] Ya. B. Zel'dovich and Yu. P. Raizer. *Physics of Shock Waves and High Temperature Hydrodynamic Phenomena*. Dover Publication, Inc., NY, 2002.
- [42] E. Zahavi. *The Finite Element Method in Machine Design*. Prentice-Hall, NJ, 1992.

Appendix A

Results of LAW in a Thin Rod

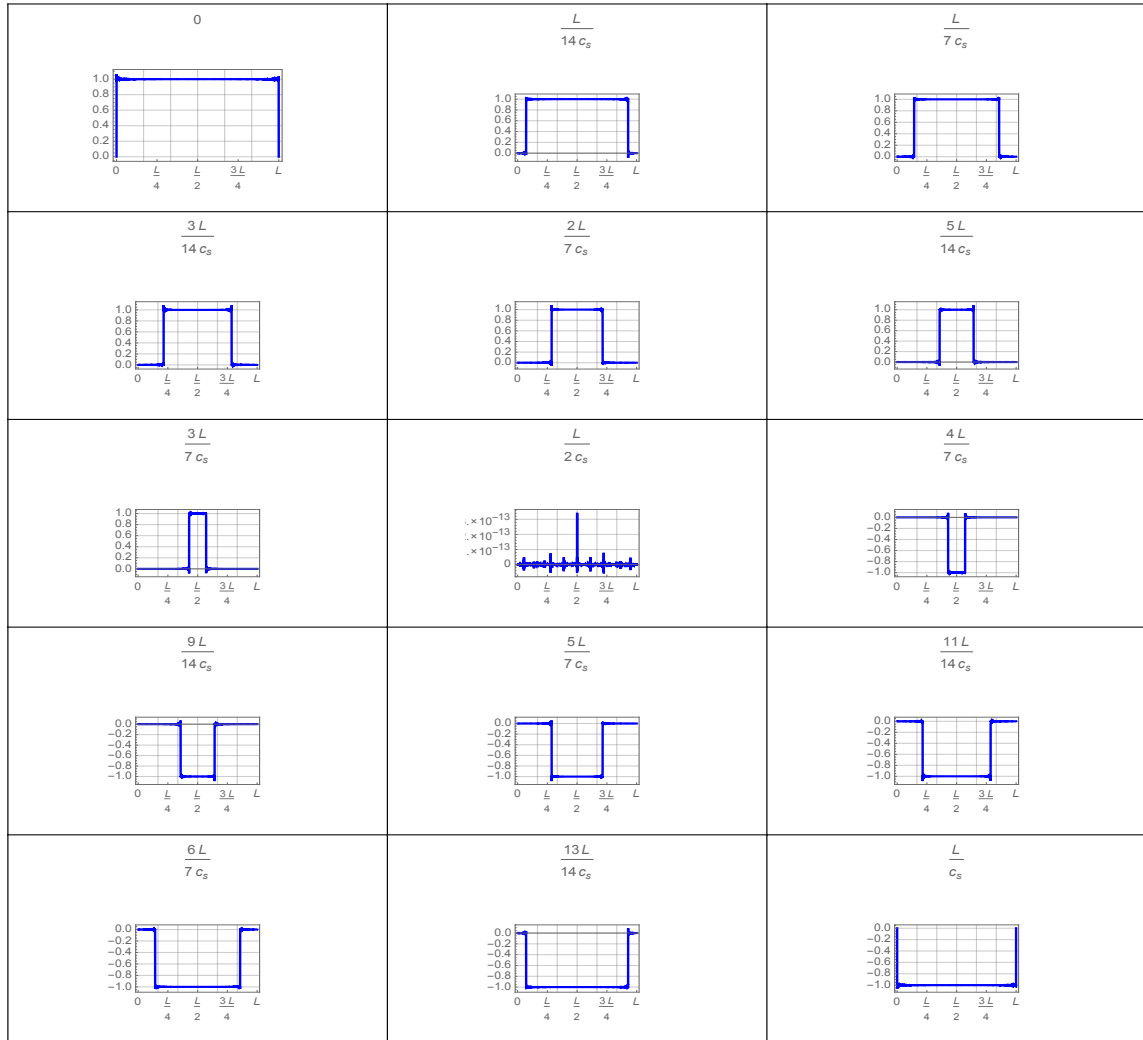
Table A.1: *Typical Case Analysis: Copper Target Material Parameters (same as Table 3.1).*

Parameters	Symbol	Unit	Value
Length	L	m	0.12
Standard deviation	σ_z	m	0.037
Mean	B	m	0.12
Speed of sound	c_s	m/s	3570

A.1 Dirichlet BC with Uniform Energy Distribution

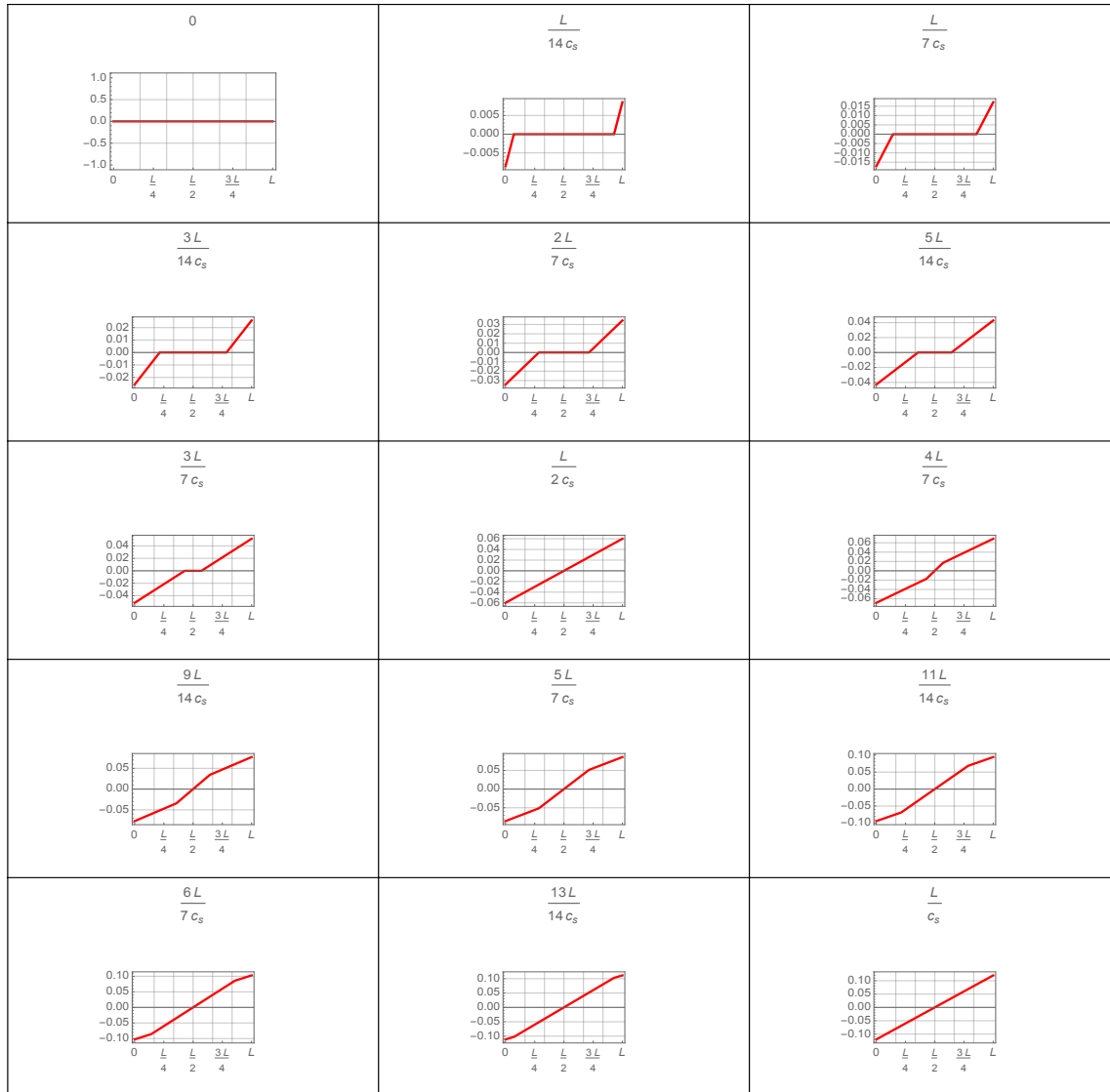
A.1.1 P (Pa) versus z (m) for different t (s)

Each plot in this subsection depicts variation of the pressure acoustic wave P (normalised by $\Gamma \frac{Q_0}{V_0}$ [Pa]) along the thin rod (z [m]) and at different time shots (t [s]). The label at the top of each plot represents the time shot, where L is the length of the rod and c_s is the speed of sound in the material (see Table A.1 for parameters).



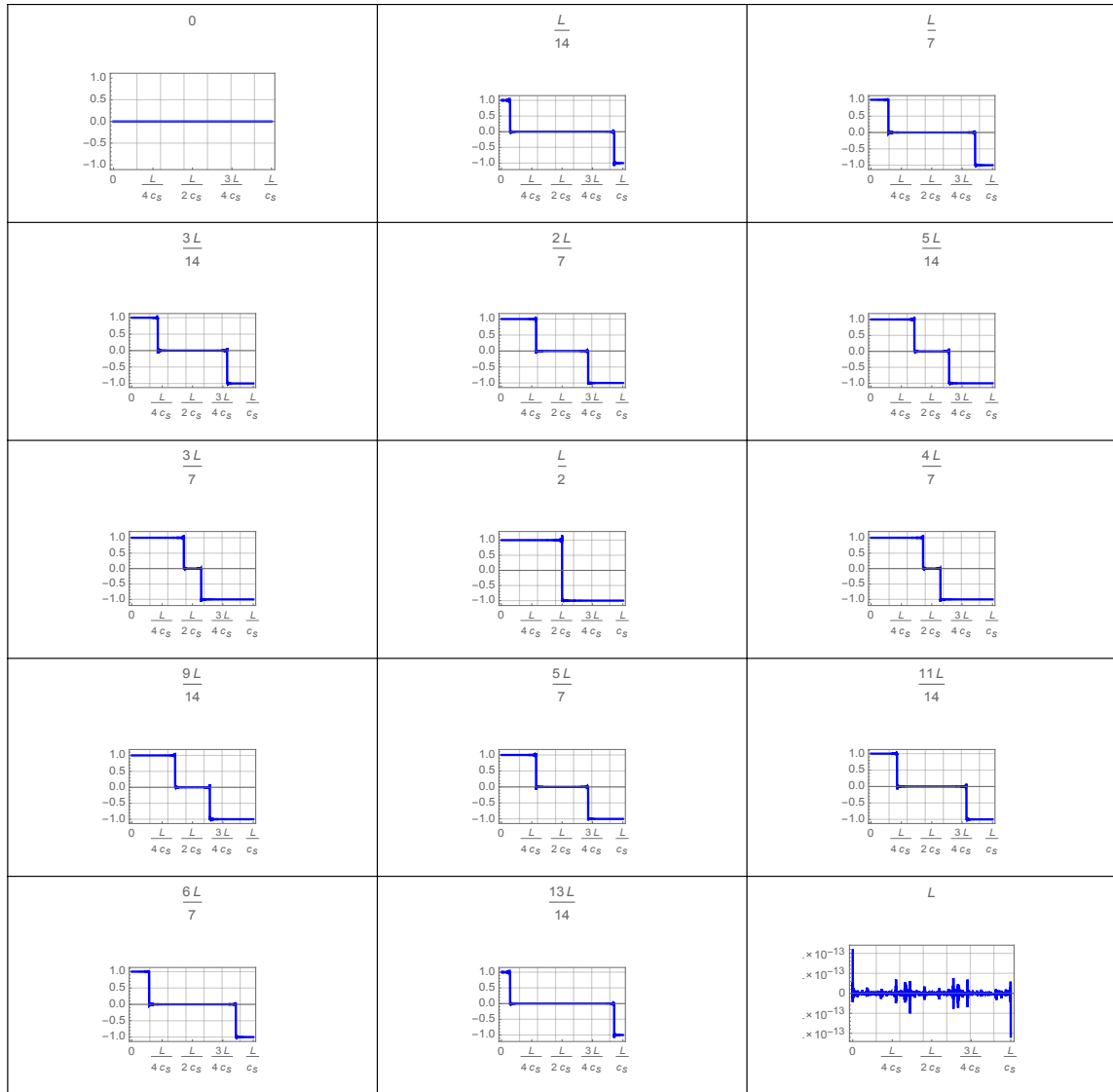
A.1.2 u (m) versus z (m) for different t (s)

Each plot in this subsection depicts variation of the displacement acoustic wave u (normalised by $\frac{\Gamma Q_0}{\rho_0 V_0 c_s^2}$ [m]) along the thin rod (z [m]) and at different time shots (t [s]). The label at the top of each plot represents the time shot, where L is the length of the rod and c_s is the speed of sound in the material (see Table A.1 for parameters).



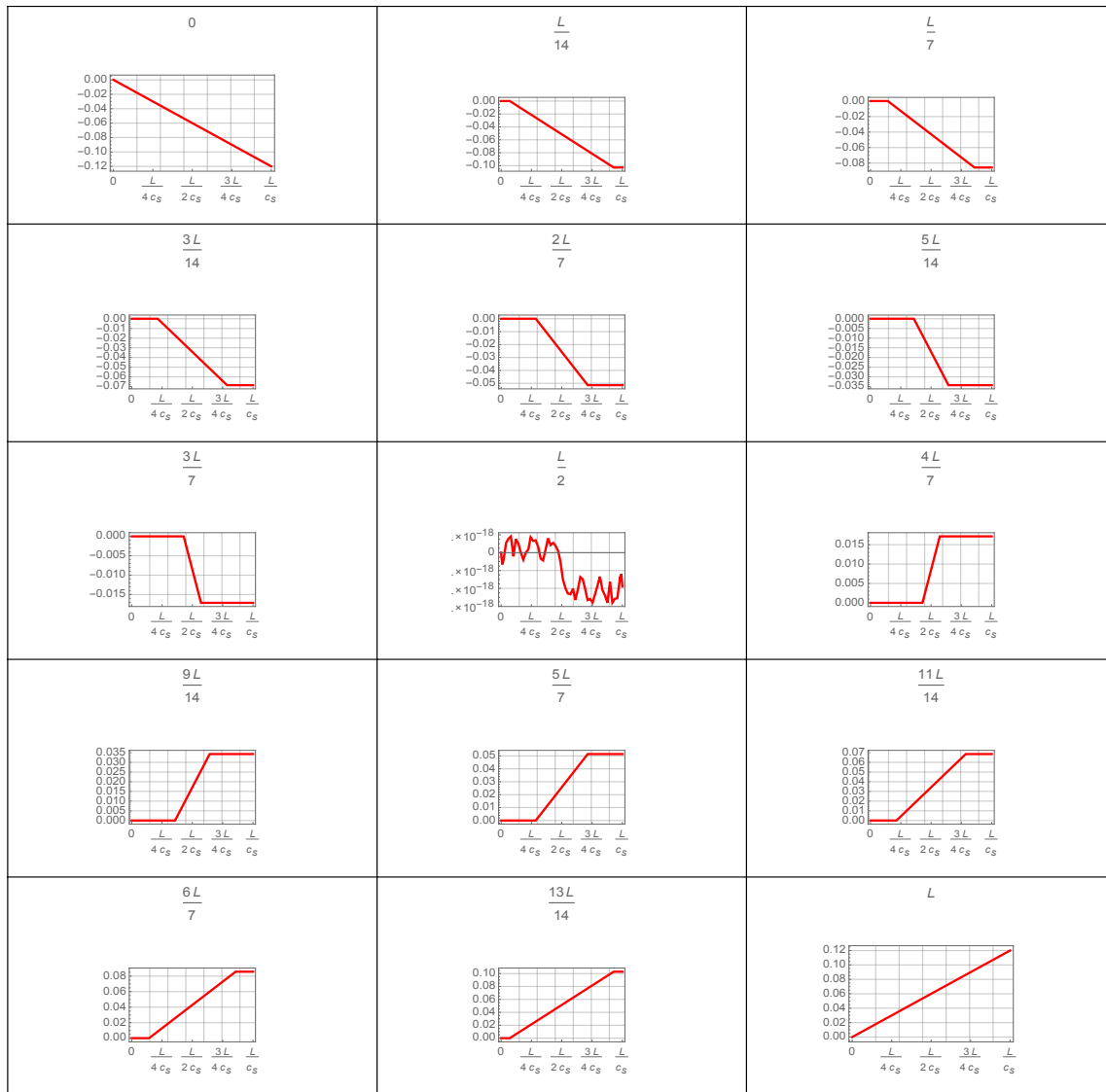
A.1.3 P (Pa) versus t (s) for different z (m)

Each plot in this subsection depicts variation of the pressure acoustic wave P (normalised by $\Gamma \frac{Q_0}{V_0}$ [Pa]) in time t [s] and at different points in the thin rod. The label at the top of each plot represents the point in the thin rod, where L is the length of the rod and c_s is the speed of sound in the material (see Table A.1 for parameters).



A.1.4 u (m) versus t (s) for different z (m)

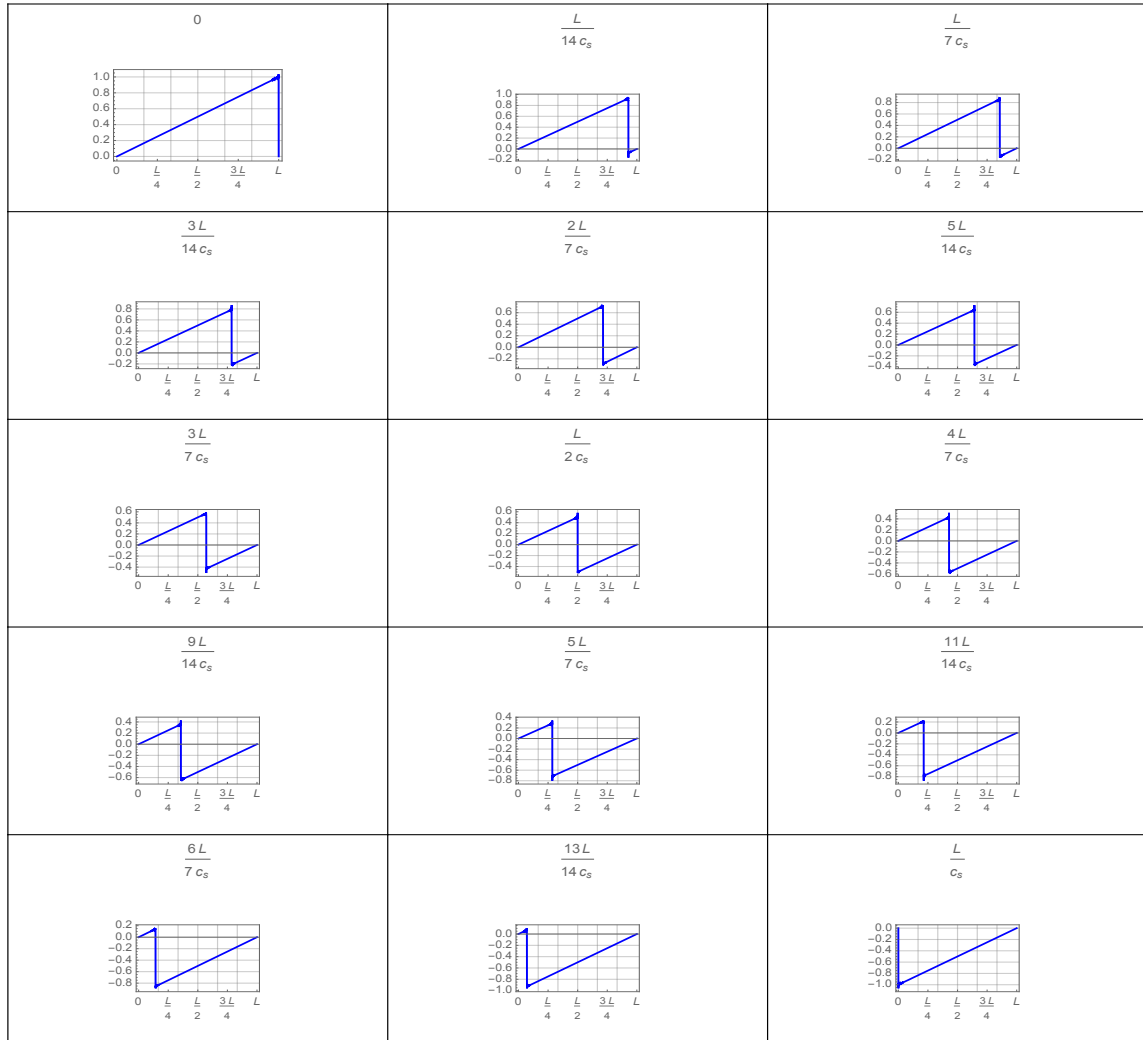
Each plot in this subsection depicts evolution of the displacement acoustic wave u (normalised by $\frac{\Gamma Q_0}{\rho_0 V_0 c_s^2}$ [m]) in time t [s] and at different points in the thin rod. The label at the top of each plot represents the point in the thin rod, where L is the length of the rod and c_s is the speed of sound in the material (see Table A.1 for parameters).



A.2 Dirichlet BC with Linear Energy Distribution

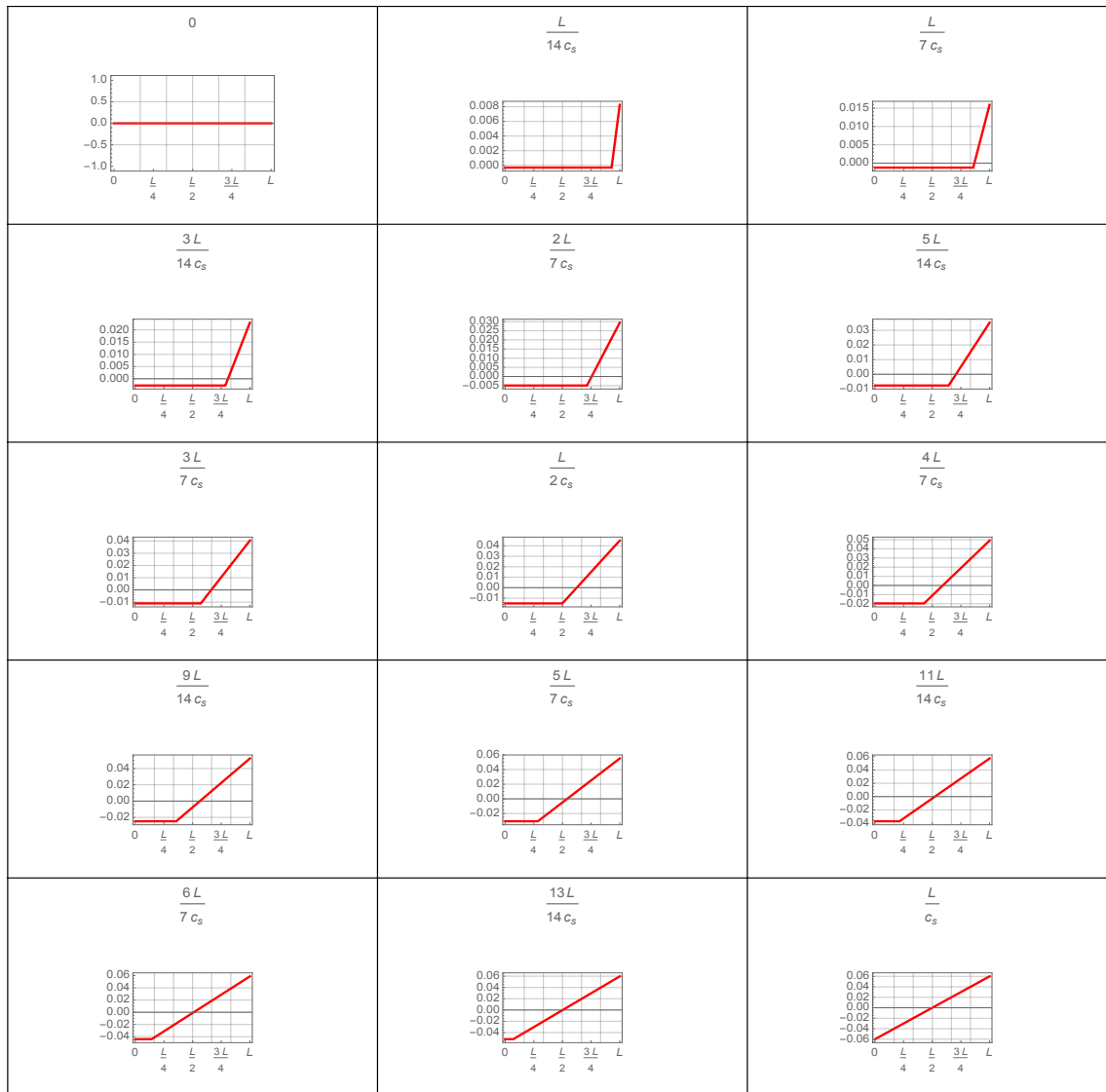
A.2.1 P (Pa) versus z (m) for different t (s)

Each plot in this subsection depicts variation of the pressure acoustic wave P (normalised by $\Gamma \frac{Q_0}{V_0}$ [Pa]) along the thin rod (z [m]) and at different time shots (t [s]). The label at the top of each plot represents the time shot, where L is the length of the rod and c_s is the speed of sound in the material (see Table A.1 for parameters).



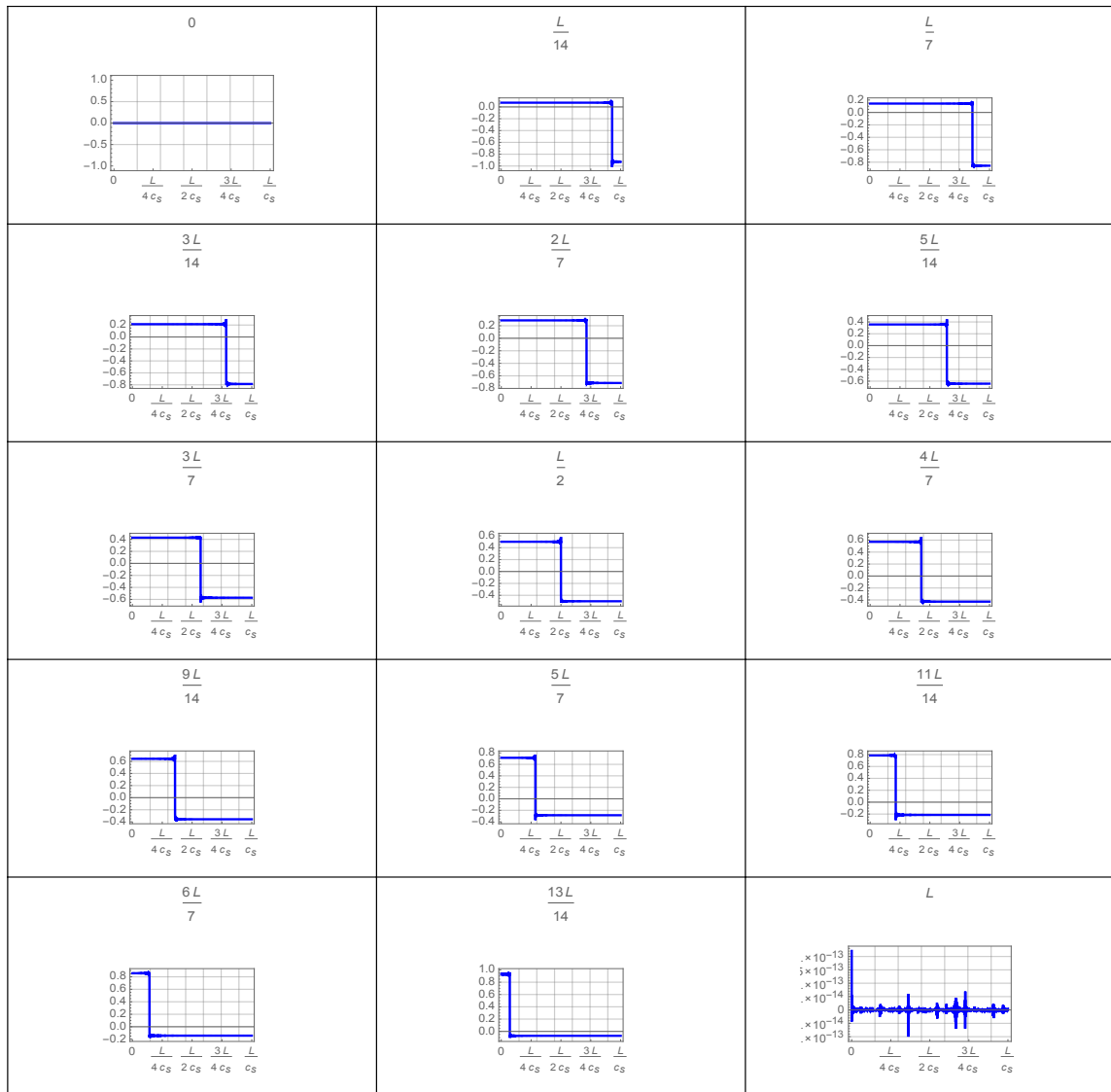
A.2.2 u (m) versus z (m) for different t (s)

Each plot in this subsection depicts variation of the displacement acoustic wave u (normalised by $\frac{\Gamma Q_0}{\rho_0 V_0 c_s^2}$ [m]) along the thin rod (z [m]) and at different time shots (t [s]). The label at the top of each plot represents the time shot, where L is the length of the rod and c_s is the speed of sound in the material (see Table A.1 for parameters)



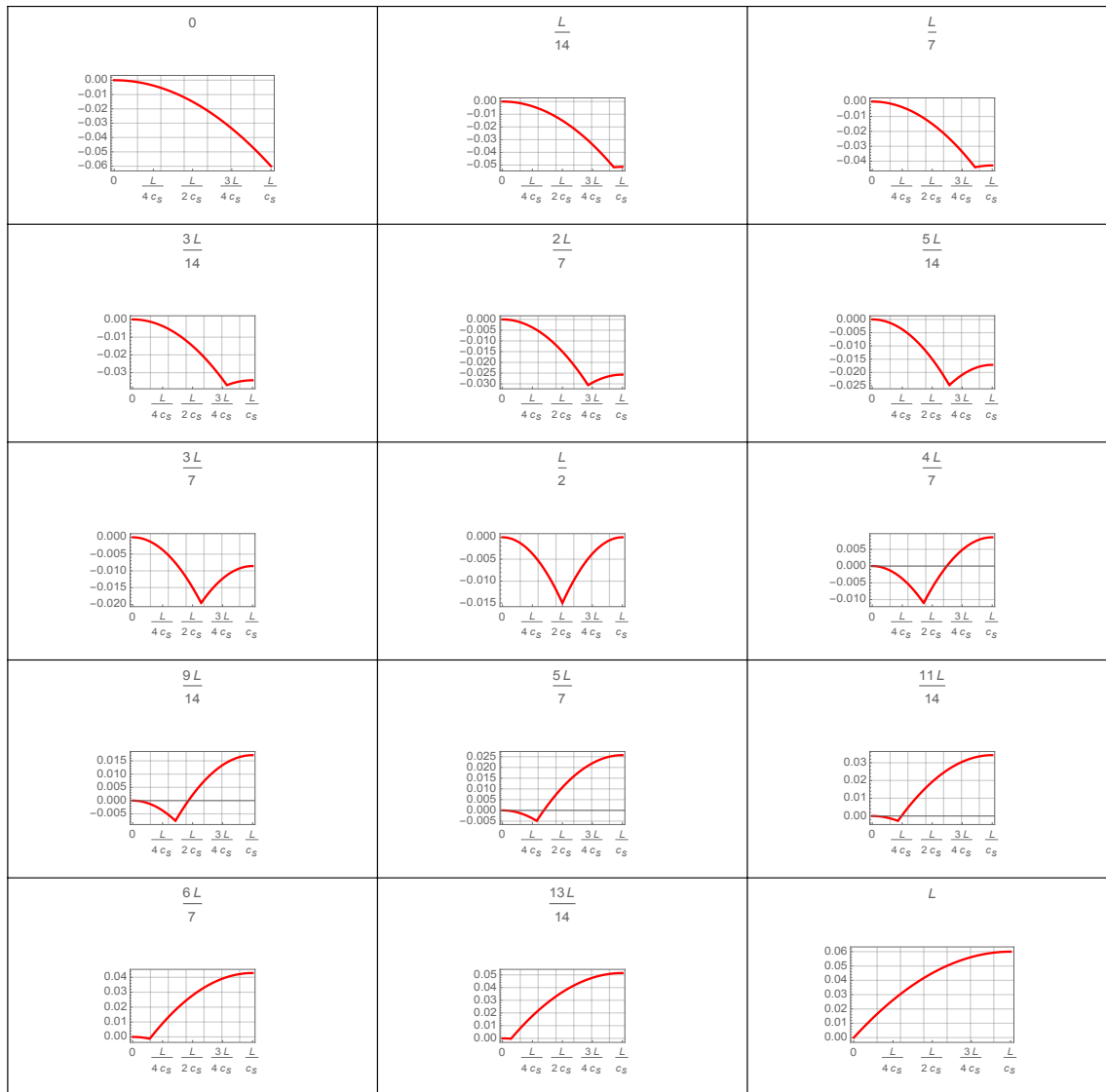
A.2.3 P (Pa) versus t (s) for different z (m)

Each plot in this subsection depicts variation of the pressure acoustic wave P (normalised by $\Gamma \frac{Q_0}{V_0}$ [Pa]) in time t [s] and at different points in the thin rod. The label at the top of each plot represents the point in the thin rod, where L is the length of the rod and c_s is the speed of sound in the material (see Table A.1 for parameters).



A.2.4 u (m) versus t (s) for different z (m)

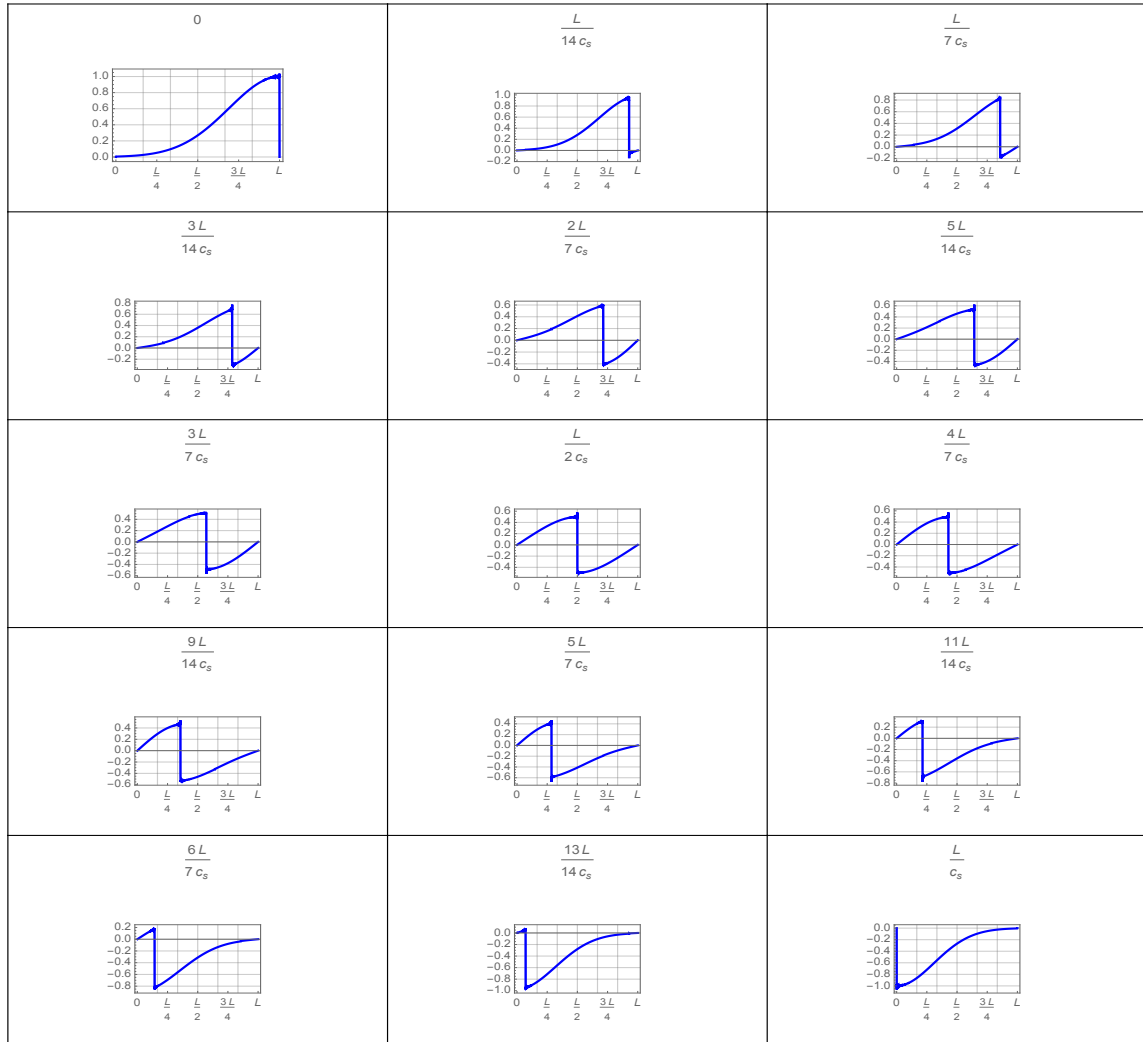
Each plot in this subsection depicts evolution of the displacement acoustic wave u (normalised by $\frac{\Gamma Q_0}{\rho_0 V_0 c_s^2}$ [m]) in time t [s] and at different points in the thin rod. The label at the top of each plot represents the point in the thin rod, where L is the length of the rod and c_s is the speed of sound in the material (see Table A.1 for parameters).



A.3 Dirichlet BC with Normal Energy Distribution

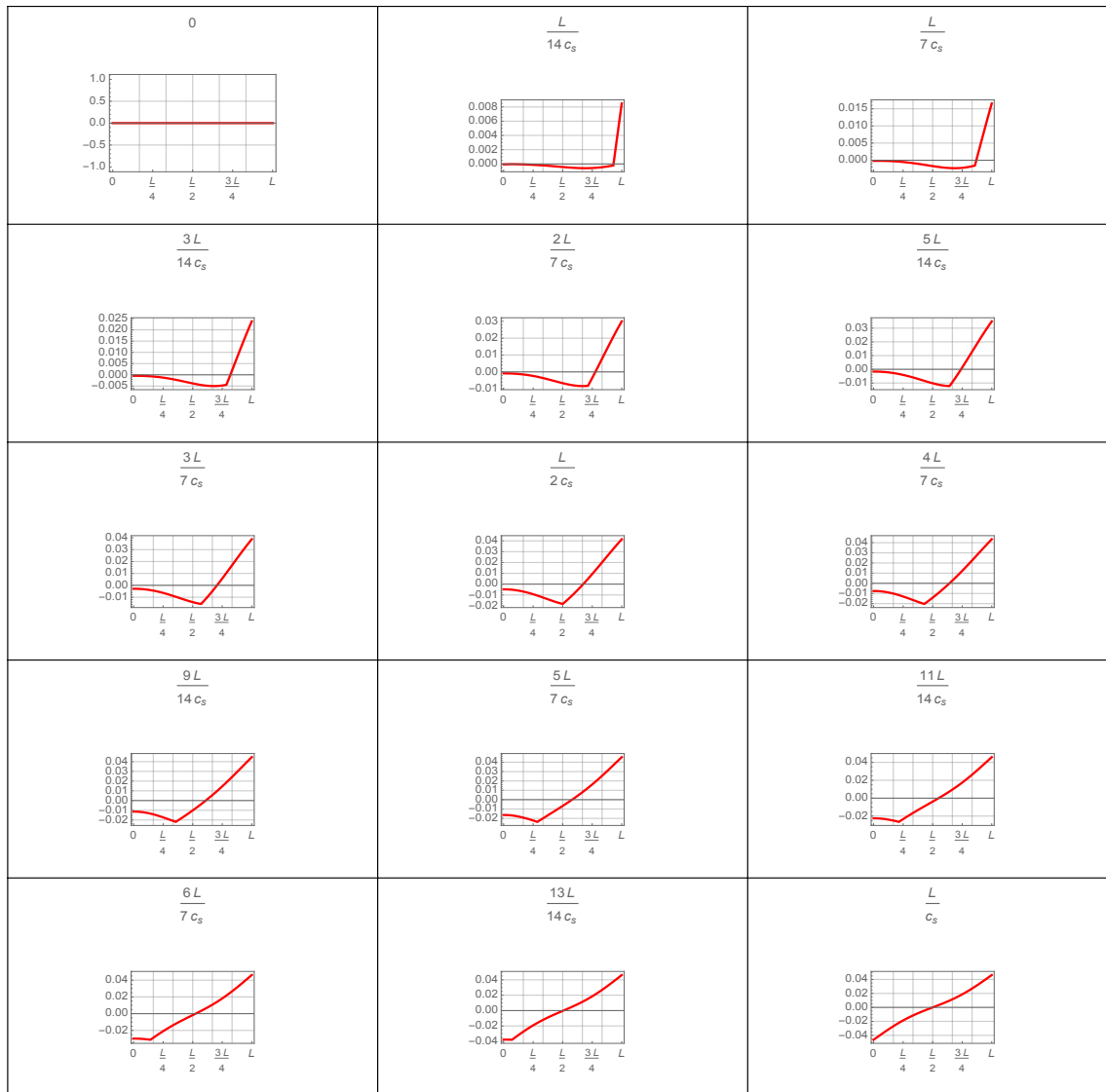
A.3.1 P (Pa) versus z (m) for different t (s)

Each plot in this subsection depicts variation of the pressure acoustic wave P (normalised by $\Gamma \frac{Q_0}{V_0}$ [Pa]) along the thin rod (z [m]) and at different time shots (t [s]). The label at the top of each plot represents the time shot, where L is the length of the rod and c_s is the speed of sound in the material (see Table A.1 for parameters).



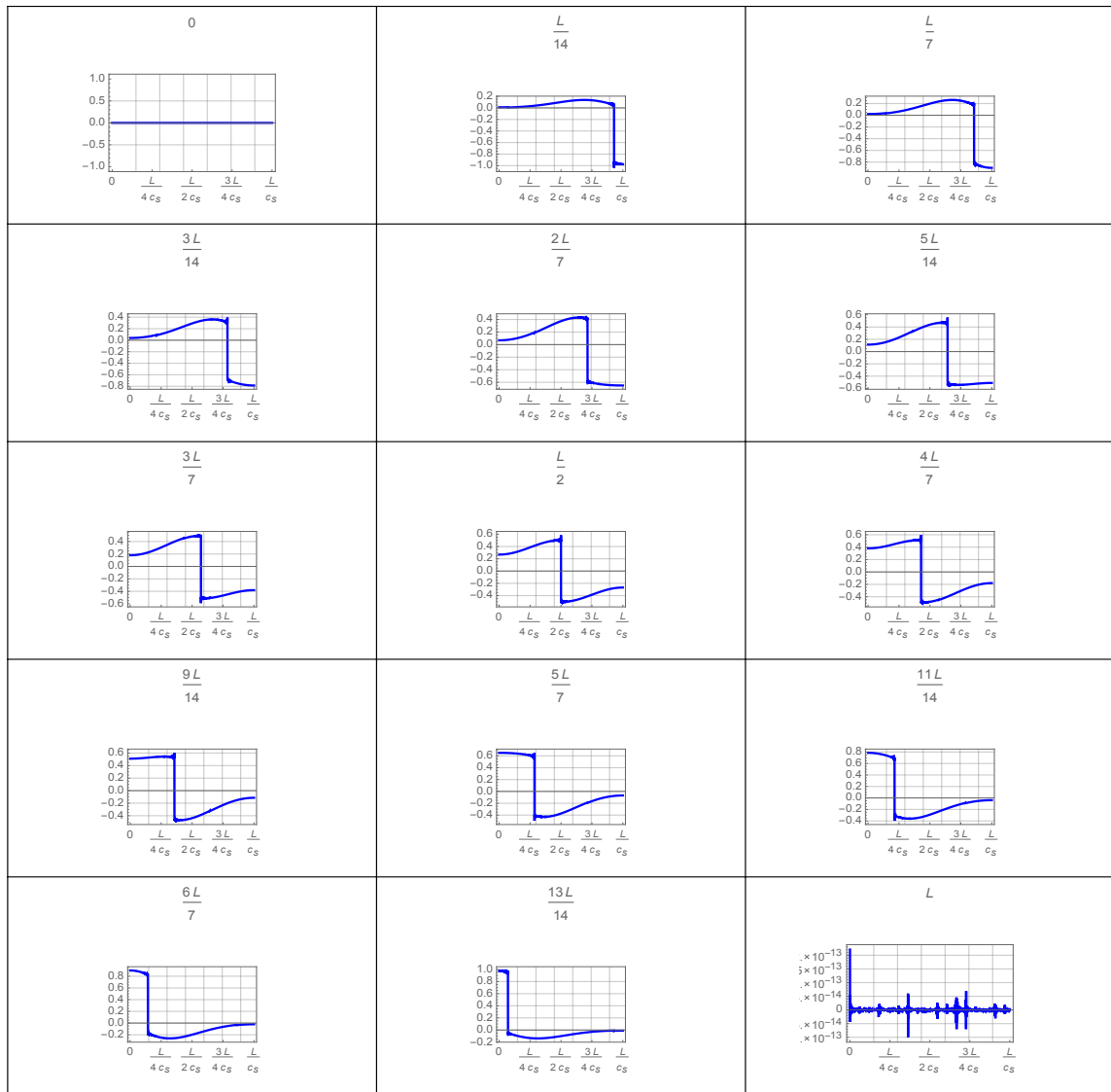
A.3.2 u (m) versus z (m) for different t (s)

Each plot in this subsection depicts variation of the displacement acoustic wave u (normalised by $\frac{\Gamma Q_0}{\rho_0 V_0 c_s^2}$ [m]) along the thin rod (z [m]) and at different time shots (t [s]). The label at the top of each plot represents the time shot, where L is the length of the rod and c_s is the speed of sound in the material (see Table A.1 for parameters).



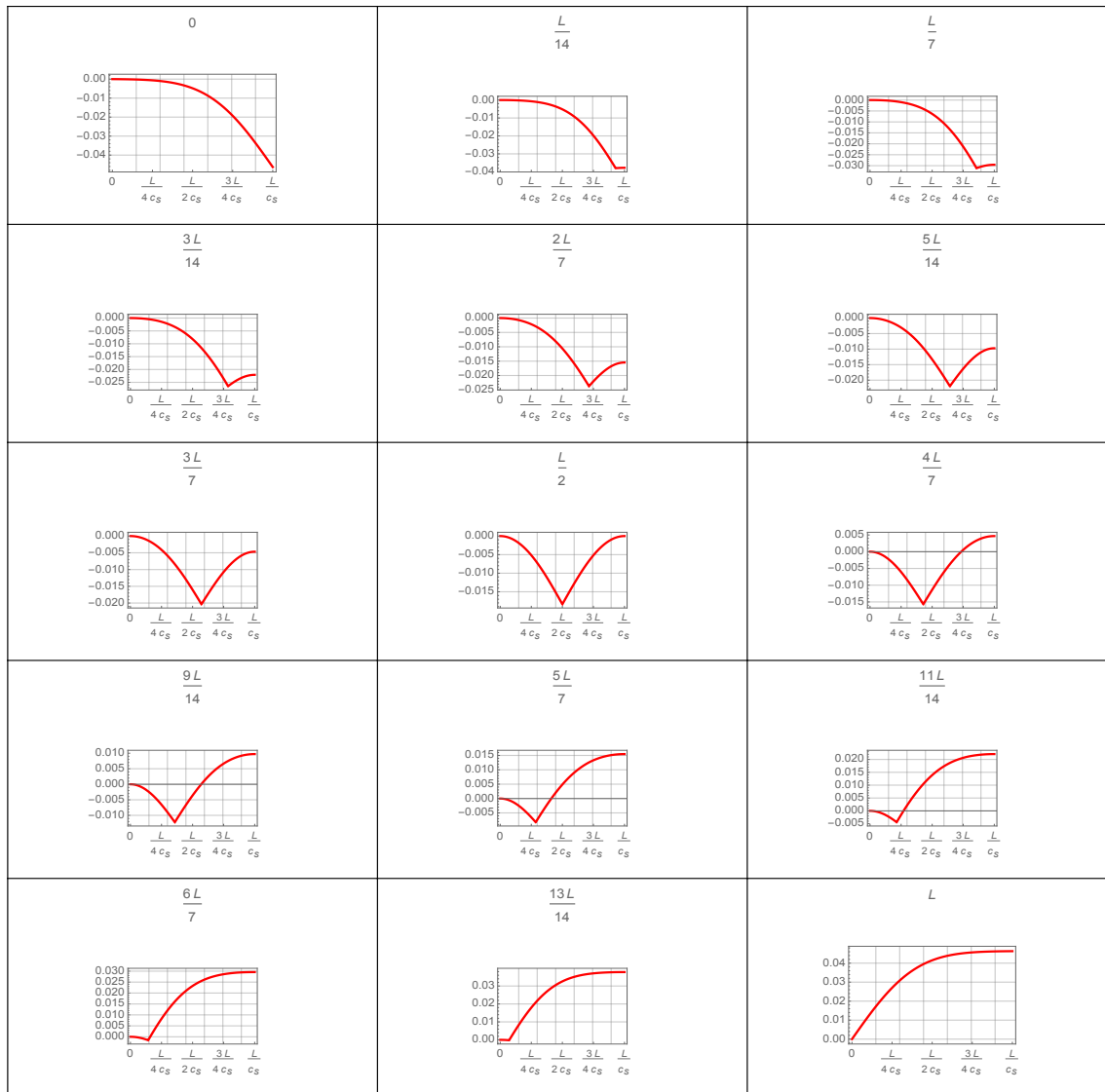
A.3.3 P (Pa) versus t (s) for different z (m)

Each plot in this subsection depicts variation of the pressure acoustic wave P (normalised by $\Gamma \frac{Q_0}{V_0}$ [Pa]) in time t [s] and at different points in the thin rod. The label at the top of each plot represents the point in the thin rod, where L is the length of the rod and c_s is the speed of sound in the material (see Table A.1 for parameters).



A.3.4 u (m) versus t (s) for different z (m)

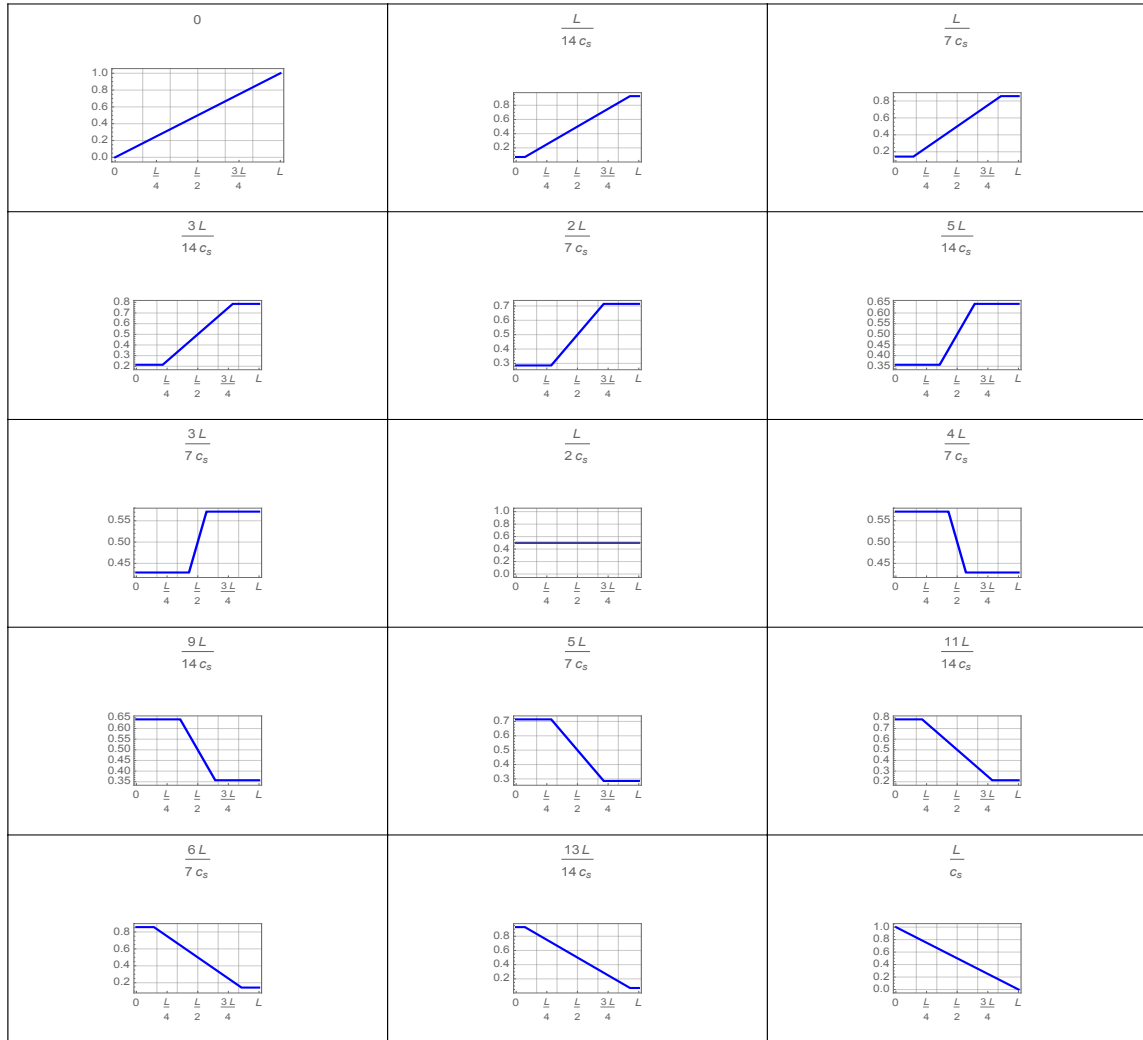
Each plot in this subsection depicts evolution of the displacement acoustic wave u (normalised by $\frac{\Gamma Q_0}{\rho_0 V_0 c_s^2}$ [m]) in time t [s] and at different points in the thin rod. The label at the top of each plot represents the point in the thin rod, where L is the length of the rod and c_s is the speed of sound in the material (see Table A.1 for parameters).



A.4 Neumann BC with Linear Energy Distribution

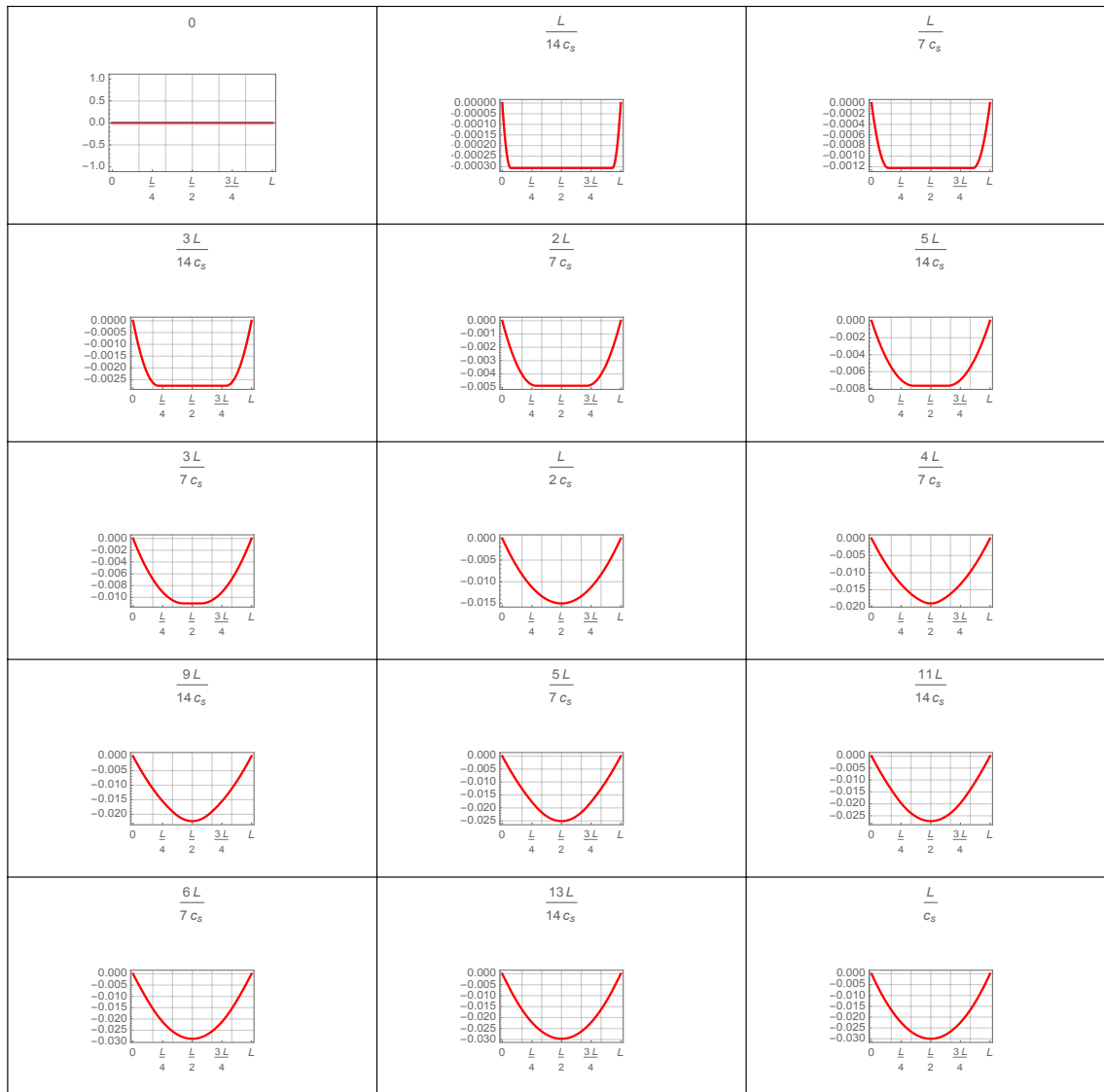
A.4.1 P (Pa) versus z (m) for different t (s)

Each plot in this subsection depicts variation of the pressure acoustic wave P (normalised by $\Gamma \frac{Q_0}{V_0}$ [Pa]) along the thin rod (z [m]) and at different time shots (t [s]). The label at the top of each plot represents the time shot, where L is the length of the rod and c_s is the speed of sound in the material (see Table A.1 for parameters).



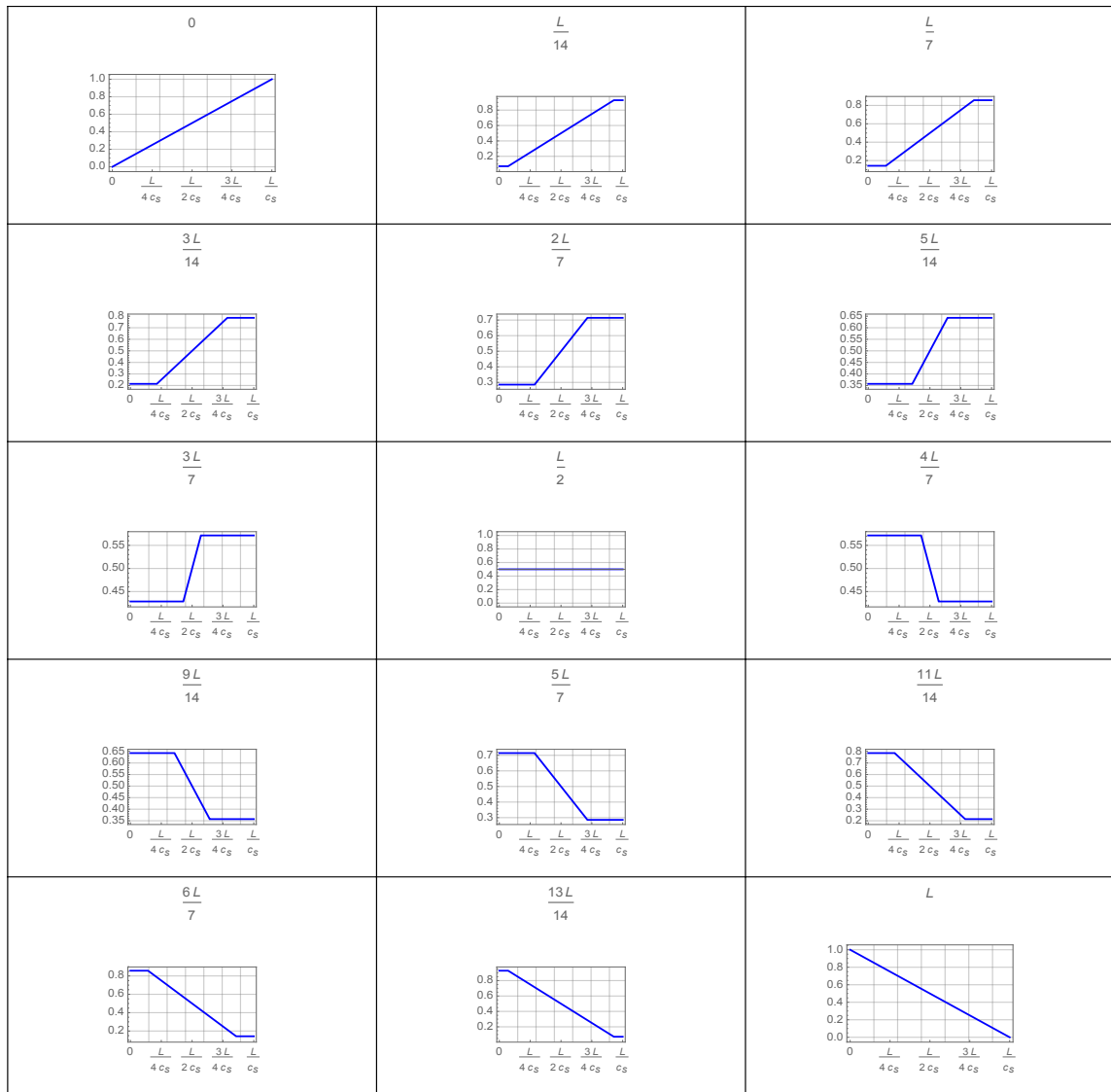
A.4.2 u (m) versus z (m) for different t (s)

Each plot in this subsection depicts variation of the displacement acoustic wave u (normalised by $\frac{\Gamma Q_0}{\rho_0 V_0 c_s^2}$ [m]) along the thin rod (z [m]) and at different time shots (t [s]). The label at the top of each plot represents the time shot, where L is the length of the rod and c_s is the speed of sound in the material (see Table A.1 for parameters).



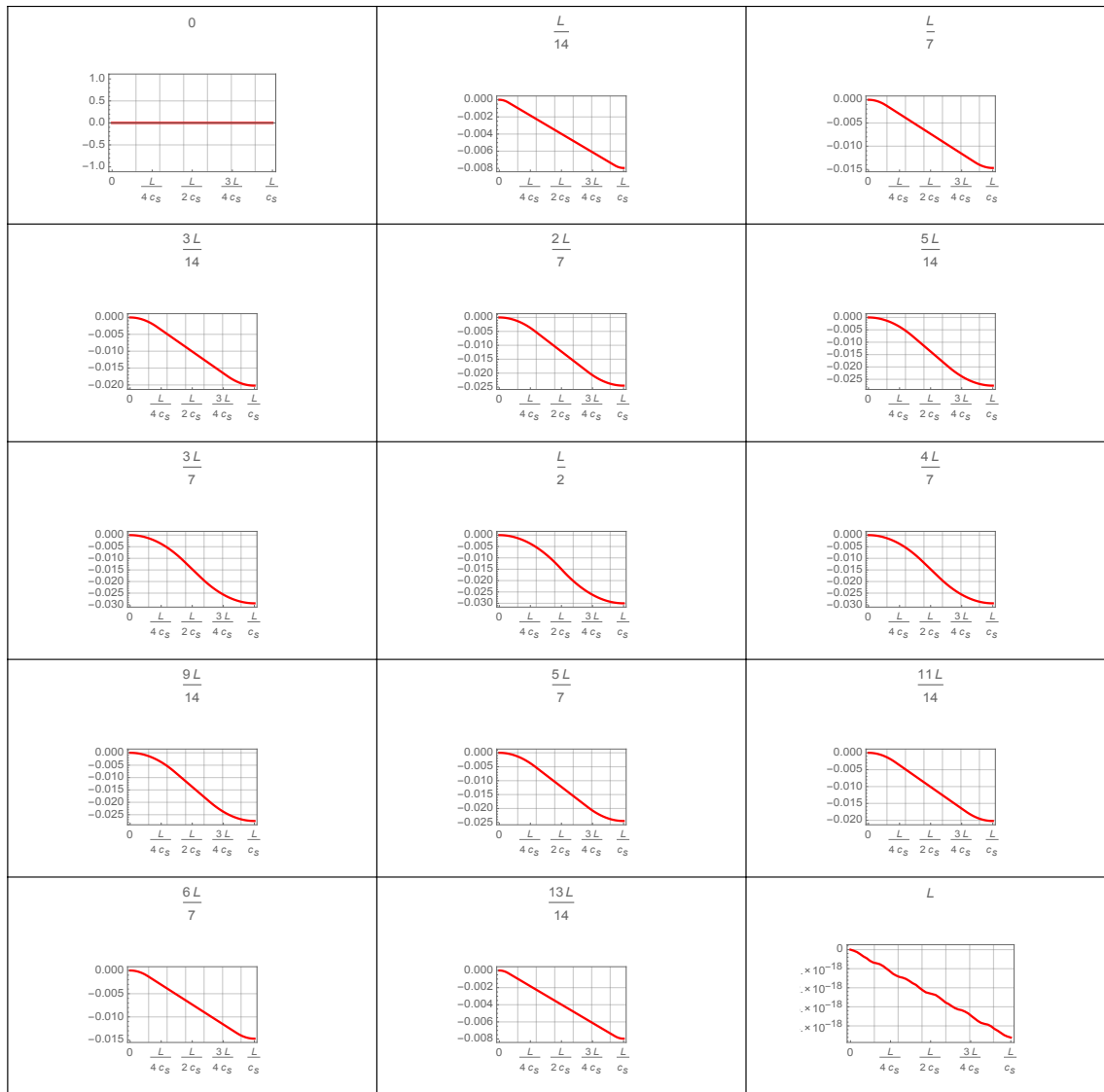
A.4.3 P (Pa) versus t (s) for different z (m)

Each plot in this subsection depicts variation of the pressure acoustic wave P (normalised by $\Gamma \frac{Q_0}{V_0}$ [Pa]) in time t [s] and at different points in the thin rod. The label at the top of each plot represents the point in the thin rod, where L is the length of the rod and c_s is the speed of sound in the material (see Table A.1 for parameters).



A.4.4 u (m) versus t (s) for different z (m)

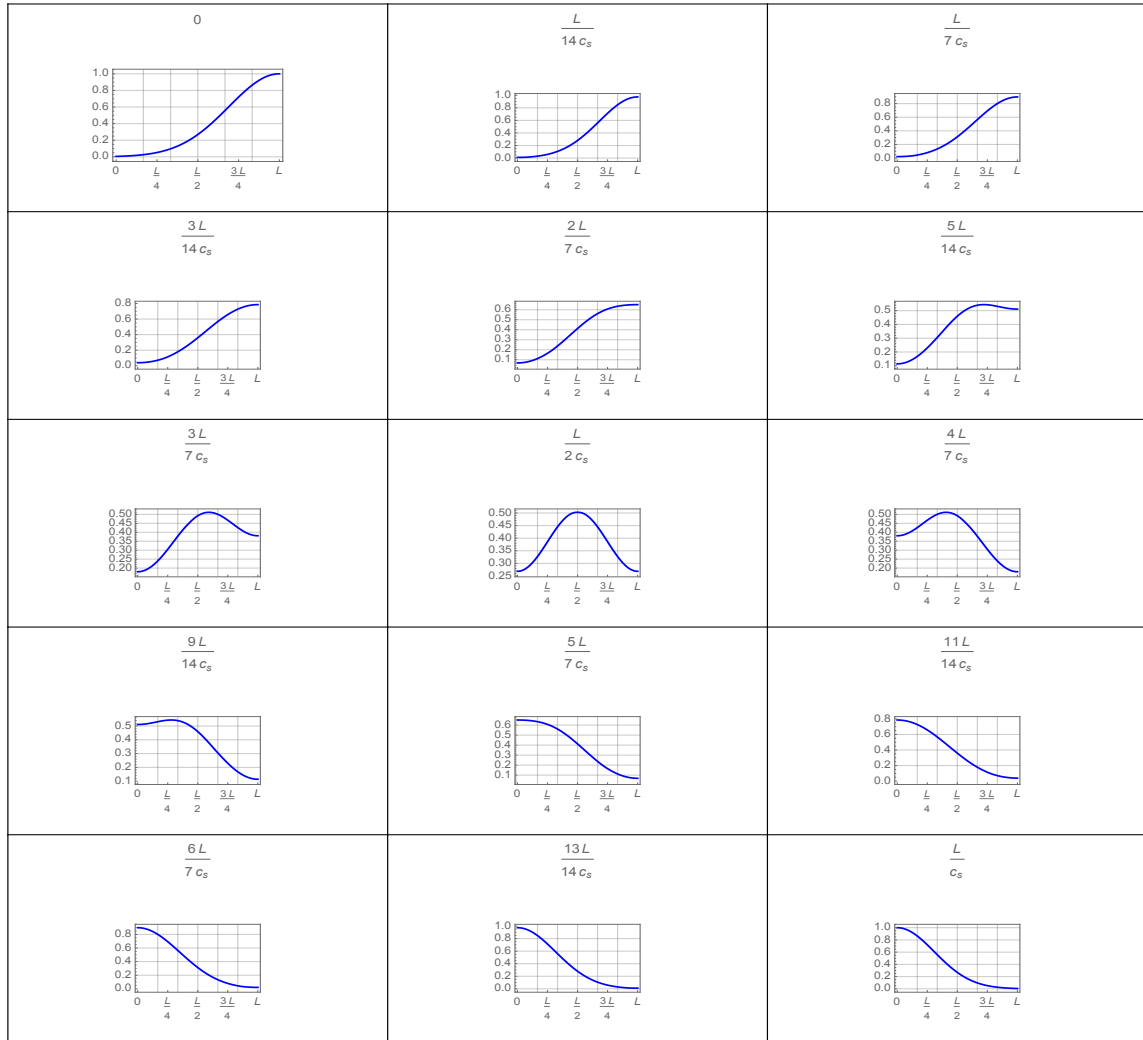
Each plot in this subsection depicts evolution of the displacement acoustic wave u (normalised by $\frac{\Gamma Q_0}{\rho_0 V_0 c_s^2}$ [m]) in time t [s] and at different points in the thin rod. The label at the top of each plot represents the point in the thin rod, where L is the length of the rod and c_s is the speed of sound in the material (see Table A.1 for parameters).



A.5 Neumann BC with Normal Energy Distribution

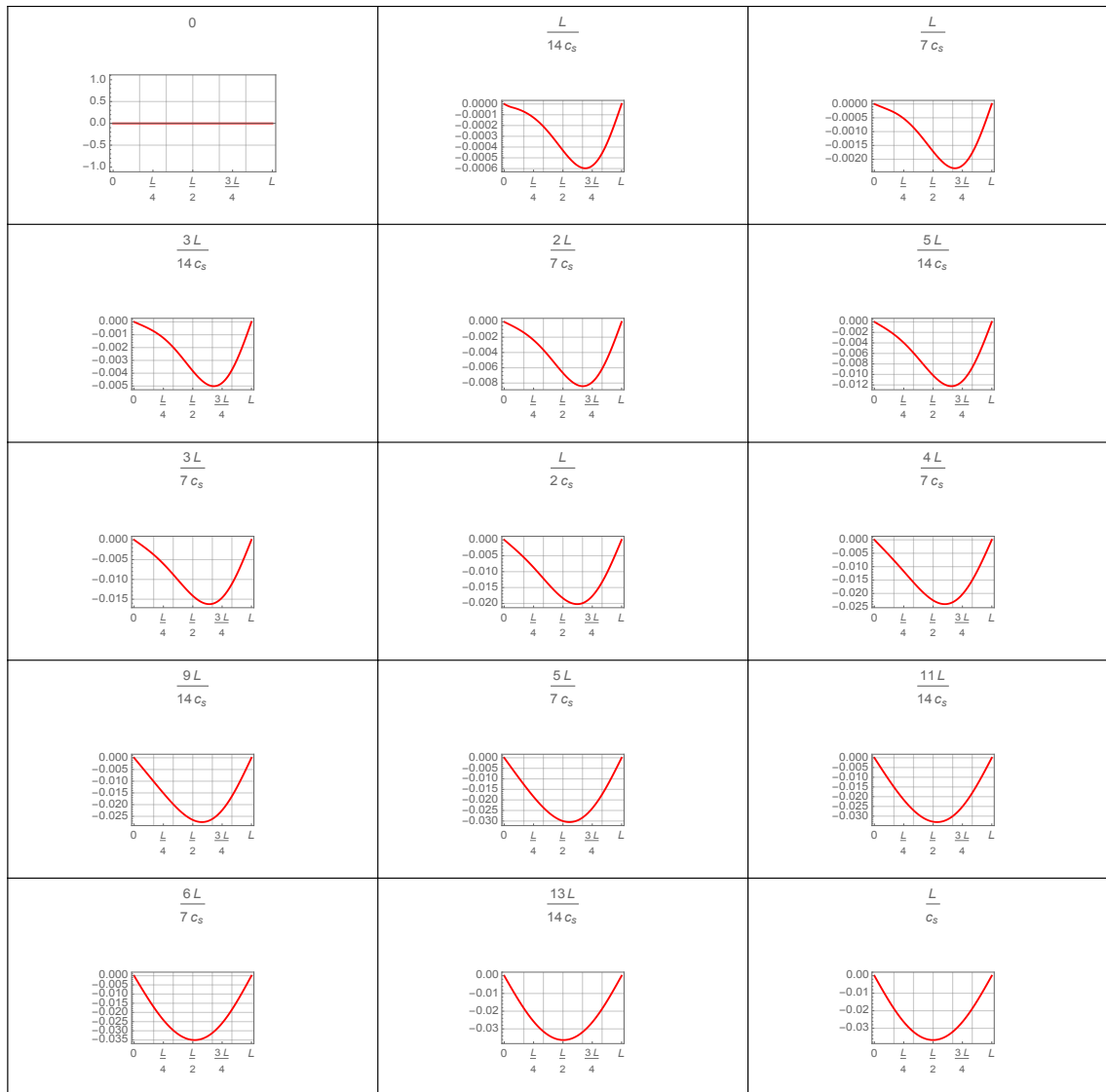
A.5.1 P (Pa) versus z (m) for different t (s)

Each plot in this subsection depicts variation of the pressure acoustic wave P (normalised by $\Gamma \frac{Q_0}{V_0}$ [Pa]) along the thin rod (z [m]) and at different time shots (t [s]). The label at the top of each plot represents the time shot, where L is the length of the rod and c_s is the speed of sound in the material (see Table A.1 for parameters).



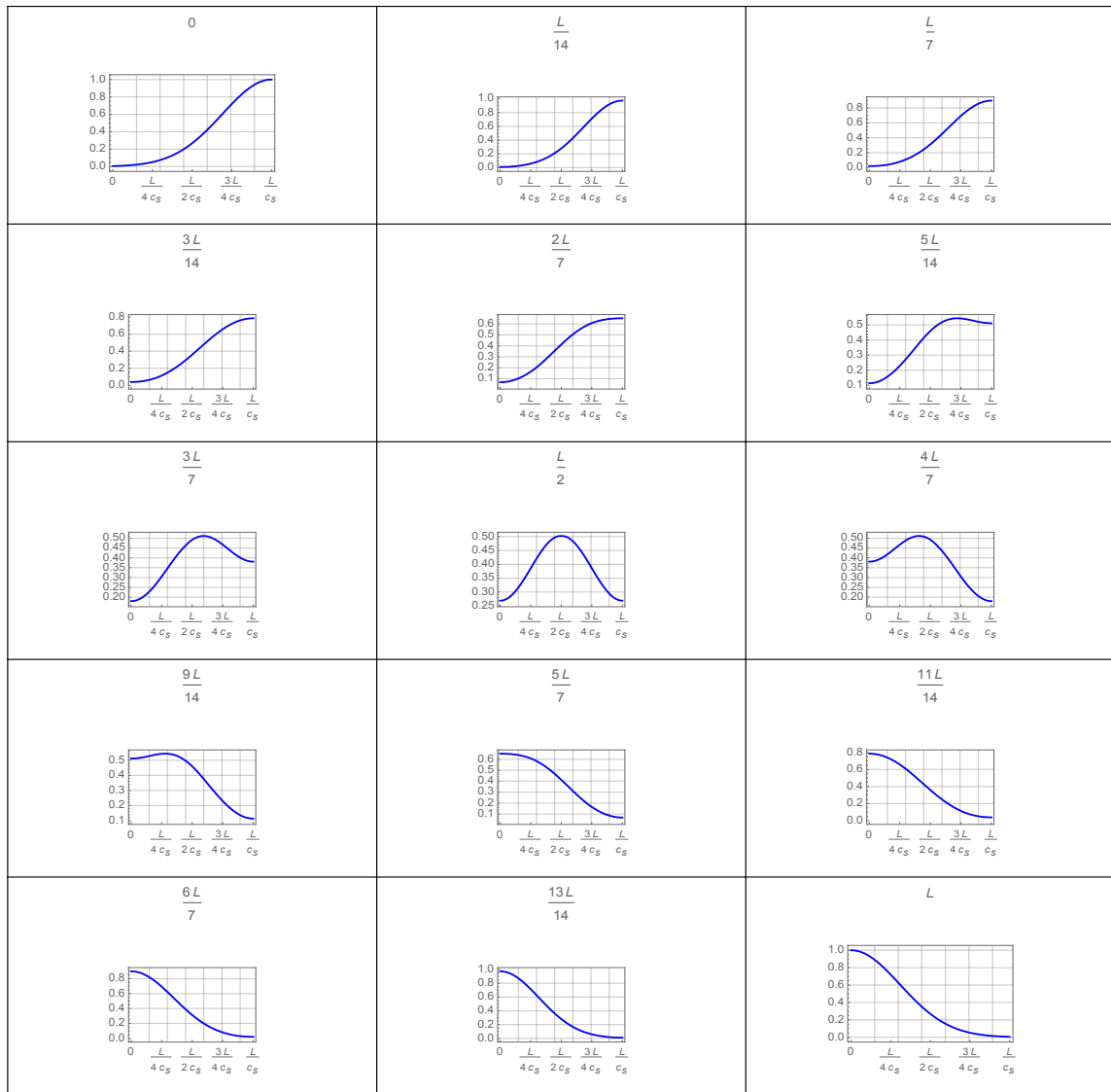
A.5.2 u (m) versus z (m) for different t (s)

Each plot in this subsection depicts variation of the displacement acoustic wave u (normalised by $\frac{\Gamma Q_0}{\rho_0 V_0 c_s^2}$ [m]) along the thin rod (z [m]) and at different time shots (t [s]). The label at the top of each plot represents the time shot, where L is the length of the rod and c_s is the speed of sound in the material (see Table A.1 for parameters).



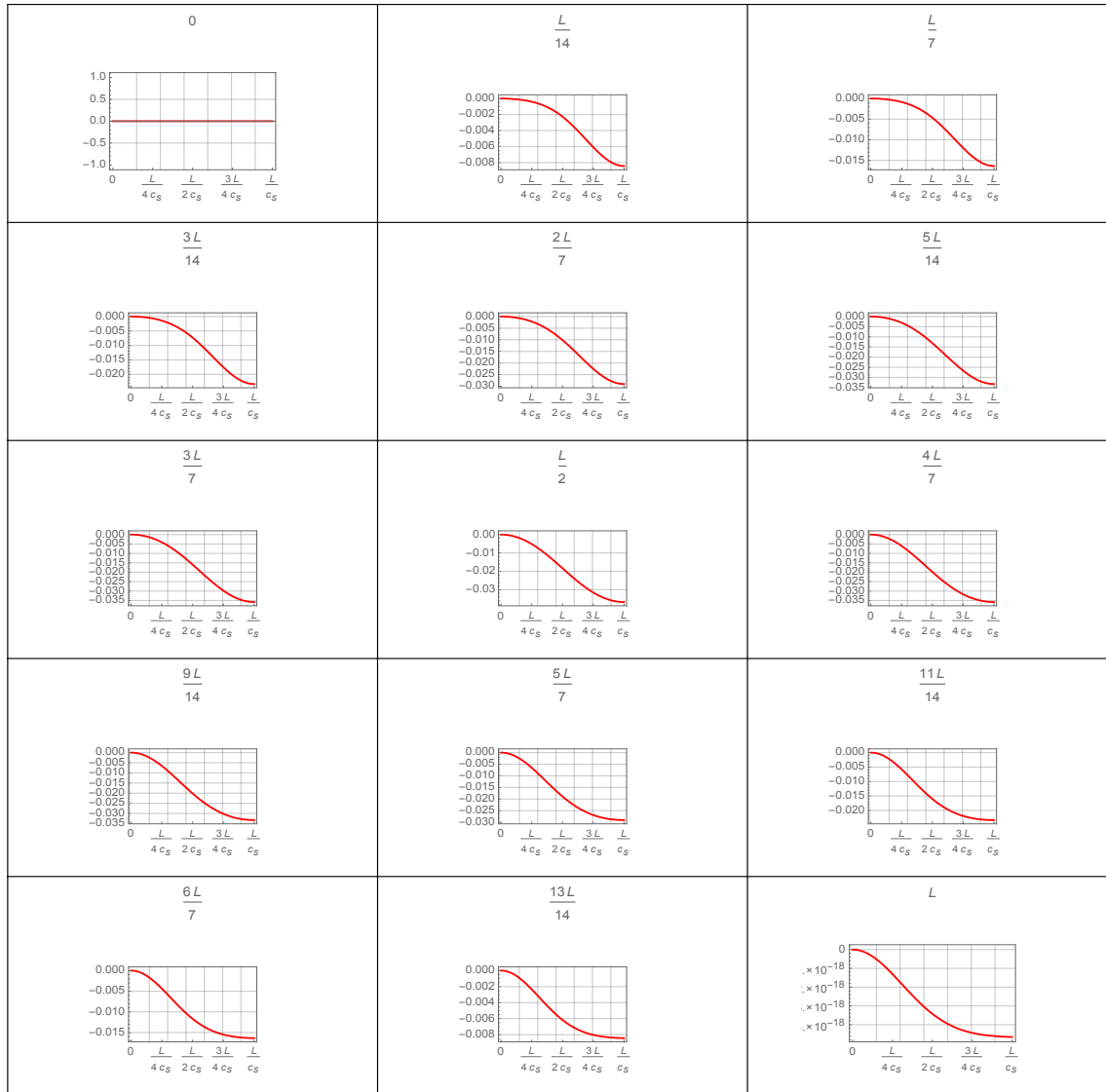
A.5.3 P (Pa) versus t (s) for different z (m)

Each plot in this subsection depicts variation of the pressure acoustic wave P (normalised by $\Gamma \frac{Q_0}{V_0}$ [Pa]) in time t [s] and at different points in the thin rod. The label at the top of each plot represents the point in the thin rod, where L is the length of the rod and c_s is the speed of sound in the material (see Table A.1 for parameters).



A.5.4 u (m) versus t (s) for different z (m)

Each plot in this subsection depicts evolution of the displacement acoustic wave u (normalised by $\frac{\Gamma Q_0}{\rho_0 V_0 c_s^2}$ [m]) in time t [s] and at different points in the thin rod. The label at the top of each plot represents the point in the thin rod, where L is the length of the rod and c_s is the speed of sound in the material (see Table A.1 for parameters).



Appendix B

Results of LAW in a Disc

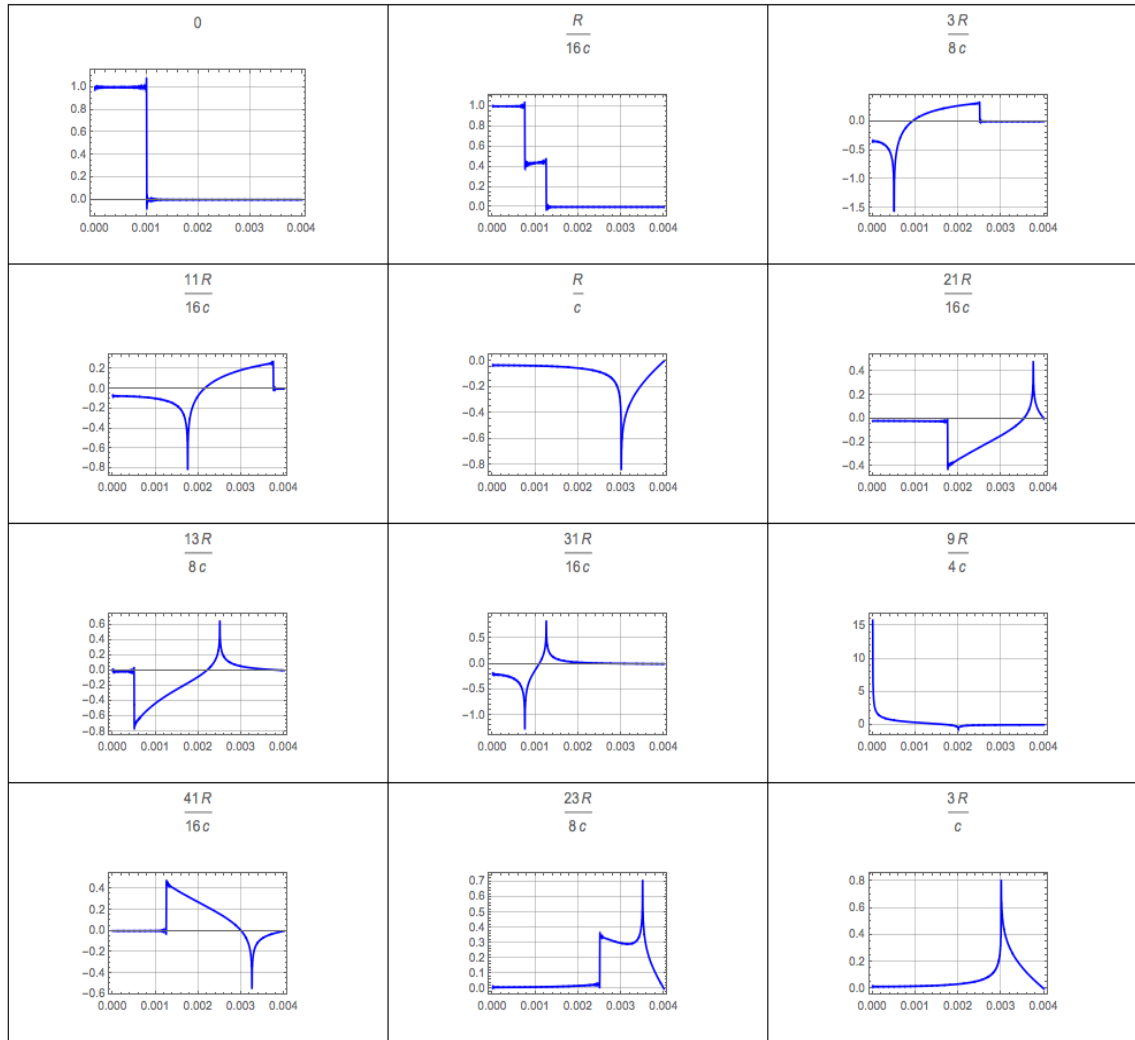
Table B.1: Typical Case Analysis: Copper Target Material Parameters (same as Table 4.1)

Parameters	Symbol	Unit	Value
Radius	R	m	0.004
Spot size	r_0	m	0.001
Speed of sound	c_s	m/s	3570

B.1 Dirichlet BC with Uniform Energy Distribution

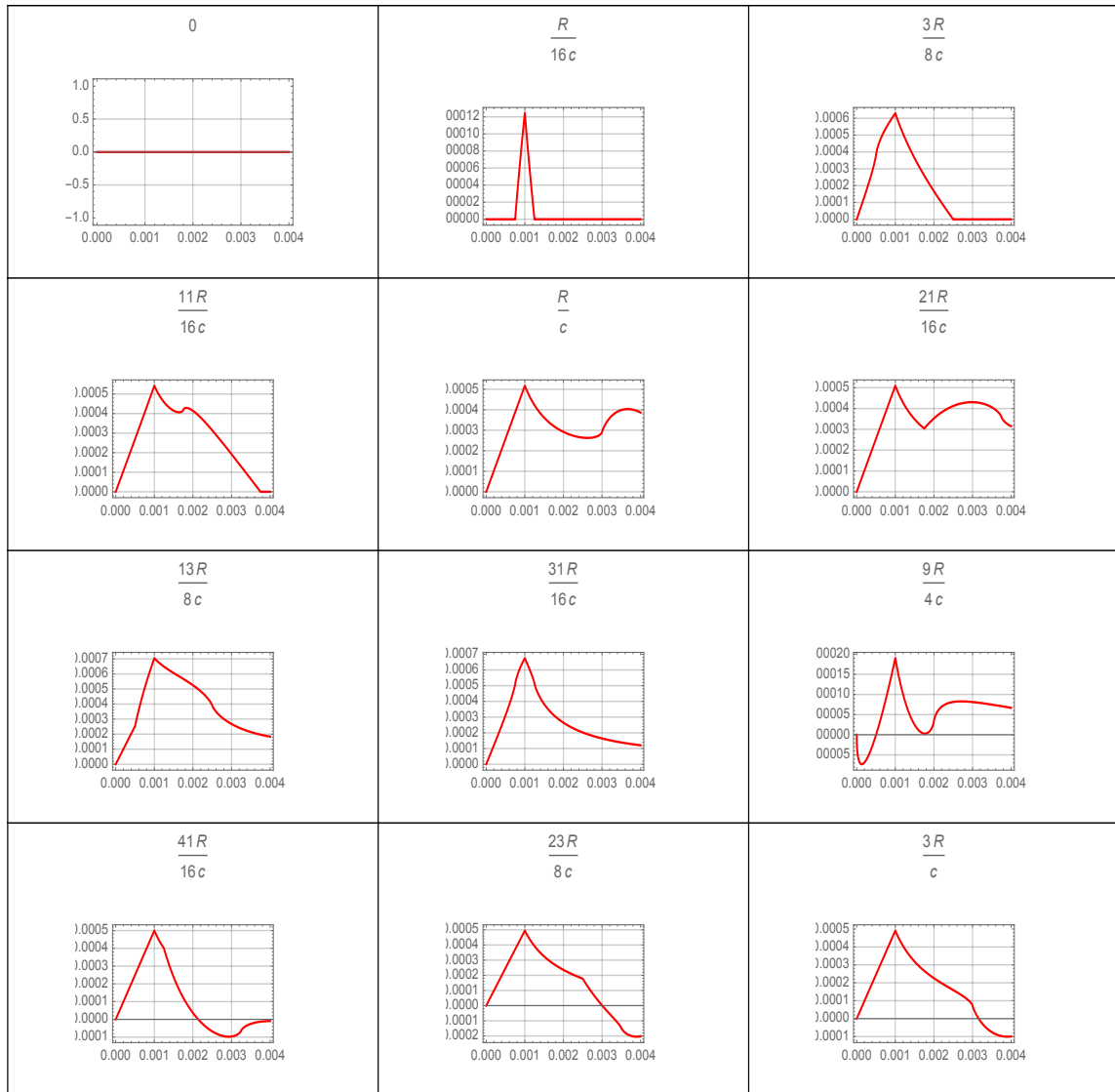
B.1.1 P (Pa) versus r (m) for different t (s)

Each plot in this subsection depicts variation of the pressure acoustic wave P (normalised by $\Gamma \frac{Q_0}{V_0}$ [Pa]) along the radius of the disc r [m] and at different time shots (t [s]). The label at the top of each plot represents the time shot, where R is the radius of the disc and c is the speed of sound in the material (see Table B.1 for parameters).



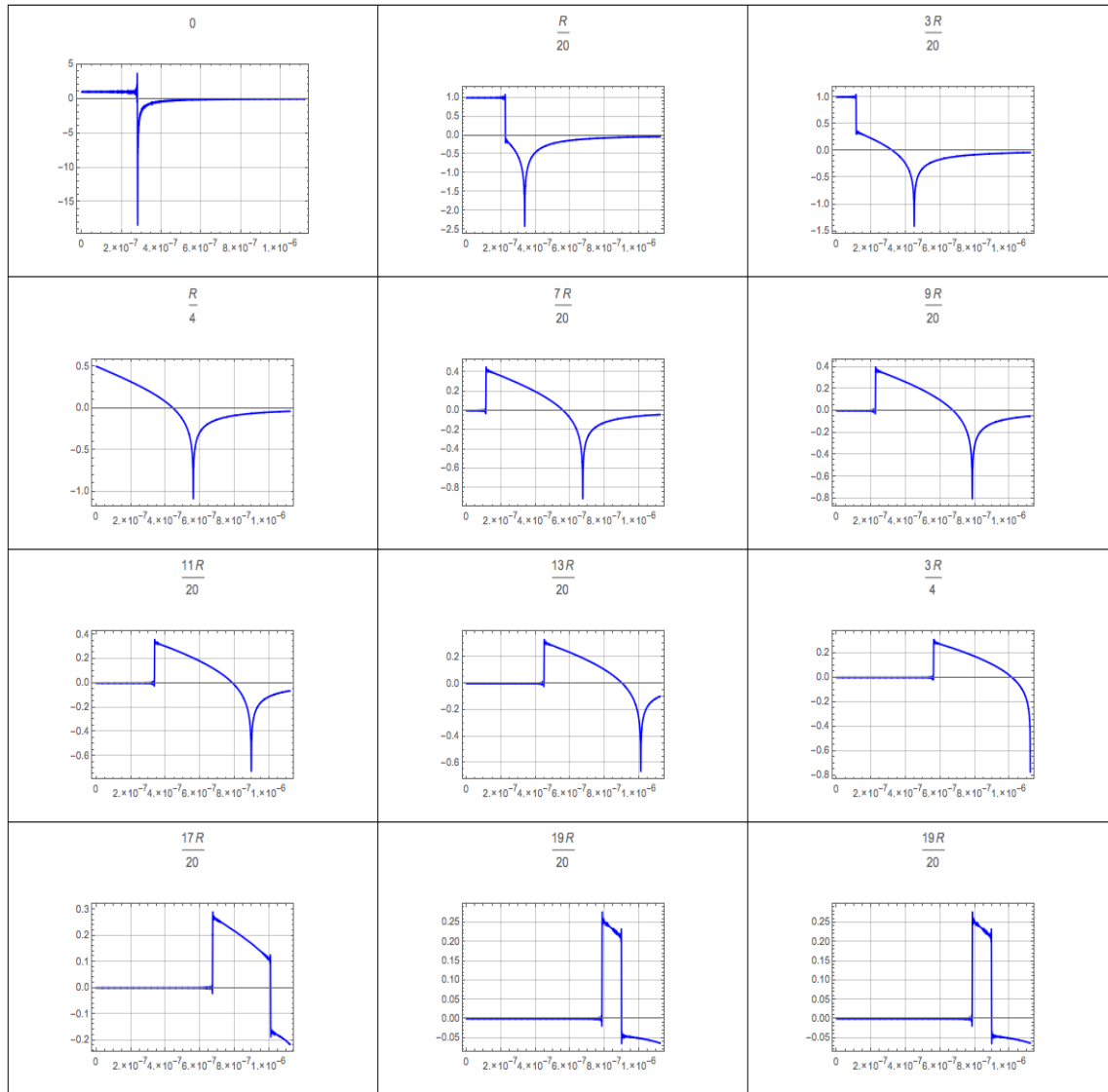
B.1.2 u (m) versus r (m) for different t (s)

Each plot in this subsection depicts variation of the displacement acoustic wave u (normalised by $\frac{\Gamma Q_0}{\rho_0 V_0 c_s^2}$ [m]) along the radius of the disc r [m] and at different time shots (t [s]). The label at the top of each plot represents the time shot, where R is the radius of the disc and c is the speed of sound in the material (see Table B.1 for parameters).



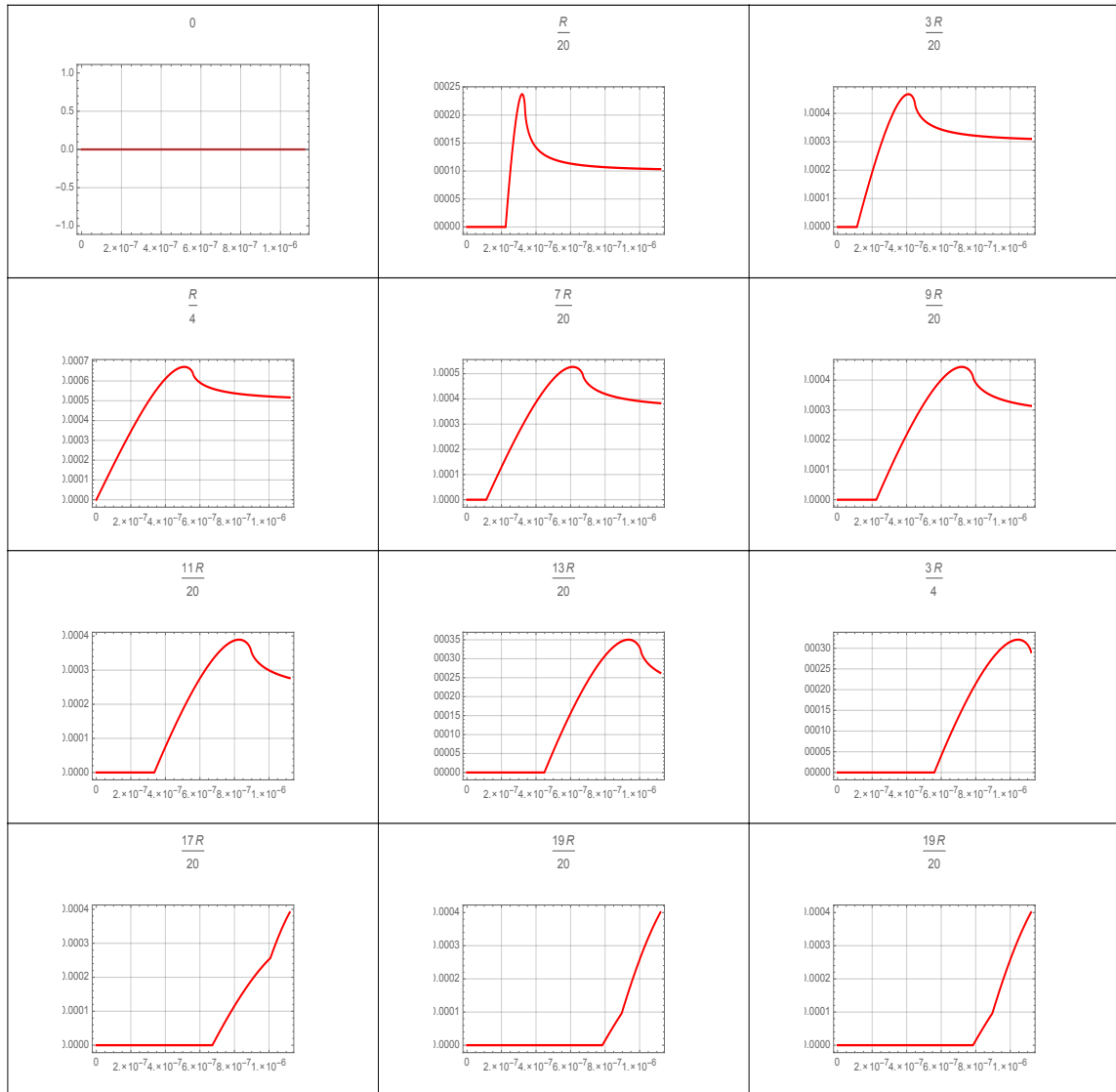
B.1.3 P (Pa) versus t (s) for different r (m)

Each plot in this subsection depicts evolution of the pressure acoustic wave P (normalised by $\Gamma \frac{Q_0}{V_0}$ [Pa]) in time t [s] and at different radial points in the disc (r [m]). The label at the top of each plot represents the point in the disc, where R is the radius of the disc (see Table B.1 for parameters).



B.1.4 u (m) versus t (s) for different r (m)

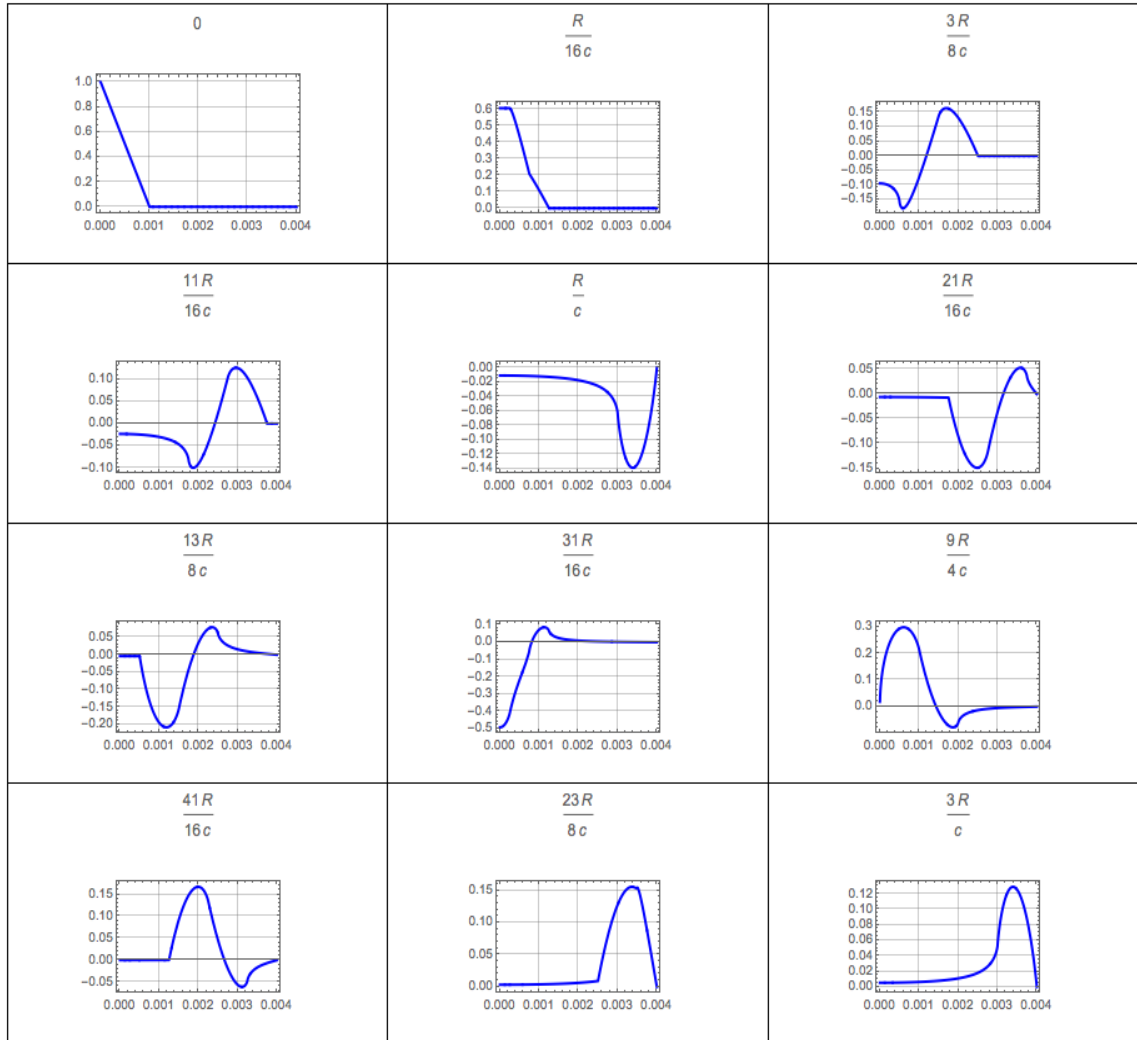
Each plot in this subsection depicts evolution of the displacement acoustic wave u (normalised by $\frac{\Gamma Q_0}{\rho_0 V_0 c_s^2}$ [Pa]) in time t [s] and at different radial points in the disc (r [m]). The label at the top of each plot represents the point in the disc, where R is the radius of the disc (see Table B.1 for parameters).



B.2 Dirichlet BC with Linear Energy Distribution

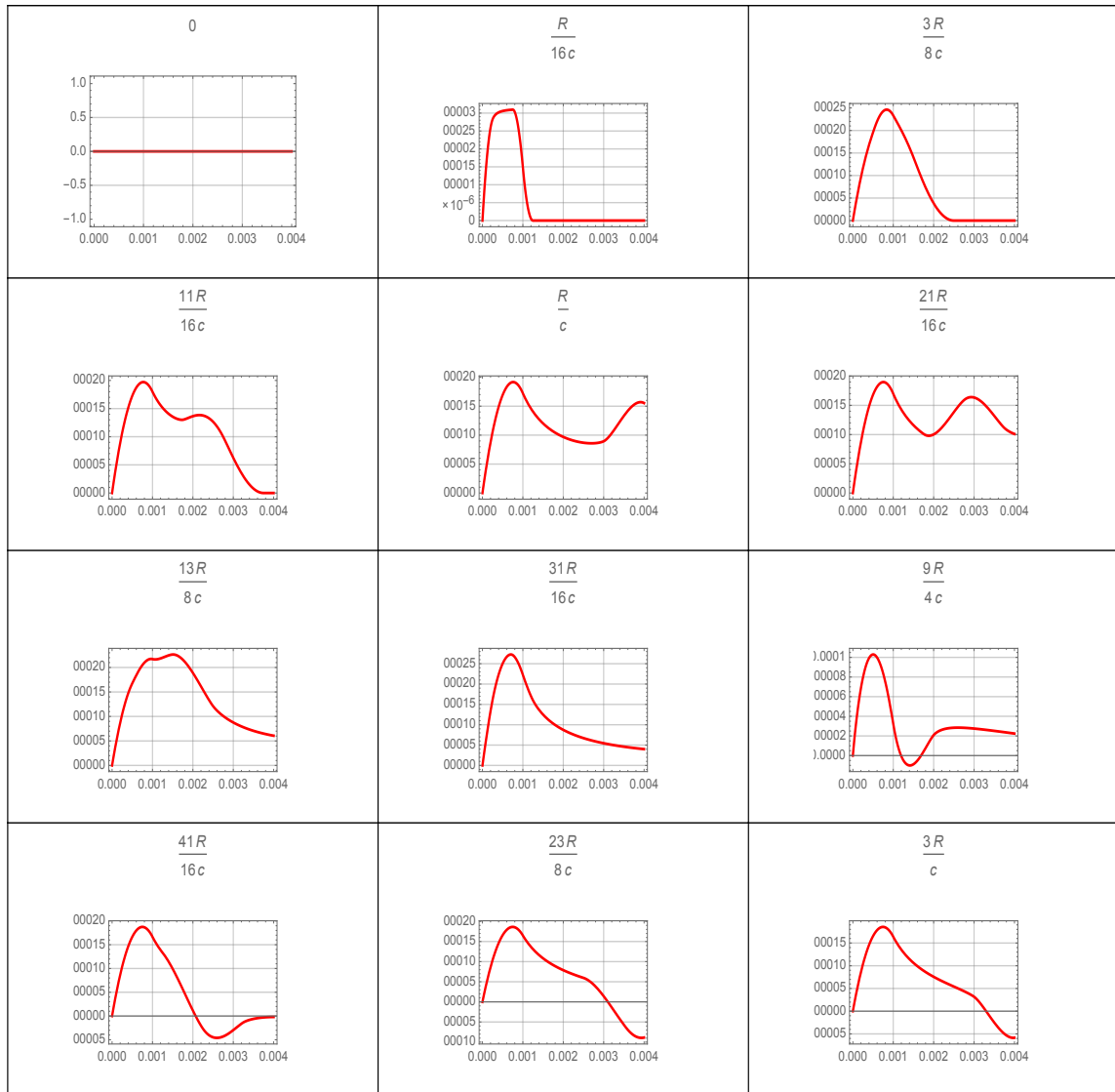
B.2.1 P (Pa) versus r (m) for different t (s)

Each plot in this subsection depicts variation of the pressure acoustic wave P (normalised by $\Gamma \frac{Q_0}{V_0}$ [Pa]) along the radius of the disc r [m] and at different time shots (t [s]). The label at the top of each plot represents the time shot, where R is the radius of the disc and c is the speed of sound in the material (see Table B.1 for parameters).



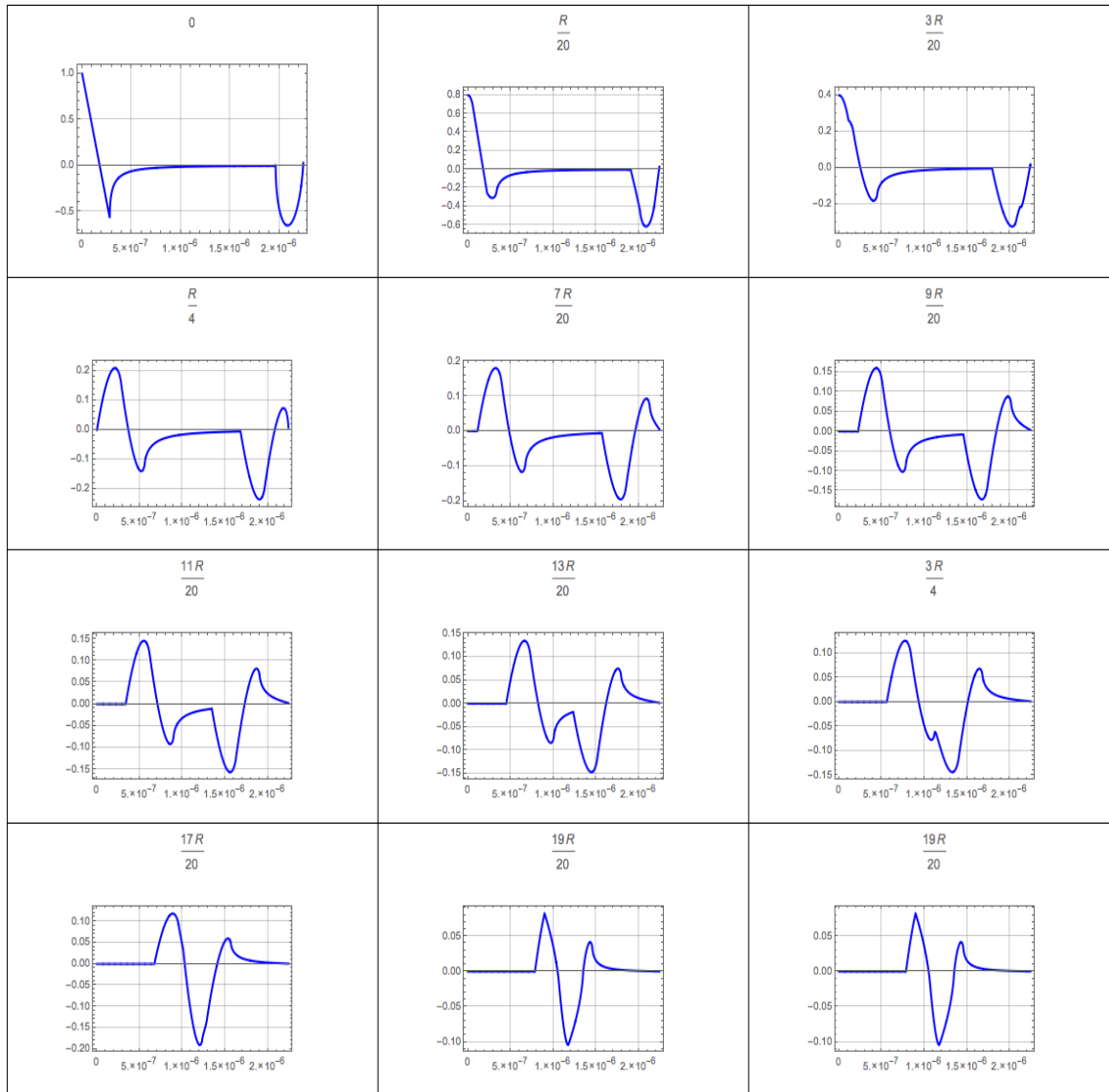
B.2.2 u (m) versus r (m) for different t (s)

Each plot in this subsection depicts variation of the displacement acoustic wave u (normalised by $\frac{\Gamma Q_0}{\rho_0 V_0 c_s^2}$ [m]) along the radius of the disc r [m] and at different time shots (t [s]). The label at the top of each plot represents the time shot, where R is the radius of the disc and c is the speed of sound in the material (see Table B.1 for parameters).



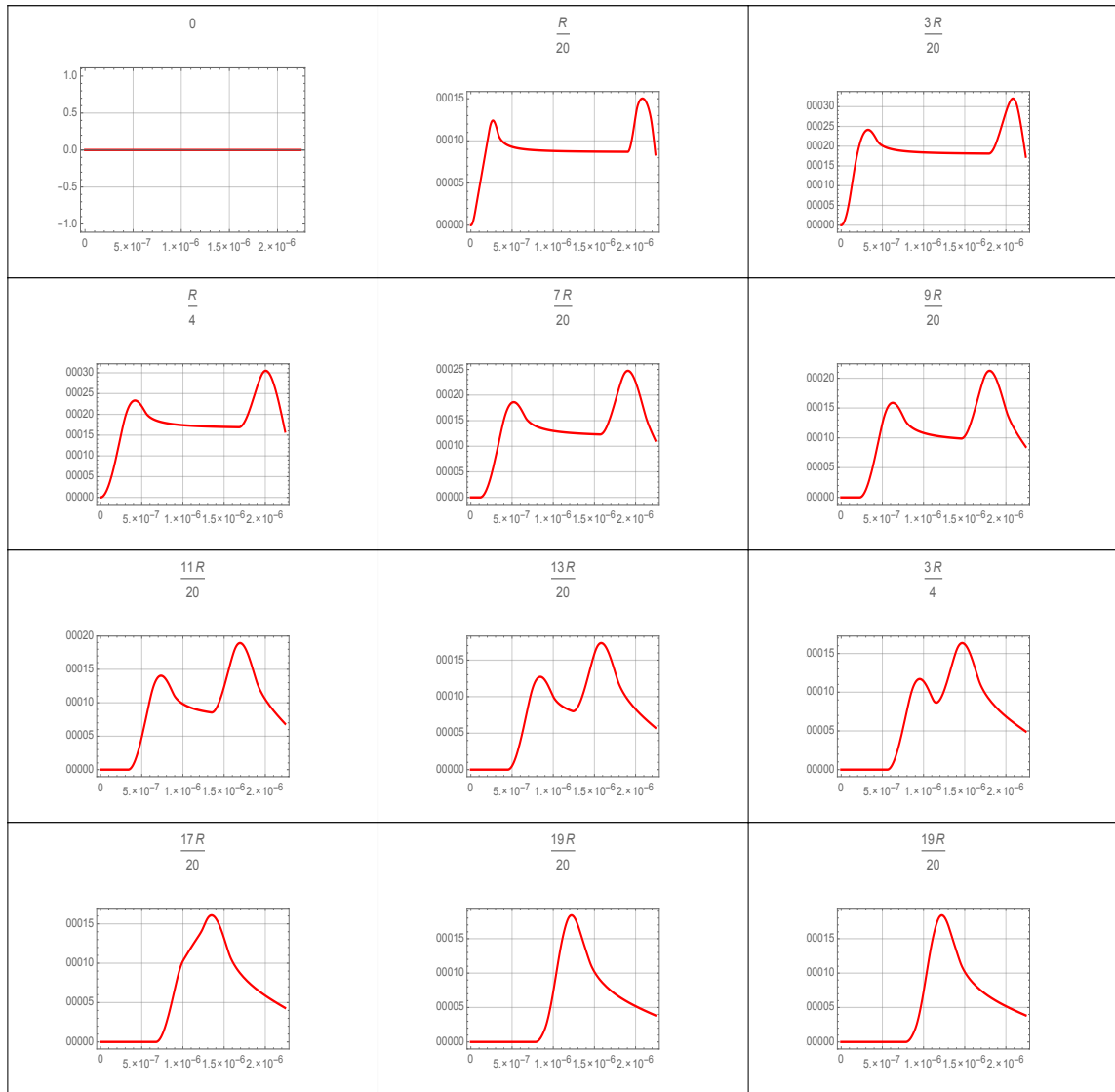
B.2.3 P (Pa) versus t (s) for different r (m)

Each plot in this subsection depicts evolution of the pressure acoustic wave P (normalised by $\Gamma \frac{Q_0}{V_0}$ [Pa]) in time t [s] and at different radial points in the disc (r [m]). The label at the top of each plot represents the point in the disc, where R is the radius of the disc (see Table B.1 for parameters).



B.2.4 u (m) versus t (s) for different r (m)

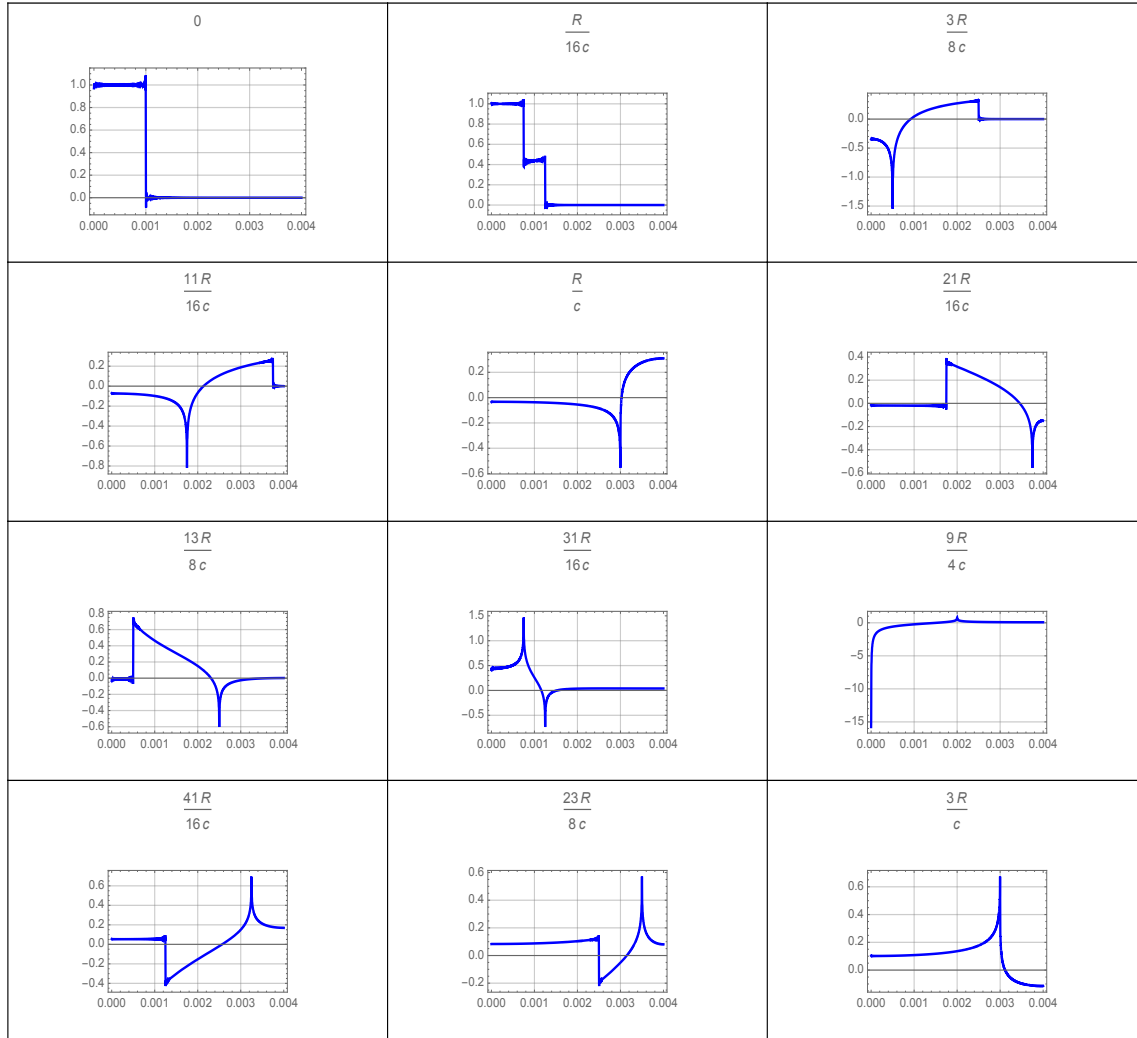
Each plot in this subsection depicts evolution of the displacement acoustic wave u (normalised by $\frac{\Gamma Q_0}{\rho_0 V_0 c_s^2}$ [m]) in time t [s] and at different radial points in the disc (r [m]). The label at the top of each plot represents the point in the disc, where R is the radius of the disc (see Table B.1 for parameters).



B.3 Neumann BC with Uniform Energy Distribution

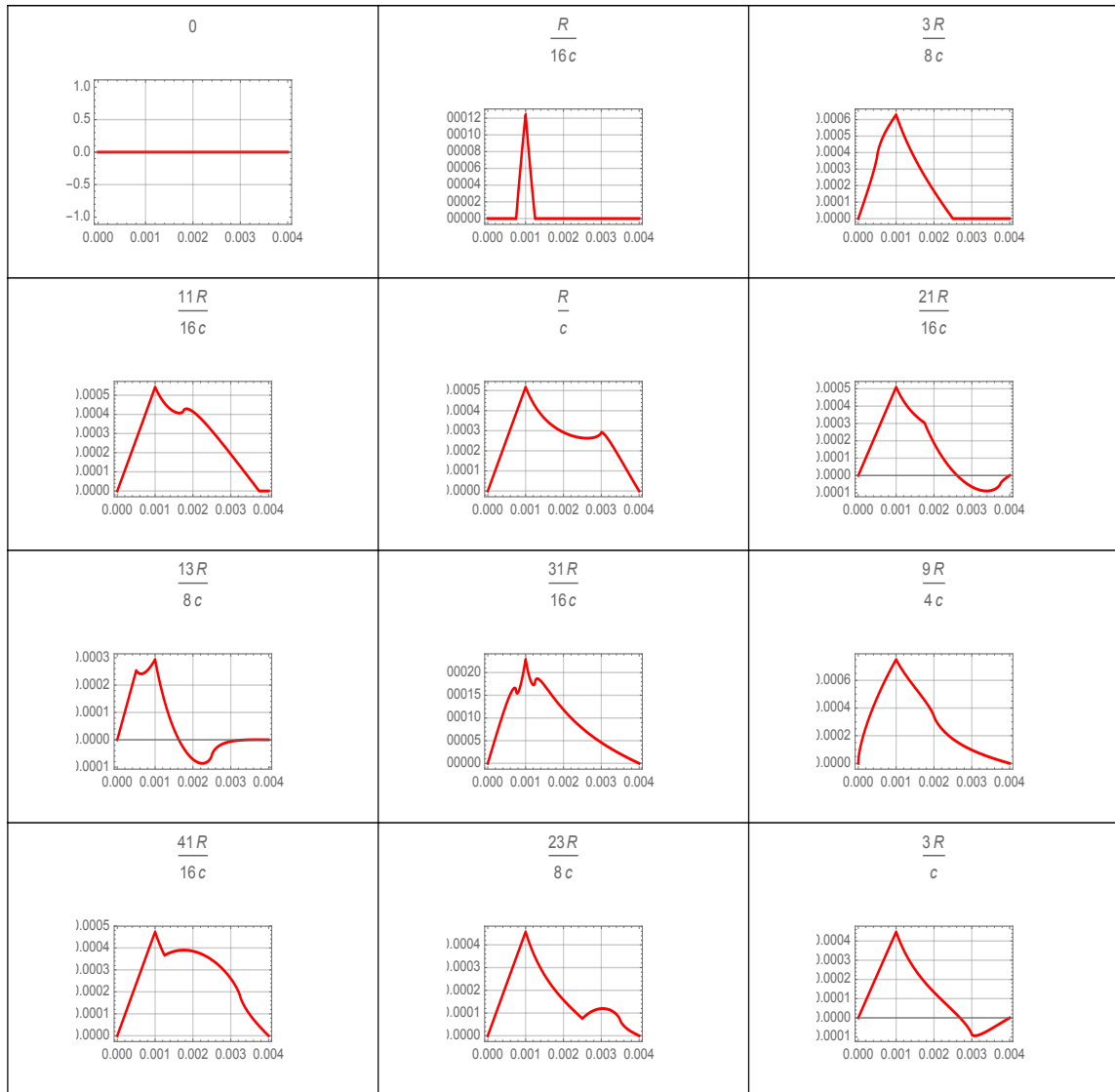
B.3.1 P (Pa) versus r (m) for different t (s)

Each plot in this subsection depicts variation of the pressure acoustic wave P (normalised by $\Gamma \frac{Q_0}{V_0}$ [Pa]) along the radius of the disc r [m] and at different time shots (t [s]). The label at the top of each plot represents the time shot, where R is the radius of the disc and c is the speed of sound in the material (see Table B.1 for parameters).



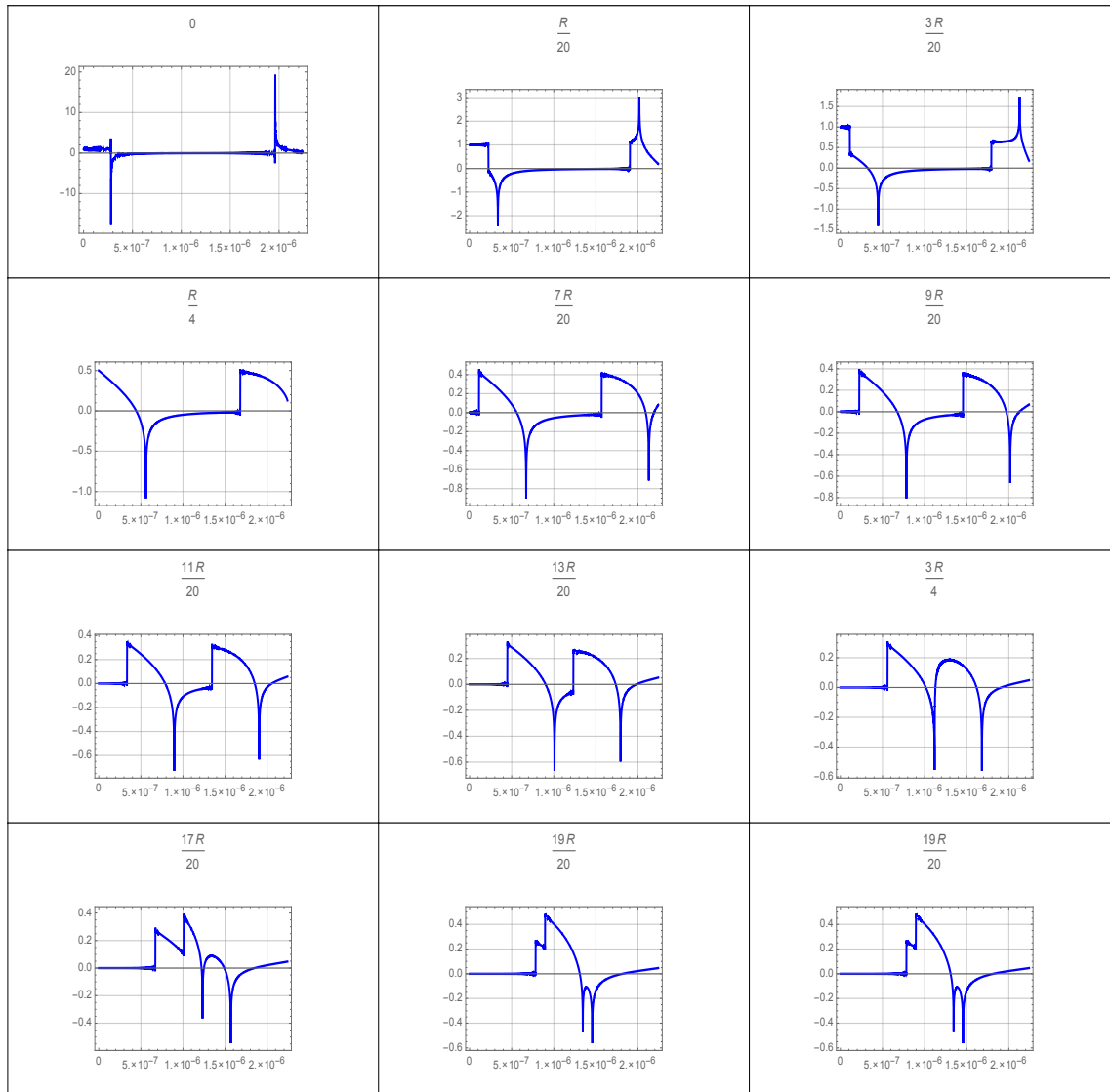
B.3.2 u (m) versus r (m) for different t (s)

Each plot in this subsection depicts variation of the displacement acoustic wave u (normalised by $\frac{\Gamma Q_0}{\rho_0 V_0 c_s^2}$ [m]) along the radius of the disc r [m] and at different time shots (t [s]). The label at the top of each plot represents the time shot, where R is the radius of the disc and c is the speed of sound in the material (see Table B.1 for parameters).



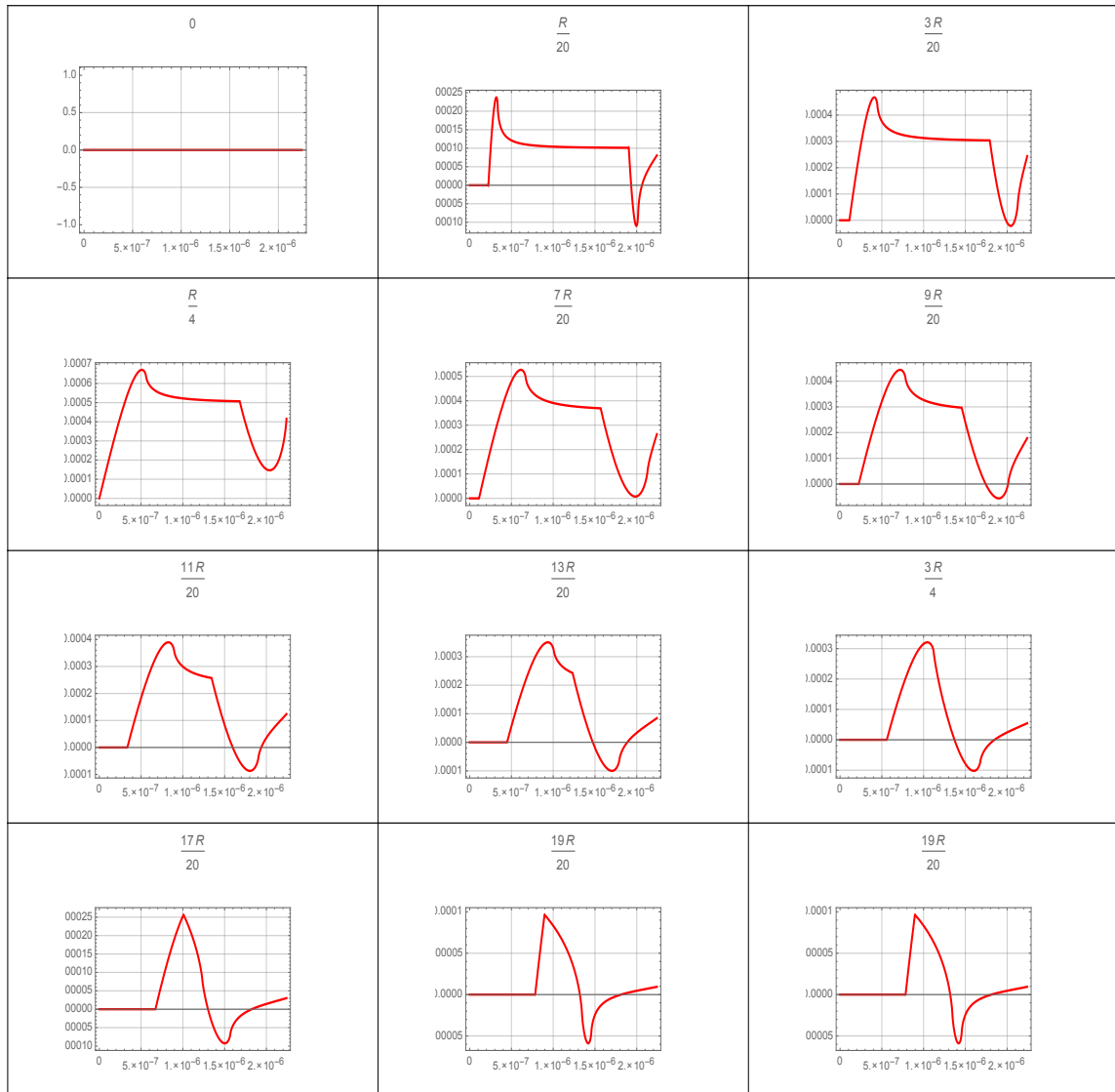
B.3.3 P (Pa) versus t (s) for different r (m)

Each plot in this subsection depicts evolution of the pressure acoustic wave P (normalised by $\Gamma \frac{Q_0}{V_0}$ [Pa]) in time t [s] and at different radial points in the disc (r [m]). The label at the top of each plot represents the point in the disc, where R is the radius of the disc (see Table B.1 for parameters).



B.3.4 u (m) versus t (s) for different r (m)

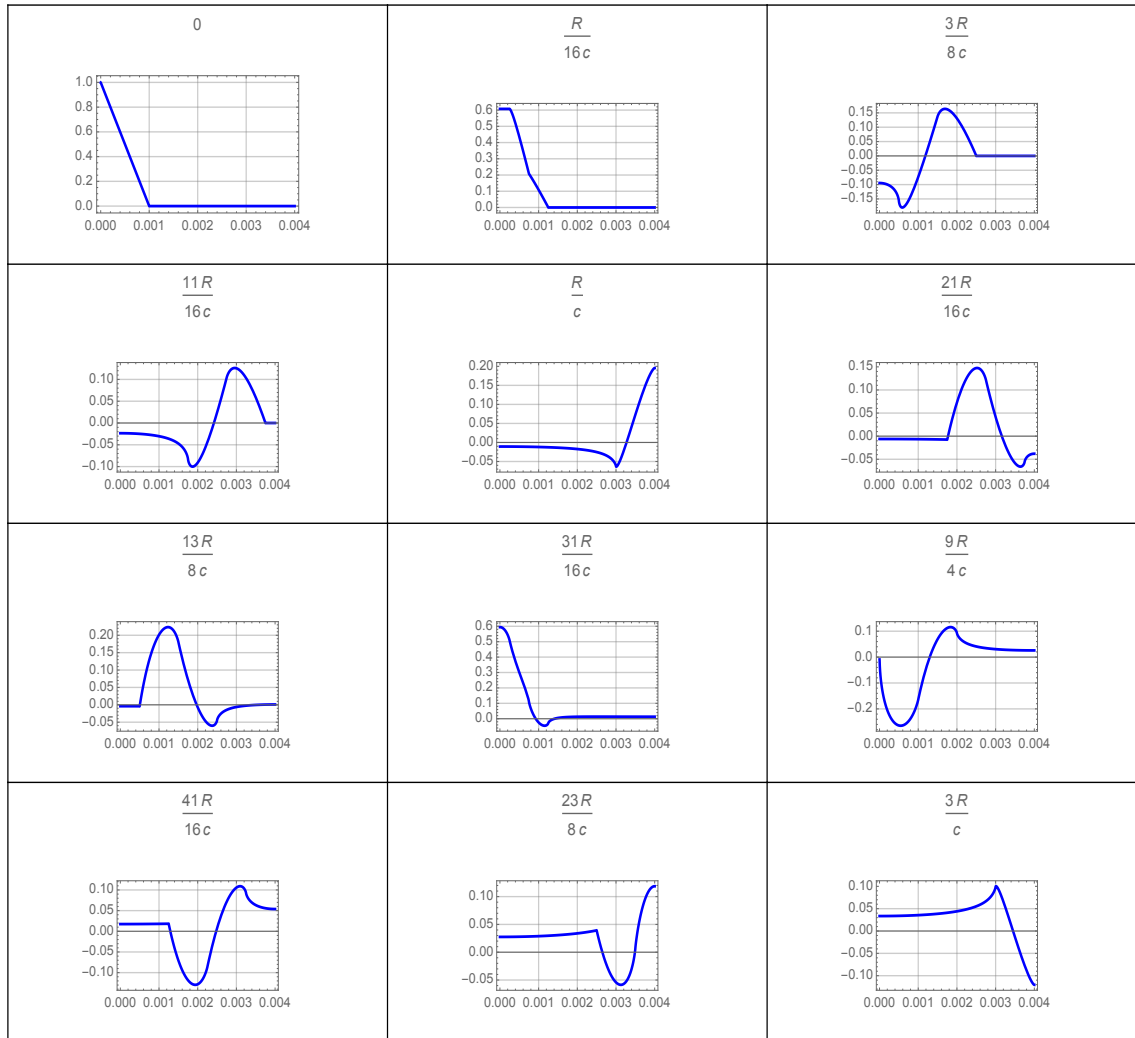
Each plot in this subsection depicts evolution of the displacement acoustic wave u (normalised by $\frac{\Gamma Q_0}{\rho_0 V_0 c_s^2}$ [m]) in time t [s] and at different radial points in the disc (r [m]). The label at the top of each plot represents the point in the disc, where R is the radius of the disc (see Table B.1 for parameters).



B.4 Neumann BC with Linear Energy Distribution

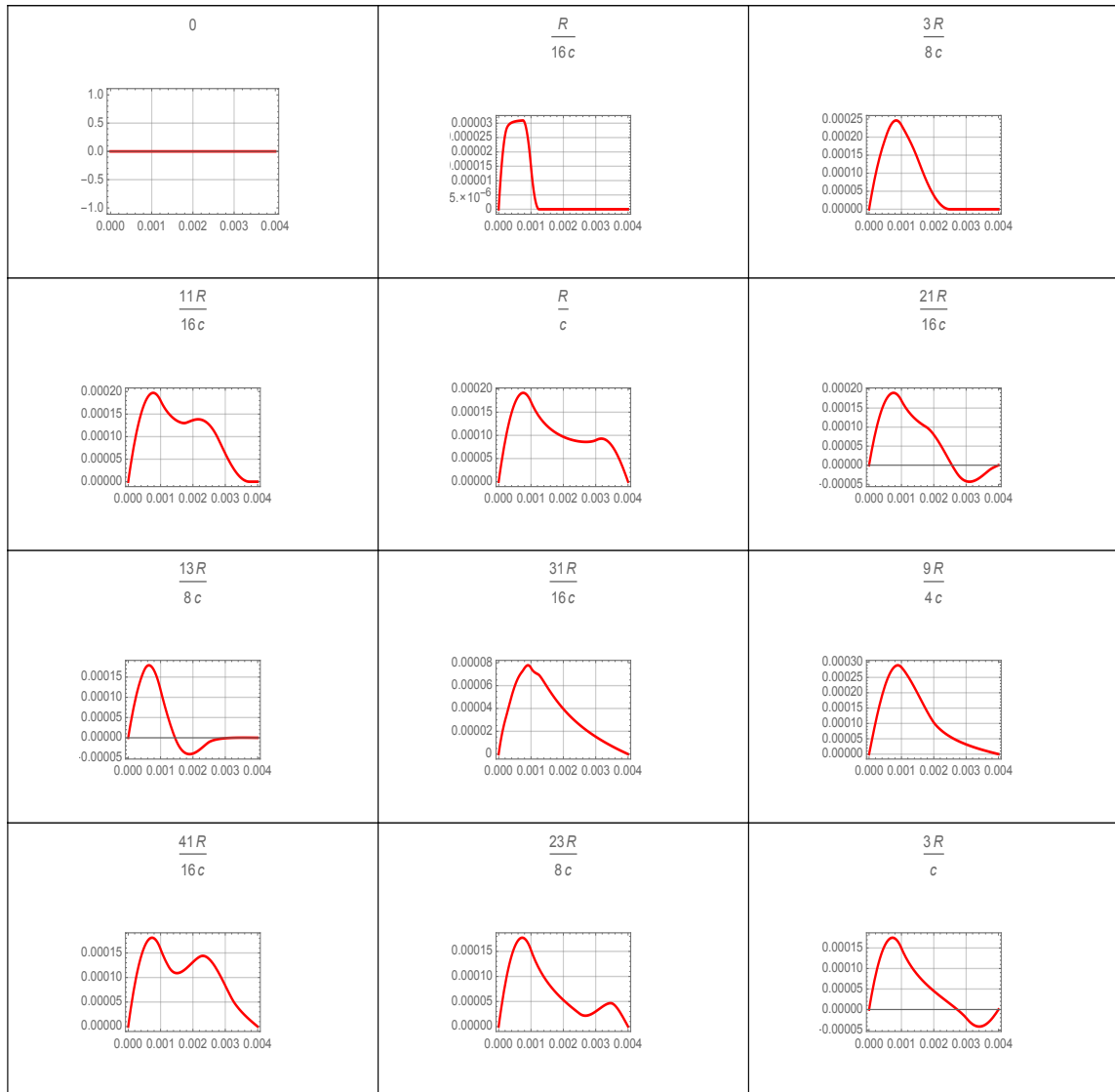
B.4.1 P (Pa) versus r (m) for different t (s)

Each plot in this subsection depicts variation of the pressure acoustic wave P (normalised by $\Gamma \frac{Q_0}{V_0}$ [Pa]) along the radius of the disc r [m] and at different time shots (t [s]). The label at the top of each plot represents the time shot, where R is the radius of the disc and c is the speed of sound in the material (see Table B.1 for parameters).



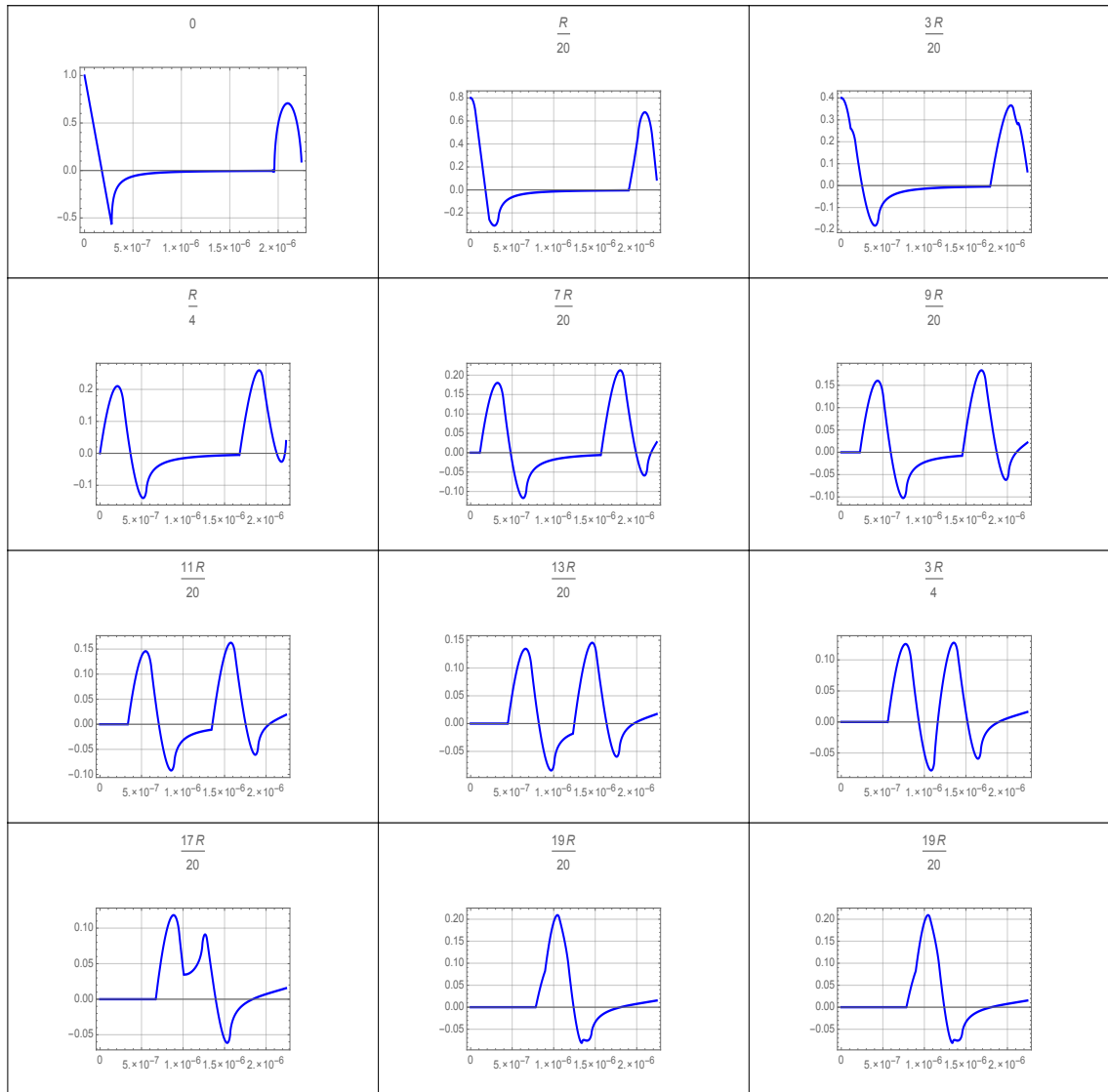
B.4.2 u (m) versus r (m) for different t (s)

Each plot in this subsection depicts variation of the displacement acoustic wave (normalised by $\frac{\Gamma Q_0}{\rho_0 V_0 c_s^2}$ [m]) along the radius of the disc r [m] and at different time shots (t [s]). The label at the top of each plot represents the time shot, where R is the radius of the disc and c is the speed of sound in the material (see Table B.1 for parameters).



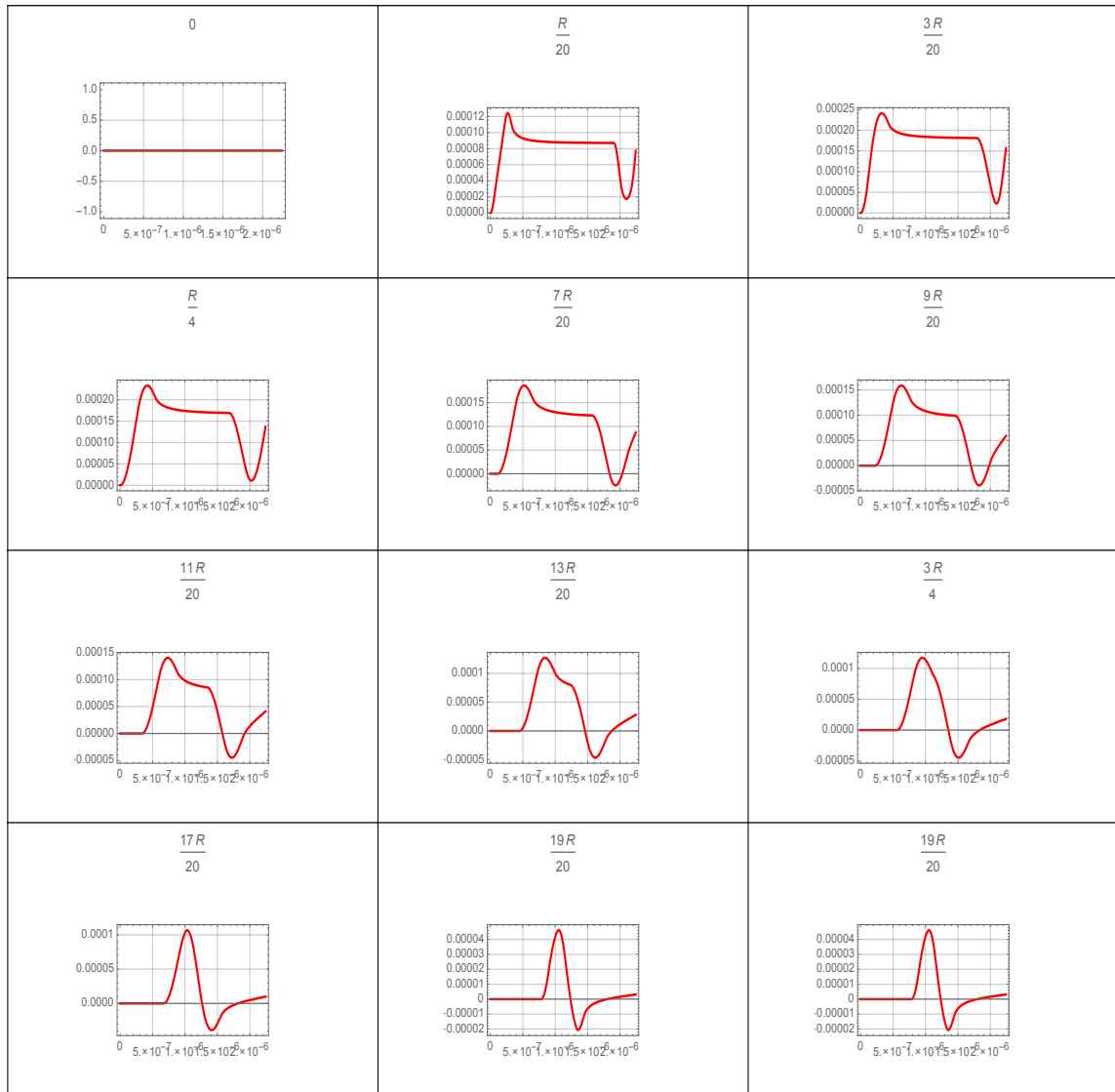
B.4.3 P (Pa) versus t (s) for different r (m)

Each plot in this subsection depicts evolution of the pressure acoustic wave (normalised by $\Gamma \frac{Q_0}{V_0}$ [Pa]) in time t [s] and at different radial points in the disc (r [m]). The label at the top of each plot represents the point in the disc, where R is the radius of the disc (see Table B.1 for parameters).



B.4.4 u (m) versus t (s) for different r (m)

Each plot in this subsection depicts evolution of the displacement acoustic wave u (normalised by $\frac{\Gamma Q_0}{\rho_0 V_0 c_s^2}$ [m]) in time t [s] and at different radial points in the disc (r [m]). The label at the top of each plot represents the point in the disc, where R is the radius of the disc (see Table B.1 for parameters).



Appendix C

Simulation Results for SLC Target

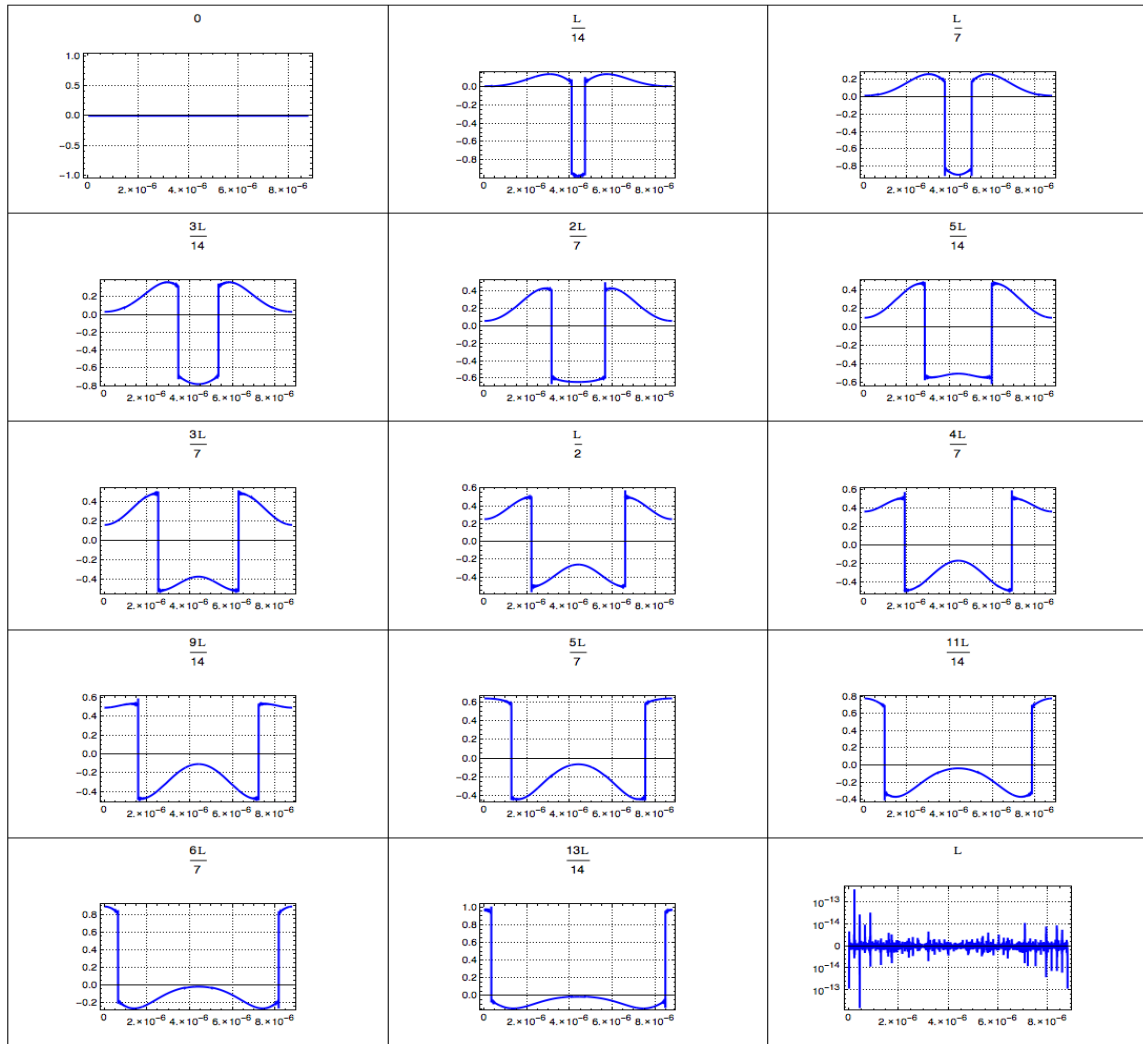
Table C.1: *SLC Target Material and Beam Parameters. Ref.: [34]* (same as Table 6.1)

Parameters	Symbol	Units	Value
Target Length	L	m	0.0205
Target Radius	R	m	0.0317
Standard deviation	σ_z	m	0.0062
mean	B	m	0.0205
beam spot size	σ	mm	0.8
Peak Energy Density Dep.	$\frac{Q_0}{V_0}$	J/m ³	5.91×10^8 [34]
Grüneisen Coef.	Γ		2.095
Initial Press.	$\Gamma \frac{Q_0}{V_0}$	Pa	1.24×10^9
Density	ρ	Kg/m ³	19700
Speed of sound	c_s	m/s	4671.982

C.1 Thin Rod Approximation

C.1.1 Dirichlet BC with Normal Energy Distribution: P (Pa) versus t (s) for different z (m)

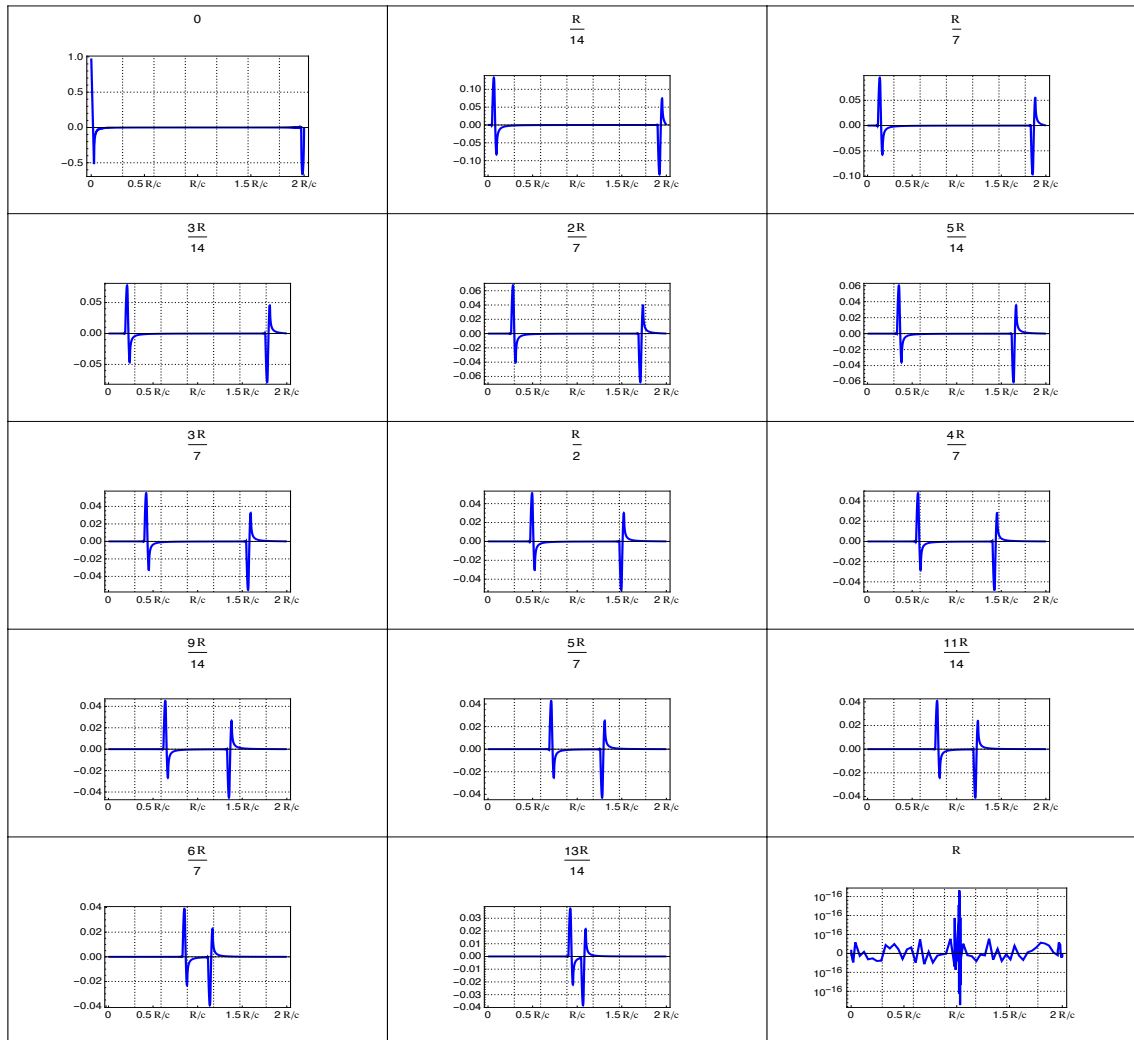
Each plot in this subsection depicts evolution of the pressure acoustic wave P (normalised by 1.24 GPa) in time t [s] and at different points in the thin rod (z [m]). The label at the top of each plot represents the point in the thin rod, where L is the thickness of the target (see Table C.1 for parameters).



C.2 Disc Approximation

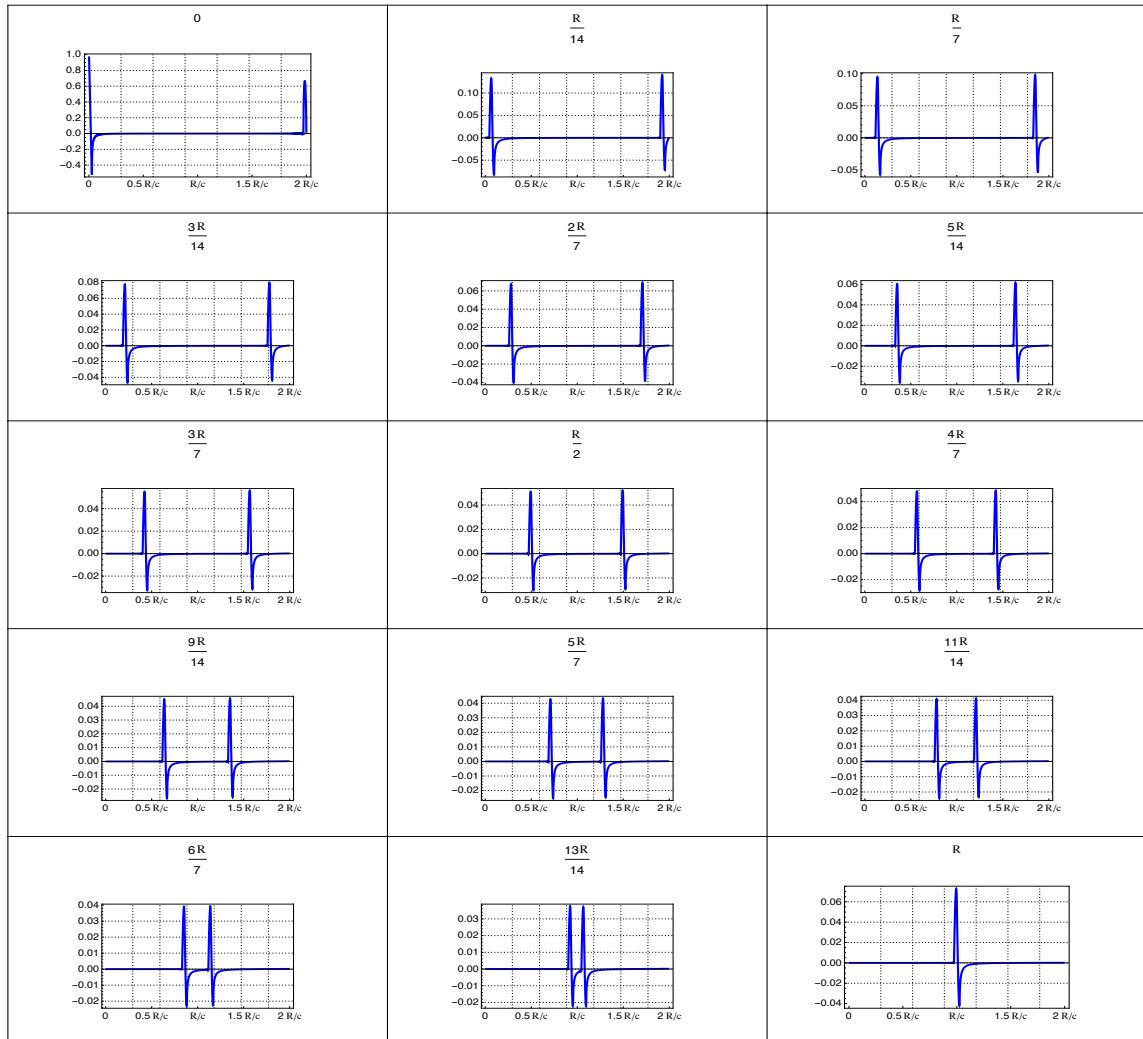
C.2.1 Dirichlet BC with Linear Energy Distribution: P (Pa) versus t (s) for different r (m)

Each plot in this subsection depicts evolution of the pressure acoustic wave P (normalised by 1.24 GPa) in time t [s] and at different radial points in the disc (r [m]). The label at the top of each plot represents the point in the disc, where R is the radius of the disc (see Table C.1 for parameters).



C.2.2 Neumann BC with Linear Energy Distribution: Pressure (Pa) versus time (s) for different r (m)

Each plot in this subsection depicts evolution of the pressure acoustic wave P (normalised by 1.24 GPa) in time t [s] and at different radial points in the disc (r [m]). The label at the top of each plot represents the point in the disc, where R is the radius of the disc (see Table C.1 for parameters).



Appendix D

Simulation Results for ILC Target

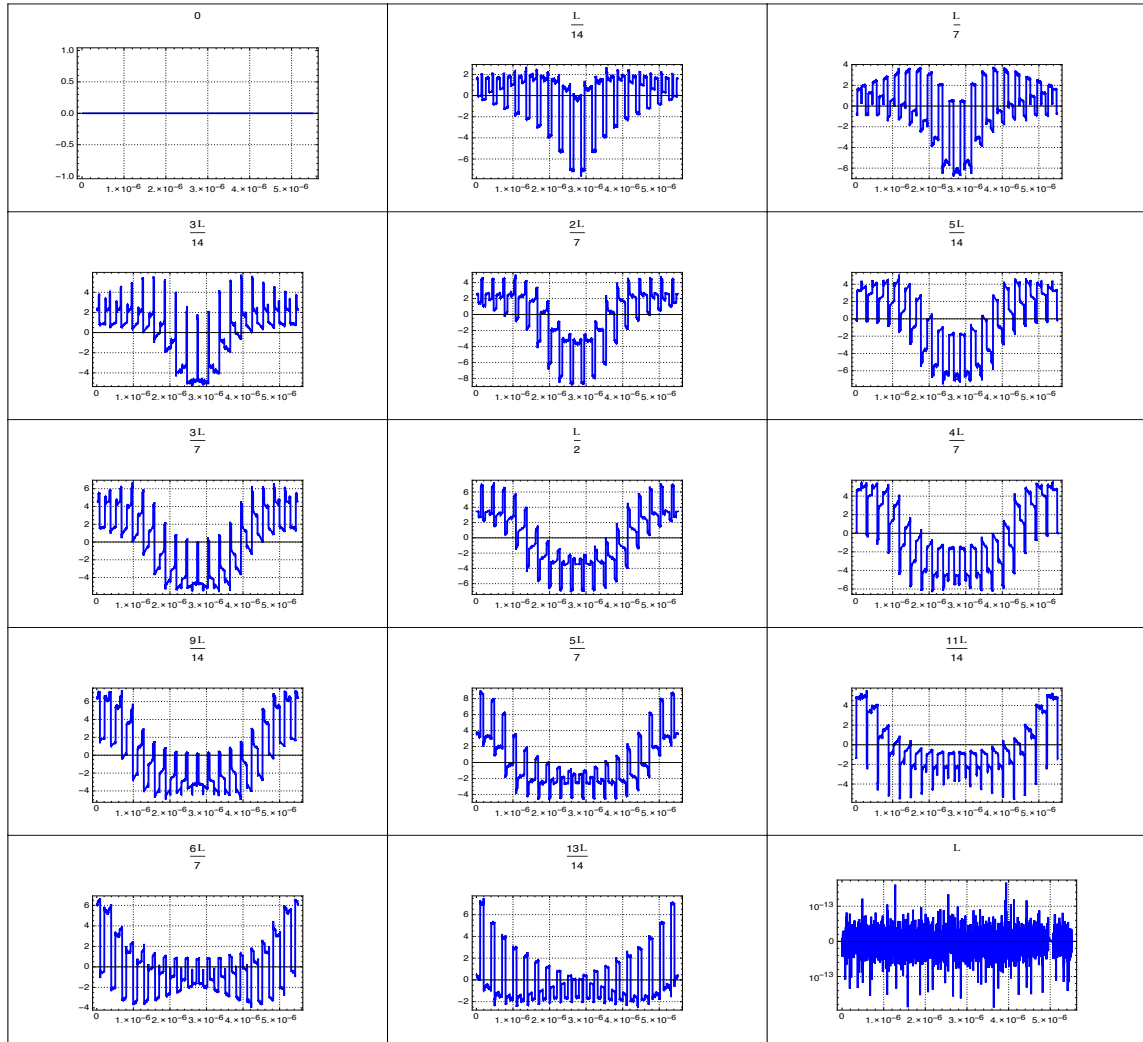
Table D.1: ILC Target Material and BeamParameters (same as Table 6.3)

Parameters	Symbol	Units	Value
Target Thickness	L	m	0.014
Target Radius	R	m	0.01
Standard deviation	σ_z	m	0.003
mean	B	m	0.014
beam spot size	r_0	m	0.003
bunch spacing	T_b	ns	300
Peak Energy Density Dep.	$\frac{Q_0}{V_0}$	J/m ³	1.8×10^6 [1]
Grüneisen Coef.	Γ		1.262
Density	ρ	Kg/m ³	4430
Initial Press.	$\Gamma \frac{Q_0}{V_0}$	Pa	2.2×10^6
Speed of sound	c	m/s	5072.833
Ultimate Tensile Strength	UTS	MPa	950 [5]

D.1 Thin Rod Approximation

D.1.1 Dirichlet BC with Normal Energy Distribution: P (Pa) versus t (s) for different z (m)

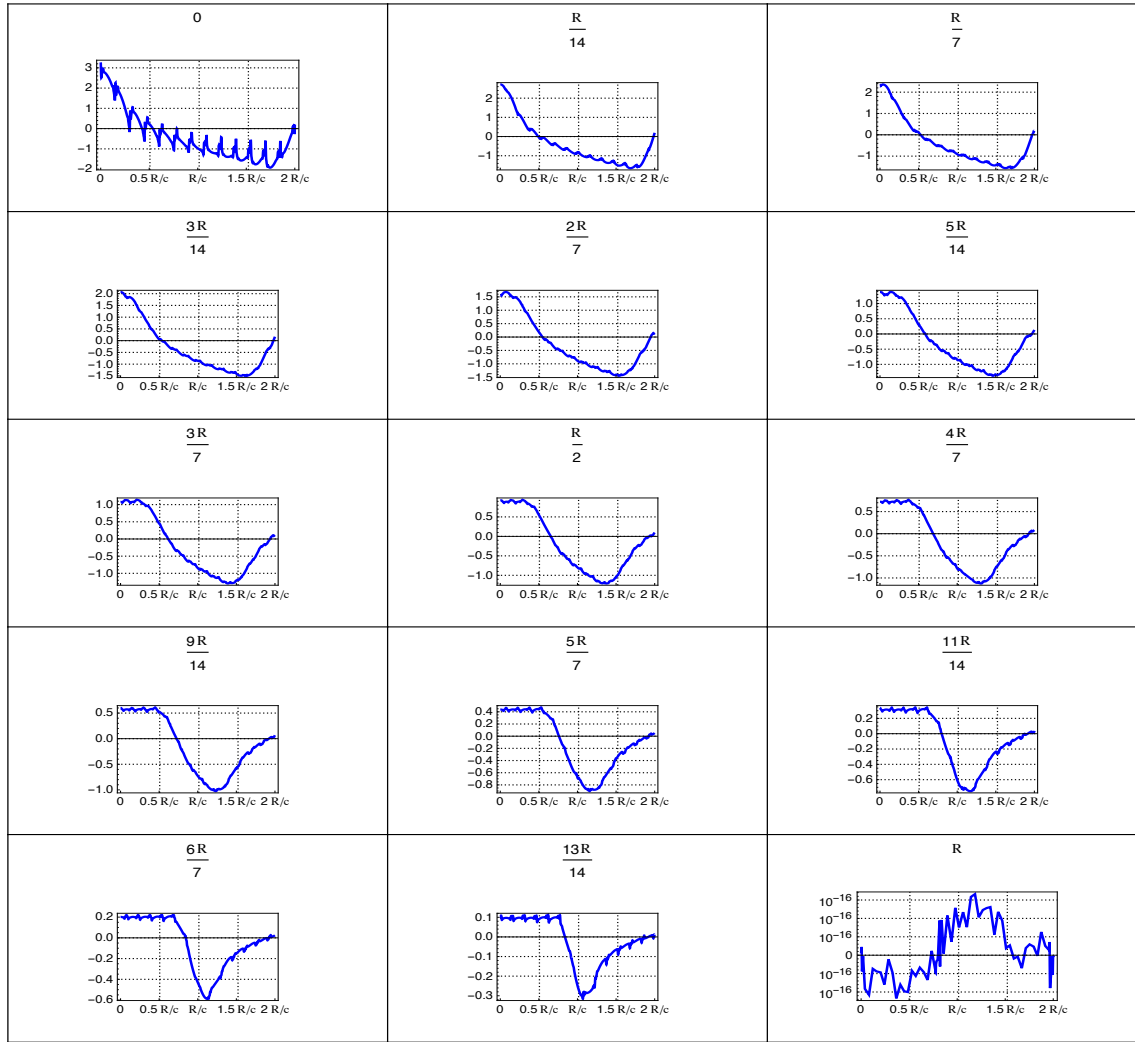
Each plot in this subsection depicts evolution of the pressure acoustic wave P (normalised by 2.2 MPa) in time t [s] and at different points in the thin rod (z[m]) after 100 bunches are deposited on the target. The label at the top of each plot represents the point in the thin rod, where L is the thickness of the target (see Table D.1 for parameters).



D.2 Disc Approximation

D.2.1 Dirichlet BC with Linear Energy Distribution: Pressure (Pa) versus time (s) for different r (m)

Each plot in this subsection depicts evolution of the pressure acoustic wave P (normalised by 2.2 MPa) in time t [s] and at different radial points in the disc (r [m]) after 100 bunches are deposited on the target. The label at the top of each plot represents the point in the disc, where R is the radius of the disc (see Table D.1 for parameters).



D.2.2 Neumann BC with Linear Energy Distribution: Pressure (Pa) versus time (s) for different r (m)

Each plot in this subsection depicts evolution of the pressure (P [Pa]) acoustic wave (normalised by 2.2 MPa) in time t [s] and at different radial points in the disc (r [m]) after 100 bunches are deposited on the target. The label at the top of each plot represents the point in the disc, where R is the radius of the disc (see Table D.1 for parameters).

